Ministry of Education and Science of the Russian Federation
Saint Petersburg National Research University of Information
Technologies, Mechanics, and Optics

NANOSYSTEMS:

PHYSICS, CHEMISTRY, MATHEMATICS

2018, volume 9(5)

Наносистемы: физика, химия, математика
2018, том 9, № 5

NANOSYSTEMS:

PHYSICS, CHEMISTRY, MATHEMATICS

Address: University ITMO, Kronverkskiy pr., 49, St. Petersburg 197101, Russia.
Phone: +7(812)312-61-31, **Journal site:** http://nanojournal.ifmo.ru/,
E-mail: popov1955@gmail.com

AIM AND SCOPE

The scope of the journal includes all areas of nano-sciences. Papers devoted to basic problems of physics, chemistry, material science and mathematics inspired by nanosystems investigations are welcomed. Both theoretical and experimental works concerning the properties and behavior of nanosystems, problems of its creation and application, mathematical methods of nanosystem studies are considered.

The journal publishes scientific reviews (up to 30 journal pages), research papers (up to 15 pages) and letters (up to 5 pages). All manuscripts are peer-reviewed. Authors are informed about the referee opinion and the Editorial decision.

CONTENT

NANOSYSTEMS: PHYSICS, CHEMISTRY, MATHEMATICS, 2018, 9 (5), P. 581–585

New extended Jacobi elliptic function expansion scheme for wave-wave interaction in ionic media

Ram Dayal Pankaj[1*], Bhawani Singh[1], Arun Kumar[2]

[1]Department of Mathematics, J. N. V. University, Jodhpur, India
[2]Department of Mathematics, Government College Kota, Kota (Raj.), India

*drrdpankaj@yahoo.com

DOI 10.17586/2220-8054-2018-9-5-581-585

New Jacobi Elliptic functions expansion scheme, more general than the hyperbolic tangent function method, is derived to construct the exact wave solutions in terms of Jacobi Elliptic functions. The coupled 1D nonlinear Schrödinger–Zakharov (CNLSZ) system is taken as the model equation for wave-wave interaction in ionic media. It is shown that more new solutions can be obtained at their limit condition.

Keywords: the coupled 1D nonlinear Schrödinger–Zakharov (CNLSZ) system, Jacobi elliptic function expansion scheme, hyperbolic tangent function expansion.

Received: 16 May 2018

Revised: 6 August 2018

1. Introduction

It is well known that nonlinear physical phenomena are related to nonlinear partial differential equations, which are employed in natural and applied science fields such as fluid dynamics, plasma physics, biology, etc. One of the most fundamental and charming phenomena in plasma physics is Langmuir turbulence [1,2]. Although, in the low-amplitude linear limit, this turbulence consists only of high-frequency electron oscillations, the presence of larger amplitude waves induces nonlinearities which couple the high-frequency electron oscillations to low-frequency ion oscillations. These nonlinearities lead to parametric instabilities, including a three-wave interaction called the parametric decay instability and a four-wave interaction called the modulational instability or oscillating two stream instability [3]. The strongly nonlinear state leads to the formation of coherent structures called solitons [4]; these structures are stable in one dimension and can collapse catastrophically in two or three dimensions [5–9]. Zakharov [5] introduced a relatively simple set of fluid equations to describe all of these physical phenomena. In the single spatial dimension, the Zakharov equations are:

$$\begin{aligned} iE_t + E_{xx} - \eta E = 0, \\ \eta_{tt} - \eta_{xx} - |E|^2_{xx} = 0, \end{aligned} \tag{1}$$

where t is dimensionless time, x is dimensionless distance, $E(x,t)$ is the dimensionless slowly varying envelope of the high-frequency electric field, and $\eta\,(x,t)$ is the dimensionless low-frequency density variation. The numerical and analytic study of the properties of equation (1) is a very active area of research in fundamental plasma physics [5–13]. Much effort has been spent on the construction of exact solutions of nonlinear equations for their important role in understanding the nonlinear problems. Physically, the wave-wave interaction or the wave collisions are common phenomena in science and engineering for both solitary and non-solitary waves. At the classical level, a set of coupled nonlinear wave equations describing the interaction between high-frequency Langmuir waves and low-frequency ion-acoustic waves were firstly derived by Zakharov [5]. Since then, this system has been the subject of a large number of studies. Currently, there are many methods of constructing exact solutions, for instance, the inverse scattering transform [14], the Hirota method [15], the Backlund method [16], the extended tanh-function method [17], the variational method [18], the Adomian methods decomposition method [19–22] and several other numerical [23–27]. In this article, we will present some new solutions of Jacobi elliptic function type of CNLSZ equation by using an extended Jacobi elliptic function method.

2. The extended Jacobi elliptic function expansion method

We now present briefly the main steps of the extended Jacobi elliptic function expansion strategy that will be applied. Consider a given (second order and cubic nonlinear) nonlinear wave equation

$$P\left(u, u_t, u_x, u_{tt}, u_{xx}, ...\right) = 0, \tag{2}$$

can be converted to an ODE

$$P\left(u, u', u'', u''', ...\right) = 0, \tag{3}$$

upon using a wave variable $\xi = \alpha\left(x - ct\right)$, where α and c are the wave number and wave speed, respectively equation (3) is then integrated as long as all terms contain derivatives where integration constants are considered zeros. Introducing a new independent variable $Y = Y\left(\xi\right)$, by the Jacobi elliptic function expansion method, $Y\left(\xi\right)$ can be expressed as a finite series of Jacobi elliptic functions,

$$Y\left(\xi\right) = \sum_{i=0}^{n} a_i \left(sn\left(\xi\right) + \lambda dn\left(\xi\right)\right)^i \tag{4}$$

is made and $a_i (i = 1, 2, 3, \ldots n)$ and $\lambda \neq 0$ are constant. Its highest degree is $O\left\{Y\left(\xi\right)\right\} = n$, n is positive number can be determined by consisting the homogeneous balance the highest order derivative and highest nonlinear appearing the ODE.

$sn\left(\xi\right) = sn\left(\xi, m\right)$, $dn\left(\xi\right) = dn\left(\xi, m\right)$ and $cn\left(\xi\right) = cn\left(\xi, m\right)$ are the Jacobi elliptic function with modulus m, where $0 < m < 1$. These functions satisfy the following formulas:

$$sn^2\left(\xi\right) + cn^2\left(\xi\right) = 1, \quad dn^2\left(\xi\right) + m^2 sn^2\left(\xi\right) = 1 \quad \text{and} \quad sn'\left(\xi\right) = cn\left(\xi\right) dn\left(\xi\right), \quad dn'\left(\xi\right) = -m^2 cn\left(\xi\right) sn\left(\xi\right).$$

These functions degenerate into hyperbolic functions when $m > 1$ as follows:

$$sn\left(\xi\right) \to \tanh\left(\xi\right), \quad cn\left(\xi\right) \to \sec h\left(\xi\right), \quad dn\left(\xi\right) \to \sec h\left(\xi\right).$$

We can select n in (4) to balance the derivative term of the highest order and the nonlinear term. So, the Jacobi elliptic function expansion method is more general than the hyperbolic tangent function expansion method.

3. Application extended Jacobi elliptic function expansion method for CNLSZ system

We introduce a transformation for (GZE) equation (1):

$$E\left(x, t\right) = U\left(\xi\right) e^{i\theta}, \quad \eta\left(x, t\right) = V\left(\xi\right),$$

$$\theta = kx - \omega t, \quad \xi = p\left(x - 2kt\right),$$

where k, ω and p are real constant. Put these transformation in equation (1), we have the ordinary differential equation (ODE) for $U\left(\xi\right)$ and $V\left(\xi\right)$:

$$\begin{gathered} p^2 U''\left(\xi\right) - U\left(\xi\right)\left(k^2 - \omega\right) - V\left(\xi\right) U\left(\xi\right) = 0, \\ \left(4k^2 - 1\right) V''\left(\xi\right) + U''\left(\xi\right) = 0, \end{gathered} \tag{5}$$

where prime denotes the differential with respect to ξ. Integration of second equation of system (5) twice with respect to ξ affords:

$$V\left(\xi\right) = \frac{C_1 - U^2\left(\xi\right)}{\left(4k^2 - 1\right)}, \tag{6}$$

where C is second integration constant and the first one is taken to zero. The value of $V\left(\xi\right)$ is put in first equation (5):

$$\begin{gathered} p^2 U''\left(\xi\right) - U\left(\xi\right)\left(k^2 - \omega + \frac{C_1}{4k^2 - 1}\right) + \frac{U^3\left(\xi\right)}{4k^2 - 1} = 0, \\ AU''\left(\xi\right) - \beta U\left(\xi\right) + cU^3\left(\xi\right) = 0, \end{gathered} \tag{7}$$

where $\beta = \left(k^2 - \omega + \dfrac{C_1}{4k^2 - 1}\right)$, $c = \dfrac{1}{4k^2 - 1}$, $A = p^2$ is obtained after integrating the ODE once and setting the constant of integration equal to zero. Balancing U'' with U^3 in equation (7) gives $m + 2 = 3m$ i.e. $m = 1$.

The new Jacobi elliptic function expansion method (5) admits the use of the finite expansion:

$$U\left(\xi\right) = a_0 + a_1 sn\left(\xi\right) + a_1 \lambda dn\left(\xi\right). \tag{8}$$

Substituting equation (8) into equation (7) and:

$$A\left[-\left(1+m^2\right)a_1 sn\left(\xi\right)+2m^2 sn^3\left(\xi\right)+\left(2-m^2\right)a_1 dn\left(\xi\right)-2a_1\lambda dn^3\left(\xi\right)\right]-\beta\left[a_0+a_1 sn\left(\xi\right)+a_1\lambda dn\left(\xi\right)\right]+$$
$$c\left[a_0^3+a_1^3 sn^3\left(\xi\right)+a_1^3\lambda^3 dn^3\left(\xi\right)+3a_1^3\lambda sn^2\left(\xi\right)dn\left(\xi\right)+3a_1^3\lambda^2 sn\left(\xi\right)dn^2\left(\xi\right)+3a_0^2 a_1 sn\left(\xi\right)+\right.$$
$$\left.3\lambda a_0^2 a_1\lambda dn\left(\xi\right)+3a_1^2 a_0 sn^2\left(\xi\right)+6a_1^2 a_0\lambda sn\left(\xi\right)dn\left(\xi\right)+3a_1^2 a_0\lambda dn^2\left(\xi\right)\right]=0$$

equating all coefficients with the powers in $sn\left(\xi\right)$, $dn\left(\xi\right)$ and constant setting each of the obtained coefficients for functions to zero, yields the set of algebraic equations for a_0, a_1, p, k, ω and λ,

$$\begin{aligned}
-\beta a_0+ca_1^3&=0,\\
-\left(1+m^2\right)Aa_1-\beta a_1+c\left(3a_0^2a_1\right)&=0,\\
A\left(\left(2-m^2\right)a_1\right)-\beta a_1\lambda+3c\lambda a_0^2a_1&=0,\\
2Am^2a_1\lambda+ca_1^3&=0,\\
-2Aa_1\lambda+ca_1^3\lambda^3&=0,
\end{aligned}$$

we obtain the sets of solutions.

Solutions – 1:

$$\lambda^2=a_1,\quad a_0^2=\frac{\left(\beta-A(2-m^2)\right)}{3c},\quad a_1^2=\frac{2\beta+A(2-m^2)}{9c}.$$

Thus:

$$U\left(\xi\right)=\sqrt{\frac{(\beta-A(2-m^2))}{3c}}+\sqrt{\frac{2\beta+A(2-m^2)}{9c}}\left\{sn\left(p\left(x-2kt\right)\right)+\lambda dn\left(p\left(x-2kt\right)\right)\right\}. \tag{9}$$

If $m\to 1$ then equation (9):

$$U\left(\xi\right)=\sqrt{\frac{(\beta-A)}{3c}}+\sqrt{\frac{2\beta+A}{9c}}\left\{\tanh\left(p\left(x-2kt\right)\right)+\lambda\sec h\left(p\left(x-2kt\right)\right)\right\}. \tag{10}$$

If $m\to 0$ then equation (9):

$$U\left(\xi\right)=\sqrt{\frac{(\beta-A)}{3c}}+\sqrt{\frac{2\beta+2A}{9c}}\left\{\tan\left(p\left(x-2kt\right)\right)+\lambda\sec\left(p\left(x-2kt\right)\right)\right\}. \tag{11}$$

Solutions – 2:

$$\lambda^2=a_1,\quad a_0^2=\frac{\left(\beta-A(2-m^2)\right)}{3c},\quad a_1^2=\frac{1+m^2}{m^2-2}.$$

Thus:

$$U\left(\xi\right)=\sqrt{\frac{(\beta-A(2-m^2))}{3c}}+\sqrt{\frac{1+m^2}{m^2-2}}\left\{sn\left(p\left(x-2kt\right)\right)+\lambda dn\left(p\left(x-2kt\right)\right)\right\}. \tag{12}$$

If $m\to 1$ then equation (12):

$$U\left(\xi\right)=\sqrt{\frac{(\beta-A)}{3c}}+\sqrt{-2}\left\{\tanh\left(p\left(x-2kt\right)\right)+\lambda\sec h\left(p\left(x-2kt\right)\right)\right\}. \tag{13}$$

If $m\to 0$ then equation (12):

$$U\left(\xi\right)=\sqrt{\frac{(\beta-2A)}{3c}}+\sqrt{-\frac{1}{2}}\left\{\tan\left(p\left(x-2kt\right)\right)+\lambda\sec\left(p\left(x-2kt\right)\right)\right\}. \tag{14}$$

Solutions – 3:

$$\lambda=\pm m,\quad a_1^2=\frac{2A}{m^2c},\quad a_0^2=1-\frac{6A}{\beta m^2}.$$

$$U\left(\xi\right)=\sqrt{1-\frac{6A}{\beta m^2}}+\sqrt{\frac{2A}{m^2c}}\left\{sn\left(p\left(x-2kt\right)\right)\pm mdn\left(p\left(x-2kt\right)\right)\right\}. \tag{15}$$

If $m\to 1$ then equation (15):

$$U\left(\xi\right)=\sqrt{1-\frac{6A}{\beta}}+\sqrt{\frac{2A}{c}}\left\{\tanh\left(p\left(x-2kt\right)\right)\pm\operatorname{sech}\left(p\left(x-2kt\right)\right)\right\}. \tag{16}$$

Solutions – 4:

$$a_1^2=\frac{A\left(m^2-2\right)-2\beta}{3c},\quad a_0^2=\frac{\beta}{c},\quad \lambda^2=\frac{6A+3m^2\left[A\left(m^2-2\right)-2\beta\right]}{\left(A\left(m^2-2\right)-2\beta\right)},$$

$$U(\xi) = \sqrt{\frac{\beta}{c}} + \sqrt{\frac{A(m^2-2)-2\beta}{3c}} \left\{ sn(p(x-2kt)) + \sqrt{\frac{6A+3m^2[A(m^2-2)-2\beta]}{A(m^2-2)-2\beta}} dn(p(x-2kt)) \right\}. \tag{17}$$

If $m \to 1$ then equation (17):

$$U(\xi) = \sqrt{\frac{\beta}{c}} + \sqrt{-\frac{A+2\beta}{3c}} \left\{ \tanh(p(x-2kt)) + \sqrt{\frac{2\beta-3A}{A+2\beta}} \sec h(p(x-2kt)) \right\}. \tag{18}$$

If $m \to 0$ then equation (17):

$$U(\xi) = \sqrt{\frac{\beta}{c}} + \sqrt{-2\frac{(A+\beta)}{3c}} \left\{ \tan(p(x-2kt)) + \sqrt{\frac{-3A}{A+\beta}} \sec(p(x-2kt)) \right\}. \tag{19}$$

4. Conclusion

The Jacobi elliptic function expansion method is proposed and applied to the coupled 1D nonlinear Schrödinger–Zakharov (CNLSZ) system. Using this method, we found some new solutions for the Jacobi elliptic function type that were not obtained by the sine-cosine method, the extended tanh-method, the mapping method, and other methods. In the limiting case of the Jacobi elliptic function (namely, modulus setting 0 or 1), we also obtained the solutions of sin-type, cos-type, tanh-type, sech-type. In the applications, the solutions are completely new and have not found in earlier. But the solutions found in the Ref. [27] are the same to our obtain solutions -3. By means of this scheme, we found some new solutions of the above mentioned equations. Therefore, the scheme can be easily applied to solve the NLDEs and provides some new solutions. The solutions obtained in this article have been verified by plugging them back into the original equation and found correct. It is shown that this scheme can be applied to more coupled equations. So many new shock wave or solitary wave solutions can also be obtained. Actually, this method can be applied to obtain solutions and classify modulational instability to more nonlinear wave equations, as long as the odd- and even-order derivative terms do not coexist in the nonlinear wave equations.

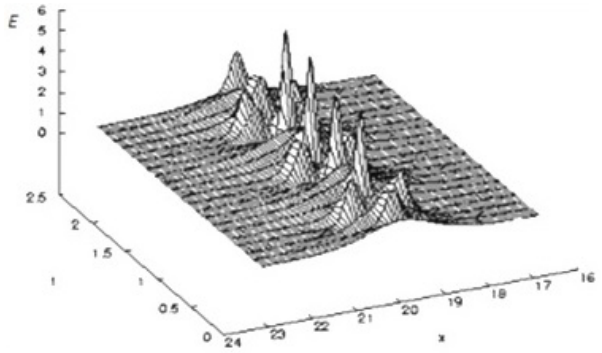

FIG. 1. Exact solitary wave solution of $E(x,t)$ with fixed value of $k = 1/2$ for different values of time

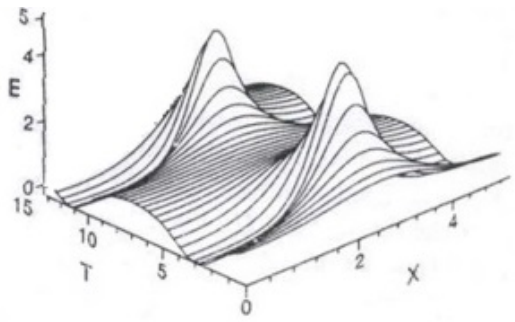

FIG. 2. Time evolution of the Nonlinear equation by the variational approach for $k = 1$

References

[1] Langmuir I. Oscillations in Ionized Gases. *Proc. Natl. Acad. Sci. U.S.A.*, 1928, **14** (8), P. 627–637.

[2] Tonks L., Langmuir I. Oscillations in Ionized Gases. *Physical Review*, 1929, **33**, P. 195–210.

[3] Chen F.F. *Introduction to Plasma Physics*, Plenum, New York, 1974.

[4] Scott C., Chu F.Y.F., Mcglaughlin D.W. The soliton: a new concept in applied science. *Proc. IEEE*, 1973, **61**, P. 1443–1483.

[5] Zakharov V.E. Collapse of Langmuir Waves. *JEPT*, 1972, **35** (5), P. 908–914.

[6] Pereira N.R., Sudan R.N., Denavit J. "Numerical study of two-dimensional generation and collapse of Langmuir solitons. *The Physics of Fluids*, 1977, **20** (6), P. 936–945.

[7] Nicholson D.R., et al. Nonlinear Langmuir waves during type III solar radio bursts. *The Astrophysical Journal*, 1978, **223**, P. 605–619.

[8] Goldman M.V., Nicholson D.R. Virial theory of direct Langmuir collapse. *Physical Review Letters*, 1978, **41** (6), P. 406.

[9] Nicholson R., Goldman M.V. Cascade and collapse of Langmuir waves in two dimensions. *Phys. Fluids*, 1978, **21** (10), P. 1766–1776.

[10] Hasegawa A. Stimulated Modulational Instabilities of Plasma Waves. *Phys. Rev. A*, 1970, **1** (6), P. 1746.

[11] Thyagaraja A. Recurrence, dimensionality, and Lagrange stability of solutions of the nonlinear Schrödinger equation. *Phys. of Fluids*, 1981, **24** (11), P. 1973–1975.

[12] Russell D.A., Ott E. Chaotic (strange) and periodic behavior in instability saturation by the oscillating twostream instability. *The Physics of Fluids*, 1981, **24** (11), P. 1976–1988.

[13] Weatherall J.C., et al. Solitons and ionospheric heating. *Journal of Geophysical Research: Space Physics*, 1982, **87** (A2), P. 823–832.

[14] Vakhnenko V.O., Parkes E.J., Morrison A.J. A Backlund transformation and the inverse scattering transform method for the generalised Vakhnenko equation. *Chaos, Solitons & Fractals*, 2003, **17** (4), P. 683–692.

[15] Ye-peng Sun, Jin-bo Bi, Deng-yuan Chen. N-soliton solutions and double Wronskian solution of the non-isospectral AKNS equation. *Chaos, Solitons & Fractals*, 2005, **26** (3), P. 905–912.

[16] Sakka A. Backland transformations for Painleve I and II equations to Painleve-type equations of second order and higher degree. *Phys. Lett. A*, 2002, **300** (2–3), P. 228–232.

[17] Yao R.X., Li Z.B. New exact solutions for three nonlinear evolution equations. *Phys. Lett. A*, 2002, **297**, P. 196–204.

[18] Kumar A. An analytical solution for a coupled partial differential equation. *Applied Mathematics and Computation*, 2009, **212**, P. 245–250.

[19] Liu Z., Chen C. Compactons in a general compressible hyper elastic rod. *Chaos, Solitons & Fractals*, 2004, **22** (3), P. 627–640.

[20] Kaya D., El-Sayed S.M. An application of the decomposition method for the generalized KdV and RLW equations. *Chaos, Solitons & Fractals*, 2003, **17** (5), P. 869–877.

[21] Hagtae Kim, Dong Pyo Hong, Kil to Chong. A numerical solution of point kinetics equations using the Adomian Decomposition Method. *Systems and Informatics (ICSAI)*, 2012 International Conference on IEEE 19–20 May 2012, 12835470.

[22] Kumar A., Ram D.P. Solitary Wave Solutions of Schrödinger Equation by Laplace–Adomian Decomposition Method. *Physical Review & Research International*, 2013, **3** (4), P. 702–712.

[23] Ghoreishi M., Ismail A.I.B., Rashid A. Numerical Solution of Klein–Gordon–Zakharov Equations using Chebyshev Cardinal Functions. *Journal of Computational Analysis & Applications*, 2012, **14** (1), P. 574–582.

[24] Zhao Xiaofei, Ziyi Li. Numerical Methods and Simulations for the Dynamics of One-Dimensional Zakharov-Rubenchik Equations. *Journal of Scientific Computing*, 2013, **59** (2), P. 412–438.

[25] Kumar A., Ram D.P., Manish G. Finite difference scheme of a model for nonlinear wave-wave interaction in ionic media. *Computational Mathematics and Modeling*, 2011, **22** (3), P. 255–265.

[26] Kumar A., Ram D.P. Finite Difference Scheme for the Zakharov Equation as a Model for Nonlinear Wave-Wave Interaction in Ionic Media. *International Journal of Scientific & Engineering Research*, 2014, **5** (2), P. 759–762.

[27] Kumar A., Ram D.P. Solitary Wave Solutions of Schrödinger Equation by Laplace–Adomian Decomposition Method. *Physical Review & Research International*, 2013, **3** (4), P. 702–712.

NANOSYSTEMS: PHYSICS, CHEMISTRY, MATHEMATICS, 2018, 9 (5), P. 586–596

Influence of copper nanoparticle film processing temperature on their structure and electrical properties

N. N. Begletsova[1,2], A. J. K. Al-Alwani[1,3], V. S. Atkin[1], V. P. Sevostyanov[2], E. G. Glukhovskoy[1,2]

[1]Saratov State University, Astrakhanskaya, 83, Saratov, 410012, Russia
[2]Scientifc Research Institute of Technology of Organic, Inorganic Chemistry and Biotechnology, Bolshaya Sadovaya, 239, Saratov, 410005, Russia
[3]Babylon University, Babylon, Iraq

nadya-beg98@yandex.ru, ammarhamlet2013@yahoo.com, ceba91@list.ru, vsevp@mail.ru, glukhovskoy@gmail.com

PACS 61.46.+w, 73.25.+i, 79.60.Bm **DOI 10.17586/2220-8054-2018-9-5-586-596**

This work is devoted to the study of the influence of the additional processing at 100, 200 and 300 °C on the morphology, microrelief, elemental composition of the surface and the electrophysical properties of glass/ITO/copper nanoparticle film structures. Studies have shown that with an increase in the processing temperature of the investigating samples reduces the amount of organic matter protecting the copper particles from oxidation. The conductivity of copper nanoparticles increases. The morphology of the surface and the elemental composition of the samples were studied by scanning electron microscopy. The microrelief of the surface and the measurement of the copper nanoparticles current-voltage characteristics were carried out using a scanning probe microscope in atomic force and scanning tunneling microscopy modes.

Keywords: Copper nanoparticles, surface morphology and microrelief, elemental composition, current-voltage characteristics.

Received: 27 June 2018

Revised: 21 August 2018

1. Introduction

The creation of thin films based on a single component or alternating heterostructures with the desired and controlled properties is one of the more promising directions for the development of modern nanoelectronics. As a component, metallic nanoparticles (NPs), in particular, copper NPs can be used. They are isolated particles with unique physicochemical [1–4] and optical properties [5, 6].

Due to their high thermal and electrical conductivity [1, 2, 7] and mechanical properties [8, 9] compared to macro objects copper NPs can be used in solid state and flexible electronics as an alternative to conductive and expensive noble metals such as gold and silver [2, 7]. The production of conductive pastes and copper inks for the formation of high conductivity structures in multilayer electronic devices, printed circuit boards, hybrid integrated circuits, photonic crystals are a special areas of application for copper NPs [2, 7, 10]. They are also used in the composition of lubricants which reduce friction between the contacting surfaces [8]. Recently copper NPs have been actively used as a material for solar cells [11, 12]. In the near future testing of copper NPs to create metal flexible electrodes of supercapacitors is planned [13].

There are different methods for deposition coating based on copper NPs and their subsequent modification. For example, film deposition in vacuum conditions: chemical vapor deposition (CVD) and physical vapor deposition (PVD) [14, 15], chemical methods of precipitation from solution (Langmuir-Blodgett technology, application in an electric field, etc.) [16, 17] are such methods. In this case, the valence state of copper atoms significantly influences the composition, structure and properties of the resulting films. Depending on this, the conditions for their application and the choice of method can be changed. Thus, it was shown in [14, 15] that the growth of the monoclinic phase of CuO begins to predominate over the cubic phase of Cu_2O with increasing O2 concentration in the gas mixture of the plasma-chemical reactor. For a liquid medium (phase) the change in the degree of oxidation can be carried out by shifting the pH of the subphase [16, 17]. As reported by the authors, the valence of copper ions changed in accordance with a change in the acidity of the aqueous solution, which led to the formation of monolayers and films of different composition and crystal structure.

Copper NPs have the potential of being introduced in electronics. In this area stability and size of particles are important parameters for the practical use them. The stability of copper NPs is important. The stability of the resulting structure or film depends on it. To protect the copper NPs surface from oxidation various stabilizers are used. The use of surfactant leads to a reduction in the aggregation of metal particles. The use of surfactant, along with preventing oxidation of the particle surfaces in air, leads to reduce in their electrical conductivity [5, 18, 19].

Thus, there is a dilemma. At the technological stage, the surfactant stabilizer must be removed from the finished products. The modification of the finished films can be different: ultraviolet (UV) treatment, dissolution, chemical transformation, evaporation in an inert atmosphere and temperature annealing in the presence of oxygen. The use of high treatment temperatures (annealing) in the range of 200 – 300 °C promotes the decomposition and evaporation of the organic layer followed by fusing the metal particles into a single continuous film. In the literature there is information about the dependence of melting temperature on the dimensions of the metal NPs [20], which is directly related to the ratio of surface and bulk energies. But the relationship "melting temperature-particle size" is non-trivial for the case when the surface of the NPs is surfactant-stabilized. This question is a great practical interest. Although it is still unexplored, any data on the heat treatment and transformation of a complex system of copper NPs in the organic matrix in the literature are represented by single articles.

The aim of this work is to study the influence of the temperature of additional processing at 100, 200 and 300 °C of glass/ITO/copper NPs samples on the morphology, microrelief, elemental composition of the surface and the electrophysical properties of film structures on their basis.

2. Experimental

In this work, copper NPs stabilized by surfactant anionic type sodium dodecyl sulfate (SDS) were investigated. The particles were obtained by using the chemical reduction method in micellar solutions of surfactants according to the previously developed procedure [18] at a pH of 11.0 and the molar ratio of the precursor (copper chloride $CuCl_2 \cdot 2H_2O$) and the reducing agent (hydrazine hydrate $N_2H_4 \cdot H_2O$) equal to 1:150.

Before depositing the solution of copper NPs on glass substrates with ITO (Indium Tin Oxide) layer in the form of electrodes sample preparation of the suspension obtained by centrifugation on an Elmi CM 70M centrifuge (Latvia) and decanting the solution to remove excess surfactant was carried out. For this purpose in an eppendorf volume of 2.0 ml, 1.5 ml of a suspension of copper NPs and 0.5 ml of distilled water were placed. Then, for 5 minutes at 5000 rpm the above solution was centrifuged. Then, 1.5 ml of the centrifuged solution was taken out of the eppendorf and the same amount of distilled water was added. Then, for 5 minutes at 5000 rpm, the above solution was centrifuged. The 1.5 ml of the centrifuged solution was again removed by decantation from the eppendorf and the same amount of distilled water was added and centrifuged under the foregoing conditions. After 1.5 ml of the solution was removed by decantation. Within 5 minutes the remaining 0.5 ml was again centrifuged. The resulting solution with copper NPs deposited on the bottom of the eppendorf was applied to a glass/ITO substrate with a track using a BIOHIT Proline dispenser. The samples were dried at room temperature for 16 hours.

Investigations of surface morphology and elemental composition of samples with copper NPs on solid substrates were performed on a scanning electron microscope (SEM) of Tescan Mira II LMU (Czech Republic) equipped with an energy-dispersive microanalysis system INCA Energy 350 using a secondary electron detector (SE – second electron) at an accelerating voltage 20 – 30 kV and pressure in the chamber $5.0 - 6.0 \cdot 10^{-2}$ Pa. Surface microrelief and electrophysical properties of samples with copper NPs were studied on the basis of the scanning probe microscope (SPM) NanoEducator II (NT-MDT, Russia) in the modes of atomic force and scanning tunneling microscopy (AFM and STM), respectively. Scanning of samples by the AFM method was carried out in a semi-contact mode at various locations on the surface with a scanning region of 5×5 μm^2. The recording of current-voltage characteristics (CVC) was performed by using STM at various points of the samples surface under study. The amplitude of the alternating voltage was set equal to $\pm$ properties 3 V.

Studies of the film structures for samples with copper NPs were carried out before and after the temperature treatment. For temperature treatment tiles ICA RCT basic (Germany) was used. Its temperature was controlled and kept constant at 100, 200 or 300 °C. The accuracy of automatic temperature maintenance was ± 5 °C. The sample was annealed at the prescribed temperatures for 10 minutes. After that, it was cooled to room temperature. Then the morphology, surface microrelief, elemental composition and electrophysical properties were studied by SEM, AFM and STM methods.

3. Results and discussion

AFM images of the surface of a glass/ITO/copper NPs sample are shown in Fig. 1. In these images, the profile of the surface areas was investigated and the average roughness (Ra) of the sample surface was determined. The choice of research areas was carried out in such a way that they contained objects of fairly uniform height [21]. In AFM images it is difficult to visually identify individual copper NPs. From the analysis of the images in Fig. 1 shows that with an increase in the values of the temperature treatment from room temperature to 300 °C there is an improvement in the visualization (sharpness of the copper particle faces) of the surface of the film under study.

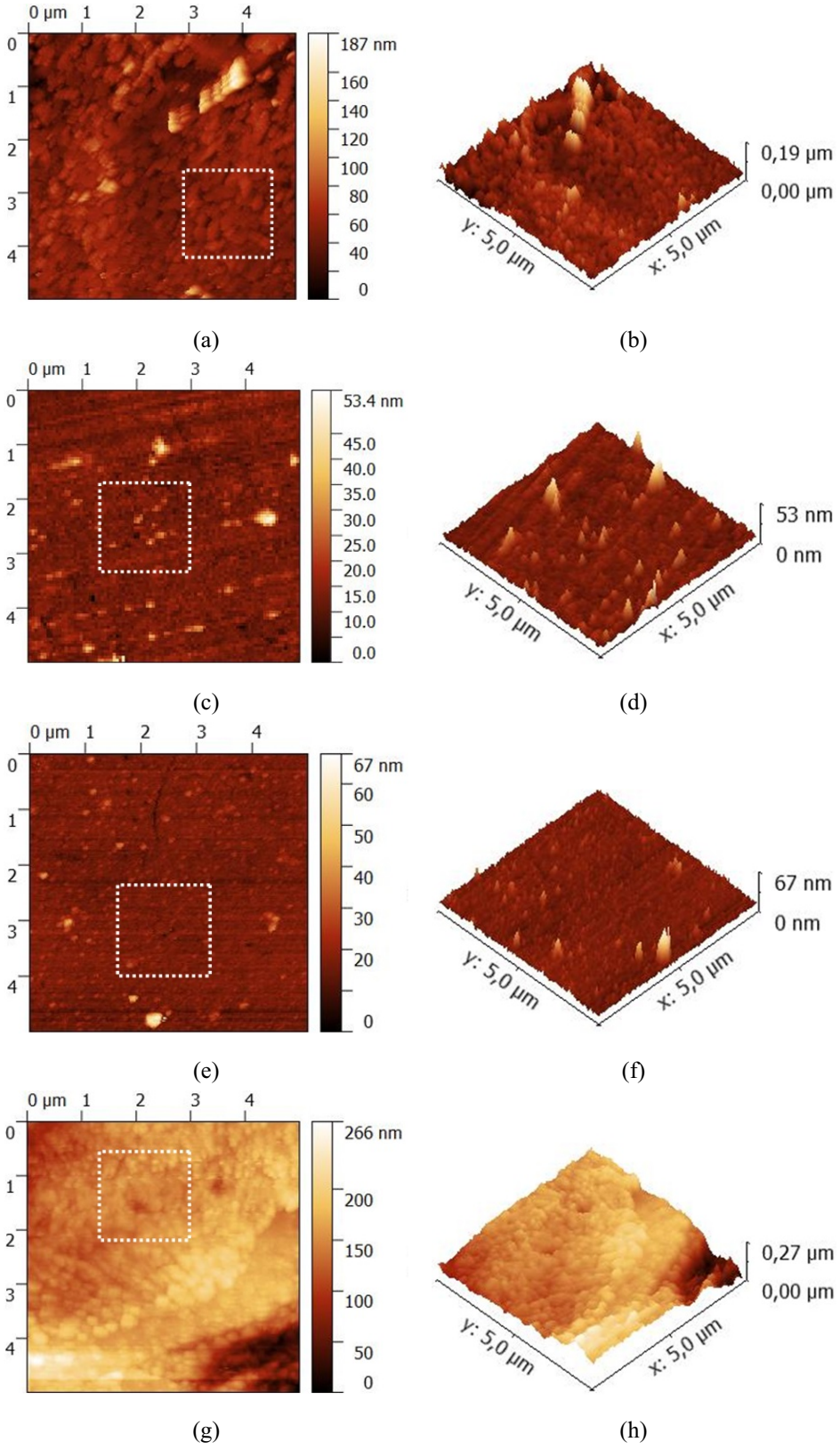

FIG. 1. 2D (a, c, e, g) and 3D (b, d, f, h) AFM images of the surface of copper NPs on glass/ITO substrates without temperature treatment (a, b) and after temperature treatment at 100 °C (c, d), 200 °C (e, f), 300 °C (g, h). Dashed sections are areas of study of the average surface roughness of the sample

The reason may be the evaporation of the organic layer of the surfactant SDS, under which there are both separate copper NPs and their aggregates. The obtained images show that the height of the surface microrelief varies in the range from 53 to 270 nm.

The study showed that the average roughness of the sample strongly depends on the temperature (Table 1, Fig. 2,). Increasing the thermal treatment temperature from 23 to 300 °C leads to a reduction in the average surface roughness from 59 to 30 nm.

TABLE 1. The change in the average roughness of the sample without and after the temperature treatment

Processing temperature, °C	23	100	200	300
R_a, **nm**	59	53	30	33

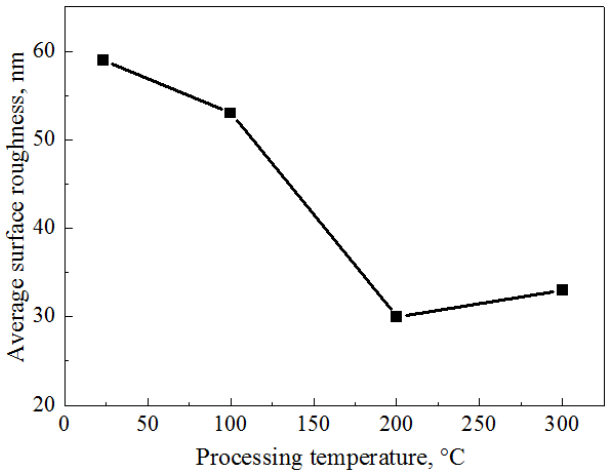

FIG. 2. The dependence of the average roughness of the sample by thermal treatment at 100, 200 and 300 °C

Such regularities are explained by the following changes in the composition and structure of the resulting film. When the sample is heated to 200 – 300 °C with surfactant molecules, a number of changes occur (melting at 206 °C and decomposition at 216 °C). As a result, such transformations lead to a loss of the stabilizing shell of the NPs, their mutual approach to each other and, as a consequence, to reduce in the roughness and an increase in the conductivity of the film, which will be discussed below.

Investigations of surface morphology and element composition of the glass/ITO/copper NPs sample without and after temperature treatment at 100, 200 and 300 °C showed that irregularly shaped objects with sizes from 1 to 50 μm are visible on the surface, as well as objects in the form of rods which are polygons turned by a face to the substrate, a length of 6 to 26 μm and a width of 3 to 6 μm (Fig. 3(a)). When studying objects in an enlargement scale of 10 kx (Fig. 3(b)), accumulations of predominantly spherical copper particles with dimensions from 30 to 140 nm in objects with a shape in the form of irregular polygons were detected. The composition was confirmed by energy-dispersive microanalysis. Investigation of the elemental composition of the sample was carried out at various places on its surface (Fig. 4(a)). From the analysis of the obtained data (Table 2) it follows that copper is contained predominantly in polygons of irregular shape (Fig. 4(a), points 1 and 2). On the surface of the glass/ITO substrate (Fig. 4(a), point 3) copper was not detected. The maximum value of the copper content is 3.2 atomic percentages.

By increasing the treatment temperature to 100 °C, a morphology modification of the objects' surfaces occurs in the form of irregular polygons (Fig. 3(c, d)) without any noticeable change in the atomic percentages of chemical elements was observed (Fig. 4(b), Table 3). At a processing temperature of 100 °C the faces and surfaces of the polygons visually acquired a more pronounced relief. This could be due to the process of alloying copper NPs. At the same time, the images of the polygon faces were visually observed in the obtained SEM images (Fig. 3(c, d)).

After increasing the treatment temperature to 200 °C, an insignificant change was observed in the relief of the surface of the studied objects in the form of polygons (Fig. 3(e, f)). In comparison with the temperature of 100 °C,

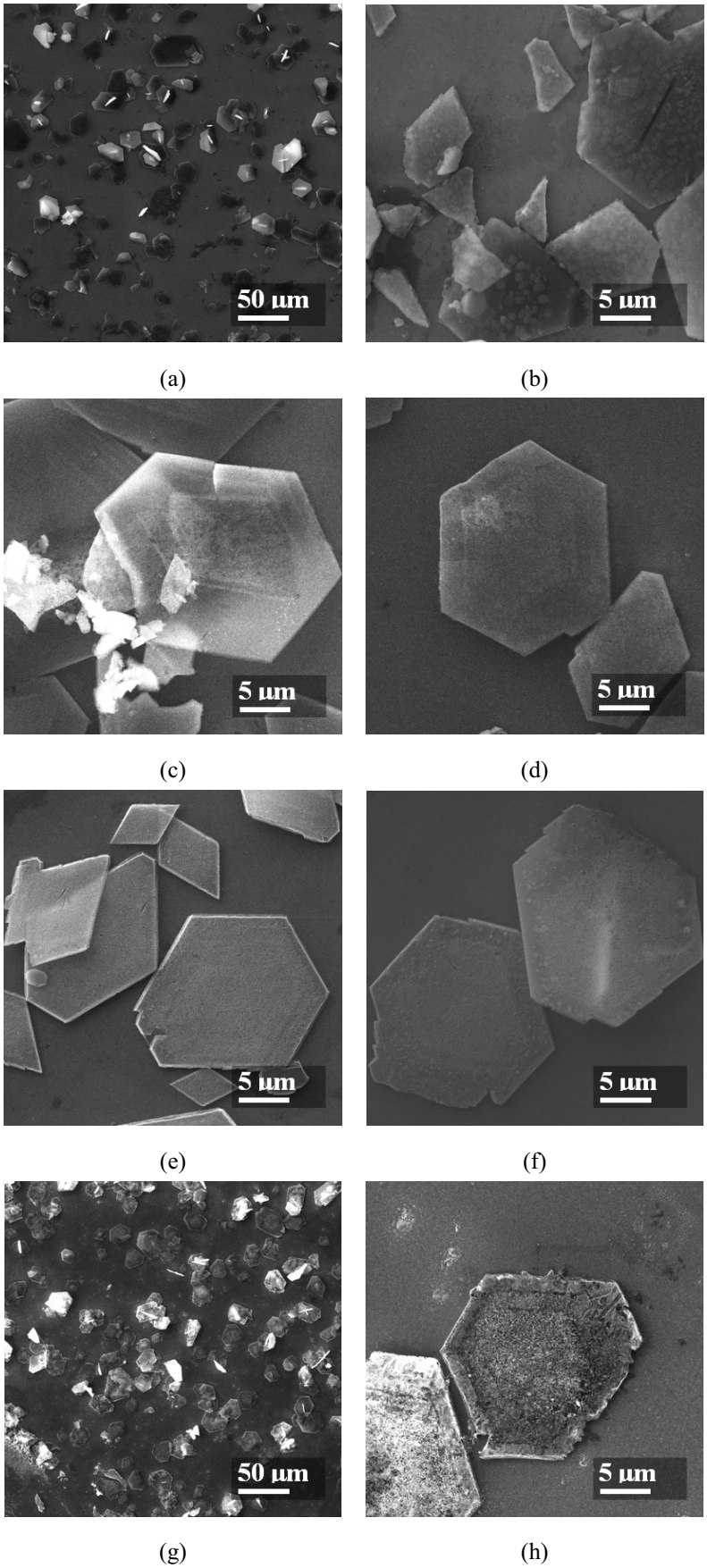

FIG. 3. SEM images of the surface of copper NPs on glass/ITO substrates without temperature treatment (a, b) and after temperature treatment at 100 °C (c, d), 200 °C (e, f), 300 °C (g, h)

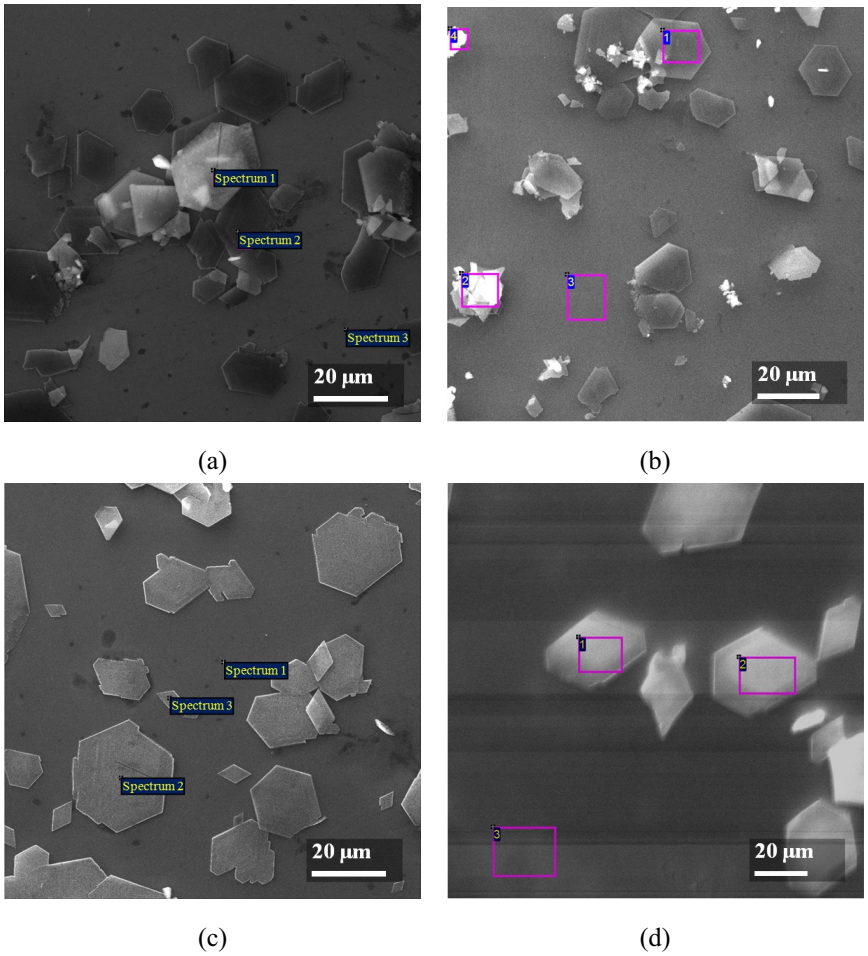

FIG. 4. SEM images of the surface of copper NPs on glass/ITO substrates without temperature treatment (a, b) and after temperature treatment at 100 °C (c, d), 200 °C (e, f), 300 °C (g, h)

TABLE 2. The elemental composition of the sample without temperature treatment (all results are given in atomic percentages)

Spectrum	C	N	O	Na	Mg	Al	Si	Cl	K	Ca	Cu	In	Sn	Result
1	18.8	28.1	35.0	—	0.5	0.3	10.6	0.4	—	2.0	3.2	1.1	—	100.0
2	23.3	28.3	30.2	—	0.3	—	10.8	0.2	0.2	2.9	2.6	1.2	—	100.0
3	—	10.4	47.0	5.3	1.5	0.8	28.2	—	0.6	4.4	—	1.5	0.3	100.0

TABLE 3. The elemental composition of the sample after the temperature treatment at 100 °C (all results are given in atomic percentages)

Spectrum	C	N	O	Na	Mg	Al	Si	Cl	K	Ca	Cu	In	Sn	Result
1	17.1	29.9	38.3	—	—	0.2	8.7	0.2	—	1.9	2.6	1.1	—	100.0
2	16.1	25.3	42.1	1.8	0.6	—	9.5	0.3	0.1	1.3	2.2	0.7	—	100.0
3	—	—	51.9	5.9	1.6	0.8	31.9	—	1.0	4.7	—	1.7	0.5	100.0
4	14.3	23.5	39.0	3.0	0.8	0.4	13.3	0.4	0.1	1.8	2.5	0.9	—	100.0

TABLE 4. The elemental composition of the sample after the temperature treatment at 200 °C (all results are given in atomic percentages)

Spectrum	C	O	Na	Mg	Al	Si	Cl	K	Ca	Cu	In	Sn	Result
1	56.2	26.1	1.9	0.6	0.2	12.0	—	0.3	1.9	—	0.6	0.2	100.0
2	31.5	40.4	—	0.6	0.4	16.6	0.3	0.3	3.6	4.6	1.7	—	100.0
3	31.1	37.7	2.7	1.0	0.3	19.7	0.3	0.4	3.2	2.3	1.3	—	100.0

TABLE 5. The elemental composition of the sample after the temperature treatment at 300 °C (all results are given in atomic percentages)

Spectrum	C	N	O	Na	Mg	Al	Si	Cl	K	Ca	Cu	In	Sn	Result
1	8.3	—	34.2	—	1.1	0.7	27.2	0.4	1.1	7.2	9.6	8.6	1.6	100.0
2	6.9	—	35.5	—	0.8	0.7	26.1	0.5	1.2	6.8	11.0	8.7	1.8	100.0
3	—	14.1	32.3	4.7	1.5	0.9	32.1	0.2	3.4	7.8	—	—	3.0	100.0

they have acquired an even more pronounced surface relief. This could be due to the evaporation of nitrogen (Fig. 4(c), Table 4).

Increasing the treatment temperature to 300 °C led to a strong surface modification (Fig. 3(g, h)) and a change in the atomic composition of the chemical elements (Fig. 4(d), Table 5). Perhaps this could be due to the decomposition and evaporation of the organic surfactant layer. As a result, the highest porosity of the face surface of the polygons as compared to other values of the temperature treatment is observed. Therefore, the choice of high temperatures for the annealing of film structures was associated with several processes. At a temperature of 100 °C, the organic layer protecting the copper NPs from oxidation begins to melt without evaporation. At processing temperatures of 200 – 300 °C, the decomposition and evaporation of short-chain hydrocarbon compounds occurs (Figs. 5 and 6, Tables 6 and 7).

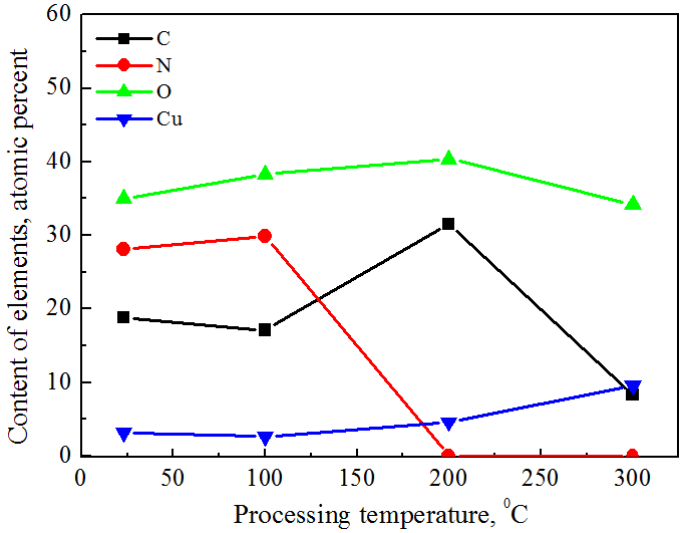

FIG. 5. Dependence of the content of elements C, N, O, Cu in the composition of the sample after the temperature treatment at 100, 200 and 300 °C

From the analysis of the obtained results of the elemental composition of the glass/ITO/copper NPs sample without and after the temperature treatment at 100, 200 and 300 °C a graph of the change in the atomic percentage content of such chemical elements as carbon (C), nitrogen (N), oxygen O), copper (Cu) from the values of processing temperatures was constructed (Fig. 5). Elemental composition data are presented in Table 6.

TABLE 6. The elemental composition of the selected chemical elements in the test sample (all results are given in atomic percentages)

Processing temperature, °C	C	N	O	Cu
23	18.8	28.1	35.0	3.2
100	17.1	29.9	38.3	2.6
200	31.5	—	40.4	4.6
300	8.3	—	34.2	9.6

Figure 6 shows the normalized curve for the selected four elements (Table 6). The normalized elemental composition of C, N, O, Cu is shown in Table 7.

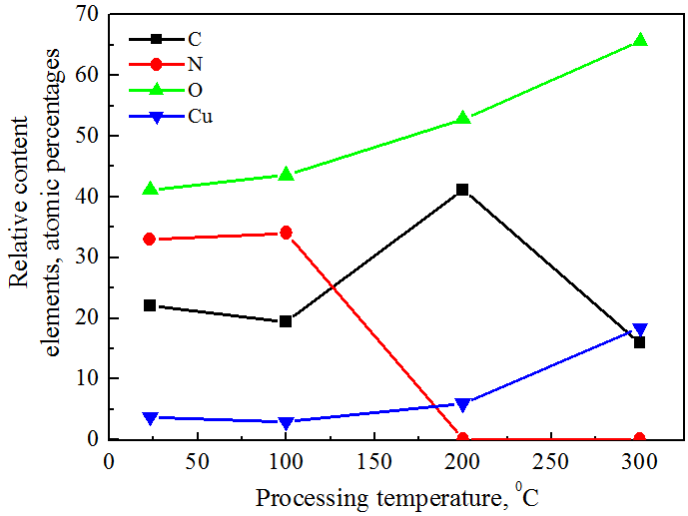

FIG. 6. Dependence of the relative content of elements C, N, O, Cu in the composition of the sample after the temperature treatment at 100, 200 and 300 °C

TABLE 7. The normalized elemental composition of the selected chemical elements in the sample under study (all results are given in atomic percentages)

Processing temperature, °C	C	N	O	Cu	Result
23	22.1	33.0	41.1	3.8	100.0
100	19.5	34.0	43.6	3.0	100.0
200	41.2	—	52.8	6.0	100.0
300	15.9	—	65.6	18.4	100.0

The results of electrophysical property measurements of a typical glass/ITO/copper NPs sample after the temperature treatment at 100, 200 and 300 °C in the STM mode is shown in Figs. 7 and 8. As seen from Fig. 7, the CVCs of the tunnel junction are nonlinear and practically symmetrical. When the copper NPs are melted and a continuous metallic layer is formed, the current transfer according to the Ohm's law could be expected. However, the nonlinear dependences of the current on the voltage were experimentally recorded, which may be a consequence of the growth of the oxide film on the surface of the NPs. Copper oxides are semiconductor materials with p-type conductivity, in which the width of the band gap depends on the degree of oxidation. The band gap of copper (I) oxide (Cu_2O) is 2.0 eV, for copper (II) oxide (CuO) takes values in the range 1.2 – 1.5 eV [22]. The CVC (Fig. 7) and differential resistances (Fig. 8) show that with increasing values of the temperature processing

the resistance of the investigated film structure on the basis of the copper NPs reduces. The decomposition and evaporation of the organic layer of a surfactant covering copper particles, which plays the role of an insulator and prevents the tunneling of electrons in the tunnel gap, with increasing the temperature to 200 – 300 °C, can make the main contribution to the reduction of the resistance of the sample. The results of elemental analysis show that with increasing temperature treatment of the sample the amount of carbon and nitrogen reduced but copper increased (Tables 6 and 7). It is possible that decomposition and evaporation of organic matter contributed to an increase in the conductivity of a film structure based on copper NPs with an increase in temperature processing.

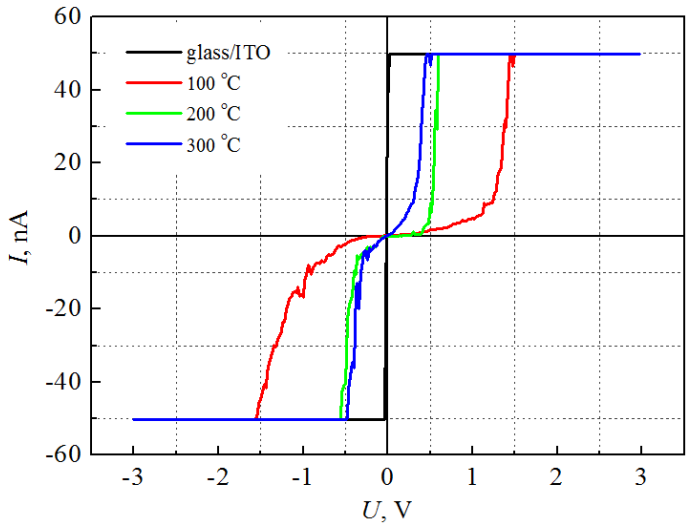

FIG. 7. CVC of sample after heat treatment at 100, 200 and 300 °C

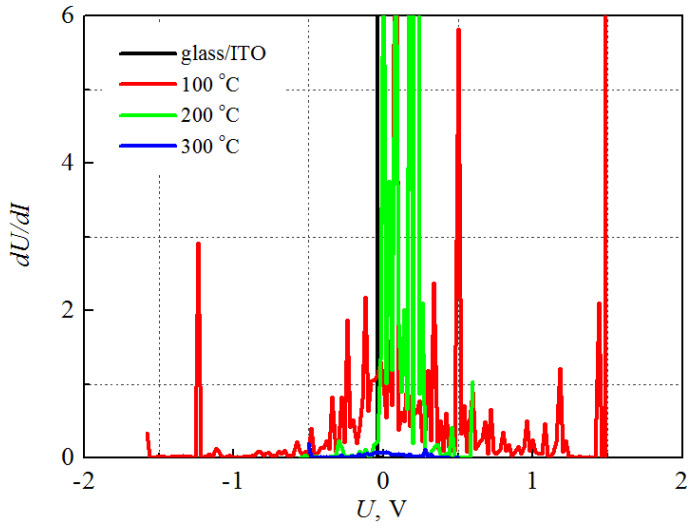

FIG. 8. Differential resistance of the sample after temperature treatment at 100, 200 and 300 °C

Figure 9 shows the spectra of the electronic states of the sample after the temperature treatment at 100, 200 and 300 °C, reconstructed in the coordinates $f(U) = (dI/dU)/(I/U)$ from the obtained CVC. The data analysis shows that with increasing annealing temperature the band gap reduces from 2.1 eV (for 100 °C) to 0.5 eV (for 300 °C) (Fig. 9). This can be due to the decomposition and evaporation of the surfactant. This reduces the organic layer of SDS protecting the surface of copper NPs.

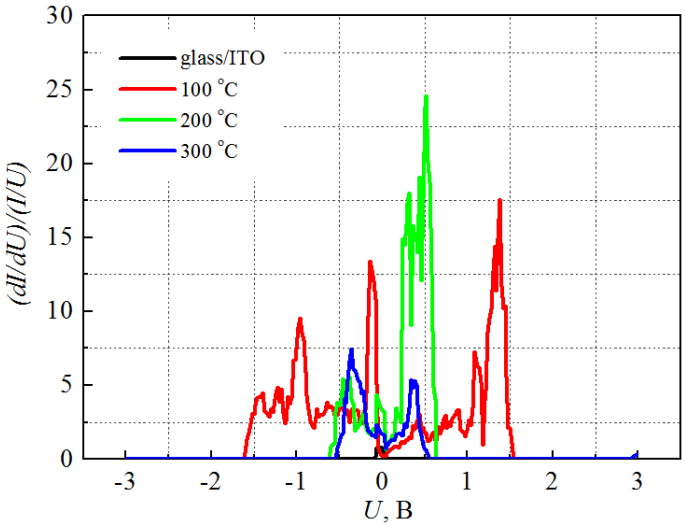

FIG. 9. The spectra of the electronic states of the sample after the temperature treatment at 100, 200 and 300 °C

4. Conclusions

Thus, concerning the influence of additional processing at 100, 200 and 300 °C on the morphology, surface microrelief, element composition and electrophysical properties of glass/ITO/copper NPs samples, SEM, AFM and STM analyses showed that with an increase in the treatment temperature of the substrate there is a modification of the surface and a change in the atomic percentage composition of the chemical elements due to the processes of decomposition and evaporation of the organic layer of the surfactant SDS. In connection with this, the porosity increases for objects having polygon-shaped surface faces. Such polyhedra contain the copper NPs. As a result, with an increase in temperature processing the average surface roughness of the film structure on the basis of copper NPs reduces. In this case, the electrical conductivity of the sample increases. The spectral peaks associated with impurity states inside the forbidden band of the dielectric are reduced.

Acknowledgements

This work was supported by RFBR grant No. 17-07-00407-a.

References

[1] Eastman A., Choi S.U.S., Li S., et al. Anomalously increased effective thermal conductivities of ethylene glycolbased nanofluids containing copper nanoparticles. *Appl. Phys. Lett.*, 2001, **78** (6), P. 718–720.

[2] Yabuki A., Arriffin N. Electrical conductivity of copper nanoparticle thin films annealed at low temperature. *Thin Solid Films*, 2010, **518** (23), P. 7033–7037.

[3] Singh P., Katyal A., Kalra R., et al. Copper nanoparticles in an ionic liquid: an efficient catalyst for the synthesis of bis-(4-hydroxy-2-oxothiazolyl)methanes. *Tetrahedron Lett.*, 2008, **49** (4), P. 727–730.

[4] Dragoi B., Ungureanu A., Chirieac A., et al. Structural and catalytic properties of mono- and bimetallic Nickel-Copper nanoparticles derived from MgNi(Cu)Al-LDHs under reductive conditions. *Applied Catalysis A: General*, 2015, **504**, P. 92–102.

[5] Begletsova N.N., Shinkarenko O.A., Chumakov A.S., et al. Copper nanoparticles obtained by chemical reduction stabilized by micelles of various surfactants. *Journal of Physics: Conf. Series*, 2017, **917**, 092014.

[6] Granata G., Yamaoka T., Pagnanelli F., et al. Study of the synthesis of copper nanoparticles: the role of capping and kinetic towards control of particle size and stability. *J. Nanopart. Res.*, 2016, **18** (133), 12 p.

[7] Li W., Chen M., Wei J., et al. Synthesis and characterization of air-stable Cu nanoparticles for conductive pattern drawing directly on paper substrates. *J. Nanopart. Res.*, 2013, **15** (1949), 10 p.

[8] Zhou J., Wu Z., Zhang Z., et al. Tribological behavior and lubricating mechanism of Cu nanoparticles in oil. *Tribol. Lett.*, 2000, **8** (4), P. 213–218.

[9] Komeily-Nia Z., Montazer M., Latifi M. Synthesis of nano copper/nylon composite using ascorbic acid and CTAB. *Colloids and Surfaces A: Physicochem. Eng. Aspects*, 2013, **439**, P. 167–175.

[10] Huang K.M., Tsukamoto H., Yong Y., et al. Stabilization of the thermal decomposition process of self-reducible copper ion ink for direct printed conductive patterns. *RSC Adv.*, 2017, **7** (40), P. 25095–25100.

[11] Parveen F., Sannakki B., Mandke M.V., et al. Copper nanoparticles: Synthesis methods and its light harvesting performance. *Solar Energy Materials and Solar Cells*, 2016, **144**, P. 371–382.

[12] Xu B., Zhou J., Ni Z., et al. Synthesis of novel microencapsulated phase change materials with copper and copper oxide for solar energy storage and photo-thermal conversion. *Solar Energy Materials and Solar Cells*, 2018, **179**, P. 87–94.

[13] Ko Y., Kwon M., Bae W.K., et al. Flexible supercapacitor electrodes based on real metal-like cellulose papers. *Nature Communications*, 2017, **8** (536), 11 p.
[14] Uschakov A.V., Karpov I.V., Lepeshev A.A., et al. The influence of oxygen concentration on the formation of CuO and Cu_2O crystalline phases during the synthesis in the plasma of low pressure arc discharge. *Vacuum*, 2016, **128**, P. 123–127.
[15] Fedorov L.Yu., Karpov I.V., Ushakov A.V., et al. Study of Phase Composition of CuO/Cu2O Nanoparticles Produced in the Plasma of a Low-Pressure Arc Discharge. *Inorganic Materials: Applied Research*, 2018, **9** (2), P. 323–328.
[16] Lin B., Bohanon T.M., Shih M.C., et al. X-ray Diffraction Studies of the Effects of Ca^{2+} and Cu^{2+} on Langmuir Monolayers of Heneicosanoic Acid. *Langmuir*, 1990, **6**, P. 1665–1667.
[17] Khomutov G.B., Yakovenko S.A., Yurova T.V., et al. Effect of compression of a stearic acid monolayer on interfacial binding of copper ions and cluster formation. *Supramolecular Science*, 1997, **4**, P. 349–355.
[18] Begletsova N., Selifonova E., Chumakov A., et al. Chemical synthesis of copper nanoparticles in aqueous solutions in the presence of anionic surfactant sodium dodecyl sulfate. *Colloids and Surfaces A: Physicochemical and Engineering Aspects*, 2018, **552**, P. 75–80.
[19] Kosolapova K., Al-Alwani A., Gorbachev I., et al. Purification non-aqueous solution of quantum dots CdSe- CdS-ZnS from excess organic substance-stabilizer by use PE-HD membrane. *Journal of Physics: Conference Series*, 2015, **643**, 012084.
[20] Kumar R., Kumar M. Effect of size on cohesive energy, melting temperature and Debye temperature of nanomaterials. *Indian J. Pure Appl. Phys.*, 2012, **50**, P. 329–334.
[21] Mikhailov A.I., Kabanov V.F., Gorbachev I.A., et al. Study of the properties of II-VI and III–V semiconductor quantum dots. *Semiconductors*, 2018, **52** (6), P. 750–754.
[22] Srivastava S., Kumar M., Agrawal A., et al. Synthesis and characterisation of copper oxide nanoparticles. *Journal of Applied Physics*, 2013, **5** (4), P. 61–65.

NANOSYSTEMS: PHYSICS, CHEMISTRY, MATHEMATICS, 2018, 9 (5), P. 597–602

Vibron transport in macromolecular chains with squeezed phonons

D. Čevizović[1], A. V. Chizhov[2,3], S. Galović[1]

[1]Vinča Institute of Nuclear Sciences, 11001 Belgrade, Serbia
[2]Bogoliubov Laboratory of Theoretical Physics, Joint Institute for Nuclear Research, Joliot-Curie, 6, Dubna, 141980, Russia
[3]Dubna State University, Universitetskaya, 19, Dubna, 141980, Russia
chizhov@theor.jinr.ru

PACS 05.60.Gg, 63.20.-e, 03.65.-w **DOI 10.17586/2220-8054-2018-9-5-597-602**

We investigate physical properties of a single vibronic intramolecular excitation propagating through a macromolecule, whose vibrational state can be described as a squeezed vacuum state. For a theoretical description of such a process, the partial dressing method of the vibronic excitation due to its interaction with phonons is used. We study the influence of the model parameters and strength of squeezing on the vibron dressing. It is demonstrated that for certain critical values of the model parameters a polaron crossover can occur, at which there is a sharp change in the migration nature of a vibron from the practically free to the heavy quasiparticle dressed by a phonon cloud. Increasing the strength of phonon squeezing is shown to increase the critical values of the model parameters, so that for high phonon squeezing the polaron crossover takes place in the very strong-coupling and adiabatic regime.

Keywords: energy transport, squeezed state, vibron, small polaron.

Received: 12 July 2018

Revised: 21 August 2018

1. Introduction

The interest in the use of organic macromolecules (e.g., protein macromolecules, DNA, polymers, and other biological macromolecular structures) in construction of nanostructures, such as nanoparticles, nanocrystals, nanowires, and molecular circuits becomes actual again. Its ability in the field of the miniaturization of microelectronic and optoelectronic devices and, at the same time, its self-assembly capabilities makes them very promising materials in microelectronic and optoelectronic technology [1–3]. The efficient application of such materials requires the knowledge of mechanisms that rule the charge and energy migration along the macromolecule spine at such distances that are comparable to the dimension of the macromolecule. Unfortunately, the formulation of a theoretical model based on the principle of quantum mechanics, which could explain such processes in a satisfactory manner, is not yet complete.

One of the earliest quantum mechanical-based models of the charge and energy transfer in protein molecules was developed by Davydov and his coworkers [4,5]. In these papers Davydov tried to explain the ability of charge and energy transfer at long distances (i.e., along the MC spine) by a soliton model, because the mean life-time of a dressed quasiparticle is much longer than the mean life-time of a bare one. This model was based on the assumption that an external excitation might be captured by a macromolecular chain (MC) due to the interaction with oscillations of the macromolecular chain structure elements. Such a self-trapped (ST) excitation becomes dressed by the phonon cloud and it can move in a soliton form through the macromolecular chain. However, because of the lack of direct experimental evidence for the existence of a soliton in such substances, Davydov's idea has been considered only as an interesting theoretical concept of academic interest. The situation changed when Alexander and Krumhansl [6] suggested that appearance of the so-called unconventional amide-I band observed in crystalline acetanilide (ACN) may be explained in the framework of small-polaron (SP) theories. They supposed that in the process of the vibron-exciton self-trapping a non-adiabatic (small) polaron appears instead of a soliton.

In the polaron theory, the basic energy parameters that determine how the ST particle process will take place and what type it will arise are as follows: the quasiparticle binding energy, the characteristic phonon energy and the energy of quasiparticle-phonon interaction. The standard SP theory works in the case of the strong quasiparticle-phonon interaction [7,8]. But the strength of vibron interaction with the phonon subsystem belongs to an intermediate or even a weak coupling regime [9]. It became clear that the standard SP model cannot be applied to biological macromolecular structures, requiring certain modifications. One way to overcome this problem is to apply the model of the partially dressed SP quasiparticles. Such a method was developed in order to intermediate between the weak and strong coupling limits of exciton-phonon interaction [10–13].

When describing the transport mechanism in macromolecular chains, it was usually assumed that the oscillations of their structural elements are due to the thermal fluctuations. However, recent experiments have demonstrated the possibility of transitioning phonon excitations in crystals to a squeezed state [14–16]. Such a phenomenon was achieved due to the action of femtosecond laser pulse radiation in a squeezed state. In particular, this effect was theoretically predicted in Refs. [17–19]. Therefore, it is possible to assume that the state of oscillations of structural elements in the molecular chain can also be brought into a squeezed state under the action of external fields in analogy with crystals.

In this paper we investigate the vibron exciton transport in the framework of partially dressed vibron states as a result of interaction of vibrons with oscillatory excitations of chain structural elements. Here we assume that the quantum state of these excitations are described by the squeezed vacuum state. Special attention is paid to calculation of the dependence of the dressing parameter on the squeezing parameter.

2. Model

The model Hamiltonian for describing the single-vibron propagation along a macromolecular chain can be given in a form of the Holstein type [7]:

$$\begin{aligned}\hat{H} &= \Delta\sum_n \hat{A}_n^\dagger\hat{A}_n - \sum_n J_g\hat{A}_n^\dagger(\hat{A}_{n+g}+\hat{A}_{n-g}) + \sum_q \hbar\omega_q\hat{B}_q^\dagger\hat{B}_q \\ &\quad + \frac{1}{\sqrt{N}}\sum_q\sum_n F_q \mathrm{e}^{iqnR}\hat{A}_n^\dagger\hat{A}_n(\hat{B}_q+\hat{B}_{-q}^\dagger). \end{aligned} \tag{1}$$

Here $\hat{A}_n$ is the vibron annihilation operator on the n-th lattice site, Δ is the vibron excitation energy, J_g is the hopping constant (i.e. it is the energy of the dipole-dipole interaction of neighboring structure elements on the MC), $\hat{B}_q$ is the phonon annihilation operator with the frequency ω_q, F_q is the vibron-phonon coupling parameter, R stands for the distance between two neighboring sites. The transition to the *partially dressed* polaron picture is achieved by applying the modified Lang-Firsov transformation [10, 12, 13, 20]

$$\hat{U} = \exp\left\{-\frac{1}{\sqrt{N}}\sum_q\sum_n f_q \mathrm{e}^{-iqnR}\hat{A}_n^\dagger\hat{A}_n(\hat{B}_{-q}-\hat{B}_q^\dagger)\right\}, \tag{2}$$

where $f_q = \delta\cdot F_q^*/(\hbar\omega_q)$, and δ is the variational parameter which measures the degree of the vibron dressing ($0\le\delta\le 1$). By introducing operators of new quasiparticles for dressed vibrons $\hat{a}_n = \hat{U}\hat{A}_n\hat{U}^\dagger$ ($\hat{a}_n^\dagger = \hat{U}\hat{A}_n^\dagger\hat{U}^\dagger$), and new phonons $\hat{b}_q = \hat{U}\hat{B}_q\hat{U}^\dagger$ ($\hat{b}_q^\dagger = \hat{U}\hat{B}_q^\dagger\hat{U}^\dagger$), one gets the transformed Hamiltonian in the form $\hat{\tilde{H}} = \hat{U}\hat{H}\hat{U}^\dagger$

$$\begin{aligned}\hat{\tilde{H}} &= E\sum_n \hat{a}_n^\dagger\hat{a}_n - \sum_n J_g\hat{a}_n^\dagger(\hat{a}_{n+g}\hat{\Phi}_n(g)+\hat{a}_{n-g}\hat{\Phi}_n(-g)) + \sum_q \hbar\omega_q\hat{b}_q^\dagger\hat{b}_q \\ &+ \frac{1}{\sqrt{N}}\sum_q\sum_n (F_q-\hbar\omega_q f_q^*)\mathrm{e}^{iqnR}\hat{a}_n^\dagger\hat{a}_n(\hat{b}_q+\hat{b}_{-q}^\dagger) \\ &+ \frac{1}{N}\sum_q[\hbar\omega_q|f_q|^2 - F_q(f_q+f_{-q}^*)]\sum_{n\neq n'}\mathrm{e}^{iqR(n-n')}\hat{a}_n^\dagger\hat{a}_n\hat{a}_{n'}^\dagger\hat{a}_{n'}, \end{aligned} \tag{3}$$

where $E = \Delta - (1/N)\sum_q[F_q(f_q+f_{-q}^*) - \hbar\omega_q|f_q|^2]$ is energy of dressed vibron (which is shifted from the energy of the energy of bare excitation), and

$$\hat{\Phi}_n(g) = \exp\left\{\frac{1}{\sqrt{N}}\sum_q f_q\mathrm{e}^{-iqnR}(\hat{b}_{-q}-\hat{b}_q^\dagger)(\mathrm{e}^{-iqRg}-1)\right\}.$$

Defining exciton states in the representation of wave vectors k by $\hat{a}_k = (1/\sqrt{N})\sum_n \mathrm{e}^{iknR}\hat{a}_n$, the Hamiltonian (3) for the single vibron excitation reads:

$$\begin{aligned}\hat{\tilde{H}} &= E\sum_k \hat{a}_k^\dagger\hat{a}_k + \sum_q \hbar\omega_q\hat{b}_q^\dagger\hat{b}_q + \frac{1}{\sqrt{N}}\sum_q\sum_k (F_q^*-\hbar\omega_q f_q)\hat{a}_k^\dagger\hat{a}_{k+q}(\hat{b}_{-q}+\hat{b}_q^\dagger) \\ &- \frac{1}{\sqrt{N}}\sum_{k_1}\sum_{k_2} J_g\hat{a}_{k_1}^\dagger\hat{a}_{k_2}\{\mathrm{e}^{-ik_2gR}\hat{\Phi}_{k_1-k_2}(g)+\mathrm{e}^{ik_2gR}\hat{\Phi}_{k_1-k_2}(-g)\}, \end{aligned} \tag{4}$$

where $\hat{\Phi}_k(g) = (1/\sqrt{N})\sum_n \mathrm{e}^{iknR}\hat{\Phi}_n(g)$.

In order to account for the influence of the mechanical oscillation of the chain structure elements on the properties of the ST vibron, we apply the mean-field approach by the averaging of the transformed Hamiltonian over the phonon subsystem. The averaged Hamiltonian obtains the form:

$$\begin{aligned}\hat{\tilde{H}}_{MF} &= E\sum_k \hat{a}_k^\dagger \hat{a}_k + \frac{1}{\sqrt{N}}\sum_q\sum_k (F_q^* - \hbar\omega_q f_q)\hat{a}_k^\dagger \hat{a}_{k+q}\langle \hat{b}_{-q} + \hat{b}_q^\dagger\rangle_{ph} \\ &- \frac{1}{\sqrt{N}}\sum_{k_1}\sum_{k_2} J_g \hat{a}_{k_1}^\dagger \hat{a}_{k_2}\{\mathrm{e}^{-ik_2gR}\langle\hat{\Phi}_{k_1-k_2}(g)\rangle_{ph} + \mathrm{e}^{ik_2gR}\langle\hat{\Phi}_{k_1-k_2}(-g)\rangle_{ph}\},\end{aligned} \tag{5}$$

in which the symbol $\langle\ldots\rangle_{ph} = \mathrm{Tr}\{\hat{\varrho}_b\ldots\}$ denotes the average over the phonon ensemble.

3. Squeezed-vacuum phonon state

The non-classical behavior of phonons upon the action of ultrashort laser pulses on a crystal, as shown in Ref. [21], is due to the generation of biphonon-like states. Such states are characterized by the excitation of phonon modes with equal frequencies and identical in absolute value, but opposite in sign wave vectors, i.e. they are associated with operators $\hat{b}_q$ and $\hat{b}_{-q}$. Thus, one can presume that it corresponds to the generation of a multimode squeezed vacuum state of phonons, $|0\rangle_{MSVS}$, which is defined by the unitary operator [22]:

$$\hat{S} = \exp\left\{\sum_q \left[\xi_q^* \hat{b}_q\hat{b}_{-q} - \xi_q \hat{b}_q^\dagger \hat{b}_{-q}^\dagger\right]\right\}, \tag{6}$$

with the squeezing parameter $\xi_q = r_q\mathrm{e}^{i\theta_q}$, satisfying the conditions:

$$\begin{aligned}\hat{S}^\dagger \hat{b}_q \hat{S} &= \cosh r_q \hat{b}_q - \mathrm{e}^{i\theta_q}\sinh r_q \hat{b}_{-q}^\dagger, \\ \hat{S}^\dagger \hat{b}_q^\dagger \hat{S} &= \cosh r_q \hat{b}_q^\dagger - \mathrm{e}^{-i\theta_q}\sinh r_q \hat{b}_{-q},\end{aligned} \tag{7}$$

so that

$$|0\rangle_{MSVS} = \hat{S}|0\rangle_b, \tag{8}$$

where $|0\rangle_b$ is the phonon vacuum state, i.e. $\hat{b}_q|0\rangle_b = 0$. Then, for the averages over the phonon ensemble in such a state, we have:

$$\langle\hat{b}_{-q} + \hat{b}_q^\dagger\rangle_{ph} \equiv \langle\hat{b}_{-q} + \hat{b}_q^\dagger\rangle_{MSVS} = 0, \tag{9}$$

since $\langle\hat{b}_q\rangle_{MSVS} = \langle\hat{b}_q^\dagger\rangle_{MSVS} = 0$, and

$$\langle\hat{\Phi}_{k_1-k_2}(g)\rangle_{ph} = \frac{1}{\sqrt{N}}\sum_n \mathrm{e}^{i(k_1-k_2)nR}\langle\hat{\Phi}_n(g)\rangle_{MSVS}, \tag{10}$$

where the average $\langle\hat{\Phi}_n(g)\rangle_{MSVS}$, as it turns out, does not depend on the site number n, i.e.

$$\langle\hat{\Phi}_n(g)\rangle_{MSVS} = \exp\left\{-\frac{1}{N}\sum_q |f_q|^2(1-\cos qgR)(\cosh 2r_q - \sinh 2r_q\cos\theta_q)\right\} \equiv \mathrm{e}^{-W_{SV}(g)}, \tag{11}$$

so that

$$\langle\hat{\Phi}_{k_1-k_2}(g)\rangle_{ph} = \mathrm{e}^{-W_{SV}(g)}\ \delta_{k_1,k_2}. \tag{12}$$

Here the function

$$\begin{aligned}W_{SV}(g) &= \frac{1}{N}\sum_q |f_q|^2(1-\cos qgR)(\cosh 2r_q - \sinh 2r_q\cos\theta_q) \\ &= \frac{1}{N}\sum_q |f_q|^2(1-\cos qgR)\left[\mathrm{e}^{-2r_q}\cos^2(\theta_q/2) + \mathrm{e}^{2r_q}\sin^2(\theta_q/2)\right]\end{aligned} \tag{13}$$

is positive definite and might play a role of the vibron-band narrowing factor that is caused by the exciton interaction with squeezed phonons.

Thus, the mean-field Hamiltonian (5) takes the form:

$$\hat{\tilde{H}}_{MF} = \sum_k E_{\mathrm{SP}}(k)\hat{a}_k^\dagger \hat{a}_k, \tag{14}$$

with the energy of the small-polaron band state:

$$E_{\rm SP}(k) = \Delta - \frac{1}{N}\sum_q [F_q(f_q + f^*_{-q}) - \hbar\omega_q |f_q|^2] - 2J_g {\rm e}^{-W_{SV}(g)} \cos(gkR). \tag{15}$$

4. Degree of small-polaron dressing

The optimal polaron state should be determined by the minimization of the polaron ground-state energy (15), namely

$$\mathscr{E}_{GS} = E_{SP}(k=0) = \Delta - \frac{1}{N}\sum_q \left[F_q(f_q + f^*_{-q}) - \hbar\omega_q |f_q|^2\right] - 2J_g {\rm e}^{-W_{SV}(g)}. \tag{16}$$

Consequently, for the fixing of the variational parameter δ in the unitary transformation (2) the procedure of minimization of the small-polaron ground state energy $\mathscr{E}_{GS}$ is to be used, i.e. $\partial\mathscr{E}_{GS}/\partial\delta = 0$ provided $\partial^2\mathscr{E}_{GS}/\partial\delta^2 > 0$. Under the assumption that the vibron interacts with optical phonon modes, one can use the dispersionless approximation $\omega_q = \omega_C$ and $F_q = F_C$, so that $f_q = \delta \cdot F^*_C/(\hbar\omega_C)$. Then it is convenient to introduce two system dimensionless parameters, namely the adiabatic parameter $B = 2|J_g|/(\hbar\omega_C)$ and the coupling constant $S = E_{\rm B}/(\hbar\omega_C)$ (where $E_{\rm B} = (1/N)\sum_q \{|F_q|^2/(\hbar\omega_q)\} = |F_C|^2/(\hbar\omega_C)$ is the lattice deformation energy). These parameters are very convenient for describing the polaron properties. The adiabatic parameter B determines the character of the lattice deformation engaged in the polaron formation, while the coupling constant S (which was originally introduced by Holstein) determines the polaron spatial size [7, 8] Thus the problem of minimization of $\mathscr{E}_{GS}$ reduces effectively to minimization of the function

$$\mathscr{E} = -S(2-\delta)\delta - B{\rm e}^{-\delta^2 W_{SV}(S)}, \tag{17}$$

where $\mathscr{E}$ is the polaron ground state energy normalized to the characteristic phonon energy $\hbar\omega_C$. The first therm in Eq. (17) corresponds to the polaron binding energy, while the second one corresponds to the width of the quasiparticle energy band. The vibron-band narrowing factor (13) in the case when $r_q = r$ and $\theta_q = \theta$ takes the form

$$W_{SV}(S) = S(\cosh 2r - \sinh 2r \cos\theta) = S\left[{\rm e}^{-2r}\cos^2(\theta/2) + {\rm e}^{2r}\sin^2(\theta/2)\right]. \tag{18}$$

It is worth noting that the vibron-band factor (18) for squeezed phonons is principally different from the analogous factor for thermal phonons [12]. This is due to the fact that with an appropriate choice of squeezing phase, e.g., when $\theta = 0$ and Eq. (18) has the form $W_{SV}(S) = S\exp(-2r)$, for a fixed parameter S the narrowing factor can be made arbitrarily small for large values of the strength of squeezing r, while the narrowing factor for thermal phonons is limited by the value $W_T(S) = S$ at zero temperature. Thus, by choosing the phase and the strength of squeezing of phonons in a proper way, it opens up new opportunities for control of the character of energy transport through macromolecular chains.

5. Results

Here we consider the case of a quasi 1D macromolecular chain, so we take the parameter g equal to 1 that corresponds to the interaction of the nearest neighboring structural elements of the chain. In our theoretical analysis we considered the case when $\theta = 0$ in order to explore the parameter region inaccessible to the case of thermal phonons. For the strength of phonon squeezing we have chosen the following three values, namely $r = 0.1$, 0.2, and 0.4, although recent experiments with crystals generate rather moderate degrees of squeezing of phonon states. The results of minimization of Eq. (17) for various model parameters in terms of B, S, and the strength of phonon squeezing r are plotted in Fig. 1 and Fig. 2.

In these figures, one can see that for various values of the model parameters there are two different regimes of the dressed vibron nature. In the first regime, vibron dressing changes continuously with changing the model parameters, while in the second regime it undergoes an interrupted transition for certain values of model parameters. Additionally, we can see that the strength of phonon squeezing significantly influences these processes.

More precise details of vibron properties depending on the model parameters are given in Fig 2. Here one can remark that in the non-adiabatic regime (i.e., for small values of B) vibron dressing increases continuously with increasing strength of the exciton-phonon coupling S. In this regime an exciton is a strongly dressed quasiparticle, even in the case of a weak exciton-phonon coupling regime. At the same time, the ground state energy of the vibron decreases continuously with increasing S. This dependence is typical for standard non-adiabatic polarons (where the process of the exciton dressing is quite adequately described by the standard Lang–Firsov approach [20]). With an increase in B, the initial value of the dressing parameter decreases, but with increasing S it smoothly increases and approaches its maximum value equal to unity (i.e., exciton becomes fully dressed by a phonon cloud). With

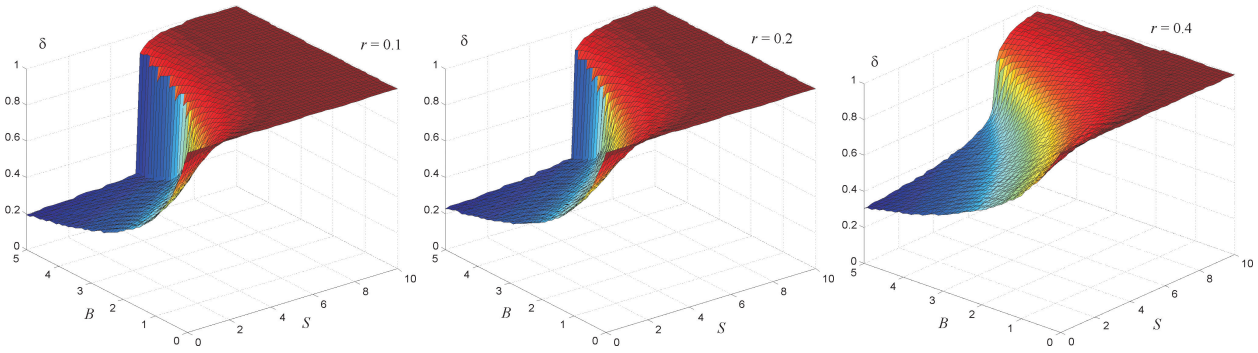

FIG. 1. Dressing fraction δ as a function of the adiabatic parameter B and the coupling constant S for various strengths of squeezing r ($\theta = 0$)

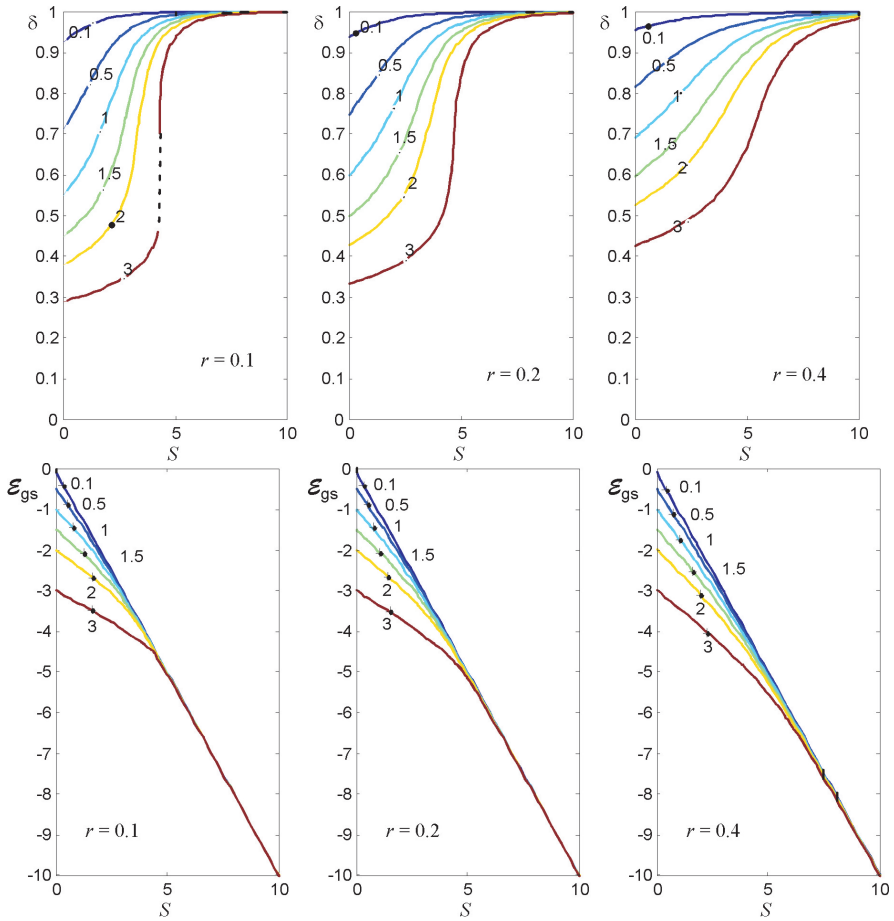

FIG. 2. Dressing fraction δ (first row) and polaron ground-state energy $\mathscr{E}_{GS}$ (second row) as functions of the coupling constant S for various values of the adiabatic parameter B (indicated on the curves) and the strengths of squeezing r ($\theta = 0$)

a further increase in B, it reaches such a critical value B_C for which δ becomes a discontinuous function of S for the critical value S_C and suffers interruption (such a behavior of the dressing fraction δ at the critical point is represented by a dashed curve in the left plot of the first row of Fig. 2). At the same time, at the critical point $\mathscr{E}_{GS}$ ceases to be a smooth function of S and has a break (lower curve in the left plot of the second row of Fig. 2). With a further increase in B, the excitation becomes slightly dressed and enters the adiabatic regime.

On the other hand, the effect of increasing B can be moderated by an increase in the value of the parameter r. As a consequence, with the help of increasing the strength of squeezing it is possible to influence the increase in the system adiabaticity and to keep it in the model-parameter area, that is characteristic for non-adiabatic systems.

Figure 1 shows that there is a whole set of critical values of the model parameters (S_C, B_C) under which the polaron crossover occurs. With such a crossover there appears a sharp change in the migration nature of a vibron from the practically free to the heavy quasiparticle "dressed" by a phonon cloud. These critical values of the adiabatic parameter B_C and the coupling constant S_C increase with increasing the strength of phonon squeezing. It means that for high phonon squeezing the polaron crossover takes place in a very strong-coupling and adiabatic regime.

6. Conclusion

We have studied propagation of a single vibronic intramolecular excitation along a 1D macromolecule under the assumption that its vibrational state is described by a squeezed vacuum state. Using the partial dressing method of the vibronic excitation due to its interaction with phonons, for various model parameters and the degree of phonon squeezing we have demonstrated the existence of a polaron crossover, at which a sudden change in the migration nature of a vibron from the practically free to the heavy quasiparticle dressed by a phonon cloud occurs. Increasing the strength of phonon squeezing is shown to increase the crossover critical values of the model parameters, so that for high phonon squeezing the polaron crossover takes place in the very strong-coupling and adiabatic regime. With increasing the strength of squeezing, the crossover critical values of the adiabatic parameter and the coupling constant were shown to increase, so that for high phonon squeezing the polaron crossover takes place in the very strong-coupling and adiabatic regime.

Acknowledgements

This work is partly supported by the bilateral project between the Serbian Ministry of Education and Science and "Theory of Condensed Matter" at JINR, Dubna, and by Serbian Ministry of Education and Science, under Contract Nos. III–45010 and III–45005.

References

[1] Dekker C., Ratner M. A. Electronic properties of DNA. *Phys. World*, 2001, **14** (8), P. 29–34.
[2] Convell E. Polarons and transport in DNA. *Top. Curr. Chem.*, 2004, **237**, P. 73–102.
[3] Mirkin C. A., Letsinger R. L., Mucic R. C., Storhoff J. J. A DNA-based method for rationally assembling nanoparticles into macroscopic materials. *Nature*, 1996, **382** (6592), P. 607–609.
[4] Davydov A. S. The theory of contraction of proteins under their excitation. *J. Theor. Biol.*, 1973, **38** (3), P. 559–569.
[5] Davydov A. S. Solitons in molecular systems. *Phys. Scr.*, 1979, **20** (2), P. 387–394.
[6] Alexander D. M., Krumhansl J. A. Localized excitations in hydrogen-bonded molecular crystals. *Phys. Rev. B*, 1986, **33** (10), P. 7172–7185.
[7] Holstein T. Studies of polaron motion: Part I. The molecular-crystal model. *Annals of Physics*, 1959, **8** (3), P. 325–342.
[8] Rashba E. I. Self-trapping of excitons. *Excitons*, North-Holland, Amsterdam, 1982, P. 543–602.
[9] Pouthier V. Vibron phonon in a lattice of H-bonded peptide units: A criterion to discriminate between the weak and the strong coupling limit. *J. Chem. Phys.*, 2010, **132** (3), 035106.
[10] Brown D.W., Ivić Z. Unification of polaron and soliton theories of exciton transport. *Phys. Rev. B*, 1989, **40** (14), P. 9876–9887.
[11] Yarkony D., Silbey R. Comments on exciton phonon coupling: Temperature dependence. *J. Chem. Phys.*, 1976, **65** (3), P. 1042–1052.
[12] Čevizović D., Galović S., Ivić Z. Nature of the vibron self-trapped states in hydrogen-bonded macromolecular chains. *Phys. Rev. E*, 2011, **84** (1), 011920.
[13] Čevizović D., Galović S., Reshetnyak A., Ivić Z. Vibron self-trapped states in biological macromolecules: Comparison of different theoretical approaches. *J. Phys.: Conf. Ser.*, 2012, **393** (1), 012033.
[14] Garret G. A., Rojo A. G., Sood A. K., Whitaker J. F., Merlin R. Vacuum squeezing of solids: Macroscopic quantum states driven by light pulses. *Science*, 1997, **275** (5306), P. 1638–1640.
[15] Beaud P. *et al*. Spatiotemporal stability of a femtosecond hard-X-ray undulator source studied by control of coherent optical phonons. *Phys. Rev. Lett.*, 2007, **99** (17), 174801.
[16] Johnson S. L. *et al*. Directly observing squeezed phonon states with femtosecond X-ray diffraction. *Phys. Rev. Lett.*, 2009, **102** (17), 175503.
[17] Nazmitdinov R. G., Chizhov A. V. Effect of compressed light on pumping of a crystal. *Pis'ma v ZhETF*, 1990, **52** (7), P. 993–996.
[18] Artoni M., Birman J. L. Non-classical states in solids and detection. *Opt. Commun.*, 1994, **104** (4–6), P. 319–324.
[19] Hu X., Nori F. Quantum phonon optics: Coherent and squeezed atomic displacements. *Phys. Rev. B*, 1996, **53** (5), P. 2419–2424.
[20] Lang I. G., Firsov Yu. A. Kinetic theory of semiconductors with low mobility. *ZhETF*, 1962, **43** (5/11), P. 1843–1860.
[21] Misochko O. V., Hu J., Nakamura K. G. Controlling phonon squeezing and correlation via one- and two-phonon interference. *Phys. Lett. A*, 2011, **375** (46), P. 4141–4146.
[22] Loudon R., Knight P. L. Squeezed light. *J. Mod. Opt.*, 1987, **34** (6–7), P. 709–759.

NANOSYSTEMS: PHYSICS, CHEMISTRY, MATHEMATICS, 2018, 9 (5), P. 603–608

Flintstone as a nanocomposite material for photonics

P. P. Fedorov[1], V. A. Maslov[1], V. V. Voronov[1], E. V. Chernova[1], O. S. Kudryavtsev[1], V. G. Ralchenko[1], I. I. Vlasov[1], A. S. Chislov[1], M. N. Mayakova[1], E. G. Yarotskaya[1], R.V. Gaynutdinov[2], P. A. Popov[3], A. I. Zentsova[3]

[1]Prokhorov General Physics Institute of the Russian Academy of Sciences, 38 Vavilov Street, Moscow, 119991 Russia

[2]Crystallography and Photonics Federal Research Center, Russian Academy of Sciences, 59 Leninskii Prospect, Moscow, 119991 Russia

[3]Petrovskii State University, 14 Bezhitskaya Street, Bryansk, 241036 Russia

ppfedorov@yandex.ru

DOI 10.17586/2220-8054-2018-9-5-603-608

Studying natural flintstone samples' properties, including optical transparency and thermal conductivity, by various physical methods (X-ray diffraction, atomic force microscopy, optical microscopy, etc.) revealed that said specimens contain chalcedony nanoparticles bund into the complex hierarchial structure.

Keywords: flintstone, quartz, chalcedony, thermal conductivity, nanocomposite, nanographite photonics.

Received: 17 September 2018

Revised: 26 September 2018

1. Introduction

Recently, significant progress has been made in the manufacturing of various nanophotonic structures with novel optical properties. Photonic crystals possess ordered distribution of identical elements making up said structures. Usually, such elements are considered monodispersed with regard to their geometric and dielectric parameters; and such materials properties are determined by the whole particle ensembles [1]. In contrast with the latter materials, there are other objects previously described in the literature which consist of disorderly arranged particles. The latter objects can also generate so-called random lasing, and such lasing opens enormous opportunities in miniaturizing laser devices [2–5]. Media with disorderly distributed particles can contain particles of the same or different sizes (i.e., photonic glasses and/or Levy glasses, respectively). Photonic glass properties, in contrast with photonic crystals, are determined by the individual properties of the scattering elements. Such features provide photonic glasses with unique properties and allow novel venues for light propagation in disordered media [2–5],whereas photon transfer in Levy glasses is determined by Levy statistics.

Precipitation of fluoride and oxide nanopowders from aqueous solutions produced unusual monolithic optically transparent precipitates that consisted of agglomerated nanopowders and aqueous solutions binding said nanoparticles together; such precipitates were named as transparent compacts [6–12]. As per our data [6–12], such ability to form these transparent compacts is independent from the nature of the forming nanoparticles: transparent compacts have been obtained for numerous fluorite- and tysonite-type phases (cubic and trigonal systems, respectively) as well as for oxide precursors of aluminum-yttrium garnets and aluminum-magnesium spinels.

Formation of the above materials proceeded via various multistep agglomerations that were very typical for nanotechnology [13–15]. Such processes, which were performed under laboratory conditions, are quite common under natural conditions, too, and one can easily observe their results in the natural formations like quartz minerals, such as chalcedonies, agates, and opals [16–20]. A common feature of these minerals is the presence of small crystalline quartz particles and certain amount of water in them. Opals are characterized by an ordered distribution of spherical silica particles of micron size; and chalcedonies, in general, contain disorderly distributed particles and lower water contenet than other quartz minerals. Flintstones, in turn, are characterized by their various contaminants.

We focused our present work on studying natural flintstones by physical and chemical methods in order to clarify its structure and determine whether flintstone's natural properties were the same as those of laboratory-synthesized samples. We chose black flintstone specimens from the vicinity of Tarusa, Russia, since such flintstones have been widely used for human toolmaking in the Upper Paleolithic and Neolithic Ages and for the manufacture of musket flints in the 18^{th} century.

2. Experimental

Investigated samples were prepared as 0.8 mm thick plates cut out from natural flintstone and thoroughly polished. These specimens were used for X-ray diffraction study, optical transmittance spectra recording and microhardness measurements.

Optical transmittance spectra were recorded with a Carry 5000 spectrometer.

Mineralogical thin sections were used for the sample optical characterization (POLAM L-213 microscope, LOMO, St. Petersburg).

Specimen microhardness was tested using a PRECIDUR DM-8 device under 50 g weight load.

X-Ray diffraction patters were recorded with the use of Bruker D8 Advanced diffractometer (Cu Kα irradiation); obtained data were processed by TOPAS software package; and coherent scattering domain sizes were estimated by Selyakov–Sherer equation: $D = 0.9 \cdot \lambda / B \cdot \cos\theta$, where λ is an X-ray irradiation wavelength, B is an integral peak width, θ is a peak reflection angle.

Surface relief was studied using the scanning probe microscope Ntegra Prima (NT-MDT Spectrum Instruments, Russia) in the contact mode. Employed silicon cantilevers HA_C lever A (Tipsnano, Estonia) are characterized by the following parameters: resonance frequency $f \sim 37$ kHz, tip radius $R \sim 10$ nm, and stiffness constant $k \sim 0.65$ N/m. All experiments on the precision study of the samples surface were carried out under controlled conditions of the TRACKPORE ROOM-05 measuring complex (5 ISO (100) class, humidity of 40 rel. %$\pm$1% and temperature of 24 ± 0.05 °C).

The thermal conductivity of the specimens was measured by the absolute stationary technique of longitudinal thermal flux [21] from 50 – 300 K. Thermal conductivity coefficient values were calculated by Fourier equation within ± 5 % error interval. In the high temperature region 323 – 573 K, thermal conductivity was measured by the dynamic method on an ITλ-400 facility accurate to ± 10 %.

Luminescence and Raman spectra were recorded using confocal HORIBA Jobin Yvon HR800 spectrometer (473 nm wavelength, 10 mW excitation radiation of CIEL Quantum Laser focused by X50 lens to form a 2 micron spot on the sample specimens). For the latter study, we used cleavage faces without any trace of mechanical treatment.

3. Results and Discussion

In our studies, we have used the specimens of dense monolithic appearance with volume about a few cubic centimeters and flinty fractures (1044 $\pm$ 19 kg/mm^2 microhardness; 2.68 g/cm^3 density). A typical X-Ray diffraction pattern for the flintstone samples (Fig. 1) did not change its appearance when taken from monolithic plates or flintstone powder ground in the sapphire mortar.

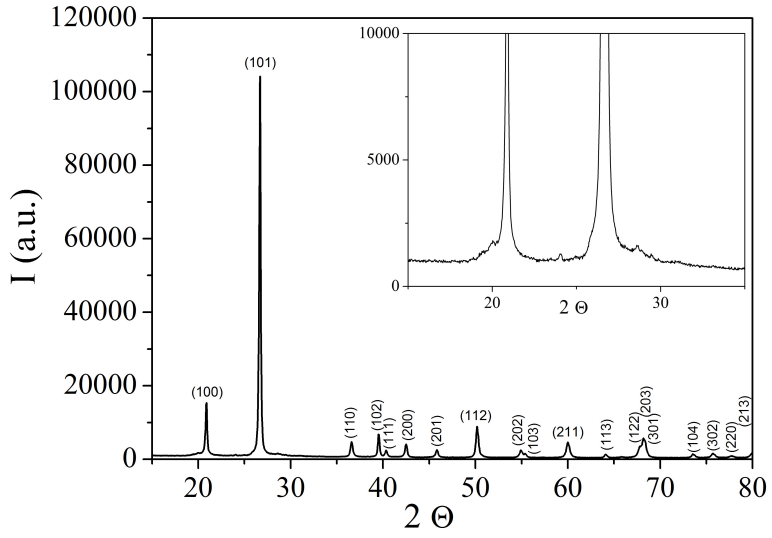

FIG. 1. X-ray diffraction pattern of flintstone specimen

A flintstone diffraction pattern coincides with well-known pattern for alpha-quartz (hexagonal system; $a = 4.913$, $c = 5.405$ Å). Extremely weak reflections at about 20 – 30 2θ degrees (Fig. 1) may be attributed to the rare silica

modification known as moganite (JCPDS card 079-2403). Considering the specimen black color, one may suggest the presence of graphite in the samples masked by overlapping (101) quartz line and the strongest reflection line of said graphite. It is worth noting that flintstone sample reflection lines exhibited different intensities compared to the standard data for alpha-quartz: I_{110}/I_{102} and I_{102}/I_{111} intensity ratios were 0.62 and 4.0, respectively. Such type of the texture has indicated that, according to the known criteria, silica-forming mineral should be characterized as chalcedony [20].

Sizes of the coherent scattering domains D, estimated with the use of the data for (112) and (211) lines, were 31 and 24 nm, respectively.

Atomic force microscopy data for the fresh cleavage face are presented in Fig. 2. They unequivocally confirmed the presence of round-shaped particles (ca. 0.5 microns diameter) in the three-dimensional flintstone framework. One can also see clearly cavities/channels with ca. 2 microns cross-sections in the bodies of said flintstone specimens (Fig. 2).

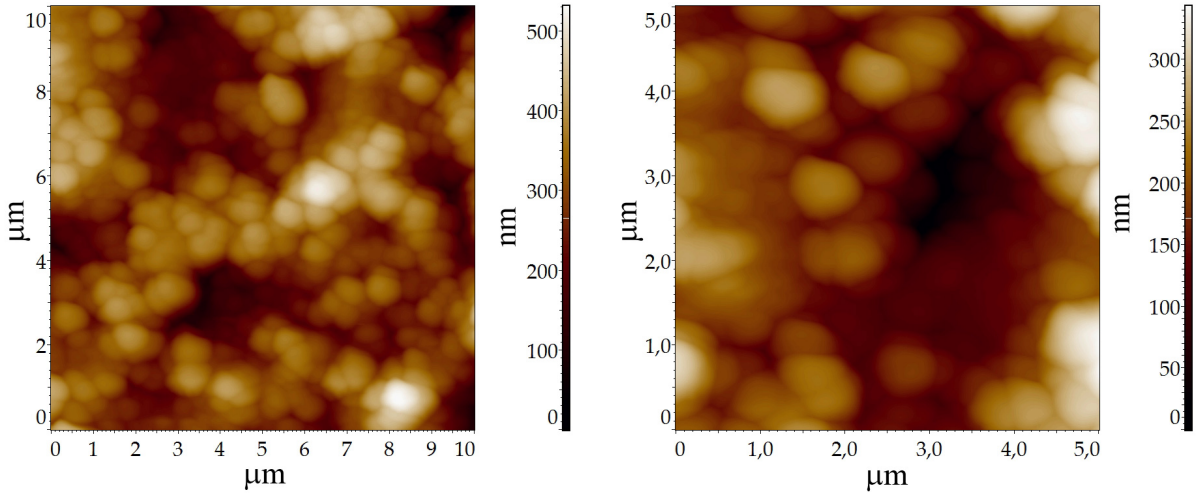

FIG. 2. Atomic Force Microscopy images for flintstone fresh cleavage faces

A typical optical microscopy image of the flintstone mineralogical slide is presented in Fig. 3. Black and white areas with typical size about 10 microns in the said image corresponded to the crystal areas of various orientations: lightening and darkening of each individual area in the slide occurred gradually when the samples were rotated.

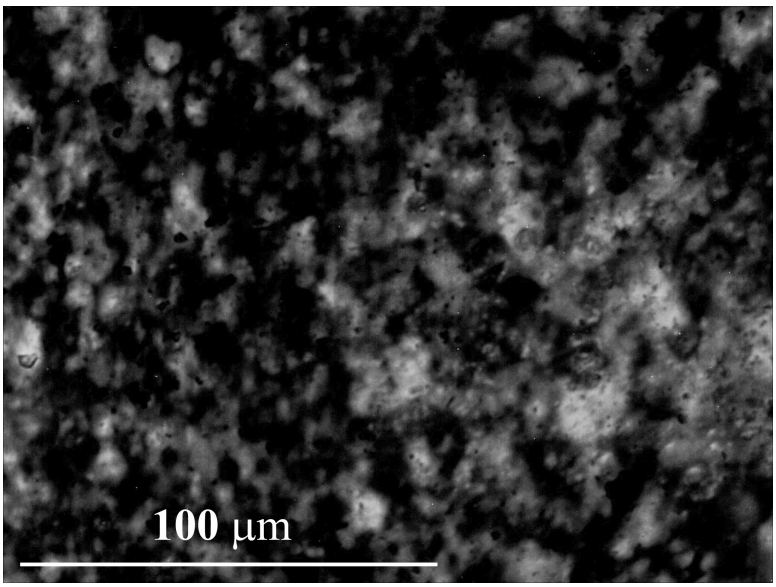

FIG. 3. Optical microscopy image (crossed polarizers)

Analysis of the above data from X-ray diffraction, atomic force microscopy and optical microscopy studies allowed us to conclude that the flintstone structure has several hierarchical levels of organization: nanoparticles with their size of about 30 nm formed round-shaped agglomerates with about 500 nm diameter containing about 5,000 – 10,000 the former 30 nm particles. In turn, the secondary 500 nm nanoparticles formed an easily visible framework in Fig. 2. Comparison of data in Figs. 2 and 3 indicated that merge of the secondary nanoparticles had an oriented crystallographic character (i.e., they intergrew in the right crystallographic orientation), so the whole volume of the flintstone specimen in Fig. 3 was made up of strangely intertwined branched crystal clots.

Despite the black coloration of the studied flintstone specimens, they could be transparent when relatively thin, so their optical transmittance spectra could be recorded (Fig. 4).

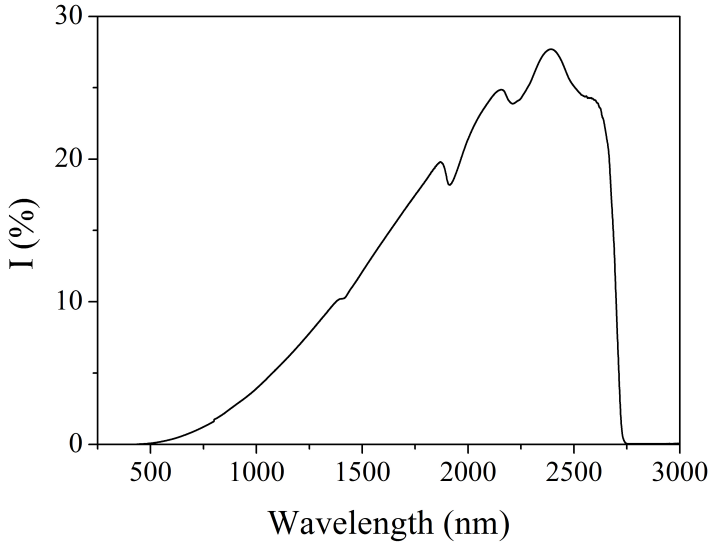

FIG. 4. Optical transmittance spectrum of the 0.8 mm thick flintstone specimen

Flintstone spectra exhibited absorption bands at about 1420, 1920 and 2250 nm wavelengths. The absorption at ∼2180 to 2380 nm has been interpreted as a combination effect of silanol group (Si–OH) and siloxane (Si–O–Si) vibrations. The absorption from 1900 to 2060 nm has been related to the sum of the OH modes in molecular water. The absorption in 1420 nm area was an overtone of OH vibrational modes [22].

Heating flintstone samples under air at 1,000 °C for 1 hour resulted in their discoloration (samples became white) and mass loss of 0.98 wt.%. This might have been related to elimination of the water and previously-mentioned carbon micro-impurities (said carbon might have organic origins). Whereas lines of carbon polymorphs could not be clearly observed in the X-ray diffraction patterns, micro-Raman scattering has been used to determine the presence of carbon and possible types of its inclusions.

The Raman spectrum of the thermally-untreated flintstone specimen (confocal HORIBA spectrometer; Fig. 5) contained one intensive broad line and two weak lines at about 1.400 and 1.600 cm^{-1}. Such lines are typical for Raman scattering of nanographite; the latter lines have been labeled as D and G lines [23], and the former line corresponded to nanocarbon luminescence [24] (Fig. 5 data represent Raman spectrum of flintstone after luminescence component subtraction).

Results of thermal conductivity measurements for various materials are presented in Fig. 6. The data presented unequivocally indicate that the thermal conductivity for flintstone is relatively low and could be placed between the thermal conductivities of single quartz crystals and amorphous quartz glass. Compared to the quartz single crystal data, maximum of the thermal conductivity temperature correlation moved to the higher temperature range, but decreased almost by three orders of magnitude. The same phenomenon has been observed for the disordered crystalline media including $M_{1-x}R_xF_{2+x}$ fluorite-type solid solutions (M = Ca, Sr, Ba; R = rare earth elements) [29].

As we have previously mentioned, flintstone samples are composite materials with complex hierarchic structures. The latter is in complete agreement with literature data: “Thin sections exhibit structure of at least two levels, the larger one of quartz or chalcedony grains ordered aggregates of 1–50 μm size and the smaller grains, combined conformally, that fill in available spaces and have web-toed or amoeboid shapes chalcedony grains are not single crystals, and they fade in a narrow-wave, hand-fan or cross-type style, in contrast with quartz crystals.

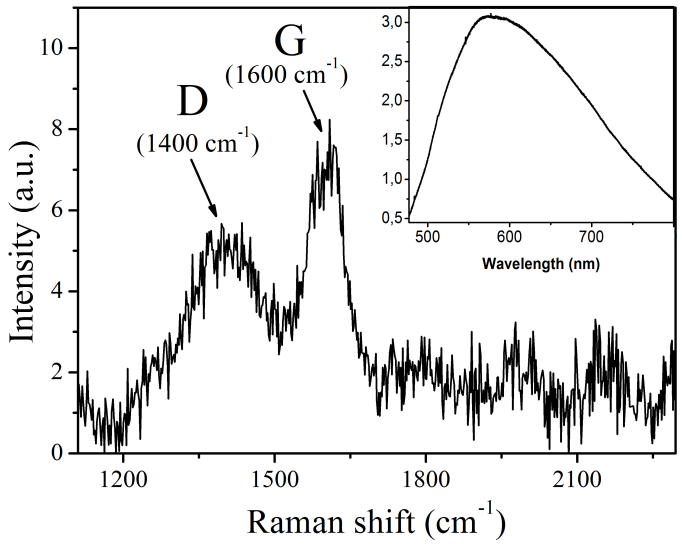

FIG. 5. Raman spectrum of flintstone sample after luminescence component subtraction

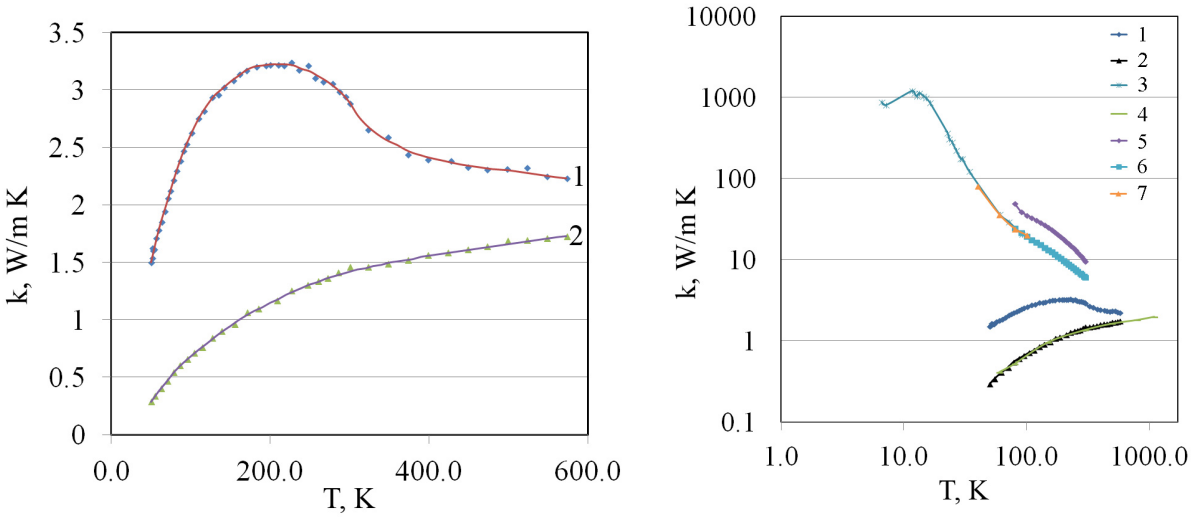

FIG. 6. Thermal conductivity of flintstone (our measurements) (1), quartz glass (our measurements) (2), quartz single crystal [25] (3), quartz glass [26] (4), quartz single crystal [27] (measured parallel to quartz optical axis) (5), quartz single crystal [27] (measured perpendicularly to quartz optical axis) (6), quartz single crystal [28] (7)

Thus, said chalcedony grains are the aggregates of very thin fibers that are invisible in optical microscope (their size indicates their colloidal nature); these fibers are allocated in the orderly, subparallel manner, i.e., in a radial pattern" [19]. However, our data amend the above observation with novel nano-level atomic force microscopy results.

The studied natural flintstone samples have a similar structure with laboratory-synthesized compacts of various chemical compositions prepared as nanopowders [11] as per the aforementioned atomic force microscopy in combination with X-ray phase analysis results, also confirming said hierarchic structure. Optical transmittance spectrum of flintstone has shown the unequivocal presence of water/hydroxyl moieties; but said water content in flintstone is essentially less than observed ca. 1 wt.% mass loss under heating, for such weight change corresponds to elimination of both water and elementary carbon. Also, it is worth mentioning that natural flintstone's hardness is higher than that of laboratory-synthesized compacts due to the different ripening time of these artificial and natural materials.

In addition, the studied flintstone specimens were nano-mineralogy objects [30] and, in general, black flintstones, exhibiting efficient luminescence, belong to nano-photonics.

Acknowledgement

The authors express their appreciation to V. Kuzin and E.M. Spiridonov for their optical treatment of the samples and to E.M. Spiridonov, A. M. Generalov and S. V. Kuznetsov for their discussion of the results.

This work was performed as a part of research plan of General Physics Institute. Some measurements were done in the Collective Use Centers of General Physics Institute and Institute of General and Inorganic Chemistry of the Russian Academy of Sciences.

References

[1] *Diffraction Nanophotonics*. Ed. V. A. Soifer. Moscow, Fizmatlit, 2011, 680 p. (in Russian).
[2] *Optical properties of photonic structures: interplay of order and disorder*. Ed. M.F. Limonov, R.M. De La Rue. Boca Raton, CRC/Taylor& Francis Group, 2012, XVII, 514 pp.
[3] Wiersma D. The smallest random laser. *Nature*, 2000, **406,** P. 132–133.
[4] García P.D., Sapienza R., Lo'pez C. Photonic Glasses: A Step Beyond White Paint. *Adv. Mater.*, 2010, **22**, P. 12–19.
[5] Barthelemy P., Bertolotti J., Wiersma D.S. A Le'vy flight for light. *Nature*, 2008, **453**, P. 495–498.
[6] Kouznetzov S.V., Yarotskya I.V., Fedorov P.P., Voronov V.V., Lavristchev S.V., Basiev T.T., Osiko V.V. Preparation of nanopowdered $M_{1-x}R_xF_{2+x}$ (M = Ca, Sr, Ba; R = Ce, Nd, Er, Yb) solid solutions. *Rus. J. Inorg. Chem*., 2007, **52**, P. 315–320.
[7] Fedorov P.P., Tkatchenko E.A., Kouznetzov S.V., Voronov V.V., Lavristchev S.V. Preparation of MgO nanoparticles. *Inorg. Mater*., 2007, **43**, **5**, P. 502-504.
[8] Kuznetsov S.V., Fedorov P.P., Voronov V.V., Samarina K.S., Ermakov R.P., Osiko V.V. Synthesis of $Ba_4R_3F_{17}$ (R stands for rare earth elements) powders and transparent compacts on their base. *Rus. J. Inorg. Chem.*, 2010, **55**(4), P. 484–493.
[9] Kuznetsov S.V., Fedorov P.P., Voronov V.V., Osiko V.V. Synthesis of $MgAl_2O_4$ Nanopowders. *Inorg. Mater.*, 2011, **47**, P. 895–898.
[10] Fedorov P.P., Kuznetsov S.V., Mayakova M.N., Voronov V.V., Ermakov R.P., Baranchikov A.E., Osiko V.V. Coprecipitation from aqueous solutions to prepare binary fluorides. *Rus. J. Inorg. Chem*., 2011, **56**(10), P. 1525–1531.
[11] Mayakova M.N., Kuznetsov S.V., Fedorov P.P., Voronov V.V., Ermakov R.P., Boldyrev K.N., Karban' O.V., Uvarov O.V., Baranchikov A.E., Osiko V.V. Synthesis and characterization of fluoride xerogels. *Inorg. Mater.*, 2013, **49**, **11**, P. 1152–1156.
[12] Mayakova M.N., Luginina A.A., Kuznetsov S.V., Voronov V.V., Ermakov R.P., Baranchikov A.E., Ivanov V.K., Karban' O.V., Fedorov P.P. Synthesis of SrF_2-YF_3 nanopowders by co-precipitation from aqueos solutions. *Mendeleev Commun.*, 2014, **24**(6), P. 360–362.
[13] Niederberger M., Colfen H. Oriented attachment and mesocrystals: Non-classical crystallization mechanisms based on nanoparticle assembly. *PhysChemChemPhys*, 2006, **8**, P. 3271–3287.
[14] Fedorov P.P., Ivanov V.K. Cooperative formation of crystals by aggregation and intergrowth of nanoparticles. *Dokl. Phys.*, 2011, **56**(4), P. 205–207.
[15] Ivanov V.K., Fedorov P.P., Baranchikov A.Y., Osiko V.V. Oriented aggregation of particles: 100 years of investigations of non-classical crystal growth. *Russ. Chem. Rev.*, 2014, **83**(12), P. 1204–1222.
[16] Smol'yaninov N.A. *Practical guide to mineralogy*. Moscow, Nedra, 1955, 432 p.
[17] Godovikov A.A., Ripinen O.I., Motorin S.G. *Agates*. Moscow, Nedra, 1987, 368 p (in Russian).
[18] Zdorik T.B. Opal. *Priroda*, 1990, **10**, P. 40–43 (in Russian).
[19] Frolov V.T. *Lithology*. Book 1. Moscow, Lomonosov St.Univ., 1992, 336 p. (in Russian).
[20] Spiridonov E.M., Ladygin V.M., Yanakieva D.Ya., Frolova Yu.V., Semikolennyh E.S. Agates in metavolcanics. Geological conditions, parameters and time of transformation of volcanites into mandelites with agates. Ed. Panchenko V.Ya. "MOLNET" Special issue of the magazine "Herald of RFBR", Moscow, 2014, 72 p. (in Russian).
[21] Popov P.A., Sidorov A.A., Kul'chenkov E.A., Anishchenko A.M., Avetissov I.Ch., Sorokin N.I., Fedorov P.P. Thermal conductivity and expansion of PbF_2 single crystals. *Ionics*, 2017, **23**, **1**, P. 233–239.
[22] Anderson J. H., Wickersheim K. A. Near infrared characterization of water and hydroxyl groups on silica surfaces. *Surface science*, 1964, **2**, P. 252–260.
[23] Ferrari A.C., Meyer J.C., Scardaci V., Casiraghi C., Lazzeri M., Mauri F., Piscanec S., Jiang D., Novoselov K.S., Roth S., Geim A.K. Raman spectrum of graphene and graphene layers. *Phys. Rev. Lett*., 2006, **97**, P. 18740.
[24] Khomich A.A., Kudryavtsev O.S., Dolenko T.A., Shiryaev A.A., Fisenko A.V., Konov V.I., Vlasov I.I. Anomalous enhancement of nanodiamond luminescence upon heating. *Laser Phys. Lett.*, 2017, **14**, P. 025702.
[25] Berman R. The thermal conductivities of some dielectric solids. *Proc. R. Soc. Lond. A*, 1951, **208**, P. 90–108.
[26] Sergeev O.A., Shashkov A.G., Umanskii A.S. Thermophysical properties of quartz glass. *J. Eng. Phys.*, 1982, **43**(6), P. 1375–1383.
[27] Novitsky L.A., Kozhevnikov I.G. *The thermophysical properties of materials at low temperatures (handbook)*. Mashinostroenie, Moscow, 1975 (in Russian).
[28] *Thermal Conductivity of Solids. Reference Book*. Ed. by A.S. Okhotin. Moscow, Energoatomizdat, 1984 (Russian).
[29] Popov P.A., Fedorov P.P., Kuznetsov S.V., Konyushkin V.A., Osiko V.V., Basiev T.T. Thermal conductivity of single crystals of $Ca_{1-x}Yb_xF_{2+x}$ solid solutions. *Dokl. Phys*., 2008, **53**(4), P. 198–200.
[30] Sedletskiy I.D. *Colloidal-dispersed mineralogy*. Ed. A.E. Fersman. Moscow, Leningrad, Academy of Science of the USSR, 1945, 114 p. (in Russian).
[31] Yushkin N.P., Askhabov A.M. et. al. *Nanomineralogy. Ultra- and micro-dispersed state of mineral matter*. St. Petersburg, Nauka, 2005, 581 p. (in Russian).

NANOSYSTEMS: PHYSICS, CHEMISTRY, MATHEMATICS, 2018, 9 (5), P. 609–613

Near-field optical microscopy of surface plasmon polaritons excited by silicon nanoantenna

I. S. Sinev, F. E. Komissarenko, I. S. Mukhin, M. I. Petrov, I. V. Iorsh, P. A. Belov, A. K. Samusev

St. Petersburg National Research University of Information Technologies,
Mechanics and Optics,
Kronverkskiy, 49, St. Petersburg, 197101, Russia
i.sinev@metalab.ifmo.ru

PACS 42.25.Fx, 71.45.Gm, 07.79.Fc **DOI 10.17586/2220-8054-2018-9-5-609-613**

An optical nanoantenna is a device that transforms far-field electromagnetic radiation into near-field and vice versa. Naturally, it can serve as a conduit between free space light and localized optical modes, including surface waves. With the recent rise of all-dielectric nanophotonics, nanoantennas made of high-index materials were found to offer unparalleled means for manipulation of light due to presence of equally strong electric and magnetic responses in the visible spectral range. Here, we demonstrate excitation of surface plasmon polaritons by single silicon nanosphere on gold layer measured by means of scanning near-field optical microscopy. The interference patterns observed in the measured near-field maps allow us to retrieve information on directivity and relative excitation efficiency of surface plasmon polariton in the longer wavelength part of the visible spectral range. Our results demonstrate that all-dielectric nanoantennas could prove to be a valuable tool for controlling directivity and efficiency of excitation of surface waves.

Keywords: near-field optical microscopy, silicon nanoparticles, all-dielectric nanoantennas, surface plasmon polaritons.

Received: 13 September 2018

1. Introduction

Within the last decade, all-dielectric nanophotonics established itself as a viable alternative for plasmonics due to lower losses and additional opportunities for light manipulation due to possibility of achieving non-unitary effective magnetic permeability. The concept of all-dielectric nanoantennas for the visible spectral range became reality with the discovery of strong scattering resonances of silicon nanospheres of 100 – 200 nm size [1, 2]. Initially, the studies of high-index nanoantennas for the visible range were mainly focused on the operation with bulk electromagnetic waves. A number of fascinating effects stemming from interference of equally strong electric and magnetic dipole resonances were discovered since then. Those are directional scattering of light [3], generalized Brewster effect [4], etc. At the same time, the performance of high-index nanoantennas in the domain of surface waves remained mostly unexplored with a few exceptions [5].

Here, we demonstrate that resonant silicon nanoparticle on metal film can act as an effective nanoantenna that converts free space light into surface plasmon polaritons. We visualize the excitation of SPP from silicon nanosphere on gold film using scanning near-field optical microscopy with aperture-type probe. In the near-field maps measured for oblique incidence of linearly polarized laser beam on the nanosphere, the surface wave excitation is manifested due to interference with the incident wave. We show that the obtained near-field maps can be used to retrieve information on directivity of excited surface plasmon polariton and compare the SPP excitation efficiency for s- and p-polarized light.

2. Methods

Resonant silicon nanoparticles were fabricated using laser ablation from thin films of amorphous silicon on glass following a well-established routine [6]. The ablation was performed using Yb^{3+} femtosecond laser (Avesta TeMa-150). Nanoparticles deposited back on silicon film were then transferred to 200 nm layer of crystalline gold using nanoscale manipulations under an electron beam [7].

The scheme of experimental setup for mapping the near-field of silicon nanoantenna on gold is shown in Fig. 1(a). The nanoparticle is excited with mildly focussed linearly polarized laser beam incident at $\theta \approx 65$ degrees. During the experiment, the near-field probe represented by a tapered metallized optical fiber with a subwavelength (100 nm) aperture at its tip is scanned within a plane at a fixed distance from the sample surface. As compared to standard regime with shear-force feedback, this regime allows one to avoid artifacts of near-field signal close to the sphere as well as accidental displacement of the sphere during the scan. Signal collected with the near-field probe was measured with photomultiplier tube (Hamamatsu H10792) in lock-in detection scheme.

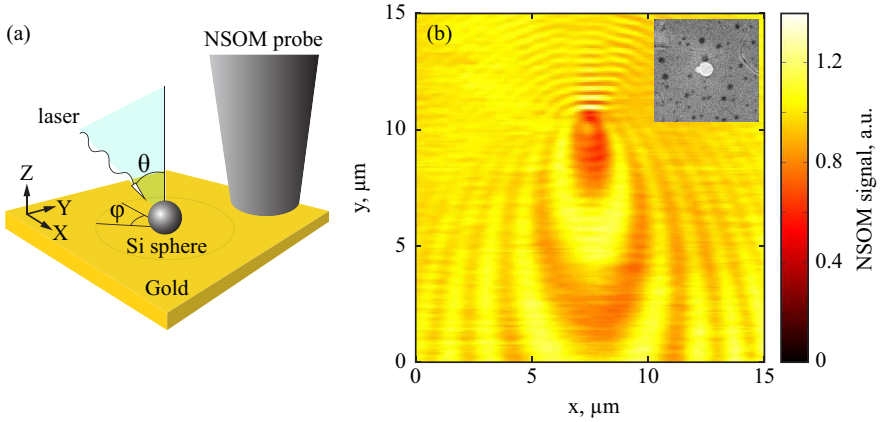

FIG. 1. (a) Sketch of the scanning near-field optical microscopy of surface plasmon polariton from silicon nanoantenna on gold. (b) Near-field map of resonant 200 nm silicon nanoantenna on gold excited with laser beam at a wavelength of 780 nm. The inset shows SEM image of silicon nanoantenna on gold

To study the spectral dependence of the near-field maps of surface plasmon polariton excited with the silicon nanosphere, we employed supercontinuum laser source (Fianium WhiteLase SC400-6) with tunable filter (Fianium SuperChrome). The central wavelength of the beam yielded by the system was tuned within 600 – 800 nm spectral range, while the bandwidth of the beam was 10 nm.

Theoretical modelling of the optical properties of silicon nanosphere on gold was performed using analytical model based on Green function approach [8]. Within this model, silicon nanosphere is described as a superposition of point electric and magnetic dipoles placed in its center. The corresponding electric and magnetic polarizabilities of the nanoparticle are first calculated using Mie theory [9] and then renormalized with account for the influence of the substrate as described elsewhere [8]. Using the calculated polarizabilities, it is then possible to find both the far-field scattering cross section of the particle and the fields of the SPP excited by the particle. The angular dependence of the intensity of the excited SPP wave is described by the formula [10]:

$$I_{SPP} \sim \left|\cos\varphi(m_y - i\kappa p_x) - \tilde{k}_{SPP} p_z\right|^2, \tag{1}$$

where φ is the direction of SPP excitation with respect to the plane of incidence, m_y and p_x are in-plane (parallel to the substrate) components of magnetic and electric polarizability of the nanosphere, and p_z is electric dipole component oriented normally to the substrate. $\tilde{k}_{SPP} = \sqrt{\varepsilon_m/(\varepsilon_m + 1)}$ stands for the normalized wavevector of the SPP on the interface of air and metal with dielectric permittivity ε_m, while $\kappa = -i\sqrt{1/(\varepsilon_m + 1)}$ characterizes the SPP localization in the direction normal to the substrate.

3. Results and discussion

Surface plasmon polaritons are localized modes that propagate along the interface between dielectric and metallic materials. Therefore, they cannot be directly addressed with common far-field microscopy techniques, and auxiliary devices or structures are needed for their excitation and detection. Namely, the characteristics SPP are studied using prisms in frustrated total internal reflection geometry [11] or via grating couplers and decouplers that provide additional momentum required to match the wavevector of light with that of SPP. Another option is offered by near-field scanning optical microscopy (NSOM), which allows to directly probe the evanescent components of SPP field. In this case, the parameters of SPP waves, such as wavelength and directivity, are manifested through near-field interference. For example, in case of scattering type NSOM, the surface waves are characterized using standing wave pattern that forms due to interference of surface waves launched by the probe and reflected from the sample edges or other defects [12]. In case of aperture-type NSOM, which detects free-space radiation as well, the excitation of surface plasmon polariton can be detected through interference with the incident wave. For example, in work by Permyakov *et al.* [13] the measured near-field maps of a hole in silver film manifested double-lobe interference pattern characteristic for SPP excited with a point magnetic dipole, which in that case was represented by the subwavelength hole in metal film [14].

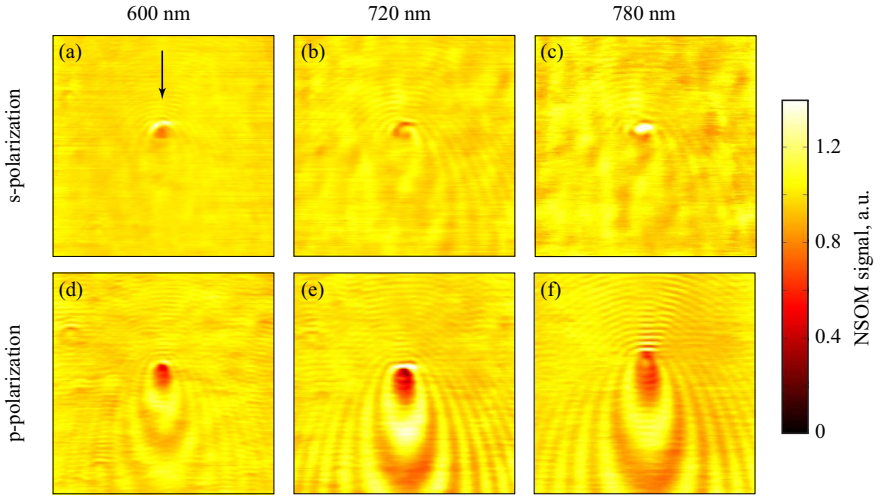

FIG. 2. Measured NSOM maps of SPP from 200 nm silicon nanosphere for three different wavelengths for s-polarization (a–c) and p-polarization (d–f). The size of each image is $15 \times 15\ \mu m^2$. The direction of incident light is shown with an arrow in panel (a)

In the experimental configuration used in our work, due to non-zero angle of incidence of the excitation beam the period of the observed interference pattern, T depends on the azimuthal angle (see characteric maps in Fig. 1b and Fig. 2). This dependence can be described with a simple formula:

$$T(\varphi) = \frac{2\pi}{k_0 \sin\theta \cos\varphi + k_{SPP}}, \tag{2}$$

where θ stands for the angle of incidence, φ is the azimuthal angle, and $k0, k_{SPP}$ are the wavevectors of free space light and SPP, respectively (see also Fig. 1a). Another factor affecting the near-field maps is the azimuthal dependence of the SPP excitation efficiency, which defines the relative amplitude of the modulation in a given direction and can be evaluated using eq. 1. Finally, total SPP excitation efficiency governs the maximum modulation depth of the interference pattern.

Fig. 2 shows the near-field maps of a 200 nm silicon nanosphere on gold substrate measured for s- and p-polarized incident light with wavelengths within 600-800 nm spectral range. As the figure clearly shows, the maps for different polarizations demonstrate different interference patterns. For p-polarized excitations, the maximum modulation is observed in forward direction. At the same time, for s-polarization the modulation is much weaker and is virtually suppressed in forward and backward directions. At the same time, for the same polarization the modulation depth increases towards 780 nm wavelength. These features can be explained using the formula for SPP intensity, eq. 1. First, it reveals that for s-polarized light, SPP is not excited in forward and backward directions as both p_y and m_x dipole moments contributing to SPP in such configuration do not couple to SPP along the x-axis. Moreover, the SPP intensity is much higher for p-polarized excitation. Indeed, m_y and p_z momenta induced in the sphere excited with p-polarized light couple to SPP with much higher efficiency (factors of 1 and $\tilde{k}_{SPP}$, respectively, the latter being close to unity in the considered spectral range [15]). On the contrary, coupling of p_y moment induced for s-polarization into SPP is suppressed by a factor of $1/\kappa \sim \sqrt{\varepsilon_m + 1}$, which reaches 5 – 7 for gold in the same spectral range. The observed spectral maximum of the SPP excitation efficiency corresponds to the onset of magnetic dipole resonance of the sphere (m_y). The contribution of electric dipole to SPP p_z is non-resonant, as it was demonstrated in our earlier work [16].

Finally, to retrieve the information on the directivity of excited SPP from the measured maps, we performed Fourier transform of the experimental data represented in polar coordinates (r, φ), where r is the distance from the center of the sphere. The NSOM map for 780 nm excitation wavelength processed accordingly is shown in Fig. 3a. The map reveals angle-dependent maximum which corresponds to the inverse period of the interference pattern. Its position is in great agreement with the interference period calculated from eq. 2 with account for the dispersion of gold dielectric permittivity at a given wavelength [15]. The Fourier-transformed data also allows to reconstruct the directivity pattern of the excited SPP by plotting the angular dependence of the intesity of the peak corresponding to SPP. Directivity pattern reconstructed from the NSOM data for 780 nm excitation is shown in Fig. 3b.

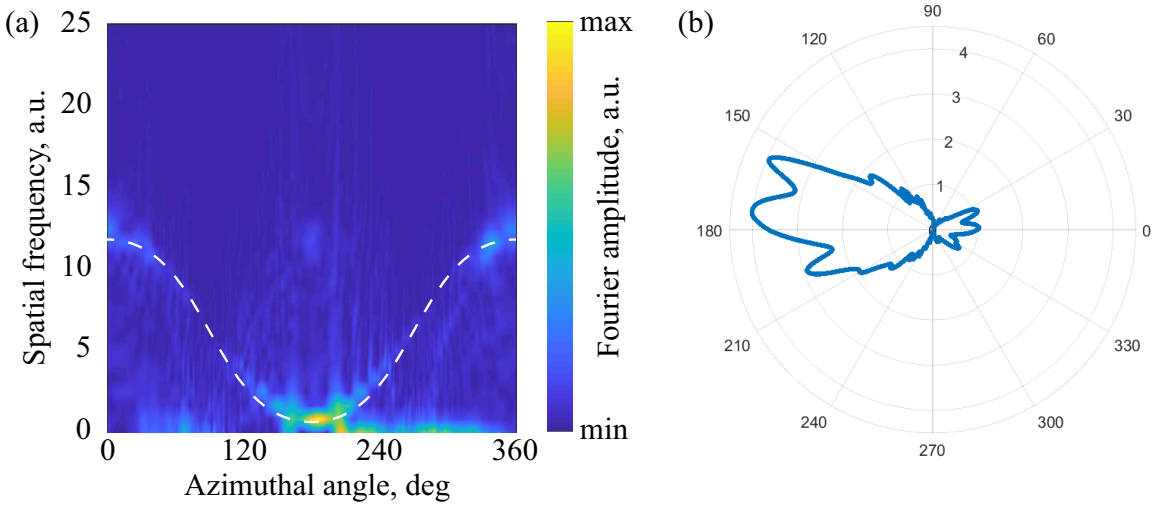

FIG. 3. (a) Fourier transform of NSOM map measured at 780 nm represented in polar coordinates. The dashed line represents the angular dependence of the period of interference pattern analytically calculated from eq. 2. (b) SPP directivity pattern reconstructed from (a)

Here, it is important to mention that the backward directivity of SPP retrieved from NSOM maps measured in such configuration is slightly underestimated due to the dependence of the excitation efficiency on the position of NSOM probe. Indeed, whenever the near-field probe moves into the "backward" half-space (top part of the maps in Fig. 1b and Fig. 2), it shades the nanosphere from the incident light, thus decreasing the effective amplitude of the incident wave at the nanosphere. Another factor influencing the reconstructed pattern is different data sampling for different angles due to changes in the period of the interference.

4. Conclusion

To conclude, in this work, we studied the surface plasmon polaritons excited by a resonant silicon nanosphere on gold film. The observed near-field maps exhibit signal modulation due to interference between the incident light and surface plasmon polariton excited from the silicon nanoantenna. The radial dependence of the interference fringes allowed us to evaluate the directivity pattern of the surface waves as well as their relative excitation efficiency. Our results show that single silicon nanoparticles can be used as compact yet effective antennas for directional excitation of surface plasmon polaritons.

Acknowledgements

This work was supported by the Ministry of Education and Science of the Russian Federation (project No 14.584.21.0024 with unique identificator RFMEFI58417X0024).

References

[1] Evlyukhin A. B., Novikov S. M., Zywietz U., Eriksen R. L., Reinhardt C., Bozhevolnyi S. I., Chichkov B. N. Demonstration of magnetic dipole resonances of dielectric nanospheres in the visible region. *Nano letters*, 2012, **12**(7), P. 3749–3755.

[2] Kuznetsov A. I., Miroshnichenko A. E., Fu Y. H., Zhang J., LukYanchuk B. Magnetic light. *Scientific reports*, 2012, **2**, P. 492.

[3] Fu Y. H., Kuznetsov A. I., Miroshnichenko A. E., Yu Y. F., Lukyanchuk B. Directional visible light scattering by silicon nanoparticles. *Nature communications*, 2013, **4**, P. 1527.

[4] Paniagua-Domnguez R., Yu Y. F., Miroshnichenko A. E., Krivitsky L. A., Fu Y. H., Valuckas V., Gonzaga L., Toh Y. T., Kay A. Y. S., LukYanchuk B., Kuznetsov A. I. Generalized Brewster effect in dielectric metasurfaces. *Nature communications*, 2016, **7**, P. 10362.

[5] Evlyukhin A. B., Bozhevolnyi S. I. Resonant unidirectional and elastic scattering of surface plasmon polaritons by high refractive index dielectric nanoparticles. *Physical Review B*, 2015, **92**(24), P. 245419.

[6] Dmitriev P. A., Makarov S. V., Milichko V. A., Mukhin I. S., Gudovskikh A. S., Sitnikova A. A., Samusev A. K., Krasnok A. E., Belov P. A. Laser fabrication of crystalline silicon nanoresonators from an amorphous film for low-loss all-dielectric nanophotonics. *Nanoscale*, 2016, **8**(9), P. 5043–5048.

[7] Denisyuk A. I., Komissarenko F. E., Mukhin I. S. Electrostatic pick-and-place micro/nanomanipulation under the electron beam. *Microelectronic Engineering*, 2014, **121**, P. 15–18.

[8] Miroshnichenko A. E., Evlyukhin A. B., Kivshar Y. S., Chichkov B. N. Substrate-Induced Resonant Magnetoelectric Effects for Dielectric Nanoparticles. *ACS Photonics*, 2015, **2**(10), P. 1423–1428.

[9] Born M., Wolf E. *Principles of optics: electromagnetic theory of propagation, interference and diffraction of light*. Elsevier, 2013, 836 p.

[10] Sinev I. S., Bogdanov A. A., Komissarenko F. E., Frizyuk K. S., Petrov M. I., Mukhin I. S., Makarov S. V., Samusev A. K., Lavrinenko A. V., Iorsh I. V. Chirality driven by magnetic dipole response for demultiplexing of surface waves. *Laser & Photonics Reviews*, 2017, **11**(5), P. 1700168.

[11] Otto A. Excitation of nonradiative surface plasma waves in silver by the method of frustrated total reflection. *Zeitschrift fur Physik A Hadrons and nuclei*, 1968, **216**(4), P. 398–410.

[12] Woessner A., Lundeberg M. B., Gao Y., Principi A., Alonso-Gonzalez P., Carrega M., Watanabe K., Taniguchi T., Vignale G., Polini M., Hone J., Hillenbrand R., Koppens F. H. L. Highly confined low-loss plasmons in grapheneboron nitride heterostructures. *Nature materials*, 2015, **14**(4), P. 421.

[13] Permyakov D. V., Mukhin I. S., Shishkin I. I., Samusev A. K., Belov P. A., Kivshar Y. S. Mapping electromagnetic fields near a subwavelength hole. *JETP letters*, 2014, **99**(11), P. 622–626.

[14] Bethe H. A. Theory of diffraction by small holes. *Physical review*, 1944, **66**(7-8), P. 163.

[15] Johnson P. B., Christy R. W. Optical constants of the noble metals. *Physical review B*, 1972, **6**(12), P. 4370.

[16] Sinev I., Iorsh I., Bogdanov A., Permyakov D., Komissarenko F., Mukhin I., Samusev A., Valuckas V., Kuznetsov A. I., Luk'yanchuk B. S., Miroshnichenko A. E., Kivshar Y. S. Polarization control over electric and magnetic dipole resonances of dielectric nanoparticles on metallic films. *Laser & Photonics Reviews*, 2016, **10**(5), P. 799–806.

NANOSYSTEMS: PHYSICS, CHEMISTRY, MATHEMATICS, 2018, 9 (5), P. 614–621

Nanoscale architecture of graphene oxide membranes for improving dehumidification performance

E. A. Chernova[1], D. I. Petukhov[1], O. O. Kapitanova[1], O. V. Boytsova[1,2], A. V. Lukashin[1], A. A. Eliseev[1]

[1]Lomonosov Moscow State University, Leninskiye Gory, Moscow, 119991, Russia
[2]Kurnakov Institute of General and Inorganic Chemistry, Russian Academy of Sciences, Leninsky prospect, 31, Moscow, 119991, Russia

wellastra@gmail.com, di.petukhov@gmail.com, olesya.kapitanova@gmail.com, boytsova@gmail.com, alexey.lukashin@gmail.com, eliseev@inorg.chem.msu.ru

PACS 81.05.Rm, 47.56.+r **DOI 10.17586/2220-8054-2018-9-5-614-621**

Thin composite graphene oxide (GO) membranes prepared from the mixture of GO nanoflakes and nanoribbons are proposed to enhance membrane stability at elevated pressure gradients. It is shown that addition of 5 – 15 % of GO nanoribbons to medium flake graphene oxide during deposition allows up to a 60 % increase in the porosity of GO membranes. The membranes illustrate strong barrier properties to permanent gases with a permeance below 0.01 $m^3/(m^2 \cdot bar \cdot h)$, while revealing high permeance to water vapor over 50 $m^3/(m^2 \cdot bar \cdot h)$. This results in H_2O/N_2 selectivity up to 12500 at water vapor fluxes over 1 $m^3/(m^2 \cdot h)$ at relative humidity of feed stream of 90 %. Despite $\sim$ 10 % loss of membrane performance with addition of nanoribbons, the membranes reveal an improved stability to pressure gradients. Irreversible permeance loss of composite membranes does not exceed 10 % as compared to $\sim$ 35 % performance loss for pure medium flake graphene oxide (MFGO) after long term exposure to 0.1 MPa pressure difference. An improved stability is invoked for the prevention of the irreversible conglomeration of GO flakes and appearance of permanent channels for water transport along the edges of nanoribbons.

Keywords: graphene oxide flakes, nanoribbons, anodic alumina, pressure stability, dehumidification, water transport.

Received: 4 August 2018

Revised: 9 September 2018

1. Introduction

Graphene oxide (GO) is an advanced 2D material with a variety of applications including membrane separation technologies [1]. The unique microstructure of GO is represented by a laminar assembly of stacked 2D nanosheets covered with hydrophilic oxygen-containing groups. Under standard conditions, graphene oxide shows barrier properties towards most of gases but exhibits high selectivity for water vapor, which makes it a perfect candidate for gas dehumidification processes [2–4]. Gases and vapors can migrate through graphene oxide structure by interlayer diffusion, cross-layer channels and defects in GO nanosheets [5]. The proportion between these diffusion pathways is dictated by both the GO oxidation degree and the GO microstructure friability. The last property is mainly governed by the stacking order of GO nanosheets, GO nanosheet sizes, and the method of GO membrane preparation [6]. The interrelation of GO microstructure and its separation properties under real operational conditions is the key factor for successful design of industrial GO-based membranes. It should be kept in mind, that a huge number of membrane separation processes are conducted at elevated pressures and large pressure gradients. Due to its layered structure, graphene oxide exhibits compaction under pressure gradients. This becomes a keystone problem for industrial utilization of GO membranes.

To date, a lack of attention is payed to the separation properties and stability of GO under elevated pressure. The reported results on water vapor-gas separation were obtained without absolute pressure difference between feed and permeate side [2,3]. Only few studies on permeation of liquid water across GO membranes at elevated pressure in nanofiltration processes have been published [7–10]. In [7], the decline of liquid water permeation with pressure increase was shown: at 10 bar the final water flux on a GO-based membrane was lower than 10 % of its initial value. Such a strong reduction of water permeance was attributed to the compacting of the GO's laminar structure, resulting in extension of diffusion pathways for water molecules and decreasing the overall permeance. Notably, according to [7], the GO membrane can be partially regenerated after pressure exposure by drying. GO compaction is detrimental, as water molecules cannot flip through interlayer spacing and a prolonged time is required to restore the original high-water permeable GO structure.

To reduce compaction, stabilization of GO d-spacing by cross-linking can be achieved. The intercalation of cross-linking agents, cations, different nanostrands, or even single-walled carbon nanotubes has been suggested [11–14]. Alternatively, the prolonged high performance of GO membranes can be achieved by inserting

rigid components resistive to pressure into its interlayer spacing. Such components create incompressible persistent channels for water permeance in GO nanostructure providing stable membrane performance. The best candidates for this purpose are graphene oxide nanoribbons obtained by oxidation of single walled carbon nanotubes as being most compatible with GO matrix.

Thus, here we report the results on pressure stability of composite membranes based on GO nanolfilms intercalated with GO nanoribbons deposited on anodic alumina substrates. The pressure stability of GO-based membranes is tested. It is shown that composite membranes based only on GO nanoflakes lose their water permeance with pressure, whereas addition of GO nanoribbons improves the pressure resistance of GO membranes.

2. Experimental section

Graphene oxide nanoflakes (MFGO) and nanoribbons (CNTGO) were prepared by oxidation of medium flake graphite and single-walled carbon nanotubes, respectively, using a modified Hummer's method [15,16]. A detailed description of the procedure is reported in [5].

Anodic alumina membranes, with pore diameter of ~ 100 nm and a thickness of 100 μm, were chosen as the support for GO-based composite membranes due to their excellent performance [17–19]. The AAO substrates were prepared by anodic oxidation of high purity aluminum in oxalic acid at 120 V. To enhance the permeance of the supports, a two-stage oxidation process was employed. The detailed description of the AAO preparation is given in [17,18,20,21].

To prepare composite membranes, mixed water-methanol suspensions of GO nanoflakes and GO nanoribbons in weight ratios of 20:1 (5 % CNTGO) and 7:1 (15 % CNTGO) and total GO concentration of 1 mg/L were deposited on AAO substrates using spin-coating technique at the rotation speed of 2500 rpm. The samples were denoted as MFGO-CNTGO-5 and MFGO-CNTGO-15, respectively. A reference sample of MFGO was also prepared by deposition of water-methanol suspension of pure MFGO nanoflakes.

The microstructure of AAO supports and GO-based composite membranes was studied using SEM Carl Zeiss NVision 40 (5 kV, InLens detector) electron microscopes. Raman maps of the graphene oxide selective layers were recorded by Renishaw InVia spectrometer with Leica DMLM optics (50$\times$ objective) using 20 mW 633 nm He–Ne laser. Streamline accumulation mode with line-focused laser beam (a length of ~ 50 mm and a thickness below 1 mm) was used to collect the scans with total accumulation time of 200 s for each point. The obtained maps were treated in Wire 3.4 Renishaw software. The positions and the intensity of characteristic graphene oxide bands (~ 1350, and ~ 1590 cm^{-1}) were obtained using full profile analysis in 1000 – 1900 cm^{-1} spectral region with Pseudo-Voigt fitting of the peaks and applying 3-rd order baseline to a final tolerance factor for each spectrum of 0.01.

The permeance of AAO supports and GO-based composite membranes was measured in two-compartment cross-flow cell using a permeance setup equipped with SLA5850 mass-flow controllers (Brooks, England), PD-100-DI pressure transducers (OVEN, Russia) and T-Station 75 vacuum system (BOC Edwards, England). The measurements were performed at ambient temperature (22 ± 2 °C). Both differential (continuous pumping, flow is registered by flow controllers) and integral (closed volume, flow is registered by pressure transducers) schemes were used to measure the permeance. The water permeance was measured using a setup equipped with temperature and humidity sensors HIH-4000 (Honeywell, USA). Dew point of the sweep gas from permeate side was also registered with a dew-point hygrometer TOROS-3VY (Ukraine). The pressure in experiments was controlled using Carel SPKT00E3R pressure transducers. More details of the experiment can be found in [5].

3. Results and discussion

The idea for development of composite membranes comprising graphene oxide nanoflakes mixed with GO nanoribbons was originally dictated by the necessity to provide stable transport channels for water molecules, independent on pressure induced changes of GO microstructure. Indeed, rather small MFGO flakes with average sizes of ~ 500 nm are extremely flexible in the layered structure, resulting in sliding and conglomeration of GO flakes under pressure gradients. Hindered intercalation of water into the interlayer space of conglomerates results in irreversible losses of membrane permeance [7]. With the introduction of GO nanoribbons with characteristic sizes of 10×2000 nm between GO flakes we have expected the formation of voids the edges of ribbons those could not be overlayed by GO (Fig. 1). Moreover, irregular deposition of nanoribbons in between GO nanoflakes should result in increased microporosity with characteristic diameter of the pores in the order of ~ 1 nm. We expected that microstructural changes induced by nanoribbons will allow us to avoid the strong degradation of membranes that appear due to exclusion of water from the GO interlayer space under pressure gradients [5].

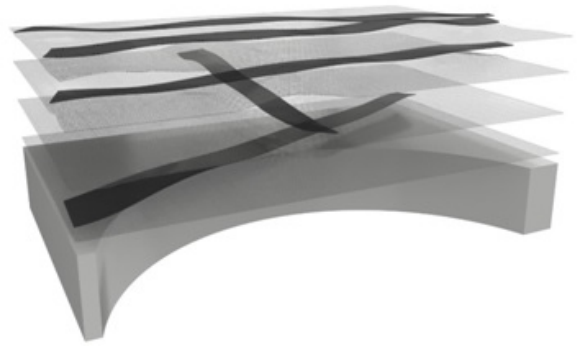

FIG. 1. Schematic illustration of the structure of MFGO-CNTGO composite membranes illustrating incompressible diffusion channels for water molecules along GO nanoribbons. Grayscale difference of nanoflakes and ribbons is given for better representation

According to SEM, addition of small amounts of graphene oxide nanoribbons (5 – 15 %) does not introduce critical changes to the membranes' microstructure (Fig. 2). All composite films illustrate formation of continuous GO layers on the surface of AAO substrates with characteristic thickness of ~ 100 nm. Detectable increase of the coating thickness from ~ 80 to ~ 100 nm was obtained by statistical analysis of cross-sectional images. Top-view micrographs indicate remarkable difference in coatings microstructure. Additionally, a visible increase of the quantity of nanoribbons at the surface from pure MFGO to MFGO-CNTGO-15 membrane, micrographs also reveal much less pronounced corrugation of GO layers with increasing ribbons content. Such corrugations are attributed to the high flexibility of MFGO layers appearing as a result of sliding of nanoflakes during methanol evaporation. Both the increased flatness of the films and increased visible thickness can originate from decreasing density of the layers due to porosity introduced by addition of nanoribbons.

Since the porosity of films with characteristic thickness of ~ 100 nm cannot currently be measured by any direct methods, we have suggested an approach based on the determination of total graphene oxide quantity from Raman scattering with subsequent normalization to statistical thickness of the layers derived by SEM. Total Raman scattering from sp^2 and sp^3-carbon (both D- and G-modes) was involved in the calculations. A film of graphene oxide produced from large-flake thermally expanded graphite with statistically measured thickness (25±5 nm) and porosity of 10 % was used as an external standard [5]. Despite rather a large possible error produced with this semi-quantitative approach, it allowed us to determine the porosity of GO films with relative accuracy of ±20 % of the value.

Raman maps acquired for MFGO and MFGO-CNTGO samples illustrate diminishing of scattered signal from carbon (D+G modes, Fig. 3(b, e), Table 1) with increasing nanoribbons content. Moreover, intensity distribution (RSD) degrades strongly in series attaining ~ 10 % for MFGO-CNTGO-15 sample. This effect is obviously connected with irregular deposition of highly anisotropic nanoribbons. The porosity of GO films extracted from an average scattering intensity normalized to film thickness illustrates strong expansion of GO film with nanoribbons content. For the MFGO-CNTGO-15 sample, the porosity attains 60 % which is comparable to pure CNTGO films (~ 70 % porosity) [5].

TABLE 1. Microstructural parameters and statistical analysis of Raman spectroscopy maps for composite membranes

Sample	Membrane thickness (SEM), nm	D+G-mode		D/G mode ratio		Derived porosity, %
		Signal intensity, cps·10^5	RSD, %	Average	RSD, %	
MFGO	80±20	3.5	3.5	2.68	4.4	10±5
MFGO-CNTGO-5	90±20	3.0	6.7	2.87	7.9	30±10
MFGO-CNTGO-15	100±20	1.8	8.7	2.94	13.8	60±10

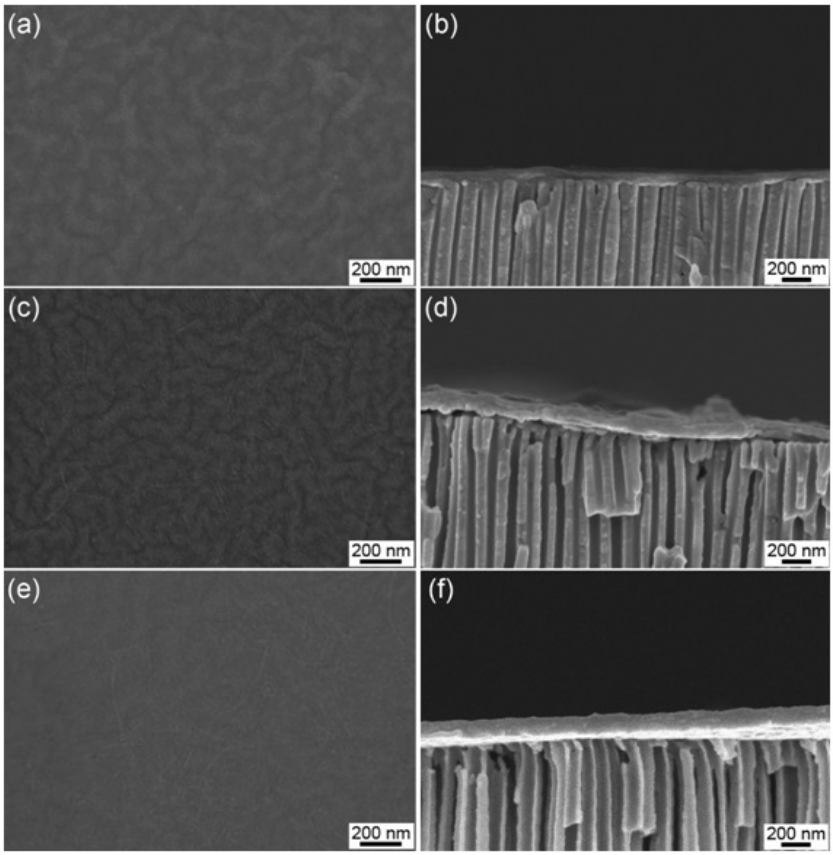

FIG. 2. Top-view and cross-sectional SEM images of composite membranes: (a, b) MFGO; (c, d) MFGO-CNTGO-5; (c, d) MFGO-CNTGO-15

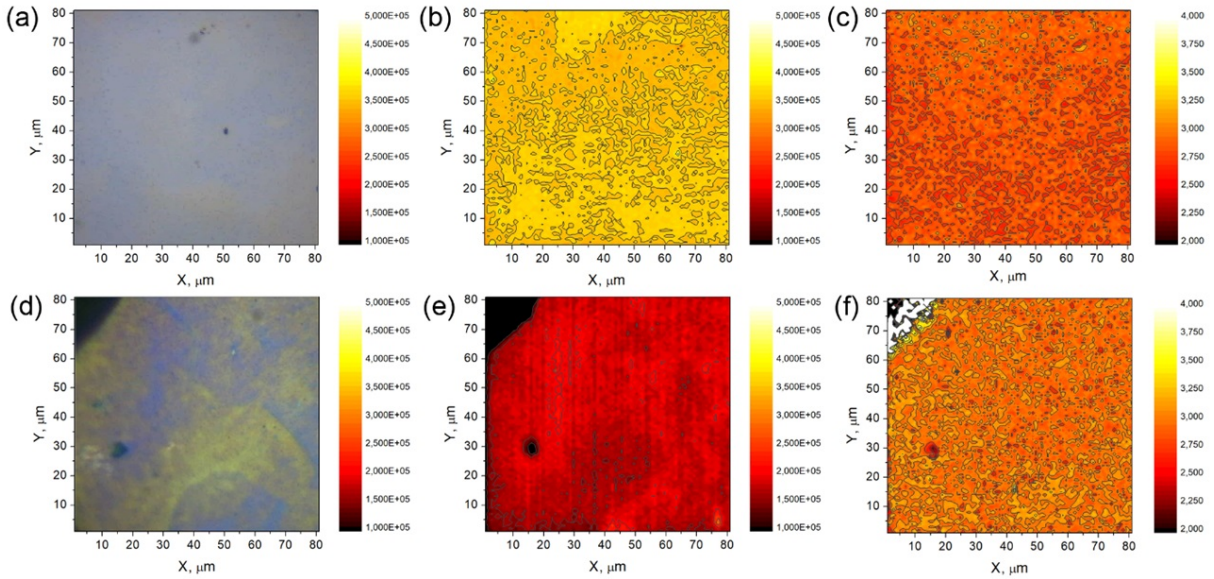

FIG. 3. Optical microscopy images (a, d) and Raman spectroscopy maps of sum of D- and G-modes intensity (b, e) and G-mode/D-mode intensity ratio (c, f) for MFGO (a, b, c) and MFGO-CNTGO-15 (d, e, f) samples. Black triangle in the top-left corner of (d, e, f) corresponds to an edge of sample after sample preparation for SEM

According to Raman data, the samples illustrate minimal difference in D/G modes ratio in the films (Fig. 3(c, f); Table 1) indicating similar deposition geometry of the layers. I.e. MFGO flakes preferably lay parallel to the substrate surface forming a layered structure regardless of the presence of nanoribbons. A slight increase in both D/G mode ratio and D/G-modes dispersion can be associated with tilting of GO flakes alongside the ribbons. Thus, introducing GO nanoribbons into MFGO films leads to an increased porosity and inhomogeneity of the films, however providing no serious effect on the layered packing of GO flakes.

Due to a rather uniform structure, the composite membranes reveal gas barrier properties towards permanent gases while maintaining high water permeance, which is favorable for dehumidification process. Typical permeabilities for membranes do not exceed 0.5 Barrer for all gases except water vapor. The membranes have a tendency to display Knudsen diffusion with the permeance of permanent gases lowering proportional to square root from molecular weight (Table 2). Such transport mechanism corresponds to gaseous diffusion through interflake edges [22]. The permeance of membranes generally increases with content of GO nanoribbons which obviously corresponds to additional pathways created by introduction of ribbons to the layered structure.

TABLE 2. Gas permeance of composite membranes

Sample	Permeance, l/(m^2·bar·h)						H_2O/N_2 selectivity at RH 90 %
	CH_4	N_2	O_2	CO_2	C_4H_{10}	H_2O at RH 90 %	
MFGO	5.2	3.9	3.7	3.2	2.1	63050	14650
MFGO-CNTGO-5	6.1	4.4	3.96	3.7	2.5	55100	12520
MFGO-CNTGO-15	16	9.7	8.9	8.3	4	51500	3220
$1/\sqrt{M}$, mole$^{0.5}$/kg$^{0.5}$	7.90	5.98	5.59	4.77	4.15	7.45	

Notably, the permeance of composite membranes for permanent gases was found to be two orders of magnitude lower as compared to pure CNTGO membranes, revealing much lower quantity of direct pathways for gaseous transport. Moreover, N_2 permeance also diminishes as compared to thin (30 nm) MFGO film, which is accounted for by an overall increase of the diffusion lengths and blocking of the diffusion pathways through interflake edges due to increased film thicknesses.

Diminishing the permeance for permanent gases is only partly accompanied by permeance losses for water vapor. The MFGO membrane, with a thickness of 80 nm, exhibits water vapor permeance over 60 m^3/(m^2·bar·h), compared to $\sim$ 100 m^3/(m^2·bar·h) for 30 nm membrane. Nonlinear behavior of permeance can be attributed to the changes in an equilibrium interlayer distance of GO in the surface layers at different partial water pressures on permeate sides of membrane [5]. With increased nanoribbon content, the water vapor permeance slightly decreases in all the humidity range (Fig. 4). In all likelihood, a portion of rather large voids emerges in GO membrane volume due to crossing of nanoribbons. Such pores can persist as gas-filled, even at high vapor pressures, which prevents capillary transport of liquefied water through membrane. In concert with enhanced transport of permanent gases, this results in loss of selectivity of membranes. However absolute selectivities still exceed 3000 at water permeance of ~ 1.0 m^3/(m$^2 cdot$h), remaining sufficient for technological dehumidification process.

Notably, the humidity dependence of water permeance of MFGO is reproduced well by composite membranes (Fig. 4). This indicates that general permeation mechanism for water molecules in GO films is irrespective of the porosity introduced by GO nanorribbons. This fact supports the major role of cross-layer transport of water molecules through the defects in the graphene layer [5, 23].

The pressure stability of membranes was tested under stepwise elevation of feed pressure followed by exposure to pressure gradient and stepwise pressure release. Total experiment duration for each membrane exceeded 20 h. The reference MFGO membrane illustrates low water permeance stability under transmembrane pressure. Initially, being the most permeable to water vapor, this membrane loses 25 % of permeance at first 0.02 MPa pressure step. At 0.1 MPa water permeance falls to $\sim$ 25 m^3/(m^2·bar·h). The reduction of GO permeance stays in agreement with earlier studies explaining the effect by the pressure-driven ousting of water molecules from the interlayer space of GO induced by bearing reaction of the support [5]. However, at pressure release, MFGO membrane exhibits a strong hysteresis, regenerating to $\sim$ 40 m^3/(m^2·bar·h) only, thus loosing $\sim$ 35 % of the initial permeance after pressure exposure. This is obviously caused by irreversible changes in membrane microstructure, attributed to sliding and conglomeration of flexible GO flakes under transmembrane pressure. Those changes hinder further intercalation of water into the interlayer space of GO conglomerates resulting in membrane permeance losses.

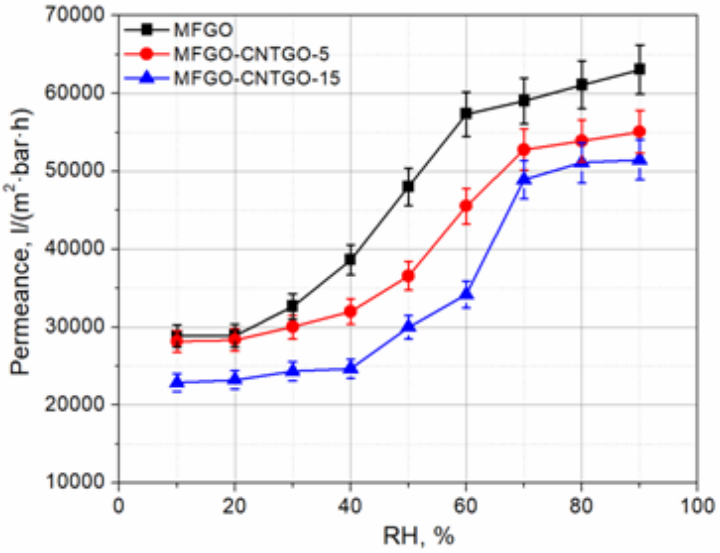

FIG. 4. The dependencies of water vapor permeance on feed gas humidity for composite membranes. Both sides of membrane were kept at atmospheric pressure, while permeate side was swept with dry He stream

Composite membranes exhibit similar behavior under an elevated pressure. At high pressure difference the permeance of these membranes becomes nearly equal to that of pure MFGO membrane, reflecting the pressure-driven ousting of water and permeance limitation by surface layers. A small permeance gain is achieved for the MFGO-CNTGO-5 sample at a transmembrane pressure of 0.1 MPa. On pressure release, both membranes restore permeance close to initial values with irreversible losses not exceeding 10 %. The losses are reduced with increasing the content of nanoribbons, indicating improved stability of the structure. Notably, both the composite membranes illustrate higher water permeance after pressure exposure as compared to pure MFGO membrane. These facts prove applicability of the proposed strategy for stabilization of GO structure and allow quick restoration of GO permeability through the introduced transport channels after membrane compression.

The proposed approach does not require any expensive linking agents or any special membrane modification steps and can be readily utilized at an industrial scale for the production of GO dehumidification membranes. We also believe the methodology is further applicable for the creation of permanent flexible transport channels in layered membranes for other challenging issues of membrane science and technology.

4. Conclusions

Thus the proposed strategy for the creation of composite membranes comprising graphene oxide nanoflakes mixed with GO nanoribbons allows improvement of membrane resistance towards elevated pressure gradients, while maintaining high performance and selectivity of graphene oxide. The insertion of 5 – 15 wt% of GO nanoribbons into medium flake graphene oxide during deposition gave rise to an increase in the porosity of GO membranes up to 60 %. The obtained composite membranes possess high permeance towards water vapor (over 50 $m^3/(m^2 \cdot bar \cdot h)$), while exhibiting strong barrier properties to permanent gases, resulting in H_2O/N_2 selectivity up to 12,500 at water fluxes over 1 $m^3/(m^2 \cdot h)$ at the relative humidity of feed stream of 90 %. The GO nanoflake-nanoribbons network reveals enhanced stability to pressure gradients but at a cost of $\sim$ 10 % loss of membrane performance. Irreversible permeance loss of composite membranes based on the MFGO-CNT mixture does not exceed 10 % as compared to $\sim$ 35 % performance loss for pure MFGO after long term exposure to 0.1 MPa pressure difference. Enhanced pressure stability is attributed to the prevention of the irreversible conglomeration of GO flakes and the formation of permanent flexible channels for water transport across the edges of nanoribbons. This simple approach permits the wide application of graphene oxide in separation technologies.

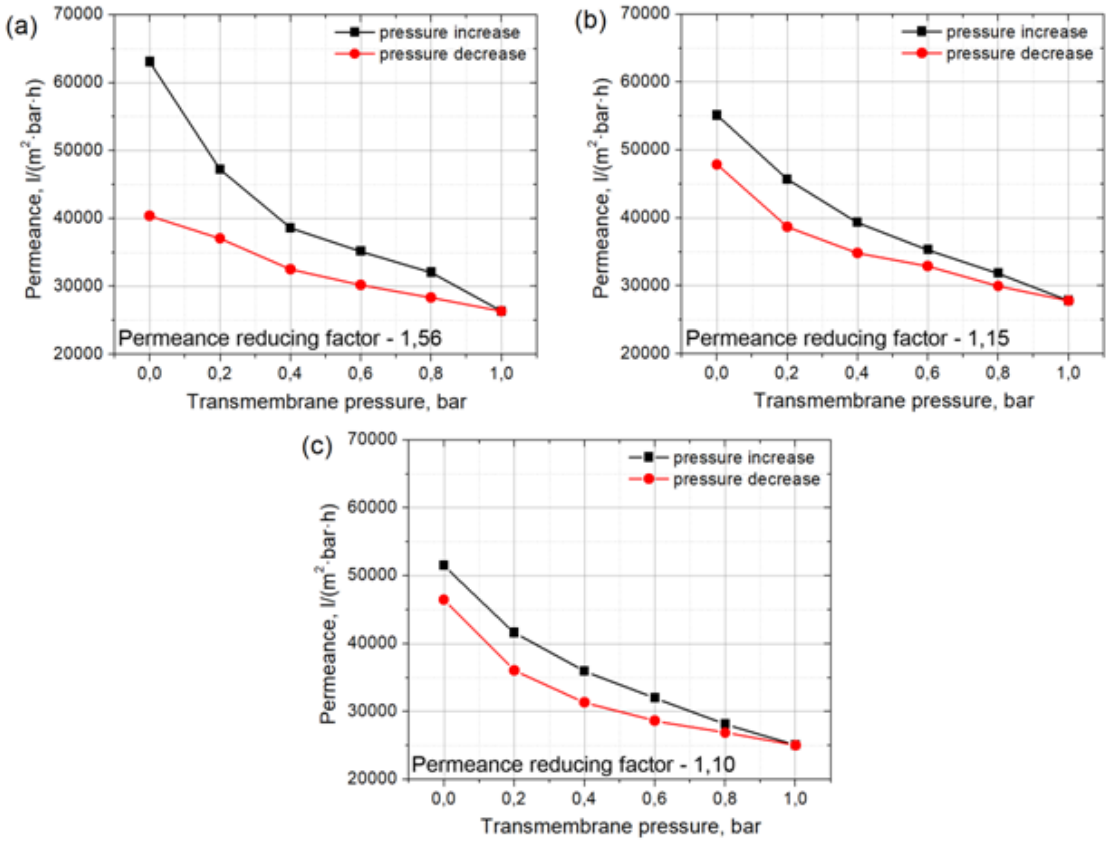

FIG. 5. Pressure dependencies of water vapor permeance for graphene oxide membranes (a) MFGO; (b) MFGO-CNTGO-5; (c) MFGO-CNTGO-15. The black curve corresponds to increasing pressure gradient from standard conditions, red curve – to pressure gradient decrease after exposure to 0.1 MPa pressure difference. A feed stream with 90 % RH at absolute pressures of 1 – 2 bar was used in experiments. Absolute permeate pressure was always maintained at atmospheric pressure with He sweep gas

Acknowledgements

The work is supported by the Ministry of education and science of the Russian Federation within a Federal Targeted Programme for "Research and Development in Priority Areas of Development of the Russian Scientific and Technological Complex for 2014–2020" (Agreement No. 14.604.21.0177, unique Project Identification RFMEFI60417X0177).

References

[1] Ma J., Ping D., Dong X. Recent Developments of Graphene Oxide-Based Membranes: A Review. *Membranes*,2017, **7** (3), P. 52–81.
[2] Shin Y., Liu W., et al. Graphene oxide membranes with high permeability and selectivity for dehumidification of air. *Carbon*, 2016, **106**, P. 164–170.
[3] Athanasekou C., Pedrosa M., et al. Comparison of self-standing and supported graphene oxide membranes prepared by simple filtration: Gas and vapor separation, pore structure and stability. *Journal of Membrane Science*, 2017 **522**, P. 303–315.
[4] Nair R.R., Wu H.A., et al. Unimpeded Permeation of Water Through Helium-Leak-Tight Graphene-Based Membranes. *Science*, 2012, **335** (6067), P. 442–444.
[5] Petukhov D.I., Chernova E.A., et al. Thin graphene oxide membranes for gas dehumidification. *Journal of Membrane Science*, (submitted), 2018.
[6] Nandy K., Palmeri. M., et al. Stop Motion Animation Reveals Formation Mechanism of Hierarchical Structure in Graphene Oxide Papers. *Advanced Materials Interfaces*, 2016, **3** (6), 1500666.
[7] Chong J.Y., Wang B., Mattevi C., Li K. Dynamic microstructure of graphene oxide membranes and the permeation flux. *Journal of Membrane Science*, 2018, **549**, P. 385–392.
[8] Yi H., Zhen X., Chao G. Ultrathin Graphene Nanofiltration Membrane for Water Purification. *Advanced Functional Materials*, 2013, **23** (29), P. 3693–3700.

[9] Wei Y., Zhang Y., et al. Declining flux and narrowing nanochannels under wrinkles of compacted graphene oxide nanofiltration membranes. *Carbon*, 2016, **108**, P. 568–575.
[10] Wei N., Peng X., Xu Z. Understanding Water Permeation in Graphene Oxide Membranes. *ACS Applied Materials & Interfaces*, 2014, **6** (8), P. 5877–5883.
[11] Huang K., Liu G., Jin W. Vapor transport in graphene oxide laminates and their application in pervaporation. *Current Opinion in Chemical Engineering*, 2017, **16**, P. 56–64.
[12] Han Y., Jiang Y., Gao C. High-Flux Graphene Oxide Nanofiltration Membrane Intercalated by Carbon Nanotubes. *ACS Applied Materials & Interfaces*, 2015, **7** (15), P. 8147–8155.
[13] Hung W.-S., Tsou C.-H., et al. Cross-Linking with diamine monomers to prepare composite graphene oxide-framework membranes with varying d-spacing. *Chemistry of Materials*, 2014, **26** (9). P. 2983–2990.
[14] Huang H., Song Z., et al. Ultrafast viscous water flow through nanostrand-channelled graphene oxide membranes. *Nature Communications*, 2013, **4**, P. 2979.
[15] Marcano D.C., Kosynkin D.V, et al. Improved Synthesis of Graphene Oxide. *ACS Nano*, 2010, **4** (8), P. 4806–4814.
[16] Kosynkin D.V., Higginbotham A.L, et al. Longitudinal unzipping of carbon nanotubes to form graphene nanoribbons. *Nature*, 2009, **458**, P. 872–876.
[17] Petukhov D.I., Napolskii K.S., et al. Comparative study of structure and permeability of porous oxide films on aluminum obtained by single- and two-step anodization. *ACS Applied Materials and Interfaces*, 2013, **5** (16), P. 7819–7824.
[18] Petukhov D.I., Napolskii K.S., Eliseev A.A. Permeability of anodic alumina membranes with branched channels. *Nanotechnology*, 2012, **23** (33), P. 335601.
[19] Petukhov D.I., Eliseev A.A. Gas permeation through nanoporous membranes in the transitional flow region. *Nanotechnology*, 2016, **27** (8), P. 85707.
[20] Napolskii K.S., Roslyakov I.V, et al. Origin of long-range orientational pore ordering in anodic films on aluminium. *Journal of Materials Chemistry*, 2012, **22** (24), P. 11922–11926.
[21] Petukhov D.I., Buldakov D.A., et al. Liquid permeation and chemical stability of anodic alumina membranes. *Beilstein Journal of Nanotechnology*, 2017, **8**, P. 561–570.
[22] Ibrahim A., Lin Y.S. Gas permeation and separation properties of large-sheet stacked graphene oxide membranes. *Journal of Membrane Science*, 2018, **550**, P. 238–245.
[23] Eliseev A.A., Kumskov A.S., et al. Mass Transport through Defects in Graphene Layers. *The Journal of Physical Chemistry C*, 2017, **121** (42), P. 23669–23675.

NANOSYSTEMS: PHYSICS, CHEMISTRY, MATHEMATICS, 2018, 9 (5), P. 622–630

Investigation of the initial stages of spark-plasma sintering of Si–Ge based thermoelectric materials

M. V. Dorokhin, I. V. Erofeeva, Yu. M. Kuznetsov, M. S. Boldin, A. V. Boryakov, A. A. Popov, E. A. Lantsev, N. V. Sakharov, P. B. Demina, A. V. Zdoroveyshchev, V. N. Trushin

N. I. Lobachevsky State University of Nizhniy Novgorod, Gagarin ave. 23/3, 603950, Nizhniy Novgorod, Russia

dorokhin@nifti.unn.ru, irfeya@mail.ru, yurakz94@list.ru, boldin@nifti.unn.ru, Boryakov@phys.unn.ru, popov@nifti.unn.ru, elancev@nifti.unn.ru, nvsaharov@nifti.unn.ru, Demina@phys.unn.ru, zdorovei@gmail.com, trushin@phys.unn.ru

DOI 10.17586/2220-8054-2018-9-5-622-630

Thermoelectric materials based on a mixture of Ge–Si nanopowders were fabricated and investigated. The materials were obtained by spark plasma sintering technique using the modes corresponding to the initial stages of sintering of the powder particles. The possibility for controlling the electrical characteristics of materials (type and magnitude of conductivity, the Seebeck coefficient) by varying the sintering parameters was shown. It was found that the analysis of electrical characteristics allows one to draw conclusions about the degree of mixing for silicon and germanium in the sintered material.

Keywords: thermoelectric power sources, Seebeck effect, nanostructures, spark plasma sintering.

Received: 5 April 2018

Revised: 3 August 2018

1. Introduction

Silicon- and germanium-based semiconductors are widely known high-temperature thermoelectric materials [1]. The main characteristic parameter for thermoelectric materials is the dimensionless thermoelectric figure of merit – ZT, which in turn depends on such macroscopic parameters as thermal conductivity κ, electrical conductivity σ (or resistivity $\rho = 1/\sigma$), and Seebeck coefficient $\alpha = U_{te}/\Delta T$, where U_{te} is the Seebeck voltage, ΔT is the temperature difference between the "hot" and "cold" ends of the material:

$$ZT = \frac{\alpha^2 \sigma}{\varkappa} T. \tag{1}$$

As a rule, in every single material, these parameters are not independent of each other: an increase in electrical conductivity leads to a decrease in the thermoelectric voltage, etc.

Modern trends of the thermoelectric technology are associated with the fabrication of materials with ultrafine-grained polycrystalline structure, which provides low thermal conductivity while maintaining both high Seebeck coefficient and electrical conductivity [2]. In addition, unlike that of the single crystals, the figure of merit for polycrystalline thermoelectric materials is determined by the grain size, grain boundary properties, the degree of Ge and Si intermixing in a solid solution [3]. Controlling these parameters would ensure the control of the material properties for fabrication of efficient thermoelectric energy converters.

In the present paper, we report on the results of the investigation of $Si_{0.8}Ge_{0.2}$ thermoelectric materials. The selection of 0.8 vs 0.2 composition was determined by known literature data [4–6], in which it was demonstrated that such composition provides low thermal conductivity accompanied with relatively high Seebeck voltage (thus it allows one to obtain high ZT value). The $Si_{0.8}Ge_{0.2}$ was obtained by the spark plasma sintering (SPS) method using Ge and Si powders. The SPS method provides ample opportunities for controlling the polycrystalline structure parameters [7]. At the same time, the interrelation of the sintering modes, the parameters of the polycrystalline structure and the resulting thermoelectric characteristics is not trivial. To the best of our knowledge, there are no general models describing such a relationship. The influence of sintering conditions on the materials' properties is very often studied by experimental methods only, using the fabrication of a rather big set of samples in various technological modes [3–9].

We present the results for the experimental study of the initial stages of the fabrication of Si–Ge based thermoelectric materials by means of spark plasma sintering method. The evolution of the material's grain structure within the framework of varied sintering modes, as well as the influence of the grain structure on the thermoelectric characteristics were studied.

2. Experimental techniques

The investigated samples were sintered from the Ge and Si powders using the DR SINTER model SPS-625 spark plasma sintering system. As raw material for powders, ingots of single-crystal Ge and Si were used. The source of Ge was an ingot doped with the donor impurity (Sb) to a concentration of $\sim 10^{18}$ cm^{-3}. As for the Si, an ingot doped with an acceptor impurity (B) was used. The acceptor concentration was $\sim 2 \times 10^{15}$ cm^{-3}. The materials with different types of doping were chosen in order to estimate the degree of mixing by performing conductivity measurements. At this stage, the composition of the Si–Ge material was assessed, the latter corresponded to the $Si_{0.8}Ge_{0.2}$ atomic composition for all the samples studied.

The Ge and Si ingots were preliminarily milled and then mechanically activated using a Fritch Pulverisette 7 planetary mill with a ceramic container volume of 500 ml and a size of grinding balls $d \approx 10$ mm, $m \approx 5$ g. The average crystallite size in the powder was 100 nm to 50 μm, depending on the milling modes. The grain size was monitored by means of a scanning electron microscope. Complete information on the parameters of the powders is presented in Table 1. The mass of the initial feed material in all cases was 30 g. The grinding time was 1 or 6 hours. The increase in the grinding time provided a reduction in the average grain size of the obtained powders to a value on the order of hundred nanometers.

TABLE 1. Parameters of milling and sintering

No.	Powder grain size	Milling modes	Sintering modes	Grain size after sintering
1	5 – 20 μm	Pulverisette 7, 1 hour milling	Linear heating to 970 °C, 8.2 kN pressure, 400 sec.	5 – 20 μm
2	5 – 20 μm	Pulverisette 7, 1 hour milling	Linear heating to 970 °C, 8.2 kN pressure, 370 sec.	5 – 20 μm
3	0.1 – 5 μm	Pulverisette 7, 6 hours milling	Linear heating to 930 °C, 8.2 kN pressure, 370 sec.	0.1 – 5 μm
4	0.1 – 15 μm	Pulverisette 7, 6 hours milling	1) Same as for sample 3; 2) Linear heating to 1200 °C, 22 kN pressure, 700 sec.	100 – 400 μm
5	Control sample – p-type Si:B plate ($p \sim 2 \times 10^{15}$ cm^{-3})			

The resulting powder was placed into a graphite mold and subjected to sintering in various modes (data are given in Table 1). Two types of samples were fabricated. Samples 1, 2 and 3 were sintered in one step at a constant heating rate to the limiting temperature of 930 – 970 °C (Table 1). Sample 4 was fabricated in two steps: within the first step, the sample was heated at a constant rate to $T = 930$ °C, thus preliminary sintering and compacting of the powders were performed. Within a second step, the pre-compacted powder was placed in a new (larger) mold and further sintered at a constant heating rate to a higher temperature of $T = 1200$ °C; the latter point corresponds to the melting of the Si–Ge material. Thus, Samples 1,2 and 3, fabricated in one step, correspond to the initial stages of sintering, during which the powder compaction takes place and Ge and Si mutual diffusion starts at the grain boundaries. Sample 4 represents the next sintering step, during which a solid solution of $Si_{1-x}Ge_x$ and a new polycrystalline structure are formed. The control Sample 5 was the p-Si plate with the same doping level as the initial material for the silicon powder. This sample was studied for the purpose of monitoring and comparing the results.

The crystalline structure and phase composition of the deposited films were studied using a Shimadzu 7000 X-ray diffractometer (Japan), the CuKα radiation with a focal spot size of 0.4×12 mm^2 was used. The illumination area size of the surface was 1.2×1.8 mm^2. Phase analysis of the samples was carried out on the basis of the DIFFRAC.EVA software complex, using a powder database PDF-2. Based on the analysis, conclusions were drawn about the phase composition.

The composition of the resulting material was determined by X-ray microanalysis using the Jeol JSM-IT300LV scanning electron microscope with the Oxford Instruments X-MaxN 20 energy dispersive attachment (equipment of the "New Materials and Resource-Saving Technologies" Center). An accelerating voltage of 20 kV was used; the probe current was several nA. The measurements were carried out in a high vacuum mode. When determining the composition and constructing maps of the distribution of elements over the surface, the SiKα, GeKα, and GeLα lines were used. The composition was calculated by the method of fundamental parameters implemented

on the basis of the software of the microanalysis system. The determined Si–Ge composition corresponded to the calculated and prepared Si and Ge atomic ratio of the material ($Si_{0.8}Ge_{0.2}$).

Sintered bulk samples were cut into plates with dimensions (length/width/height) of $10 \times 5 \times 3$ mm. One of the plate surfaces was subjected to mechanical abrasion and polishing. To measure the thermoelectric characteristics, metallic ohmic contacts were deposited on the surface of the samples. The polished surface of the samples was examined by scanning electron microscopy using the Jeol JSM-IT300LV device. Maps of the elemental distribution along the surface of structures were constructed on the obtained electron-microscopic images.

The thermoelectric characteristics were measured for each structure at temperatures ranging from 50 to 350 °C. The edges of the sample were placed on two independent furnaces. A constant temperature difference of ± 10 K was created between the ends of the sample. As a result, a Seebeck voltage appeared at the ends of the sample, this voltage was measured with a voltmeter. The value of the Seebeck coefficient was calculated as:

$$\alpha = \frac{1}{2}\left(\frac{U_+}{+10\ \mathrm{K}} + \frac{U_-}{-10\ \mathrm{K}}\right), \tag{2}$$

where $U_+(U_-)$ – is the thermoelectric voltage for arbitrary positive (negative) temperature difference (taking into account the sign). As the measurement temperature, an average value between the temperatures of the "hot" and "cold" ends was used. The measurements were carried out under vacuum with a residual vapor pressure of about 10^{-3} Torr.

At zero temperature difference, the electrical resistance of the sample was also measured as a function of temperature. Taking into account the known geometric dimensions of the sample, the resistivity of each structure was calculated.

3. The structure and composition measurements

The X-Ray diffraction (XRD) spectra of all fabricated samples are shown at Fig. 1. The spectra represent the set of peaks corresponding to Si, Ge and Ge–Si solid solutions. We first should note the lower intensity of XRD peaks revealed for the Sample 4. This is the evidence of the lower crystalline quality of the sample as compared with Samples 1–3. For the Sample 3 (fabricated at the lowest temperature of 930 °C) the set of peaks is attributed with the phases of pure silicon, pure germanium and $Si_{1-x}Ge_x$ solid solution. This allows us to suggest that sintering at the Sample 3 modes (Table 1) did not lead to significant mixing of Ge and Si particles (although the mixing process was initialized). In Samples 1 and 2, the Ge-related XRD peak was not revealed although Si and Ge–Si related peaks are still present at the spectra. We suggest that increase of the sintering temperature for the Sample 1 and 2 (to 970 °C) has enhanced the sintering process thus the relative content of Ge–Si solid solution was increased whereas Ge content was decreased to the undetectable value.

However, the presence of Si-related peaks evidences that unmixed Si particles remain in the bulk of the material. Finally, in the Sample 4 (which was sintered at 1200 °C) no Si and Ge-related peaks were revealed. Instead, a set of peaks related with different atomic composition of $Si_{1-x}Ge_x$ solid solution are detected. We believe that the mixing of Si and Ge particles occurred for the high-temperature grown samples and new atomic structure with two phases of $Si_{1-x}Ge_x$ solid solution with different Ge–Si composition was formed.

Figure 2 shows the enlarged images of the polished surface of Si–Ge samples obtained by a scanning electron microscope. A grain structure can be revealed, the grain dimensions correspond to the characteristic grain sizes of the original powder. In particular, a higher grinding time for Sample 3 leads to a registration of smaller grains (Fig. 2(c)) as compared to Samples 1 and 2 (Fig. 2(a) and (b), respectively). In addition, some pores were detected on the surface of Samples 1–3 are (dark areas on microscopic images), the presence of the pores is believed to be due to the selected modes of sintering, i.e. a combination of pressure and heating. Modification of the sintering regime (changing the algorithm for applying pressure to the mold) leads to a reduction in the number of pores for Sample 1 as compared to Sample 2 (Figures 2a and b, respectively). This in turn corresponds to a greater shrinkage of the powder during sintering of Sample 1. Note that the Sample 4, obtained with the melting of the powder, is characterized by a grain structure that is fundamentally different from the previous ones.

For Sample 4, a significantly increased grain size was revealed, that does not correspond to the grain size of the original powder; additionally, significantly fewer pores were noted in its structure (Fig. 2(d)). These characteristics are associated with the features of sintering the material in the melting mode. We note that the single-crystal p-Si plate is characterized by an atomically smooth homogeneous surface (data not shown).

Both the data on the grain structure and XRD spectra can be supported by the results of the composition investigations, which were performed by the energy-dispersive X-ray spectroscopy in the microanalysis mode. Fig. 3 shows maps of the lateral distribution of Ge and Si for all the investigated samples. For better authenticity

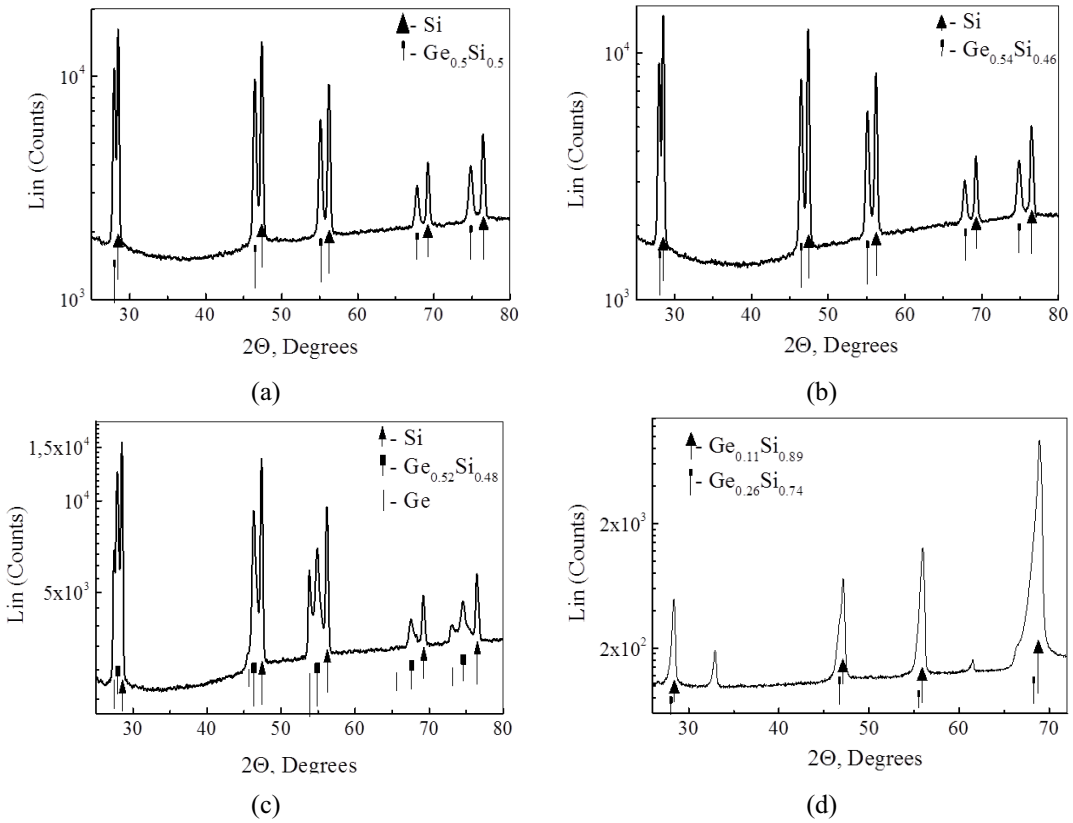

FIG. 1. XRD spectra of investigated samples (a) Sample 1; (b) – 2; (c) – 3; (d) – 4. Arrows indicate the position of diffraction lines for the different Ge, Si and $Si_{1-x}Ge_x$ phases. The Ge content in the $Si_{1-x}Ge_x$ phase was calculated from the lattice constant parameters revealed from the peak position, the x value was derived from formula given in [10]. The revealed $Si_{1-x}Ge_x$ phase is indicated at each graph. Two unmarked peaks at Fig. 1(d) could not be attributed to any of the peaks in the database

of the results, additional measurements in the regions corresponding to the maxima of the Ge and Si concentrations were also made.

From the data presented in the Fig. 3, one can reveal the regions with the composition close to 100 at. % Si, and regions with a composition close to 100 at. % Ge can (Fig. 3(a-c)). The size of these regions correspond exactly to the size of the grains detected in electron-microscopic studies; the area ratio of Si and Ge grains corresponds to the $Si_{0.8}Ge_{0.2}$ composition. Such results are in good agreement with the XRD phase analysis; they confirm the absence of significant mixing of Ge and Si atoms in the sintering modes 1–3 (modes without to melting of the material). A similar trend is maintained for Sample 3, with a smaller grain size (Fig. 3(c)). Thus, Samples 1–3 represent a two-phase system of mostly unmixed Ge and Si. When sintering in the melting mode (Sample 4), a mixing of Ge and Si takes place, which is shown by a rather uniform distribution of Si and Ge over the sample surface (Fig. 3(d)).

We note regions with locally high Ge content, the location of these regions corresponds to the boundaries of large grains. One can draw a conclusion that Ge atoms are accumulated in the grain boundary region. The latter result is again in the good agreement with XRD phase analysis (Fig. 1(d)) where two phases with the different Ge content were revealed. Thus, we can note a fundamental difference between the properties of Sample 4 and Samples 1–3: Sample 4 is a GeSi solid solution characterized by a large (100 μm) grain structure.

4. Thermoelectric properties measurement

Figure 4 shows the temperature dependences of the Seebeck coefficient for all investigated samples, as well as for the p-Si plate.

The sign of the Seebeck coefficient measured for the Samples 1–3, as well as for the p-Si plate is negative over the entire temperature range, i.e. the potential of the “hot” end of the sample is lower than that of the “cold” end.

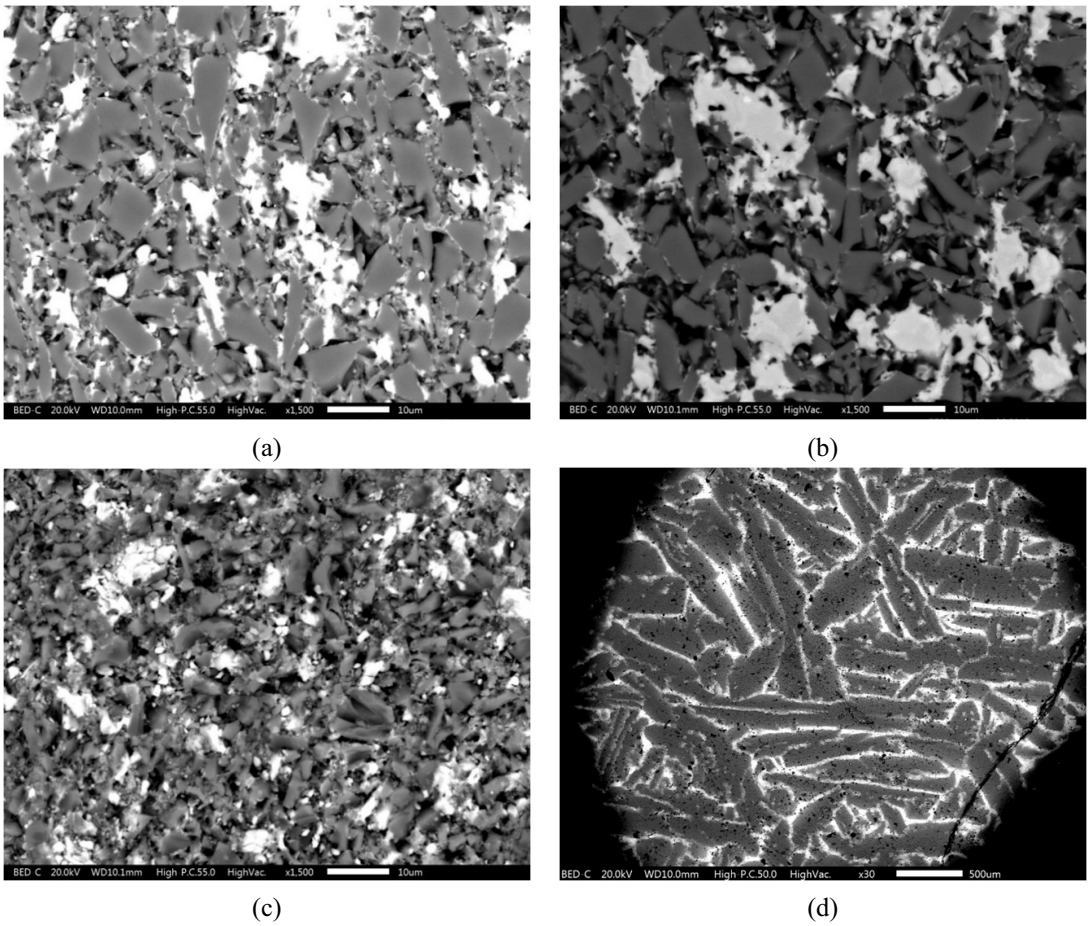

FIG. 2. The image of the polished surface of Samples 1 – 4 (a – d, respectively) obtained by a scanning electron microscope in the regime of back-reflected electrons

This situation corresponds to p-type conductivity of the samples. The absolute value of α decreases monotonically with increasing temperature. The largest absolute value of α is ~ 0.5 mV/K, the smallest one is ~ 0.15 mV/K (at a temperature of 350 °C). No significant differences between the $\alpha(T)$ dependences for Samples 1–3 were revealed. For the Sample 4, the sign of α coefficient is positive, which corresponds to the electronic type of conductivity. The value of α is ~ 0.1 mV/K at 50 °C and it slightly decreases in the absolute value with increasing measurement temperature.

Figure 5 shows the temperature dependences of the resistivity of the investigated samples. For Samples 1–3, as well as for p-Si plate, one can note the semiconductor type of the $\rho(T)$ dependence: there is an exponential decrease of resistivity with increasing temperature. Curves 1–3 and 5 demonstrate similar behavior with the only difference in the resistivity values. We note a sharper temperature dependence of the resistivity of Samples 1–3 as compared with the control structure. At a temperature of 50 °C, the resistivity of Samples 1–3 is almost two orders of magnitude higher than for the p-Si (Fig. 5, curves 1–3 and curve 5, respectively). At 350 °C, the resistivity values of Samples 1–3 and the control sample differ only by a factor of 2. For sample 4, which is characterized by n-type conductivity, a significantly lower value of the resistivity (~ 0.006 Ω×m) was obtained. This value varies slightly over temperatures ranging 50 – 350 °C (Fig. 5, curve 4). Unlike Samples 1–3, the resistivity of Sample 4 is by two orders of magnitude lower than that of p-Si plate.

Using the Seebeck coefficient and the resistivity measurements, the values of the thermoelectric power factor were calculated from the formula:

$$p_{TE} = \frac{\alpha^2}{\rho}. \tag{3}$$

The temperature dependences of the power factor are shown at Fig. 6. The largest values ($\sim 2 \times 10^{-6}$ W/m×K^2) are characteristic for the Sample 4.

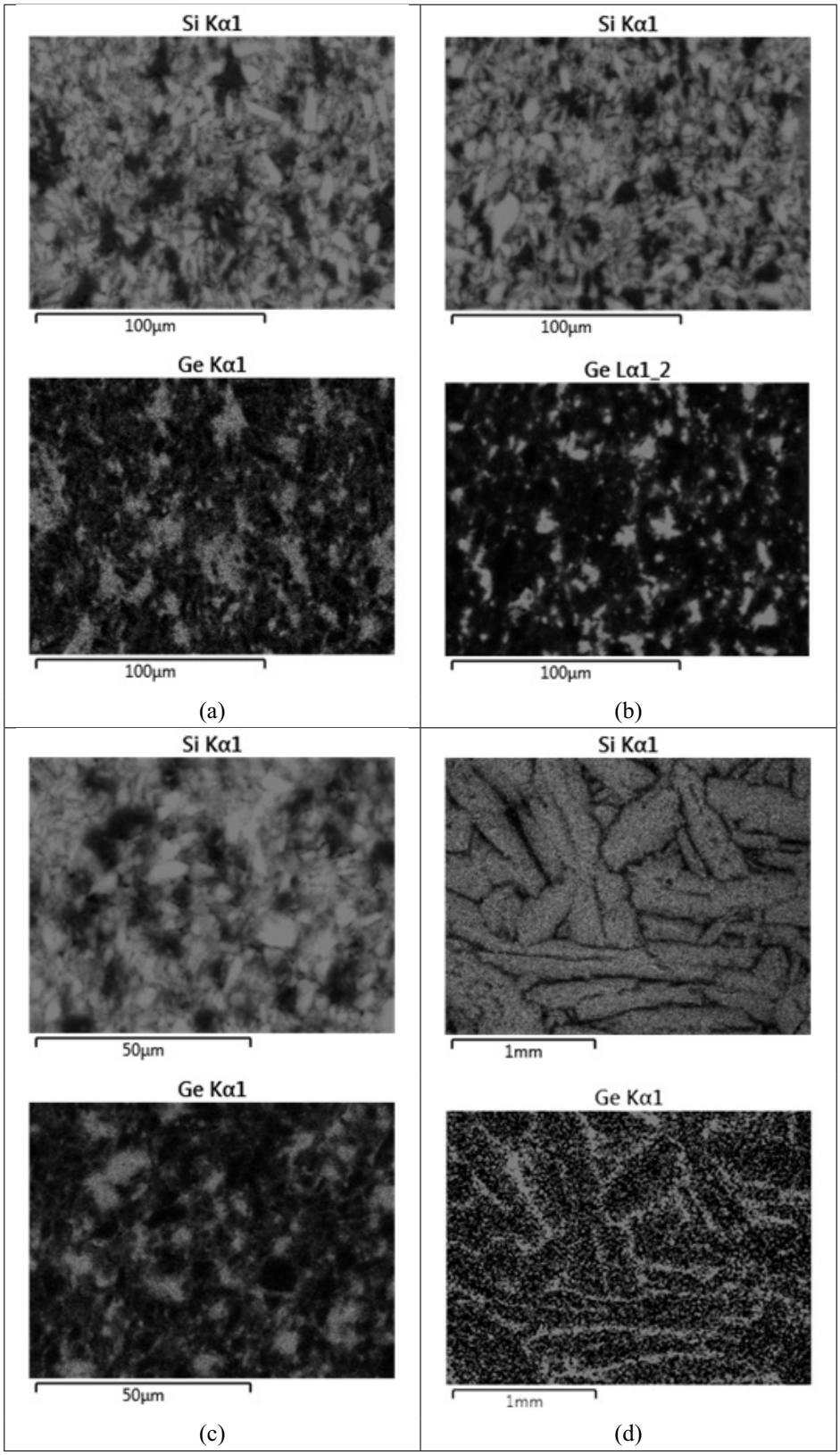

FIG. 3. Maps of the Ge and Si distribution along the polished surface of the Samples 1 – 4 (a – d, respectively)

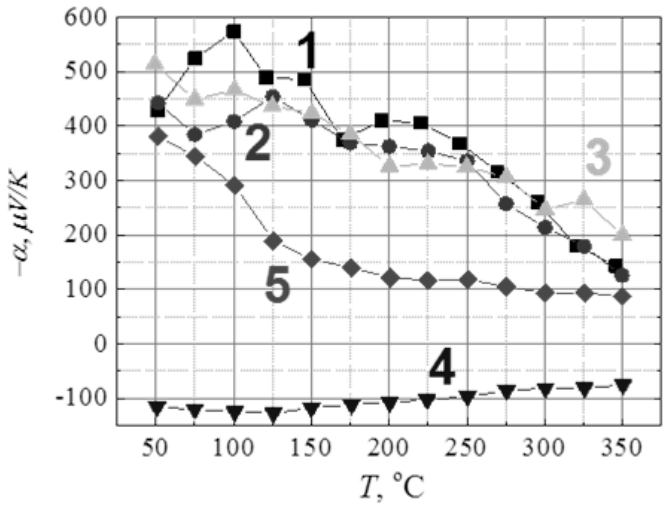

FIG. 4. Temperature dependences of the Seebeck coefficient for Samples 1 (curve 1), 2 (curve 2), 3 (curve 3), 4 (curve 4), p-Si (curve 5)

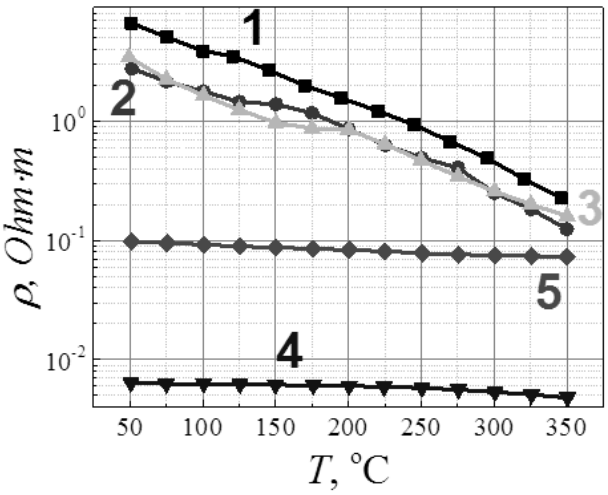

FIG. 5. Temperature dependences of the resistivity for Samples 1 (curve 1), 2 (curve 2), 3 (curve 3), 4 (curve 4), p-Si (curve 5)

The power factor values of Samples 1–3 increase monotonically with increasing measurement temperature, but do not exceed 2×10^{-7} W/m×K^2. For the control structure, the strongest temperature dependence of the power factor was obtained, while the value of p_{TE} decreases significantly above 100 °C, and the maximum values are somewhat lower than the values obtained for Sample 4.

5. Discussion

First of all, we emphasize that the fabrication technology for Samples 1–3 correspond to the initial stages of Ge and Si sintering, during which the powder is compressed and mutual diffusion processes is started, however no mixing takes place yet. Such material is a combination of Ge and Si particles, whose grain structure is determined by the properties of the initial powders. Sample 4 represents the subsequent stages of sintering, during which the material is mixed and a new grain structure is formed. In this case, the properties of grain structure are determined by the sintering modes. The revealed features of thermoelectric characteristics are thus associated with the features of the grain structure formed for each sample.

For the control structure, the resistivity and the Seebeck coefficient are determined by the intrinsic material properties, in particular by the level of acceptor doping. The calculated values of the p-Si power factor are typical

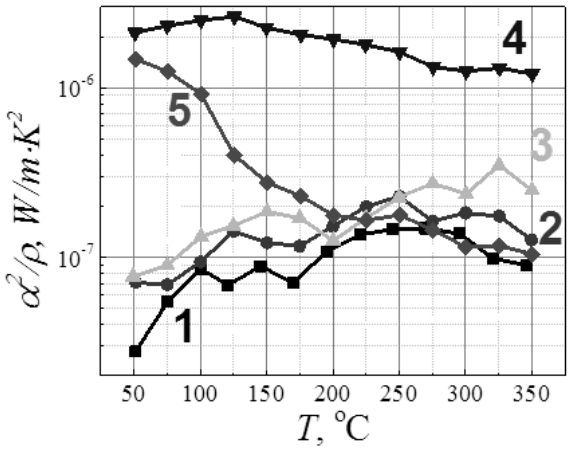

FIG. 6. Temperature dependences of the power factor calculated according to formula (2) for Samples 1 (curve 1), 2 (curve 2), 3 (curve 3), 4 (curve 4), p-Si (curve 5)

for crystalline silicon [11, 12]. For the latter, relatively high values of the power factor can be obtained, however, the relatively high thermal conductivity for silicon leads to lowering of the ZT (formula 1) [11, 12].

The samples consisting of mostly unmixed Ge and Si particles (1–3) differ in the grain size (see Table 1), the porosity and the degree of Ge–Si intermixing. However, the thermoelectric parameters obtained for Samples 1–3 only slightly differ from one another. This can lead us to the conclusion that all three of the above content mentioned parameters do not exert a determining influence on both Seebeck coefficient and electrical conductivity. We believe that Seebeck coefficient and electrical conductivity are mostly determined by the carriers transfer between the Si granules in the sintered material. The electrical conductivity through Ge grains is negligible because Ge particles do not form a closed path for current flow (Fig. 3(a–c)). Because of the hole type of conductivity for the initial Si source, the electrical conductivity of samples 1–3 is also determined by holes. The increase in the resistivity in the latter case, as compared with the original structure (p-Si), is attributed to the influence of the internal barriers between grain boundaries, as well as with the carried depleted regions on the Si–Ge interfaces that are formed due to different types of doping (by analogy with space charge regions at the border of p-n junctions [13]).

The magnitude of the Seebeck coefficient for the samples with unmixed Ge and Si grains is apparently determined by Si granules, as is shown by the sign of the Seebeck voltage. The difference between α values for Samples 1–3 is insignificant; such difference can be attributed to the experimental error and to the difference between the resistivity values. It is known that the Seebeck coefficient value for a material increases with increased resistivity [1].

From such point of view, the variation of the grain parameters, the porosity and Ge–Si mixing in samples 1–3 only lead to some small changes of thermoelectric properties. For example, sample 1 is a denser material, in which a greater number of boundaries between Ge and Si grains are formed and the effect of depleted regions on the electrical resistivity is higher. For this sample, slightly greater resistivity value was obtained as compared with the Samples 2 and 3 (Fig. 4, curve 1).

A fundamentally different character of the temperature dependences of thermoelectric coefficients was revealed in Sample 4. For this sample, the mixing of Ge and Si atoms was confirmed by both the XPS phase analysis and the energy-dispersive spectroscopy analysis. The crystalline structure is not determined by the initial grain size and a certain decrease in the crystalline quality was revealed (Fig. 1). The influence of the new crystal structure on the thermoelectric properties is hard to derive because the most significant influence on Seebeck coefficient and conductivity is exerted by the carrier concentration. Because of the much greater doping level of the original Ge material (about 10^{18} cm^{-3} donors as compared with 2×10^{15} cm^{-3} acceptors in Si), the acceptor impurity from Si was compensated and, accordingly, the sign of the conductivity was changed; greater doping levels also provided lower resistivity values. In addition, one can suggest that the absence of internal p-n junctions in Sample 4 additionally reduces the resistivity value.

We emphasize that the use of the initial Ge and Si materials with different types of doping makes it possible to determine the degree of mixing of Ge and Si in the sintered material by the measuring the evolution of the resistivity. In the case of effective mixing, conductivity is determined by the material with a higher level of doping.

The lower absolute value of the Seebeck coefficient revealed for Sample 4, as compared with the one for the rest of the samples, is explained by:

(1) lower resistivity of Sample 4. The dependence of α on the resistivity of a semiconductor material is a well-known fact [1];
(2) change of the type of conductivity (the electrons are characterized by the greater mobility as compared with holes);
(3) change of the grain structure type and the intrinsic properties of the material (a $Si_{1-x}Ge_x$ solid solution was obtained of instead of isolated Ge and Si grains).

In addition, we also note the increase in the power factor of the new polycrystalline solid solution as compared with the initial p-Si material. The latter is simply due to the greater doping level of the fabricated solid solution, such increase is also a well-known fact [1].

In conclusion, in the presented paper, the initial stages of Ge and Si nanopowder sintering during the fabrication of thermoelectric materials were studied. It was shown that in the first stage of sintering, there is no significant mixing of the Ge and Si atoms, and thermoelectric properties mostly depend on the carrier transport through Si grains in the sintered material. As the sintering process continues, Ge and Si are mixed, which results in the fabrication of a new material with increased power factor value.

Acknowledgements

This work was supported by Russian Science Foundation (grant #17-79-20173).

References

[1] Rowe Ed.D.M. *Termoelectric hand book macro to nano*. CRC Press, Boca Raton, 2006.
[2] Hicks L., Dresselhaus M. Thermoelectric figure of merit of a one-dimensional conductor. *Physical Revew B*, 1993, **47**, P. 16631–16634.
[3] Minnich A.J., Dresselhaus M.S., Ren Z.F., Chen G. Bulk Nanostructured Thermoelectric Materials: Current Research and Future Prospects. *Energy & Environmental Science*, 2009, **2** (5), P. 466–479.
[4] Cook B.A., Harringa J.L., Han S.H., Vining C.B. $Si_{80}Ge_{20}$ thermoelectric alloys prepared with GaP additions. *J. Appl. Phys.*, 1995, **78**, P. 5474–5480.
[5] Cook B.A., Harringa J.L., Han S.H., Beaudry B.J. Parasitic effects of oxygen on the thermoelectric properties of $Si_{80}Ge_{20}$ doped with GaP and P. *J. Appl. Phys.*, 1992, **72**, P. 1423–1428.
[6] Lahwal A., Bhattacharya S., et al. Impact of yttria stabilized zirconia nanoinclusions on the thermal conductivity of n-type $Si_{80}Ge_{20}$ alloys prepared by spark plasma sintering. *J. Appl. Phys.*, 2015, **117**, 145101.
[7] Usenko A., Moskovskikh D., et al. Thermoelectric Properties of n-Type $Si_{0.8}Ge_{0.2}$–$FeSi_2$ Multiphase Nanostructures. *Scripta Materialia*, 2017, **127**, P. 63–69.
[8] Bathula S., Jayasimhadri M., Dhar A. Mechanical properties and microstructure of spark plasma sintered nanostructured p-type SiGe thermoelectric alloys. *Materials & Design*, 2015, **87**, P. 414–440.
[9] Zamanipour Z., Shi X., et al. The effect of synthesis parameters on transport properties of nanostructured bulk thermoelectric ptype silicon germanium alloy. *Physica status solidi (a)*, 2012, **209** (10), P. 2049–2058.
[10] Dismukes, J.P., Ekstrom L., et al. Thermal and electrical properties of heavily doped Ge–Si alloys up to 1300 K. *J. Appl. Phys.*, 1964, **35**, P. 2899–2907.
[11] Weber L., Gmelin E. Transport properties of silicon. *Applied Physics A*, 1991, **53**, P. 136–140.
[12] Boukai A.I., Bunimovich Y., et al. Silicon Nanowires as Efficient Thermoelectric Materials. *Nature*, 2008, **451**, P. 168–171.
[13] Sze S.M., Ng Kwok K. *Physics of Semiconductor Devices*. John Wiley & Sons. Hoboken, New Jersey, 2006, 832 p.

NANOSYSTEMS: PHYSICS, CHEMISTRY, MATHEMATICS, 2018, 9 (5), P. 631–640

$BiFeO_3$-Montmorillonite intercalated nano composites – synthesis and its characterization

K. Karthikeyan[1], A. Thirumoorthi[2,*]

[1]Research and Development centre, Bharathiar University, Coimbatore, Tamilnadu, India
[2]Assistant Professor, P. G. Department of Chemistry, Government Arts College, Udumalpet – 642 126, Tamilnadu, India

*dramoorthiudt@gmail.com

DOI 10.17586/2220-8054-2018-9-5-631-640

Bismuth Ferrite (BFO) intercalated Montmorillonite clay (MMT) nano composites have been synthesized using ascorbic acid and its optical behavior has been investigated. The characterization of BFO-MMT nano composites has been done using FT-IR, UV-visible, X-ray diffraction (XRD), Scanning Electron Microscope (SEM). Also, electron hole recombination has been investigated by photoluminescence (PL). From the analytical techniques, it has been found BFO entered into the layered host which was proved by elongation of basal plane and therefore agglomerated BFO was formed. The particle size can be calculated by Scherrer formula, is in good agreement with SEM. The strong absorption band in UV-Visible region attributed BFO nano composites can be used for photo catalytic degradation of Rhodamine-B (Rh-B). From the electrochemical studies, BFO-MMT clay nano composites showed a good specific capacitance at a scan rate of 10 mVs^{-1}.

Keywords: Bismuth ferrite, intercalation, montmorillonite clay, photoluminescence, specific capacitance.

Received: 19 February 2018

Revised: 20 September 2018

1. Introduction

The intercalation of new species into layered materials has great attraction in a wide range of applications [1]. The organic and inorganic guest species can easily be penetrated into the interlayer spaces of smectites to give intercalation compounds [2]. Zhaohui Han et al. [3] investigated the light absorbance and varying pore volume and pore size of CdS intercalated Laponite, Saponite, Hectorite, Montmorillonite clay (MMT). Peng Yuan et al. reported that synthesis of Fe-pillared interlayer clay samples possess good thermal stability and higher specific area with porosity [4]. The immobilization of MnS and NiS in the interlayer spaces of Montmorillonite and low luminescence intensities of MnS and NiS in Montmorillonite has been investigated by Nithima Khaorapapong et al. [5]. Also, Yasushige Mori et al. [6] have been reported that PL intensity was enhanced due to increase of particle surface area in Zinc sulphide nanoparticles suspended in Laponite XLG. The different photodecomposition behaviors of Rhodamine B on Laponite XLG and Montmorillonite have been studied by Peng Wang et al. [7].

The enhanced textural properties have been developed in two types of clay mineral/TiO_2 composites by Bahranowski et al. [8]. The enhanced textural properties of clay mineral was compared with TiO_2 and it was found that pillared montmorillonite materials have structural organization upon composite formation. They also found that the use of dialyzed clay mineral enhances strongly the adsorption properties of montmorillonite/TiO_2 composites obtained by conventional pillaring. Particularly, the specific capacitance behavior improved for nitrogen doped porous carbon ensemble on MMT nanocomposites of 223 Fg^{-1} at current density of 1 Ag^{-1} [9]. Montmorillonite has tetrahedral and octahedral sheet arrangement with gallery space and is shown in Fig. 1.

Bismuth ferrite (BFO) have been attracted considerable interest due to their unique optical and electrical properties, and a wide variety of potential applications for photovoltaic ferroelectric, piezoelectric, or magneto electric capabilities, as well as in spintronics [10–12]. $BiFeO_3$ constitutes a most important material being a semiconductor with the absorption edge in the visible region, $BiFeO_3$ NPs have been successfully tested in the degradation of Rhodamine B, methyl orange, methylene blue and bisphenol-A [13–15] and its capacitance properties have been improved by metal oxide doping [16].

From the literature survey, BFO can be used for optical, magnetic, photo catalytic applications and its capacitance behavior could be improved by doping with metal oxides. Additionally, capacitance properties has been enhanced by using layered types of materials such as Montmorillonite clay, layered doubled hydroxides (LDHs) in the form of composites. These facts spur us to synthesis the BFO intercalated MMT nanocomposites and investigate their capacitance and photocatalytic behaviors (Fig. 2).

In the present study, we report the synthesis of BFO and its intercalation into MMT clay to obtain nanocomposites of layered host of clay materials. The obtained composite was characterized using FT-IR, UV-Visible

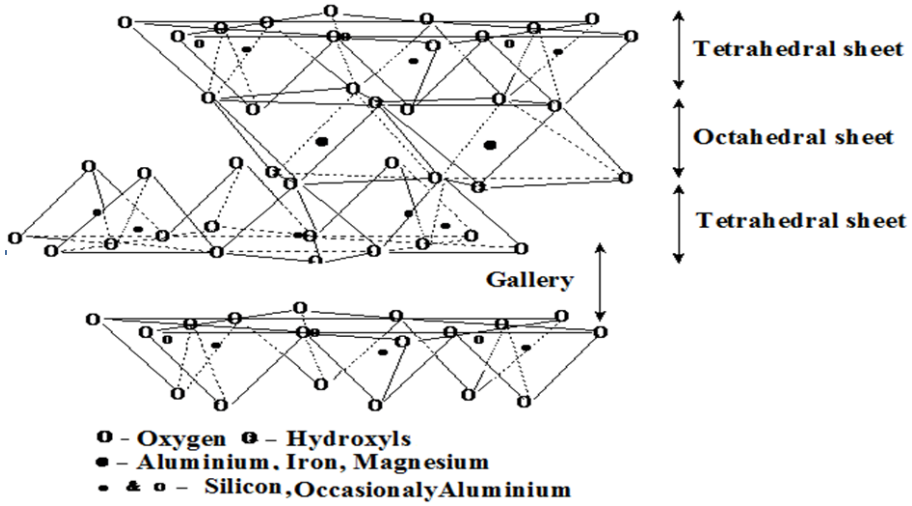

FIG. 1. Montmorillonite clay layered structure

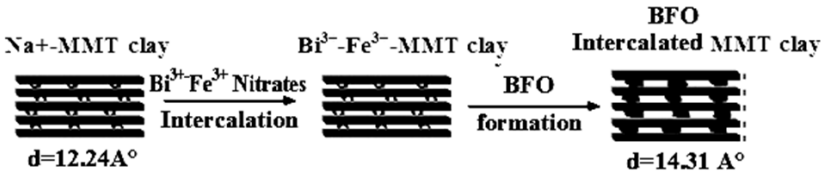

FIG. 2. A schematic diagram of BFO intercalated Na^{+}-Montmorillonite clay

spectra, XRD and SEM analysis, PL techniques. Also, the electrochemical behavior of BFO intercalated MMT nanocomposites for capacitance was investigated using Cyclic Voltammetric (CV) studies and the photo catalytic degradation of Rhodamine-B using intercalated BFO-Montmorillonite nanocomposites have been investigated.

2. Experimental section

2.1. Materials and methods

Bismuth nitrate [$Bi(NO_3)_3 \cdot 5H_2O$], Iron nitrate [$Fe(NO_3)_3 \cdot 9H_2O$], Ascorbic acid from Merck have been used as such without any further purification. Nitric acid and acetic acid from Merck of Analar grade reagents (A.R) were used as such and de-ionized water was used for the sample preparation.

2.2. Preparation of intercalated BFO

Bismuth nitrate and Ferric nitrate (in 1:1 molar ratio) were mixed with ascorbic acid and then add 1.2 mL of nitric acid (99.5 %). The solution was magnetically stirred at room temperature for 30 min. and the dark green colored solution was obtained. The mixture was vigorously heated until a dark brown solution was formed, then, the solution was cooled.

5 mM Fe/g clay suspension was taken and the cold BFO solution was added dropwise with constant stirring for about 24 h. where the intercalation took place [17]. The clay particles were converted into intercalated clay composites and then separated as yellow color clay composites. Then it was heated at 500 °C in Muffle furnace for 1h. to produce a brown clay.

2.3. Characterization of materials

UV-Visible absorption spectrum of the compound was recorded by using UV-Visible spectrometer (UV-1800, Shimadzu, Japan). FT-IR spectrometer of the type IR Prestige-21, Shimadzu, used to record IR spectrum using KBr pellets. The crystalline structure of BFO-MMT clay intercalated nano materials was identified by X-ray diffraction instrument (XRD, Shimadzu labX-6000). Sample morphology and size were examined using Scanning electron microscope (SEM, Jeol JSM-6390). The photoluminescence emission spectra of the samples were recorded with fluorescence spectrophotometer (PL, Horiba Jobin Yvon Flurolog-3). The cyclic voltammetric experiments

were carried out with a computer-controlled electrochemical working system (CH1660C Electrochemical Analyzer) between the scan rate of 10 mVs^{-1} and 50 mVs^{-1}.

3. Results and discussion

3.1. FT-IR analysis

FT-IR spectroscopy of pure MMT, BFO nanoparticles and BFO intercalated nanocomposites are shown in Fig. 3. The FT-IR spectroscopy data confirms acid activation of the clay. According to IR spectroscopic data Maria N. Timofeeva [18] reported that changes in chemical compositions in treatment with clay and leaching of Al^{3+} ions in octahedral sheet by the action of HNO_3 at the concentration of 0.125 – 0.5 mol/dm^3. The OH-bending frequencies of water 1633 cm^{-1} shift to 1625 cm^{-1} and this shift may be related to the interaction of HNO_3 with Al–OH groups.

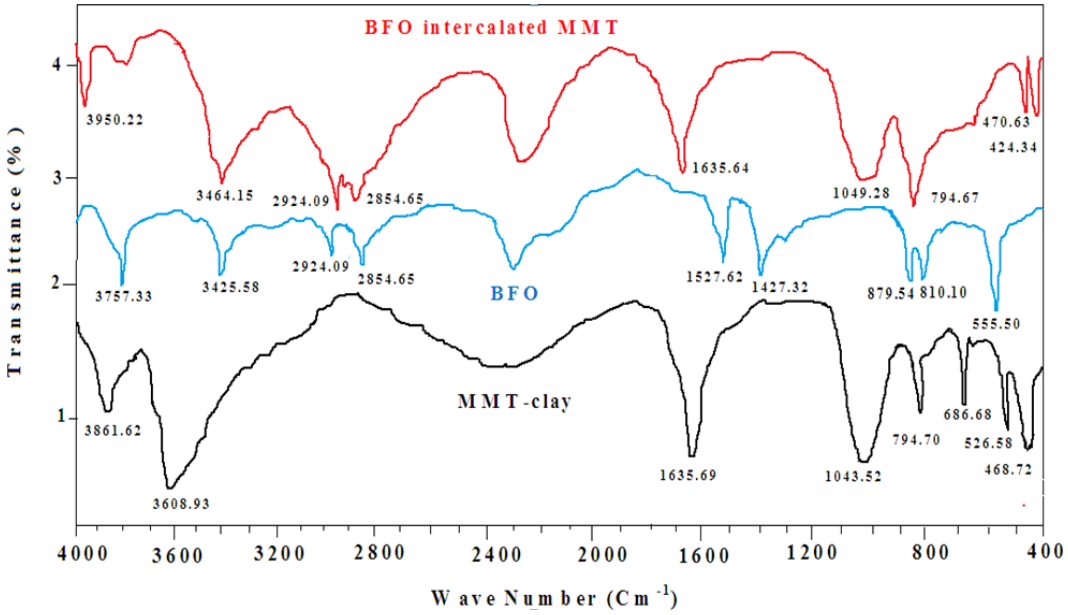

FIG. 3. FT-IR spectra of Pure Montmorillonite clay, BFO nano particles and BFO intercalated Composite

In our synthesized BFO intercalated MMT composites, the FT-IR spectral region discussed ranges from 400 – 4000 cm^{-1}. The comparison of wave number and assignment of peaks of pure MMT clay, BFO nano particles and intercalated BFO-MMT nanocomposites were listed in Table 1. The peak arises at 424.34 cm^{-1} for BFO intercalated MMT composites which confirm that BFO present in the MMT clay [19, 20]. The peak at 1635.69 cm^{-1} (due to O–H bending) does not shift and shows at 1635.64 cm^{-1} for BFO intercalated MMT due to absence of interaction of HNO_3 and Al–OH group of clay. The chemical composition (HNO_3 acid activation) changes in Montmorillonite clay and HNO_3 interaction with Al–OH group of clay was not takes place because of lower concentration of HNO_3 (0.04 mol/dm^3) for synthesis process. This has been confirmed using FT-IR spectra.

3.2. XRD analysis

X-ray diffraction patterns of Pure Na^+-Montmorillonite clay and BFO intercalated MMT clay nano composites are shown in Fig. 4(a) and (b) respectively. The XRD pattern of BFO shows pure rhombohedral perovskite structure, which are in good agreement with the powder data of JCPDS card number 86-1518 [21]. Montmorillonite clay not only shows their corresponding phase but also for quartz. The peaks 100, 101 and 110 planes corresponds to quartz and the peaks 001, 101 and 111 ($2\theta = 7.4$, 17.65 and 19.81 respectively) for MMT [22]. Manikandan et al. reported that the noble metal intercalated clay catalysts were very effective in selective hydrogenation reactions. They also found that Na-Montmorillonite clay shifted from $2\theta = 6.1°$ (d spacing value of 15 Å) to 1.5° (d spacing value of 59 Å). This confirms that the intercalation of BFO into clay minerals does not alter the crystal lattice structure, and hence, poor crystallinity of the nano composites [23]. Ecaterina Andronescu et al. reported that the diffraction peak of Montmorillonite clay (001 plane) shifts from $2\theta = 7.23°$ (basal spacing $d = 12.22$ Å) to 6.17° ($d = 14.31$ Å). The peak shifting to a lower diffraction angle is due to an increase in the clay basal spacing, which confirms the intercalation of nanoparticles in MMT interlayer spacing [24].

TABLE 1. Comparison of wave number of pure MMT clay and BFO-MMT nanocomposites

Montmorillonite clay		**BFO**		**BFO intercalated MMT nano composites**	
Peak position (cm^{-1})	Assignment	Peak position (cm^{-1})	Assignment	Peak position (cm^{-1})	Assignment
—	—	—	—	424.34	Fe–O stretching
468.72	Si–O–Si deformation	—	—	470.63	Si–O–Si deformation
526.58	Al–O–Si deformation	555.50	Fe–O stretching	—	—
686.68	Al–O and Si–O stretching	—	—	—	—
794.70	Si–O stretching	—	—	794.67	Si–O stretching
—	—	810.10 and 879.54	Fe–O and Bi–O frequencies	—	—
—	—	1427.32	C–H bending	—	—
—	—	1527.62	C=C stretching		
1043.52	Si–O–Si stretching	—	—	1049.28	Si–O–Si stretching
1635.69	OH-bending of water	—	—	1635.64	OH-bending of water
—	—	2854.65	C–H symmetric stretching	2854.65	C–H symmetric stretching
—	—	2924.09	C–H ssymmetric stretching	2924.09	C–H asymmetric stretching
3608.93	O–H stretching of water molecules	3425.58	O–H stretching of water molecules	3464.15	O–H stretching of water molecules
3861.62	O–H stretching of water molecules	3757.33	O–H stretching of water molecules	3950.22	O–H stretching of water molecules

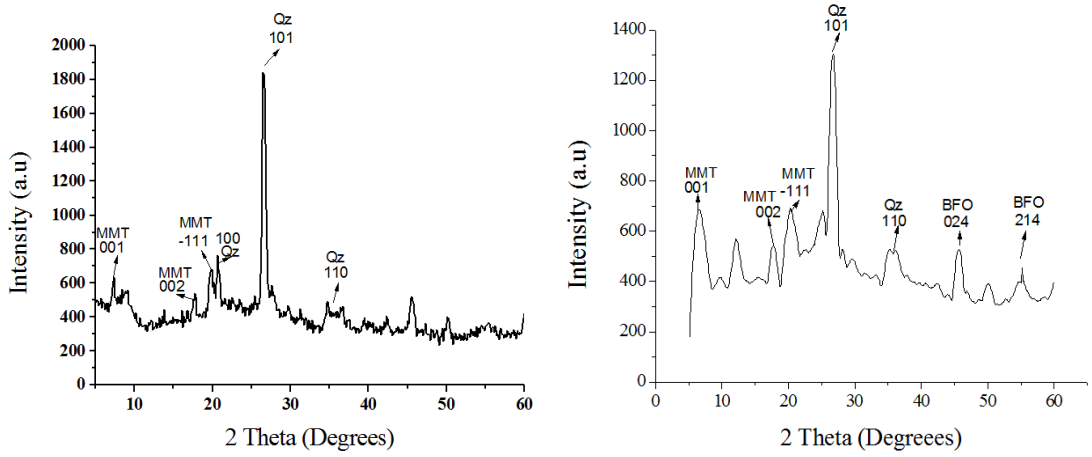

FIG. 4. XRD pattern of (a) Pure Montmorillonite Clay (b) BFO-MMT composites

From the literature survey, it has been observed that in BFO-MMT clay intercalation takes place, as a result the shifting of 2θ from 7.40° to 6.12°. In the present work, the XRD pattern of intercalated clay-bismuth ferrite was compared with untreated Montmorillonite clay and it has been found that untreated Montmorillonite clay (001 plane) peak at 2θ = 7.40° (basal spacing $d = 11.93$ Å), which corresponds to the spacing of clay layers, was shifted to 2θ = 6.12° (basal spacing $d = 14.41$ Å), due to intercalation of BFO in between the clay platelets. In MMT-BFO composites, the 024 and 214 planes were assigned to BFO phase (JCPDS card No. 86-1518) and the plane 024 for BFO was merged with MMT and hence the plane 214 at 55.3° was used to compute the size of BFO. Also, it has been observed that the increase in the basal spacing and the change in color of the products were caused by the intercalation of BFO and the formation of BFO in the interlayer spaces of MMT. The particle size of BFO can be estimated using the Debye Scherer formula:

$$2d = 0.9\lambda/\beta\cos\theta,$$

where β is the full width at half maximum intensity [FWHM] corresponding to then Diffraction angle 2θ in radian, and λ is the wave length of Cu-Kα radiation [25, 26]. The average crystallite size of the BFO nano particles was found to be 47.84 nm.

3.3. Scanning electron microscope

Figure 5(a) and (b) shows the SEM images of MMT-clay and BFO intercalated MMT-clay respectively. The preparation and sedimentation behavior of Montmorillonite clay-magnetite particles at various pH was reported by Galindo-Gonzalez et al. [27], suggesting that magnetic particles were well-adhered to sodium Montmorillonite clay in aqueous suspensions. The SEM images of magnetic covered clay particles at pH = 3 shows a great aggregation and at pH = 10 the coating was thinner leads to formation of less homogeneous particles. In SEM analysis, Vedhi et al. [28] found that a gradual change of uneven layered granular agglomerated clay – polymer nanocomposites to a fused well-organized layered morphology with flaky structure, predominantly due to clay mineral concentration. Figueras et al. [29] reported that the intercalation (d-space) decreases with enhancing the calcination temperature above 400 °C.

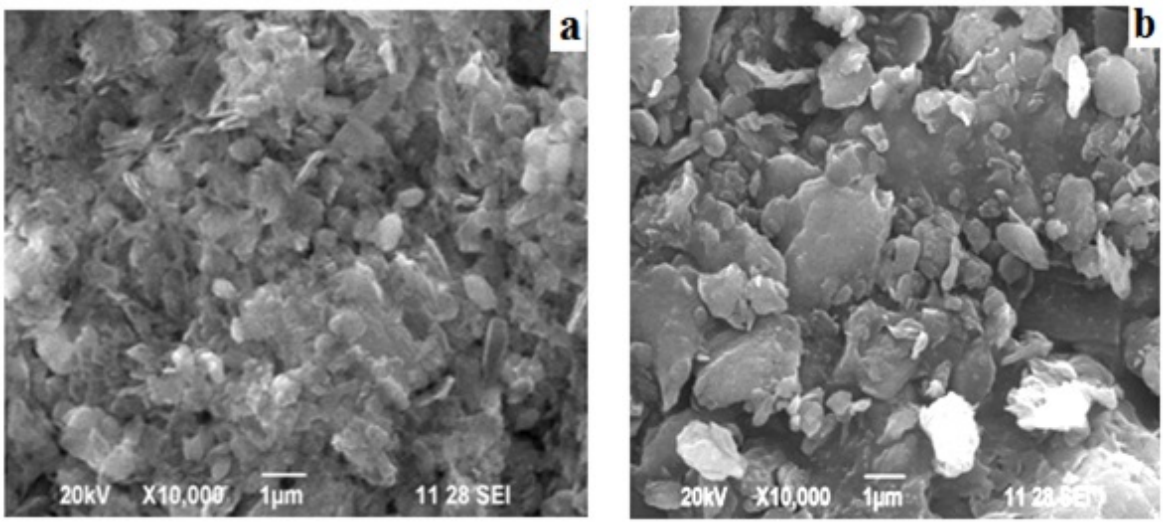

FIG. 5. SEM images of (a) MMT-clay (b) BFO intercalated MMT-clay

From the literature survey, it has been found that BFO-MMT nano composites only small amount of BFO intercalation takes place due to the calcination temperature at 500 °C. Also, the change of dense granular MMT clay morphology to uniform agglomerated flakes like shape of BFO due to intercalation and their crystallite size was found to be 47 nm shown in Fig. 4.

3.4. PL spectra

PL Spectra of pure MMT, BFO nano particles and BFO intercalated nano composite is shown in Fig. 6(a), (b) and (c) respectively. Dai et al. reported that $BiFeO_3$-Graphene nano composites have improved photocatalytic

activity of methyl orange and the peak was obtained at 429 nm [30]. Also Ramya et al. suggested that Montmorillonite clay peak has a maximum at 466 nm [31]. In the present studies, BFO nanoparticles and MMT shows acceptable peak range of 400 – 450 nm for BFO nano particle and 420 – 430 for MMT clay materials.

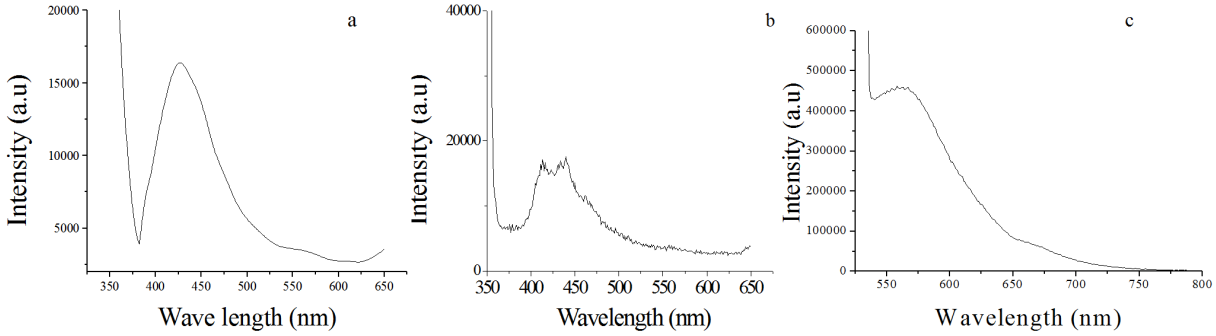

FIG. 6. Photoluminescence spectra of (a) Pure Montmorillonite (MMT) clay (b) Bismuth ferrite (BFO) and (c) BFO intercalated MMT nanocomposites

Yao et al. found that the optical behavior of $BiFeO_3$–KNSBN tri layer thin films and suggested that the multiple band gap energies are due to the combination of band gap energy of KNSBN and BFO films and the band centered at 530 – 540 nm due to the presence of oxygen vacancies [32]. The optical properties of BFO thin films have been studied at three different annealing temperatures. It has been found that the absorption shifts towards the longer wavelengths with increasing annealing temperature, suggesting that the band gap decreases with the annealing temperature. The optical band gap of the film was found to decrease from 2.67 eV to 2.57 eV with increasing temperature. Also two strong emissions around 2.53 and 2.36 eV were observed, indicating their potential applications as optoelectronic devices [33]. The PL spectrum of the pure BFO sample shows only one blue emission around 454 nm (2.73 eV) due to a self-activated center [34]. Sunil Chauhan et al. found that Mn-doped BFO samples gave two emission bands in the PL spectra [35]. The peak corresponding to 484 nm (2.56 eV) is due to blue emission band and dominant yellow-orange band is found at 570 nm (2.17 eV). The blue band emission around 484 nm in Mn doped BFO is due to a self-activated center and the shift of blue band to higher wavelength reported by Yu. X et al. owing to large crystallite size which leads to decrease in band gap. Based on this, they found the incorporation of Mn^{2+} in the BFO lattice [36]. From the literature [31] it has been found for nanocomposites of the type montmorillonite/chitosan/para pheylenediamine, the peak of MMT shifted towards higher wavelength region and red shift occurs.

It has been found that in BFO-MMT nanocomposites, the band shift occurs towards higher wavelength, thus producing a red shift. A band at around 570 nm (2.16 eV) for BFO-MMT composites confirms the intercalation (doping) of BFO in clay layered host. This emission will enhance the opportunities of intercalated BFO nano particles for both further fundamental studies and nano scale optical applications.

3.5. UV-Visible spectra

UV-Visible spectra of pure Montmorillonite clay, BFO, BFO intercalated MMT nanocomposites and their Tauc's plot are shown in Fig. 7(a,b,d) and (d) respectively. The absorption peaks of pure MMT and BFO corresponds to about 300 – 320 nm and 520 – 530 nm respectively and the band gap of BFO was found to be 1.75 eV.

In this present work, BFO intercalated MMT visible spectra shows a new peak at 256 nm and the band gap energy can be calculated by using Tauc's equation:

$$(\alpha h\nu)^n = k(h\nu - E_g),$$

where α is the absorption coefficient, k is the effective masses associated with the valence and conduction bands, n is 2 for a direct transition and 1/2 for an indirect transition, $h\nu$ is the absorption energy and E_g is the band-gap energy [37–39]. The band gap energy was found by extrapolating the linear portion of $(\alpha h\nu)^2$ against $h\nu$ plot to the point $\alpha = 0$ and is about 2.34eV [40]. The band gap changes from 1.75 eV to 2.34 eV and hence a prominent blue shift which may cause the reduction in particle size of BFO intercalated nanocomposites. The band gap of Ca and Ba doped BFO composites widened from 1.8 to 2.3 eV was attributed to dopant ions and hence reduction of particle size. The increase in band gap by doping significantly enhanced the photocatalytic efficiency of doped $BiFeO_3$ nanoparticles [41]. Thus, the band gap calculated for BFO-MMT nanocomposites coincides

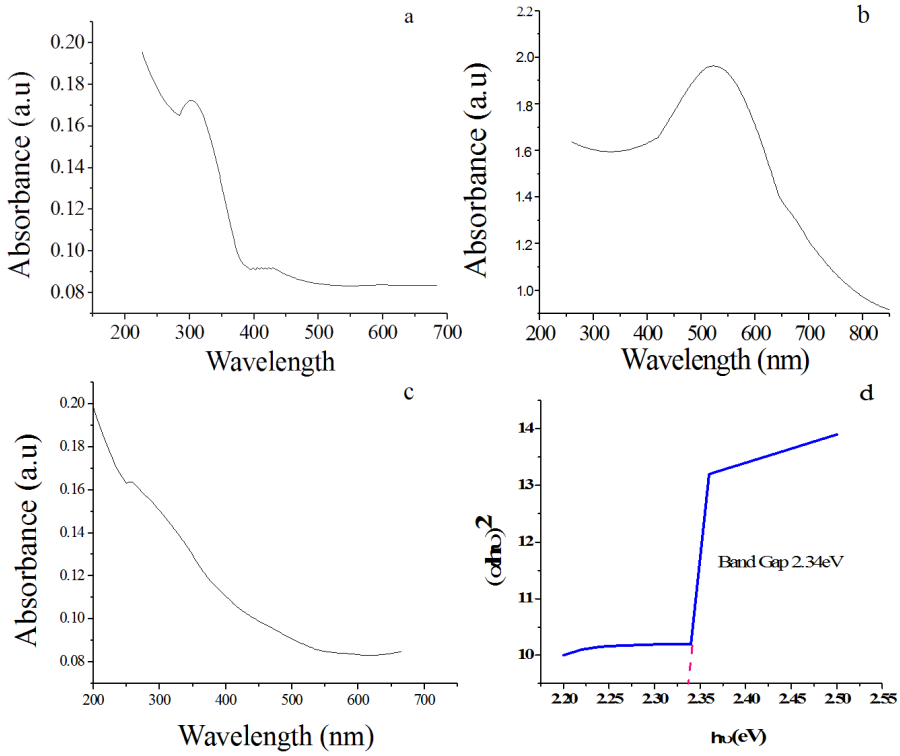

FIG. 7. UVVisible spectra of (a) Pure Montmorillonite (MMT) clay (b) Bismuth ferrite (BFO) and (c) BFO intercalated MMT nano composites (d) Taucs plot of BFO-MMT

with the literature available and hence BFO intercalated MMT may have a potential application as an appropriate photocatalyst for environmental remediation of organic contaminants under visible light irradiation.

3.6. Photocatalytic degradation

UV-Visible radiation is supported to photo catalytic degradation of BFO intercalated MMT. Rhodamine-B (RB) [0.05 g/L] was adsorbed onto Montmorillonite clay [0.05 g] at pH 7.0. Fig. 8 represents the UV-Visible spectra changes of RB in BFO-MMT clay suspension under visible irradiation. It was found that aqueous RB solution in the absence of BFO-Montmorillonite clay nano composites underwent no decomposition. Further, UV-Visible spectra changes as degradation of RB in the presence of BFO-MMT suspension under visible irradiation. The hypsochromic shift of absorption peak of RB gradually takes place from 556 to 524 nm after degradation. The hypsochromic shifts of the absorption peaks were found to result from the formation of N-deethylated mechanism [7].

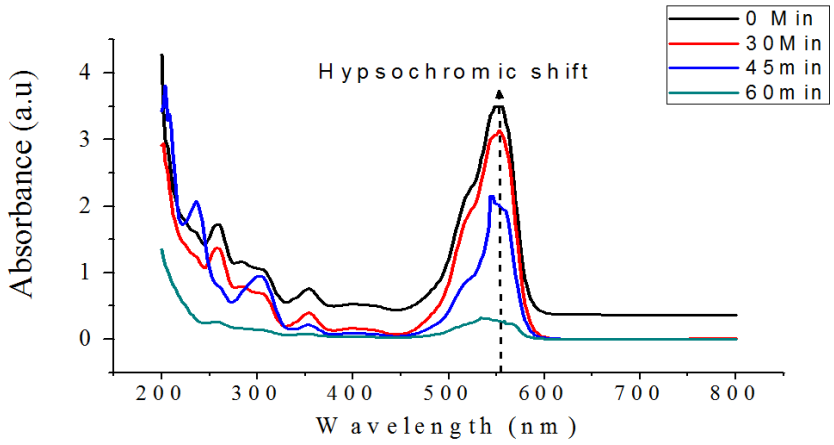

FIG. 8. Photo catalytic degradation of Rh-B by BFOMMT in various time intervals

3.7. Cyclic voltammetry

The electrochemical studies confirm the capacitance behavior of nano structured materials [42]. Baby Sunitha et.al [28] reported that o-toluidine polymerized with Montmorillonite by chemical oxidation method using potassium perdisulfate shows good solubility in both DMSO and DMF and the intercalation of the polymer in between the Montmorillonite clay layers increase in the d-spacing. Further, they found greater electrocatalytic response and stability, oxygen reduction ability and high conductivity using cyclic voltammetry and impedance studies. Ramesh et al. [43] reported that the incorporation of carbon nanotube and polyaniline with layered silicate of nano clay composites showed a higher capacitance of 331 Fg^{-1} at the scan rate of 10 mVs^{-1}. Hongjuan Li et al. [44] found from the electrochemical studies that MnO_2-pillared Ni^{2+}–Fe^{3+} layered double hydroxide nanocomposites exhibit large surface area and ideal capacitive behavior in neutral electrolyte and good cyclic properties.

The cyclic voltammograms of BFO-MMT nano composites have been investigated for their capacitance behavior in 1 mol L^{-1} NaOH at scan rate 10 – 50 mVs^{-1} with potential range -0.35 to 0.32 V is shown in Fig. 9. The CV studies gave anodic peak in positive and cathodic peak in negative potential directions. The specific capacitance of BFO-MMT nano composites at different scan rate of 10, 20, 30, 40 and 50 mVs^{-1} were 400, 262.5, 208, 169 and 155 Fg^{-1} respectively. At low scan rate of 10 mVs^{-1}, the material showed the good specific capacitance behavior due to porous layered structure and admirable electron accepting and donating behavior of montmorillonite clay. The decrease in capacitance with scan rates is attributed to the inner active sites that cannot completely proceed with the redox transitions at higher scan rates of CV and diffusion effect of proton within the electrode [45]. The decreasing trend of the capacitance suggests that the parts of the electrode surface are inaccessible at high charging-discharging rate. Hence, the specific capacitance obtained at the slowest scan rate reveals complete utilization of electrode material [46].

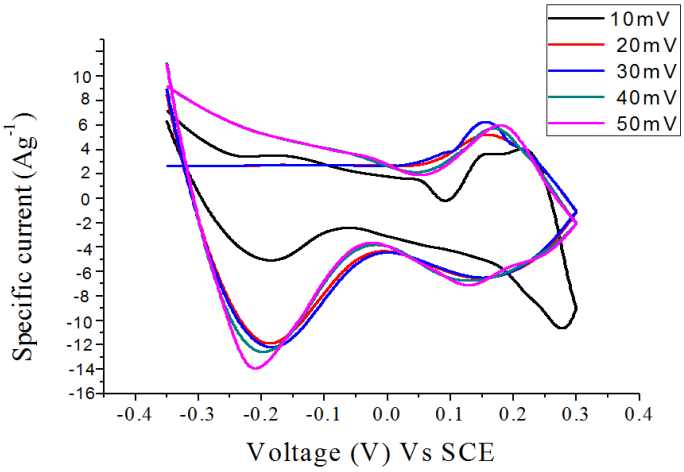

FIG. 9. Cyclic voltammetry of BFO-MMT at different scan rate

The effect of varying the scan rate with increasing peak current indicates the good adherence of the BFO-MMT composites on to electrode surface. The plot of logarithm of peak current against logarithm of scan rate is shown in Fig. 10, illustrates the current increases approximately in linear approach as described by the equation $y = 0.3936x + 0.195$; $R^2 = 0.9582$ for the anodic peak currents.

4. Conclusion

The BFO intercalated MMT nano composites were synthesized by intercalation using ascorbic acid as a supporter for improving capacitance behavior. The chemical composition changes of MMT clay affected by HNO_3 on clay, besides intercalation have been confirmed by FT-IR spectral studies. The intercalation of the BFO onto the clay layers, BFO crystalline size and composites, which are in nano scale, have been confirmed by XRD and SEM. The interaction between BFO and clay was confirmed by UV-Visible spectral analysis. The Tauc's plot showed the band gap of 2.34 eV supported for Photo catalytic activity Rhodamine-B dye in various time intervals. The photoluminescence peak revealed that luminescence behavior was improved and the band gap was found to be 2.16 eV. The electrochemical results confirmed the BFO-MMT nano composites had good specific capacitance of 400 Fg^{-1} in 1 mol L^{-1} NaOH solution at a scan rate 10 mVs^{-1}. Thus, the BFO-MMT nanocomposites can be used as a potential electrode material for capacitor applications.

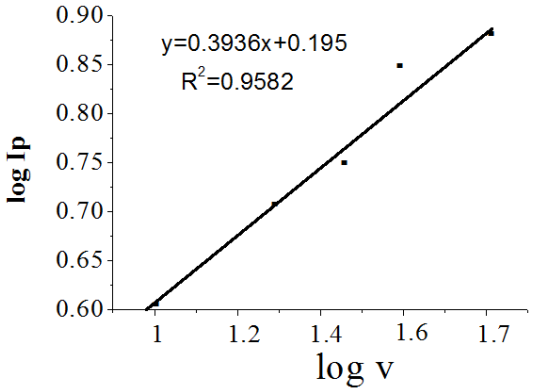

FIG. 10. Plot of anodic current against square root of scan rate

References

[1] Whittingham M.S., Jacobson A.J. *Intercalation Chemistry Academic Press*, New York, 1982, P. 1–18.

[2] Van Olphen H. *An Introduction to Clay Colloid Chemistry*, Wiley Inter science, New York, 1977.

[3] Zhaohui Hana, Huaiyong Zhu, et al. Nano composites of layered clays and Cadmium sulphide, Similarities and Difference in formation, Structure and properties. *Microporous and Mesoporous Materials*, 2008, **108**, P. 168–182.

[4] Peng Yuan, Faiza Annabi-Bergaya, et al. A combined Study by XRD, FTIR, TG and HRTEM on the Structure of delaminated Fe-intercalated/pillared clay. *Journal of Colloid and Interface Science*, 2008, **324**, P. 142–149.

[5] Nithima Khaorapapong, Areeporn Ontam, Jinda Khemprasit, Makoto Ogawa. Formation of MnS- and NiS- Montmorillonites by solid-solid reactions. *Applied Clay Science*, 2009, **43**, P. 238–242.

[6] Yasuyuki Arao, Yutaka Hirooka, Katsumi Tsuchiya, Yasushige Mori. Structure and Photoluminescence properties of Zinc Sulfide nanoparticles prepared in a Clay Suspension. *J. Phys. Chem. C*, 2009, **113**, P. 894–899.

[7] Peng Wang, Mingming Cheng, Zhonghai Zhang. On different photodecomposition Behaviours of Rhodamine B on Laponite and Montmorillonite Clay under visible light Irradiation. *Journal of Saudi Chemical Society*, 2014, **18**, P. 308–316.

[8] Bahranowski K., Gaweł A., et al. Influence of purification method of Na-Montmorillonite on textural properties of clay mineral Composites with TiO_2 Nano particles. *Applied Clay Science*, 2017, **140**, P. 75–80.

[9] Wengwen Zhang, Zhenbo Ren, et al. Activated Nitrogen-doped porous carbon ensemble on montmorillonite for high-performance supercapacitors. *Journal of alloy and compounds*, 2018, **743**, P. 44–52.

[10] Zang Y., Xie D., et al. Enhanced photovoltaic properties in grapheme/ polycrystallineBiFeO3/Pt hetero-junction structure. *Appl. Phys. Lett.*, 2011, **99**, P. 132904.

[11] Yang S.Y., Seidel J., et al. Above-band gap voltages from Ferroelectric photovoltaic devices. *Nat. Nanotechnol.*, 2010, **5**, P. 143–147.

[12] Nguyen Anh Tien, Chau Hong Diem, et al, Structural and Magnetic properties of $YFe_{1-x}Co_xO_3$ ($0.1 \leq x \leq 0.5$) perovskite nano materials synthesized by Co-precipitation method. *Nanosystems: Physics, Chemistry, Mathematics*, 2018, **9** (3), P. 424–429.

[13] Yang J., Li X., et al. Factors controlling pure-phase Magnetic $BiFeO_3$ powder synthesized by Solution combustion synthesis. *Alloys Compd.*, 2011, **509** (37), P. 9271–9277.

[14] Xian T., Yang H., et al. Photo catalytic properties of $BiFeO_3$ nano particles with different sizes. *J. Mater. Lett.*, 2011, **65**, P. 1573–1575.

[15] Gao F., Chen X., et al. Visible-Light Photocatalytic Properties of Weak Magnetic $BiFeO_3$ Nano particles. *J. Adv. Mater.*, 2007, **19**, P. 2889.

[16] Lokhande C.D., Dubal D.P. Oh-Shim joo. Metal Oxide thin film based supercapacitors. *Current applied Physics*, 2011, **11**, P. 255–270.

[17] Doff D.H., Gangas N.H.J., Allan J.E.M., Coey J.M.D. Preparation and Characterization of iron oxide pillared Montmorillonite. *Clay minerals*, 1988, **23**, P. 367–377.

[18] Timofeeva M.N., Panchenko V.N., et al. Effect of nitric acid modification of montmorillonite clay on synthesis of solketal from glycerol and acetone. *Catalyst Communications*, 2017, **90**, P. 65–69.

[19] Peng Yuan, Faiza Annabi-Bergaya, et al. A Combined study by XRD, FTIR, TG and HRTEM on the Structure of delaminated Fe-intercalated/pillared Clay. *Journal of colloid and Intreface Science*, 2008, **324**, P. 142.

[20] Yohannan Panicker C., Hema Tresa Varghese, Daizy Philip. FT-IR, FT-Raman and SERS spectra of Vitamin C. *Spectochimica Acta Part A*, 2006, **65**, P. 802–804.

[21] Tayyebe Soltani, Mohammad H. Entezari. Sono-synthesis of bismuth ferrite nanoparticles with high photocatalytic activity in degradation of Rhodamine B under solar light irradiation. *Chemical engineering Journal*, 2013, **223**, P. 145–154.

[22] Anna Rokicinska, Piotr Natkanski, et al. Co_3O_4-pillared montmorillonite catalyst synthesized by hydrogel-assisted route for total oxidation of toluene. *Applied catalyst B; Environmental*, 2016, **195**, P. 59.

[23] Manikandan D., Mangalaraja R.V., Ananthakumar S., Sivakumar T. Synthesis of metal intercalated clay catalysts for selective hydrogenation reactions. *Catalyst in Industry*, 2012, **4**, P. 215–230.

[24] Ruxandra Irina Iliescu, Ecaterina Andronescu, et al. Montmorillonite-alginate nanocomposite beads as drug carrier for oral administration of carboplatin – Preparation and characterization. *U. P. B. Sci. Bull., Series B*, 2011, **73**, P. 3.

[25] Min Zhang, Zhenfa Zi, et al. Size Effects on Magnetic Properties of $Ni_{0.5}Zn_{0.5}Fe_2O_4$ Prepared by Sol-Gel Method. *Advances in Materials Science and Engineering*, 2013, 609819, 10 pp.

[26] Ajin Sundar S., Joseph John N. Synthesis and studies on structural and optical properties of zinc oxide and manganese-doped zinc oxide Nanoparticles. *Nanosystems: Physics Chemistry Mathematics*, 2016, **7**, P. 1024–1030.

[27] Galindo-Gonzlez C., De Vicente J., et al. Preparation and Sedimentation Behavior in Magnetic Fields of Magnetite-Covered Clay Particles. *Langmuir*, 2005, **21**, P. 4410.
[28] Baby Suneetha R., Vedhi C. Synthesis, characterization and electrochemical behaviour of Montmorillonite Poly(o-toluidine) nano composites. *Applied Clay Science*, 2014, **88–89**, P. 18–25.
[29] Figueras F., Klapyta Z., et al. Use of competitive ion exchange for Intercalation Of montmorillonite with Hydroxy-aluminum cpecies. *Clay and clay Minerals*, 1990, **38**, P. 257–264.
[30] Dai J.F., Xian T., Di L.J., Yang H. Preparation of $BiFeO_3$-Graphene Nano composites and their Enhanced Photo Catalytic Activities. *Journal of Nano Materials*, 2013, 642897, 5 pp.
[31] Ramya E., Rajashree. Ch. Nayak., Narayana Rao P.L. New Hybrid organic polymer montmorillonite /chitosan/ Polyphenyenediamine composites for nonlinear optical studies. *Applied clay science*, 2017, **150**, P. 323-332.
[32] Yao Y.B., Mak C.L. Optical, ferroelectric and magnetic properties of Multi ferroelectric $BiFeO_3$–$(K_{0.5}Na_{0.5})_{0.4}(Sr_{0.6}Ba_{0.4})_{0.8}$ Nb_2O_6. *Thin films Journal of Alloys and Compounds*, 2014, **586**, P. 448.
[33] Bobby singh soram, Boinis singh ngangom, Sharma H.B. Effect of annealing temperature on the structural and optical properties of sol-gel processed nano crystalline $BiFeO_3$ thin films. *Thin solid film*, 2012, **524**, P. 57–61.
[34] Dillip K. Mishra, Xiaoding Qi. Energy levels and photoluminescence properties of Nickel-doped bismuth Ferrite. *Journal of Alloys and Compounds*, 2010, **504** , P. 27–31.
[35] Sunil chauhan, Manoj Kumar, et al. Multiferroic, Magnetoelectric and optical properties of Mn doped $BiFeO_3$ nano particles. *Solid state Communications*, 2012, **152**, P. 525–529.
[36] Yu X., An X., Enhanced Magnetic and optical properties of Pure and (Mn, Sr) doped $BiFeO_3$ nano crystals. *Solid state communications*, 2009, **149**, P. 711.
[37] Yoon M., Seo M., et al. Synthesis of Liposome-Templated Titania Nanodisks: Optical Properties and Photocatalytic Activities. *Chem. Mater.*, 2005, **17**, P. 6069–6079.
[38] Li L., Yang Y., et al. Fabrication and charecterization of single- Crytalline ZnTe Nano wire Arrays. *J. Phys. Chem. B*, 2005, **109**, P. 12394–12398.
[39] Arulmozhi S., Packiaseeli V., Rajendran R., Vijayalakshmi. Structural, Optical and morphological study of Tungsten selenide thin film. *Nanosystems: Physics, Chemistry, Mathematics*, 2016, **7**, P. 703–706.
[40] Huo Y.N., Jin Y., Zhang Y. Citric acid assisted solvothermal synthesis of $BiFeO_3$ Micro spheres with high VisibleLight photocatalytic activity. *J. Mol. Cat. A: Chem.*, 2010, **331**, P. 15–20.
[41] Bhusahan B., Das D., et al. Enhancing the magnetic characteristics of $BiFeO_3$ nano particles by Ca, Ba co-doping. *Material chemistry and physics*, 2012, **135**, P. 144–149.
[42] Balasubramaniam M., Balakumar S. Effect of precipitating agent NaOH on the Prpapration of copper oxide nanostructures for electrochemical applications. *Nanosystems: Physics, Chemistry, Mathematics*, 2016, **7**, P. 482–487.
[43] Ramesh Oraon, Amrita Adhikari, Santosh Tiwari, Ganesh Chandra Nayak. Enhanced specific capacitane of self- assembled three dimentional CNT/ Layered Silicate/ Polyaniline hybrid sandwiched nanocomposite for Supercapacitor application. *ACS Sustainable chemistry & Engineering*, 2016, **4** (3), P. 1392–1403.
[44] Hongjuan Li, Gang Zhu, et al. Preparation and Capacitance property of MnO_2-pillared Ni^{2+}-Fe^{3+} layered double hydroxide nanocomposite. *Journal of Colloid and Interfac Science*, 2010, **345**, P. 228–233.
[45] Kotz R., Carlen M. Principle and application of electrochemical capacitors. *Electrochem. Acta*, 2000, **45**, P. 2483.
[46] Lokhande C.D., Gujar T.P., Shinde V.R., Rajaram S. Mane. Electrochemical Super capacitor application of Perovskite thin films Sung-Hwan Han. *Electrochemistry communications*, 2007, **9**, P. 1805–1809.

NANOSYSTEMS: PHYSICS, CHEMISTRY, MATHEMATICS, 2018, 9 (5), P. 641–662

Thermodynamics and kinetics of non-autonomous phase formation in nanostructured materials with variable functional properties

A. N. Kovalenko[1], E. A. Tugova[1,2]

[1]Ioffe Institute, 26 Politekhnicheskaya, St. Petersburg 194021, Russia
[2]St. Petersburg Electrotechnical University "LETI", ul. Professora Popova 5, St. Petersburg 197376, Russia
ras-kan@mail.ru, katugova@inbox.ru

PACS 05.70.Ce; 05.70.Ln; 64.60.Qb **DOI 10.17586/2220-8054-2018-9-5-641-662**

The review addresses physico-chemical aspects of interaction between macro-, micro- and nano- structured units of matter with the analysis of interface and grain boundary entities (nonautonomous phases) mechanisms and formation, as well as methods of their control in order to achieve the desired functional properties of nanostructured materials. Construction of these materials involves identification of thermodynamic and kinetic regularities in the organization processes, state and genesis parameters of nonautonomous phases formed as specific nanosized structures in a limited space between the macroscopic volume phases and with the limited amount of substance, which differ significantly on their properties, structure and composition from the appropriate characteristics of volume phases. Studying them is based on the application and development of theoretical and experimental methods of non-equilibrium thermodynamics, chemical kinetics, nonlinear dynamics and fractal analysis to determine the conditions of self-organization or materials directed synthesis with a high content of nonautonomous phases.

Keywords: nanostructered materials, non-equilibrium thermodynamic processes, chemical kinetics, interaction of macro-, micro- and nanostructured elements, nonautonomous phases, conditions of self-organization, materials synthesis, functional properties.

Received: 1 May 2018

Revised: 30 July 2018

Contents

1. Introduction

The nonautonomous phase concept regards small objects formed at the junctions between the macroscale substance volumes as intermediate (transient) surface, interface or grain boundary structures which composition, structure and properties are determined by spatial or substance amount limitations, and which cannot exist as independent thermodynamic phases. Nonautonomous phases are highly important, and previously, a rarely considered part of synthesized materials, whereas determining their functional properties in many respects. Development of this concept as a physical and chemical basis for designing new functional materials, including nanocomposites, involves focusing on interactions between their macro-, micro- and nanostructured units using various methods and approaches, including theoretical and experimental methods of non-equilibrium thermodynamics, chemical kinetics, nonlinear dynamics and fractal analysis.

It would be feasible to apply these methods in addressing the given problem due to the ability to describe both equilibrium and non-equilibrium systems, with due account of metastable and intermediate structures formed as a result of these interactions. Herewith, it is of great interest to reveal the regularities of formation and state parameters of rather stable nonautonomous phases, the causes of which may be thermodynamic and kinetic characteristics of interactions between different-scaled substance structures. It is essential to identify the conditions of self-organization, as well as methods to deliberately form the nonautonomous phases with distinct physical and chemical, mechanical, thermal, electrical, magnetic and other properties, as compared to volume phases [1–25]. Nonautonomous phases are also able to concentrate impurity elements in ultrahigh concentrations [26–29]. The latter property results in significant redistribution of components between the surface (interfacial, intergranular)

formations, i.e. non-autonomous phases, and the volume phases in the materials [30–35]. Such phenomena related to the formation of nonautonomous phases as material surface nanofragmentation invoking the nanocrystalline structure fractality, improved adsorption and catalytic properties, are also of great interest [36–48].

The study of these effects by methods of non-equilibrium thermodynamics, nonlinear dynamics and chemical kinetics is aimed at identifying mechanisms and energy of the occurring processes and their dynamic parameters, in particular, in the phase space. Probabilistic multifractal dimensions can be used to quantify the scale invariance of these structures, manifested in this case, and the attractor of entropy generated in them during the substance and energy transfer. Their general expression is the Renyi dimension [49,50] which describes metric and statistical properties of these materials and processes occurring in them.

Experimental studies of structural and chemical transformations in the systems containing a large substance proportion in the nonautonomous phases, as well as of physical-chemical, mechanical, thermal physical, electrophysical, magnetic and other properties of materials based on these systems are of independent interest. Since these materials contain nanoscale elements, not only their properties but also their geometric characteristics, as well as the geometric parameters of their fragments, can be determined only based on the analysis of a set of complementary methods [51–54]. The synthesis of such materials requires the development of special approaches and methods, and represents a standalone target [55–65].

This review does not address a number of the above issues related to the development of materials with a high substance proportion in the nonautonomous phases, and is aimed primarily at describing of nonautonomous phases and materials based on systems in which a large substance proportion resides in nonautonomous phases behavior.

2. Status of nonautonomous phases and materials with the high value of matter in the nonautonomous phases study

Nonautonomous phases, as specific small-scale structures existing in a confined space between the macroscopic volume phases, or in a limited substance amount located on a surface, are significantly different in their properties, behavior and structure from the volume phases while similar in terms of chemical composition [66–73]. They are characterized by different melting temperatures, other phase transitions [74–85], and other critical parameters. Materials containing a substantial portion of nonautonomous phases show peculiar deformation characteristics, different behavior when the temperature varies due to changes in thermodynamic and transport properties of such materials [86–91]. The fundamental and applied research being done in this field is largely focused on the study of structural and functional characteristics of such materials, and on the development of technological methods to produce nano-dispersed, nano-crystalline and nano-porous materials [92–101]. Less attention is paid to research of physical and chemical mechanisms and conditions of formation and transformation of nonautonomous phases with a specific composition and structure, including the relationship between thermodynamic and other characteristics of similar nanoscale formations and their topological and metric structure, processes of environmental interaction, the extent of influence on the properties of spatially conjugated macroscopic volume phases.

Research in the field of objects, which are formed at the intersection between substance macro-volumes as intermediate (surface, interfacial) structures, dates back to the papers by T. Young (1805–1807), J. W. Gibbs (1878) and J. D. Van der Waals (1908–1912). In [102], the surface phases (thermodynamic substance state at the interface of volume phases) are described as “finite-thickness phases”, and in [103, 104], these finite-thickness phases were discussed in the context of equilibrium thermodynamics as “nonautonomous phases”, meaning that their independent (isolated from the volume phases) existence is impossible. In [1,105–107], the concept of “nonautonomous phases” was transferred to a wider range of objects and expanded to the concept of “nonautonomous substance state”, i.e. defining such a state of substance in which the composition, structure and properties are determined by various spatial limitations, i.e., depend fundamentally on the size and shape of the limiting surfaces, on the substance amount within a limited space, on the composition and structure of the limiting walls [1].

Thermodynamic ideas about the substance behavior on the interface of volume phases, and about the role of phase interfaces in the system behavior are developing in two directions to date. Historically, the first idea of the substance properties in the phase interface is based on their reference to the phase interfacial area [108, 109]. In this case, we lose information about the structure and distribution of the substance over the transition area thickness (over the nonautonomous finite-thickness phase formed at the interface between the two phases. It should be noted that this approach, as shown in [75, 82, 87], is not very effective in the analysis of kinetic processes as well, and in cases where it is required to compare the substance volume fractions in the nonautonomous and volume phases, i.e., primarily in nanoscale systems. The second approach is based on addressing the nonautonomous phases as those having a certain finite thickness, the substance of which has a specific structure. It was shown in a number of papers (for instance, [110–112]) that both approaches are equivalent in the context of equilibrium thermodynamics, which is a certain theoretical justification of equal, in a way, existence of both approaches.

Description of the behaviors of polycrystalline materials, other disperse systems, especially those consisting of nanoscale areas of autonomous phases, as well as of the materials at high temperatures, as shown in numerous papers [75, 78–82], gives more prognostic conclusions if the interface areas formed by contact of volume phases are considered as nonautonomous finite-thickness phases. In this approach, determining such parameters as the thickness of nonautonomous phases and their melting point is of considerable interest in the analysis of the behavior of both single- and multiphase powder and polycrystalline materials. [1, 75, 82, 87, 113–116] lists a variety of expressions to describe the temperature dependence of the nonautonomous phase thickness. The basic conclusion from these expressions is the fact that if the nonautonomous phase thickness has nanometer and sub-nanometer dimensions at relatively low temperatures, it increases sharply with temperature rise and with the approach to the melting point for solids, or to the critical point for liquids, thus becoming comparable to the size of volume phases. The most detailed variant of this dependence seems to be achieved in [117]. Another important property of the nonautonomous finite-thickness phase is its melting point. If early papers [75, 78, 80, 81, 117, 118] provided discussion that the melting temperature of surface (nonautonomous) phases may differ from the melting temperature of volume phases of the same composition, the recent papers generally consider only the value of these differences and expressions describing the dependence of the melting temperature of different nonautonomous phases on certain parameters [13, 15, 95, 97–99, 108, 214]. Information on the component distribution between the nonautonomous and volume phases, which makes it possible to predict the material properties and behavior over a wide temperature range, is of great importance for the analysis of polycrystalline and other disperse systems [78, 79, 117]. In this respect, it should be noted that there is a significant advantage, explained in detail in [78, 82], of considering the component redistribution between the volume phases and the nonautonomous finite-thickness phases, as compared to the approach considering the concentration of impurity components at the volume phase interface as their adsorption or segregation on a two-dimensional surface. However, the latter way of consideration is widespread and also provides useful information for analyzing the properties and behavior of materials [1, 6, 13, 15, 71, 95, 97–99, 105–107].

Consideration of nonautonomous phases as finite-thickness ones enables to analyze, in particular, the possibility of forming in them not only static but also dynamic structures resulting out of transformation processes and mass transfer in them [84, 119–125]. This possibility was used to analyze the behavior of both synthetic materials [1, 6, 13, 15, 71, 95, 97–99, 105–107, 112, 123] and natural objects, in particular, in the behavioral analysis of ice and massive bodies in ice [113, 126–130].

The structure and contribution of nonautonomous phases and properties of polycrystalline materials are greatly influenced by the size and misalignment degree of crystallites in their composition [131–135]. The thickness, structure, composition, and properties of the intercrystalline layer (nonautonomous phase) vary by the crystallite misalignment degree [1, 13, 27, 30, 40, 59, 71, 73, 85]. The ratio between crystallite size and intercrystalline layer thickness (nonautonomous surface phase), in turn, determines the volume fractions of crystallites and intercrystalline formations in the polycrystalline material [75, 78–82, 105, 106]. Moreover, any chemical interaction during a solid-phase reaction involves the mass transfer of components across the phase interface. For solid-phase reactions, the reaction zone is localized at the phase interface which is structurally heterogeneous, and therefore heterogeneous in its chemical activity. According to the data available [75, 78–82], the mass transfer of components is much swifter in nonautonomous phases (surface, grain boundary, interface areas) than in granule volume under certain conditions. The interest in considering nonautonomous phases as objects with properties unlike those of volume phases is more related to their melting processes. The process of melting is essential for describing the solid-phase process activation which occurs at the melting point of the nonautonomous phase [1, 13, 15, 59, 62, 75–82, 136, 137]. Melting of nonautonomous phases in polycrystalline systems is a key transformation that generally affects the system behavior, while the melting point of nonautonomous phase (T_{m2n}) becomes one of the key parameters relating to the outset of transformation [1, 13, 15, 59, 62, 75–82, 136, 137]. As shown in [75–82], the mass transfer of a substance will be carried out mainly in liquid-like nonautonomous phases in dispersed, including heterophase, systems, especially in case of small, nanoscale and submicron, granular sizes at temperatures$T > T_{m2n}$.

This statement is supported, for instance, by the case of autocatalytic solid-phase reaction of chrysoberyl formation, as described in [138]. A large number of papers, both on the subject of analysis of the activation temperature in sintering and inelastic deformation of materials [139, 140] and on that of the analysis of solid-phase reaction mechanisms [141–151], show that all these solid-phase processes start in the systems only after the nonautonomous phase has transitioned to a liquid-like state, i.e., they are liquid-phase reactions in a sense, as stated in [75, 78]. As another example, we can compare the findings from the study of Ruddlesden–Popper phase formation kinetics from different reagents [151–168] with data on the values of some temperature transformations in the Ln_2O_3–SrO–Al_2O_3 system [169–173], in which the compounds are formed that are promising for the production of functional and structural high-temperature materials [174–180]. This comparison has shown that

solid-phase reactions are activated in the system considered only after the nonautonomous phases have transited to a liquid-like state, as may be concluded on the basis of these papers [1,15,59,75,78–82,84,133,138–140,142,144].

The transition to nano-sized reagent particles leads to a significant increase in the volume fraction of nonautonomous phases in the reaction system [1, 117, 118]. The diagram shown in Fig. 1 illustrates the relationship between nonautonomous phase fraction and the particle size.

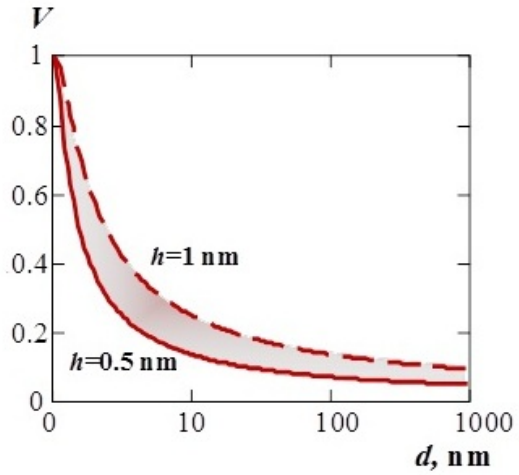

FIG. 1. Dependence of nonautonomous phase volume fraction in disperse system *vs* autonomous phase particle sizes [1]

A sharp increase in nonautonomous phase fraction in the area of nanoscale particles shows that the use of nanoscale reagents should intensify the interaction between the solid-phase components. Chemical reactions between nanoparticles should go much faster than in the case of the interaction between micro- and macroscale particles. In this regard, it seems important to develop methods which produce nanocrystalline powders of various compositions that could be precursors for the synthesis of multicomponent compounds [181–191]. However, as shown in [12, 60, 145], reducing the size of reagent particles would not imply a certain increase in the speed of their interaction. At the same time, a temperature rise above the melting point of nonautonomous phases, as shown by numerous literature data, always results in a sharp increase in the speed of component interaction in solid-phase systems. In view of the above findings, it can be concluded that an important line of research is the study of phase formation mechanisms in the systems with nanoscale reagents, inter alia, with nanoscale spatial limitations, i.e. of the processes in nanoreactors [17,192–195]. Not only the "soft chemistry" methods [5,13,37,41,59,97,196,197], but also the methods based on precursor combustion [11,61,95,99,190,198–200], in particular, the solvent combustion method [11, 16, 21, 22, 62, 95, 99, 190, 198–200] are effective for producing materials with a high proportion of nonautonomous phases.

The features of nanodispersed systems related to the phenomenon of "quantum-dimensional effects", to the changes in the crystal structure of nanoparticles by contrast to macroscale crystals, to the increased proportion of the nonautonomous phase atoms being under conditions other than those of the volume phase atoms (another coordination number, another symmetry of the local environment, the absence or other pattern of the long-range order), as well as the non-equilibrium nanoparticle state evolving due to extreme synthetic conditions, affect the properties of nanomaterials. In particular, there is a change in the following properties: mechanical – increased solidity in combination with high plasticity; electrical – small particles becoming semiconductors; magnetic – extreme dependence of magnetic properties on the particle size, with the transition to superparamagnetism; thermal – lowered sintering temperatures, changed temperatures of polymorphic transformations due to high proportion of the liquid-like nonautonomous phase; optical – changed radiation and absorption spectra; chemical – increased reactivity, etc. [115, 201–216]. As follows from the findings of a number of studies on the nanocrystals formation, their structure and properties are often governed by the chemical and thermal background of the original compositions and by the their formation mechanism [59, 95, 97–99, 119–121].

Applying the concept of nonautonomous finite-thickness phases was promising not only in terms of describing the behavior and properties of synthetic materials, but also in terms of analyzing natural systems. Previous studies [29, 215] illustrate the role of nonautonomous phases in mineral formation and their influence on properties of minerals. Such phenomena related to the nonautonomous phase properties were discovered as surface

nanofragmentation, evoking fractality of nanocrystalline structures and absorption of the elevated impurity element concentrations, both incompatible with the autonomous phase structure in the crystal-chemical sense and compatible (isomorphic) impurities. The possibility to describe the volume phase interfaces as nonautonomous phases of finite thickness, which transition temperature to a liquid (liquid-like) state is lower than the melting point of the volume phase of the same composition, made it possible to explain many features of the ice behavior [113, 126, 129].

Despite the above-mentioned examples of successful use of the concept of nonautonomous finite-thickness phases in terms of equilibrium (local-equilibrium) thermodynamics, this approach is quite limited and cannot always provide an adequate thermodynamic description of how the actualized structures are formed or identify conditions of their self-organization and methods to control interaction of disproportionate structural substance elements in the material. It is necessary to involve the methods of non-equilibrium thermodynamics and physical-chemical kinetics, along with further development of model concepts of disproportionate structural element interaction. Herewith, along with kinetic characteristics, the entropy indicators of internal conversional instability of energy related to the increasing role of conjugated thermodynamic flows and forces, to the emergence and maintenance of organized non-equilibrium states as so-called "dissipative" space-time structures of the substance are used for thermodynamic evaluation of non-equilibrium in ongoing processes and conditions of self-organization of these systems [217]. It is shown, as exemplified by [218], that in two-phase media with ongoing dissipative processes, the fluctuations of their characteristics become more favorable energetically than stationary conditions, providing smaller energy dissipation (entropy production). Increased parameters of the system state, while approximating the critical point, lead to abnormal growth of large-scale density fluctuations and the development of thermodynamic substance instability – the phenomenon which is theoretically described based on the idea of "scale invariance (scaling)" to characterize the thermodynamic potentials by generalized homogeneous functions of the non-integer (fractional) order relative to their fields [219–221], and its practical application makes it possible to disperse materials up to nanoparticles under the influence of powerful energy flows, in particular, with the electric conductor explosion (ECE), experiencing the aggregate state transition through "solid-liquid-gaseous-plasma" [222]. There are great prospects for developing this line if ECE would be implemented in various chemically active media, in particular, in supercritical aqueous fluid to produce nanoscale metal oxides with a high proportion of the substance in the nonautonomous phases [223]. The arising objectives to describe the kinetics of heat and electricity transfer in various components to such a system (metal, liquid, vapor, plasma, supercritical fluids) are usually considered through the ideas of percolation theory and models of effective coefficients of inhomogeneous media [224, 225]. They are built with aprioristic ideas about the typical sizes of heterogeneities, their mutual arrangement, the volume concentration, the nature of mutual contacts, etc. At the same time, the relationship between the transfer coefficients of each component and the characteristics of physical state of the substance (usually, the temperature and density) are assumed to be known. It is important to highlight that for liquid-metal and plasma media, the transfer coefficients are increasingly governed by the interaction between free electrons and small-and large-scale density fluctuations, along with temperature increase and approximation to the critical point of the substance [226]. In the vicinity of the critical point, this factor can be decisive for the calculation of effective transport coefficients of inhomogeneous medium and requires detailed consideration. Model concepts for the interaction of disproportionate substance structures are exemplified by the supramolecular model of eutectic [227, 228] where, in contrast to the classical supramolecular ensembles [229], it is possible to violate the principle of geometric and topological complementarity, that is, the mutual consistency between the substrate and the receptor, including at the level of formation of intermolecular bonds [230, 231]. The results of calculations performed for one-dimensional approximation within the classical Frenkel–Kontorova statistical model [232], as presented in this paper, demonstrate that suprastructures may organize themselves out of disproportionate substance structures and show that the probability of fragmentation for nonautonomous metastable suprastructures increases dramatically with an increase in the initial disproportion and with the formation of sufficiently strong intermolecular bonds. With due account to the above-mentioned significantly distinguishing properties of the substance in such "nonautonomous states" ("nonautonomous phases"), there are certain prospects for production of new functional materials with a high concentration of nonautonomous phases which use the features of metastable and intermediate structures formed as a result of these interactions, such as in the experimental material of the lithium-ion battery cathode [233]. However, there are still pending issues related to the approach of nonautonomous suprastructures to relaxation.

Research in the field of synthesis of new compounds with a high content of nonautonomous phases is aimed at both producing original functional materials with variable performance properties and developing related technologies for their production. In this regard, the synthesis of nanoceramics and other materials of constructional and functional purpose [3, 4, 7, 8, 24, 76, 192, 234–246], in particular, materials intended for use in thermoelectric energy converters [240, 241], ferrites [13, 25, 52, 59, 64, 97–99, 107, 145], high-temperature superconductors [175, 238, 244],

catalysts [13, 22, 36, 37, 39, 40, 46, 60], radioactive waste immobilization matrices [236, 237, 239], is of great interest among the developments noted in Section 2.

The analysis confirms the scientific and practical relevance and prospects of the follow-up studies on thermodynamics and kinetics of nonautonomous phase formation and transformation both to identify the fundamental laws of interaction between macro-, micro - and nano-structural substance units and to produce new materials with a large proportion of nonautonomous phases with variable functional properties.

3. Thermodynamics of the systems which include nonautonomous interphase areas and conjugated macroscale substance volumes

In thermodynamic analysis, the nonautonomous phase is represented as an intermediate small-size interphase region with a typical sub-nanometer to nanometer thickness at relatively low temperatures which separates the surrounding macroscopic volume phases, different in composition, properties, and structure, through the open boundaries of which the system can exchange energy and substance. The forces of interatomic and intermolecular interaction manifested at these boundaries are macroscopically characterized by the surface tension, the value of which in the area of interface will vary in the direction of transition from one volume phase to another, and remain the same for all directions in the area of volume phases. Thermodynamic characteristic of the work link between the forces of surface tension σ, with the change in internal energy dU and other parameters of the open system of variable composition, in the formation of interface region with the volume dV_f and the flat surface area dA_f, is the combined ratio of the first and second laws of thermodynamics $dU = TdS - PdV_f + \sigma dA_f + \sum \mu_j dn_j$, where P is the external pressure of the system, against which the interface region is formed; dS is the system entropy variation during nonautonomous phase formation at a temperature T; μ_j and n_j are chemical potential and the number of moles of the j-th component in case of variations in the interphase substance content in the mass transfer. In case of the liquid or gaseous substance state and the curved interface, the pressure in the interfacial region will exceed the external pressure by the value of Laplace additional pressure $P_L = \sigma(1/R_1 + 1/R_2)$, where R_1 and R_2 are the curvature radii of two mutually perpendicular sections of the meniscus [247]. A large number of different experimental methods to measure directly the surface tension have been developed for these media, in contrast to solids where this is not possible, except for a few special cases, and calculation methods based on different models to describe the solid surface and surface energy are used to measure the surface tension (see, for instance, [248]).

3.1. Equilibrium states of nonautonomous phases

The thermodynamic equilibrium states and quasi-stationary equilibrium processes are usually characterized by well-known thermodynamic functions. Their definitions for the macroscopic volume phases of constant composition are given as conventional expressions of enthalpy $H = U + PV$, the variation of which governs by the thermal effect of isobaric process, Helmholtz free energy $F = U - TS$, the variation of which governs a part of internal energy that can be converted to the external work of the system in an isothermal process, Gibbs free energy (enthalpy)

$$G = H - TS = U + PV - TS,$$

the variation of which governs the total enthalpy and entropy effects, and the total system work minus expansion in isobaric-isothermal processes, as well as other thermodynamic potentials depending on the set of parameters used to describe the system state [249]. However, for the interphase region with an open interface, these functions are also related to the work of surface tension forces and the work of mass transfer forces [110, 111]. Thus, from the differential form of the above definitions of thermodynamic functions

$$dH = dU + PdV + VdP, \quad dF = dU - TdS - SdT,$$

$$dG = dH - TdS - SdT = dU + PdV + VdP - TdS - SdT,$$

based on the core equations for internal energy, it follows that the net mechanical system work

$$dW = -PdV + \sigma dA_f = -[dF]_{T,ni},$$

related to the changing volume and surface of the interphase region under conditions of constant temperature ($dT = 0$) and at constant substance content ($dn_j = 0$) is determined by the decrease of Helmholtz free energy. Herewith, the respective variation of the internal energy dU causes an increase in the system entropy $dS = (dU - dW)/T$. Integration of these equations at constant values of intensive parameters (i.e. not dependent on the mass of the system) according to the Euler theorem on homogeneous functions results in the following expressions

for thermodynamic potentials of the interphase region, different from their usual expressions for volume phases due to the presence of an additional summand (σA_f):

$$U = TS - PV_f + \sigma A_f + \sum \mu_i n_i; \quad H = TS + \sigma A_f + \sum \mu_i n_i;$$

$$F = -PV + \sigma A_f + \sum \mu_i n_i; \quad G = \sigma A_f + \sum \mu_i n_i.$$

This illustrates that in the region of phase interface, changes in the extensive properties will result in specific expressions for partial thermodynamic quantities (substance properties), as well as their ratios to the normal integral properties, in particular, for chemical potentials and their ratios to the Gibbs thermodynamic potential as a corollary of the Gibbs–Duhem equation. Similarly, the Gibbs–Duhem equation itself will differ, which links the intensive (system mass dependent) parameters for each phase of the multicomponent heterogeneous system

$$SdT - VdP + Ad\sigma + \sum n_i d\mu_i = 0,$$

where n_i is the number of particles of the *i*-th component, given their different phase state. This ratio for the phase interface region, at constant temperature T and pressure P values, becomes $Ad\sigma = \sum n_i d\mu_i$, from which the Gibbs adsorption isotherm equation $d\sigma = \sum (n_i/A) d\mu_i$ is derived easily.

Although the known classical expressions given here show significant differences in the equilibrium thermodynamics of volume and surface phases, however, the local-equilibrium approach used is not able to reveal their self-organization and stability conditions in deterministic and spontaneous perturbations of thermodynamic quantities in non-equilibrium thermodynamic systems, which usually requires the use of physical-chemical kinetics methods. At the same time, the internal entropy production and internal instability values related to the increasing interaction of conjugated thermodynamic flows and forces, to the emergence and maintenance of organized non-equilibrium (metastable) states as so-called "dissipative" spatiotemporal structures of the substance, may be effectively used along with kinetic characteristics in order to evaluate thermodynamic the non-equilibrium of ongoing processes and self-organization conditions in such perturbed systems [217].

3.2. Behavior of nonautonomous phases in non-equilibrium conditions

In contrast to the above commonly accepted approach, the behavior of nonautonomous phases, as well as that of macroscopic volume phases, in non-equilibrium conditions is convenient to be considered based on the analysis of the system entropy alteration caused by irreversible processes, with the assistance of the extreme principles. Using the accepted system energy partition as heat and work during its exchange with the external environment, which is known to be

$$dU = dQ + dW + \sum n_i d\mu_i$$

for open systems, as well as the division of entropy variations, as proposed by I. Prigozhin [217], by the sum of two summands $dS = d_e S + d_i S$, one of which ($d_e S$) is determined by the substance and energy exchange with the external environment, and the other ($d_i S \geq 0$, always positive) by internal production due to irreversible processes in the system itself, the following is revealed for various conditions on its boundaries of nonautonomous phases.

1. If there is absolutely no energy and substance exchange, the state of the system, including the volume phases and interphase regions, as known for any isolated thermodynamic system, will tend to the equilibrium state with a maximum entropy value $S > S_{\max}$, which is determined by the growth of $d_i S \geq 0$ at $d_e S = 0$ due to internal irreversible processes.

2. The $d_e S$ value is equivalent to the Clausius entropy variation, i.e. $dQ = T d_e S$, in case of the energy exchange only and with no substance exchange ($\sum \mu_j dn_j = 0$) on the boundary of the system considered, then the energy change is determined by the general expression

$$dU = T d_e S + dW.$$

Given the ratio $dS = d_e S + d_i S$, it transforms as

$$dU = TdS + dW - T d_i S,$$

and as

$$dU = TdS - PdV + \sigma dA_f - T d_i S$$

after substituting the above expression for work

$$dW = -PdV + \sigma dA_f$$

related to changes in the volume and surface of the interfacial region.

It follows that in the conditions of constant temperature T, volume V and surface A of the interfacial region considered, its Helmholtz free energy $F = U - TS$ will evolve to the minimum value

$$[dF]_{T,V,n_i} = [dU - TdS - SdT = dU - Td_eS - Td_iS = dQ - Td_eS - Td_iS - PdV + \sigma dA_f]_{T,V,n_i} = -Td_iS \leq 0,$$

and its Gibbs free energy (enthalpy)

$$[dG]_{T,P,n_i} = [dH - TdS - SdT = dU + PdV + VdP - TdS - SdT = -SdT + VdP + \sigma dA_f]_{T,P,n_i} = -Td_iS \leq 0$$

will tend to the minimum in conditions of constant temperature T and pressure P. Herewith, the internal energy

$$[dU]_{S,V,n_i} = [Tds - PdV + \sigma dA_f]_{S,V,n_i} = -Td_iS \leq 0$$

will tend to the minimum value in conditions of maintaining a constant value of total entropy S by diverting its internal production to the external environment with $dS = 0$ at $d_iS = -d_eS$, which is also a direct consequence of the second law of thermodynamics.

3. For open systems with external exchange of both energy and substance, these ratios are supplemented by the term $(\sum \mu_j dn_j)$ which factors into the input of the substance transfer (diffusion) and quantifies the above analysis of the system entropy variation, while preserving the extreme principles of thermodynamic potentials, the minima of which are also points (conditions) of stable mechanical and diffuse equilibrium. It is generally essential to take account of the thermal stability conditions, the expression of which is the enthalpy tending to minimum, with keeping the values S, P, n_i:

$$[dH]_{S,P,n_i} = [dU + PdV + VdP = TdS + VdP + \sigma dA_f + \sum \mu_j dn_j]_{S,P,n_i} = -Td_iS \leq 0$$

constant, as well as of the chemical stability conditions in case of chemical reactions in the system, which, however, are not related to the additional specific extreme. The last conclusion follows from the Duhem–Jougeau theorem: the systems resistant to diffusion are resistant to chemical reactions as well [249]. As can be seen, the system state change in externally non-equilibrium conditions, aimed at achieving a stable equilibrium under the principle of thermodynamic potential minima, is related to the positive entropy production $d_iS \geq 0$ within the system itself due to irreversible processes occurring therein, which, however, occurs in isolated systems, thus determining achievement of their maximum entropy.

3.3. Stability of non-equilibrium states

Stability conditions of non-equilibrium systems can be considered on the same uniform basis, including of those with deterministic and spontaneous fluctuations of thermodynamic quantities and self-organization of dissipative regimes and structures. Herewith, the quadratic form $d_iS = \sum J_K dX_K$ is used as a common initial expression to describe entropy production in all irreversible processes according to [217]. It follows from the concept of entropy alteration in each irreversible process as the dX_K thermodynamic forces (gradients of thermodynamic potentials) multiplied by the J_K thermodynamic flows generated by them, for instance, the dQ heat flow under the action of the difference between thermal potentials $(1/T_1 - 1/T_2)$, the dn substance flow under the action of the difference between chemical potentials $(\mu_1 - \mu_2)$ etc. In this case, the synergetic principle of least energy scattering (dissipation), equivalent to Prigozhin's theorem on minimum entropy production in stationary linear systems, which was previously used heuristically in the analysis of limits of energy conversion in high-power facilities, may be assumed as a thermodynamic stability condition [218].

As shown in these papers, it is convenient to use the relative non-stationarity coefficient of the $\varepsilon = \langle \acute{E}(J_K X_K) \rangle / \acute{E}(J_{0K} X_{0K})$ form in order to generally estimate how dynamic perturbations of flows and forces effect the change in entropy production, as compared to their stationary values, and to identify the self-organization parameters on this basis. Herein, $\acute{E}(J_{0K} X_{0K}) = T\acute{S}$ is the value of energy dissipation (entropy production $\acute{S}$) in the system with stationary values of flows and forces, $\langle \acute{E}(J_K X_K) \rangle$ is the averaged value of this quantity in the system with perturbed flows and forces, determined by the standard rules of averaging. The value $\varepsilon = 1$ corresponds to the unperturbed stationary state (mode) of the non-equilibrium system; the values $-1 > \varepsilon > +1$ to the increased or reduced dissipative energy losses at various deviations from this mode. The mathematical formulation of the problem of mode stability and energy-entropy self-organization in this system is reduced to finding the lowest entropy generation value $\varepsilon = \varepsilon_{\min}$, depending on the parameters of disturbances. This is quite justifiable even for the systems which suppose a linear relation between thermodynamic flows and forces $J_K = \sum L_{Ki} X_i$,

in view of the general quadratic (bilinear) function of entropy production from the current flows and forces. In particular, the perturbation coefficient will be:

$$\varepsilon = \frac{L_{11}\langle X_1^2\rangle + 2L_{12}\langle X_1X_2\rangle + \langle X_{22}\rangle}{L_{11}X_{01}^2 + 2L_{12}X_{01}X_{02} + L_{22}X_{02}^2},$$

or

$$\varepsilon = \frac{\langle J_1X_1\rangle + \langle J_2X_2\rangle}{J_{01}X_{01} + J_{03}X_{02}}$$

if addressing the energy and substance flows jointly. Since perturbations generally represent an overlay (superposition) of deterministic and random processes, both options have been analyzed. The time averaging is chosen from the two equal averaging variants represented by the ergodic hypothesis of equality between average time and average statistical values of the functions, i.e. $\langle \acute{E}\rangle = \bar{E}$, where

$$\langle \acute{E}\rangle = \lim(1/\tau)\int_0^{\infty} E(\tau)d\tau, \quad \bar{E} = \int_{-\infty}^{+\infty} E\psi(E)dE$$

in case of deterministic periodic perturbations with one realizing function $E(\tau)$ and the statistical averaging $\bar{E}$ by the general aggregate or assemblage of random functions in case of random perturbations. Accordingly, τ is the period of oscillations; $\psi(E)$ is the density of the distribution probability of random disturbances. Thus, in the event of deterministic periodic oscillations of flows and forces, which can be considered as a harmonic process with random values of amplitude, frequency and phase $X_i(\tau) = X_{0i}[1 + n\sin(\omega_i\tau + \nu_i)]$, the averaged values will be: $\langle X_i(\tau)\rangle = X_{0i}^2[1 + n_i^2/2]$, $\langle X_1(\tau)X_2(\tau)\rangle = 0$ at $\omega_1 \neq \omega_2$ and $X_{01} = X_{02}[1 + n_1n_2\cos(\nu_1 - \nu_2)/2]$ at $\omega_1 = \omega_2$. According to the structure, these expressions are completely identical to the averaging results if perturbations of flows and forces are a purely chaotic fluctuation, for which the autocorrelation function of relation between two consecutive values in time is the δ-Dirac function, and the probability of distribution density of $\psi(X)$ random deviations from the average statistical value according to the central limit theorem of the probability theory is expressed as a normal Gaussian distribution law of corresponding dimension.

Similar results are obtained when it comes to any other laws of probability distribution for random deviations of variables from the statistically average values, since the averaged values $X_1^2(\tau)$, $X_2^2(\tau)$, $X_1(\tau)X_2(\tau)$ are quadratic functions, and the respective characteristics of their scattering are central moments of the second order, from the definition of which these structures result directly.

Minimization of expressions for ε leads to the identification of three successive system self-organization modes delimited by the roots of characteristic equation $\partial\varepsilon/\partial(n_1/n_2) = 0$. As follows from this analysis, the condition required for energetically efficient self-organization of the thermodynamic systems under consideration, along with achieving the minimum entropy production $\varepsilon = \varepsilon_{\min}$ in the range of $\varepsilon_{\min} \leq 1$, is the antiphase $(\nu_1 - \nu_2) = \pi$ feedback between the input and output flows (forces) carried out through forward and crossed conduction coefficients L_{Ki}. However, the value of this relation in linear systems with the disturbances considered is insufficient to compensate for dissipative energy losses, except for extremely conjugate systems with $q = L_{21}/(L_{11}L_{22})^{1/2} = 1$, where the maximum amplitude values of antiphase oscillations n_1, $n_2 = 1$ can be set at the same frequencies $\omega_i = \omega_j$. However, the conditions essential and sufficient for internal instability in linear systems can be realized at lower q values if both flows and forces are simultaneously exposed to disturbances. The amplitude-phase characteristics of their oscillations are set in the range of $0.5 \leq \varepsilon \leq 1.5$ where the maximum value $\varepsilon_{\max} = 1.5$ corresponds to the mode of in-phase oscillations of flows and forces $(\nu_1 - \nu_2) = 0$, $(\nu_3 - \nu_4) = 0$, and the lowest value $\varepsilon_{\min} = 0.5$ to the mode of antiphase oscillations $(\nu_1 - \nu_2) = \pi$, $(\nu_3 - \nu_4) = \pi$ with maximum values of their amplitudes. The negative correlation coefficient

$$\rho_{ij} = \pm\frac{\langle X_i(\tau)X_j(\tau)\rangle - \langle X_i(\tau)\rangle\langle X_j(\tau)\rangle}{\sigma_i\sigma_j},$$

where $\sigma_i = [\langle X_i^2(\tau)\rangle - \langle X_i(\tau)\rangle^2]^{1/2}$, $\sigma_j = [\langle X_j^2(\tau)\rangle - \langle X_j(\tau)\rangle^2]^{1/2}$ are dispersions of variables, with chaotic spontaneous fluctuations of thermodynamic flows and forces meets the latter condition.

The nature and areas of self-organization are more diverse in thermodynamic systems when taking account of nonlinear effects of the transfer at different levels – from the simplest quasi-linear relation between phenomenological coefficients and one or more forces (flows), to the most complex cases of highly nonlinear systems with oscillations of the dissipative function. However, the analysis of the resulting ratio does not reveal fundamental differences from the results presented. This is explained as follows. Although the numerator expression for the relative non-stationarity coefficient ε, allowing for nonlinearities, transits from quadratic forms characteristic of linear and quasi-linear systems with one or two real roots of the characteristic equation which delimit the self-organization

area, to forms of higher order which suppose a greater number of real roots and, accordingly, a greater number of self-organized states (modes), the number of positive roots that have a physical interpretation in the delimitation of modes does not increase. The latter is attributed to the fact that the number of sign reversals remains unchanged in the sequence of coefficients of the power polynomial in the expression for the non-stationarity coefficient when determining the dissipative function as accepted, in all cases of systems with a constant number of freedom degrees. Thus, in accordance with the Descartes rule, the uniform limit number of real positive roots of the polynomial is set and, therefore, the uniform global character of behavior of these systems is established with possible local patterns of nonlinearities in the range of complex roots.

4. Heat-and-mass transfer and kinetics of chemical reactions in materials with a high content of nonautonomous phases

A large content of nonautonomous phases is inherent in nanostructured materials, a formational characteristic of which are fractal self-organization processes in non-equilibrium systems [250]. They determine the metric-statistical self-similarity of different-scale composite structures with non-Euclidean (fractional) relation between the rate of increase in the number of elements considered and the increase in their consideration scale. This holds true for almost all synthesis techniques and methods for nanomaterials and is determined by the special role of energy and entropy characteristics of surface layers, by the correlation scale of the substance and energy transfer in different-sized macro-, micro- and nanostructured material units, as well as by the tolerance factor of their interface. Given that the transition (10 – 100 nm) layer from volumetric *3D* material to the two-dimensional *2D* surface may include several subsurface zones with gradual decrease of substance filling in the range of $3 > D > 2$ at sub-monolayer (0.5 – 1.5 nm) non-stoichiometric zone at the phase interface with dimension $2 > D > 1$, or even $1 > D > 0$, its properties are governed by a set of physical phenomena of three-dimensional volume, two-dimensional surface, and in some cases even of one-dimensional and point elements. This approach reveals an extensive rank of self-similar transition structures of fractional dimension, in which the internal energy determining the different physical properties of the material, may significantly increase not only by increasing the binding energy and the number of these bonds in the crystalline lattice, but also due to the influence of electrical and chemical surface potential, as well as due to the growth of the entropy factor. At the same time, the kinetic and dynamic characteristics of nanocomposite materials also change significantly, since the energy accumulation level that determines the rate of degradation processes therein is limited by the surface zone thickness, and the energy dissipation has a significantly higher rate in the surface layer than in the volume. This is confirmed by experimental observations of phase transitions on the surface of solids, by measurements of electrical strength and thermal conductivity in the volume and on the surface [251–253]. As shown in [254], a condition for fractal self-organization of non-equilibrium systems is achieving the threshold value of energy dissipation, starting from which the system internal irreversible processes and exchange with the environment are accompanied by excess of entropy return in comparison with its generation. An essential condition for these processes is that there is non-linear feedback between the system and the energy source, as well as fluctuations and bifurcations in the transitions between individual states of the system until it becomes stable with minimal entropy production.

The noted fundamental aspects in fractal ordering of nanostructured materials with a high content of nonautonomous phases are taken into account in the developed models to calculate the heat and mass transfer and chemical kinetics (substance and energy transfer) occurring under spatial and mass limitations of nonautonomous phases. They are analyzed in fractal (fractionally dimensioned) space on the basis of modified Fick / Fourier law and non-local coordinate and time transfer equation for fractional order derivatives in the micro-layered medium [255,256]. Herewith, the transition from whole-order derivatives to fractional-order ones is realized according to the Riemann–Liouville and Riesz–Weyl scheme after averaging the common equation of heat and substance propagation under the assumption that the thermal conductivity and mass transfer coefficients as random functions of the spatial coordinate in a micro-layered medium may be regarded as an integral operator. Its kernel in a statistically homogeneous medium is a product of Green's function which suits both the problem considered and the correlation ratio in averaging the initial equation. Given that the time and space intervals form the Hausdorff–Bezikovich set for the media of fractal structure with phenomena of spatial correlations and memory effect, this transition makes it possible to directly link the indicators of fractional derivatives with the respective ones of fractal dimension in time and space. As a result, without resorting to commonly used numerical methods (for instance, [257]), it is possible to derive the analytical model expressions for diffusion and temperature distribution problems [258], for instance, in classically shaped micro-inhomogeneous bodies (wires, films, plates, rods, bars, etc.), using well-known constructive models of regular fractal media with a regular geometric structure (Cantor comb $D < 1$; Koch snowflake $1 < D < 2$; Sierpinski sieve and fan, Menger square and sponge $2 < D < 3$), as well as walk models

with fractal generalization of Einstein's relation. Their equivalent parameters are close enough to replace the real pseudo-regular structures with a fractal model.

The obtained solutions occupy an intermediate position between relaxation and wave behavior in time, and lead to a power dependence on spatial arguments, which is confirmed by the experimental data obtained [259,260]. Thus, in the stationary case compared to the linear temperature distribution in the continuous homogeneous medium layer, the nonlinear temperature distribution with a bulge downward is inherent in the fractal micro-inhomogeneous medium layer dimensioned less than one (Cantor comb), and with a bulge upwards (Fig. 2) in the environment dimensioned more than one (Koch snowflake, Sierpinski sieve, Menger sponge), which is generally consistent with experimental results.

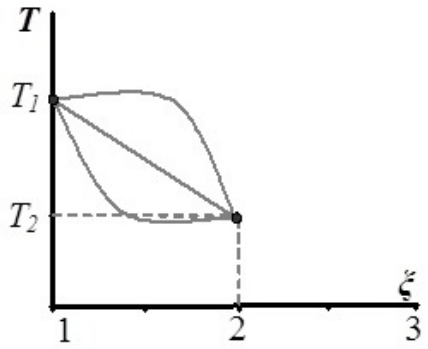

FIG. 2. Temperature distribution in a layer with a fractal structure: 1, 2, 3 – the nature of temperature distribution in a layer of a solid homogeneous medium, of a medium with a fractal dimension more or less than one, respectively [258]

However, it should be noted that this approach is sometimes insufficient to characterize the fractal structures of occasional nature, self-similarity of which cannot be adequately described using only one fractal (Hausdorff) dimension with a constant value, and which requires specifying the range of multifractal dimensions based on the generalized Renyi formula:

$$D_{Rq} = \lim_{\varepsilon\to 0}\lim_{\tau\to 0}\lim_{m\to 0}\left[\frac{1}{1-q}\frac{\ln I_{Rq}(q,\varepsilon)}{\ln(1/\varepsilon)}\right].$$

Herein, $I_{Rq}(q,\varepsilon) = \left[\sum_{i=1}^{M(\varepsilon)} p_i^q(\varepsilon)\right]$ is the generalized Renyi entropy of the q order; $M(\varepsilon)$ is the minimum number of "measuring" cubes with an ε edge required to cover the fractal in the *n*-dimensional phase coordinate space of the embedding; p_i is for the probabilities of visiting the *i*-th cube by the phase trajectory; m is the number of points used to estimate the dimension [261]. Known expressions for the Kolmogorov–Sinai entropy and Kolmogorov–Hausdorff fractal dimension ($q = 0$), Shannon entropy, and the corresponding information dimension ($q = 1$), correlation entropy, and correlation dimension ($q = 2$) follow from this relation as special cases at various q [262]. The change in fractal dimension along the layer of strongly micro-nonhomogeneous material can result in non-uniformity of its thermal and physical characteristics, as experimentally recorded in [263], and, consequently, in undulating temperature distribution (Fig. 3).

The proposed approach helped circumvent the limits of traditional macroscopic models of transfer processes in composite systems with relatively small filler concentrations and with no nonlocal effects of the influence of structural element scale on the rate of the transfer process. They are generalized in the well-known reference book [265] and are based on the generalized conductivity principle tracing its origin to the papers by Poisson, Clausius, Mossotti, Lorenz, Lorentz Maxwell, Rayleigh, Wiener, Lichtenecker, Odelevskii, etc.

One of the important integral effects of multifractal media in composite materials with electro-dual (conductive and non-conductive) components is that the coefficient of effective conductivity that occurs at the percolation threshold during formation of a conductivity chain cluster is independent of the specific arrangement of components when it is determined only by the ratio between their concentrations and electrical characteristics. The solutions obtained for the above models confirm the known results for the model of A. M. Dykhne [266] who identified this relation as $\sigma_e = [\sigma_1\sigma_2/p(1-p)]^{1/2}$, where σ_1 and σ_2 are conductivity values of the components, p and $(1-p)$ are their concentrations.

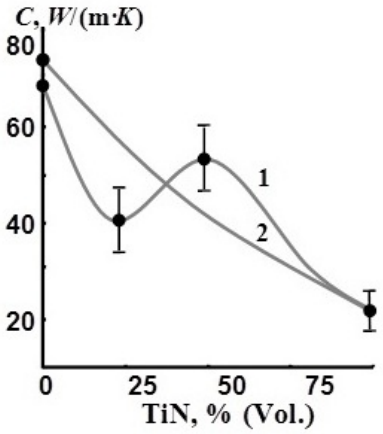

FIG. 3. Comparison of theoretical and measured values of thermal conductivity of sintered TiN–AlN composite: 1 – thermal conductivity determined on the basis of measurements at $T = 30$ °C; 2 – theoretical dependence for the "ideal" mixture of non-interacting components [264]

Modeling of chemical kinetics in the systems under consideration may also be carried out on the basis of nonequilibrium Prigozhin and Tribus's thermodynamic approach, using Janes's formalism for statistical interpretation of the results based on modern information theory in the stage-by-stage consideration of the processes presented in the experimental part of this review. These include the process of hydrothermal synthesis in autoclaves or in an electric underwater conductor explosion which is used to produce oxide nanopowders during high-temperature hydrolysis of precursor salts in the aqueous supercritical-pressure fluid capable of dissolving substances that are almost insoluble under normal conditions. The initial pH value of the medium, the synthesis duration and temperature, the system internal pressure value are basic parameters determining both the kinetics of the processes and the properties of the resulting products. Since the major cause of homogeneous particle aggregation, related to the surface tension at the phase interface, is absent under supercritical conditions, the supercritical water is able to dissolve substances which are almost insoluble under normal conditions, including some oxides [267–270]. Subsequently, the solid crystalline phase of oxide nanoparticles, of nearly the same size and with a fairly developed surface, is released if creating conditions for the solution oversaturation. The critical degree of oversaturation $\gamma = c/cs$ can be estimated by expressing the above chemical potential difference $\Delta\mu = 2\sigma(\infty)Va/R_{cr}$ of the critical nanoparticle nucleus and the phase-forming medium through the substance concentration in the supersaturated solution and its equilibrium solubility cs relative to the crystalline phase. This results in

$$\ln\gamma = \ln\left(\frac{c}{cs}\right) = \frac{\Delta\mu}{RT} = \frac{2\sigma(\infty)Va}{R_{cr}RT}$$

for the perfect solution. The critical size of the spherical nucleus R_{cr} results from the condition of the maximum $d(\Delta G)/dR = 0$ of the Gibbs free energy defined as the sum of its volume and surface components

$$\Delta G = -\frac{4}{3}\pi\frac{R^3\Delta\mu}{Va} + 4\pi R^2\sigma(R).$$

According to [271], it is

$$R_{cr} = \frac{2\sigma(\infty)Va}{\Delta\mu}$$

without factoring into the relation between the surface tension and the particle size, and

$$R_{cr} = l_0\left[1 - \frac{2\delta}{l_0} + \left(\frac{2\delta}{l_0} + 1\right)^{1/2}\right]$$

if it is factored into at small particle radii on the ratio $\sigma(R) \approx \sigma(\infty)/(1+2\delta/R)$ where $l_0 = \sigma(\infty)Va/\Delta\mu$, δ is the "tolmen length". The critical Gibbs energy at the maximum point during formation of homogeneous condensation nuclei on the surface of the nuclei emerging spontaneously as a result of fluctuations in the density and concentration of the substance in the system, without regard to the relation between the surface tension and the particle size, will be $\Delta G_{cr} = (4/3)2\pi R_{cr}(\sigma - 2/3\sigma)$, or a third of the surface energy of the nucleus. The remaining two-thirds are compensated by the chemical energy component determined by the energy benefit of phase transition. Herewith,

$\Delta\mu = 2\sigma(\infty)Va/R_{cr}$. Similarly, it is possible to make quantitative estimates for heterogeneous condensation in the new phase formation on existing surfaces (vessel walls, foreign substance particles – condensation nuclei), as well as it is also possible to estimate using the equation given in the liquid phase during solution supercooling, in view of the known relation $\Delta\mu = \Delta H_n - T\Delta S_n = \Delta H_n \Delta T/T_n$, where $\Delta T = (T_n - T)$ is supercooling, ΔH_n is the process enthalpy. These estimates show that the work of formation of solid nuclei at heterogeneous condensation will be as many times less than the work of a homogeneous process as the volume of the drop nucleus on the surface of the condensation nucleus is less than the volume of the sphere of the same curvature. These estimates relate only to a single nucleus and do not factor into the entropy component of the formation energy in the event of mass of nuclei. The entropy component can compensate the surface energy and provide spontaneous dispersion at low values of interfacial tension. Estimation of nucleus formation conditions in the nonautonomous substance state, [272–287], i.e. the substance being under spatial limitations that do not allow the formation of a critical nucleus of a new phase, in particular, due to the nanoparticles of another phase distributed in these media, is significantly complicated and requires factoring into the structure, composition and properties of the latter [106]. In case of classical nucleus forms (cube, ball, cylinder), it is possible to derive analytical expressions of the relation between their geometric characteristics and the size of the new-phase nucleus [105]. The kinetics of condensation formation of a new phase in hydrothermal synthesis, according to M. Folmer and J. I. Frenkel theory [288, 289], is defined as the rate of occurrence of condensation centers $I = A_1 \exp[-\Delta G_1/(RT)]$ and the rate of the substance transfer to the resulting condensation centers $U = A_2 \exp[-E_\eta/(RT)]$. The first of them is proportional to the probability of the condensation centers origin according to Gibbs energy ΔG_1, and the second is proportional to the probability of their "survival" according to the activation energy E_η of the substance transition from the initial phase to the nucleus surface. The total rate is determined by the product of these probabilities and can show an extreme, depending on the ratio between the energies ΔG_1, E_η, the temperature T and the proportionality coefficients A_1, A_2.

The applicability of the general thermodynamic approach to the estimation of homogeneous formation of small particles is limited by the condition of a significant excess of the specific surface energy

$$\sigma(R) \approx \frac{\sigma(\infty)}{1 + 2\delta/R}$$

over its mean-square fluctuations

$$\langle\langle \Delta\sigma \rangle 2\rangle = \frac{kT}{8\pi R}\left(\frac{\delta\sigma}{\partial R}\right)_{P,S} = \frac{kT\delta\sigma(\infty)}{4\pi R(R + 2\delta)^2}.$$

This is done in the case of $R \gg [kT\delta/\sigma(\infty)]^{1/3}$. Estimates show that the critical nucleus size may be $R_{cr} = (5 \div 10) \cdot 10^{-10}$ m at a low condensation temperature, that is, be sized as several atoms. In this case, ΔG will vary discretely when the next atom joins, which is incompatible with the thermodynamic theory assumption of continuous change of surface energy and Gibbs free energy. It is essential to shift towards the statistical nucleation theory, based on the interaction parameters for individual atoms and their agglomerates, for example, for Arrefyllius phases.

The kinetic features of nanomaterials production reactions considered in the experimental section of this review, for example, of nanomaterials produced on the basis of solid-phase synthesis technologies or solid-flame reactions of self-propagating high-temperature synthesis where combustion proceeds in the mode of reagent diffusion through a layer of solid products formed, are described satisfactorily enough by the above fractal-diffusion approach. The relationship between the traditional macroscopic characteristics of chemical kinetics and statistical interpretation of thermodynamic reaction parameters based on modern information theory is used for the model evaluation of the rate performance of chemical reactions in the nanomaterial synthesis by gas-flame combustion, occurring in the kinetic mode with the evaporation of solid or liquid reagents, as well as of the kinetics of their interaction with other chemicals. Thus, according to Eyring [290], under the assumption that the reaction rate r' in a chemically interacting system is proportional to the number of particles N_i with sufficient threshold energy E_i, where the total number of particles is N in the system, it is possible to derive well-known Arrhenius's ratio $r' \approx N \exp(-\beta E_i)$ after minimizing Shannon's expression for the information entropy $S = -k \sum p_i \ln p_i$ with additional conditions imposed on the sum of the probabilities of all possible particle states and the mathematical expectations of the macroscopic characteristics of the system. It is also possible to link

$$\frac{\partial(\ln r')}{\partial(1/kT)} = -E_i = -\frac{\Delta E}{N}$$

or

$$\frac{\partial(\ln r')}{\partial(1/T)} = -\frac{\Delta E}{R}$$

out of the Boltzmann distribution for the kinetic energy of molecules by its logarithm and differentiation by $\beta = 1/kT$, where ΔE is the activation energy. The resulting expression is of similar form with the known equation describing the change in the equilibrium constant with that in the temperature and enthalpy of the components, and the change in the free Gibbs energy $G = U + PV - TS$ through it, and then the change in the proportion of the reacted particles $\alpha = -\mu/RT$ of their total N_i. Herein, Gibbs chemical potential μ and Gibbs specific free energy (per particle) are coincident in case of the pure substance, while Gibbs free energy is defined as the sum of all components $G = \sum(\mu N)$ for all elements in case of the substance mixture.

The relationships presented also make it possible to determine the concurrent entropy variation S attributed to the ongoing chemical reactions and to assess the behavior of nonautonomous phases in non-equilibrium conditions, as well as to analyze the overall system stability in accordance with thermodynamic criteria presented earlier, involving the extreme principles.

5. Conclusion

Analysis of the problem of designing new functional materials with variable performance characteristics indicates a great role in its solution of special small-size micro- and nanoscale objects formed as intermediate (transitional) structures in a limited space between the macroscopic volume phases and with a limited substance amount. They differ greatly in their properties, structure and composition of the relevant characteristics from the volume phases and cannot thermodynamically exist in isolation from them as autonomous phases. It distinguishes fundamentally the nonautonomous phase from autonomous ones. This also determines the features of thermodynamics and kinetics of interaction of disproportionate structural units of substance in the material, the conditions of their self-organization and control methods for such interaction in the material synthesis, as important in fundamental and applied terms, but not always considered in the development of material technology.

Studying the behavior and properties of nonautonomous phases requires the use of various methods and approaches, in particular, theoretical and experimental methods of nonequilibrium thermodynamics, chemical kinetics, nonlinear dynamics and fractal analysis. The results presented show that great opportunities for providing the required functional properties of materials are related to the use of nanocomposites, which, as a rule, include a significant proportion of nonautonomous phases. The unifying characteristic of their formation in nonequilibrium systems is that of fractal self-organization. They determine the metric-statistical self-similarity of different-scale structures with non-Euclidean (fractional) relation between the rate of increase in the number of considered elements and the increase in the scale of consideration. This holds true for almost all technologies and methods for nanomaterial synthesis and is determined by the special role of energy and entropy characteristics of nonautonomous phases, the correlation scale of substance and energy transfer in different-sized macro-, micro- and nanostructured material units, as well as by the tolerance factor of their interface. At the same time, kinetic and dynamic characteristics of nanocomposite materials are also significantly changed, since the energy accumulation level, which determines the rate of degradation processes therein, is limited by the size of the border zone where the rate of energy dissipation is significantly greater than that in the volume. Achieving the threshold value of energy dissipation, starting from which irreversible processes are accompanied by excess of entropy return over its generation inside the system and in its exchange with the environment, is a condition of structural self-organization realized if there is nonlinear positive feedback from the energy source. Bifurcation transition of nonequilibrium systems to a stable state with minimal entropy production can be facilitated by antiphase deterministic and chaotic spontaneous fluctuations of thermodynamic flows and forces with negative correlation coefficient.

These factors generically determine the structural and energy approach to improve the design of functional materials with variable performance properties based on the use of nanoscale reaction zones with ongoing heat and mass transfer, chemical and phase transformations both in a relatively slow diffusion mode of hydrothermal or solid-phase high-temperature synthesis and in a high-speed kinetic mode of precursor medium combustion. Experimental studies of the effect of phase composition heterogeneity on the change in functional properties and stability of nanocomposite materials with a large proportion of nonautonomous phases generally confirm these ideas.

Promoting the concept of nonautonomous phases and their genesis in the areas discussed above opens up certain reserves for solving the problems of physical and chemical design of new functional nanocomposite materials which consist largely of nonautonomous phases, for developing technologies for their synthesis and consolidation, which ensure saving of the individual properties of nanoscale objects in the system.

References

[1] Almjasheva O.V., Gusarov V.V. The role of non-autonomous state in the formation of nanomaterials structure and properties. In *Nanomaterials: Properties and Potential Applications*, Moscow, Nauchnyi Mir, 2014, P. 384–409 (in Russian).

[2] Miyazaki C.M., Riul A. Low-Dimensional Systems: Nanoparticles. *Nanostructures*, 2017, **5**, P. 125–146.

[3] Rempel A.A. Nanotechnologies. Properties and applications of nanostructured materials. *Russ. Chem. Rev.*, 2007, **76** (5), P. 435–461.

[4] Vance M.E., Kuiken T., et al. Nanotechnology in the real world: Redeveloping the nanomaterial consumer products inventory. *J. Nanotechnol.*, 2015, **6** (1), P. 1769–1780.

[5] Byrappa K., Adschiri T. Hydrothermal technology for nanotechnology. *Progress in Crystal Growth and Characterization of Materials*, 2007, **53**, P. 117–166.

[6] Kirillova S.A., Almjashev V.I., Gusarov V.V. Phase relationships in the SiO_2–TiO_2 system. *Russ. J. Inorg. Chem.*, 2011, **56** (9), P. 1464–1471.

[7] Newnham R. Size effect and nonlinear phenomena in ferroic ceramics. *Editrice Iberica, Faenza*, 1993, **2**, P. 1–9.

[8] Dahman Y. Nanoparticles (Chapter 5). *Nanotechnology and Functional Materials for Engineers A volume in Micro and Nano Technologies*, 2017, P. 93–119 p.

[9] Gleiter H. Nanostructured materials: basic concepts and microstructure. *Acta Mater.*, 2000, **48** (1), P. 1–29.

[10] Kushnir S.E., Kazin P.E., Trusov L.A., Tretyakov Yu.D. Self-organization of micro- and nanoparticles in ferrofluids. *Russian Chemical Reviews*, 2012, **81** (6), P. 560–570.

[11] Ostroushko A.A., Russkikh O.V. Oxide material synthesis by combustion of organic-inorganic compositions. *Nanosystems: Phys. Chem. Math.*, 2017, **8** (4), P. 476–502

[12] Egorysheva A.V., Kuvshinova T.B., et al. Synthesis of high-purity nanocrystalline $BiFeO_3$. *Inorganic Materials*, 2013, **49** (3), P. 310–314.

[13] Popkov V.I., Almjasheva O.V., et al. Magnetic properties of $YFeO_3$ nanocrystals obtained by different soft-chemical methods. *Journal of Materials Science: Materials in Electronics*, 2017, **28** (10), P. 163–170.

[14] Mahalakshmi S., Srinivasa Manja K., Nithiyanantham S. Electrical properties of nanophase ferrites doped with rare earth ions. *J. Supercond. Nov. Magn.*, 2014, **27** (9), P. 2083–2088.

[15] Lomanova N.A., Gusarov V.V. Effect of surface melting on the formation and growth of nanocrystals in the Bi_2O_3–Fe_2O_3 system. *Russ. J. Gen. Chem.*, 2014, **83** (12) P. 2251–2253.

[16] Khaliullin Sh.M., Zhuravlev V.D., Bamburov V.G. Solution-combustion synthesis of $MZrO_3$ zirconates (M = Ca, Sr, Ba) in open reactor: thermodynamic analysis and experiment. *International Journal of Self-Propagating High-Temperature Synthesis*, 2017, **26** (2), P. 93–101.

[17] Krasilin A.A., Gusarov V.V. Control over morphology of magnesium-aluminum hydrosilicate nanoscrolls. *Russ. J. Appl. Chem.*, 2015, **88**, P. 1928–1935.

[18] Bandyopadhyay A.K. *Nano Materials*. New Age International (P) Ltd., Publishers, New Delhi, 2008, 321 p.

[19] Arkhipov D.I., Osmolovskaya O.M., et al. Optimization of CrO_2 magnetic characteristics in the process of hydrothermal synthesis using nucleating agents of complex structure. *Russ. J. Gen. Chem.*, 2016, **86** (4), P. 983–985.

[20] Sadovnikov S.I., Rempel A.A., Gusev A.I. Nanostructured silver sulfide: synthesis of various forms and their application. *Russ. Chem. Reviews*, 2018, **87** (4), P. 303–327.

[21] Aruna S.T., Mukasyan A.S. Combustion synthesis and nanomaterials. *Curr. Opin. Solid State Mater. Sci.*, 2008, **12** (3–4), P. 44–50.

[22] Gonzalez-Cortes S.L., Imbert F.E. Fundamentals, properties and applications of solid catalysts prepared by solution combustion synthesis (SCS). *Appl. Catal. A Gen.*, 2013, **452**, P. 117–131.

[23] Karn B., Kuiken T., Otto M. Nanotechnology and in Situ Remediation: A Review of the Benefits and Potential Risks. *Environ. Health Perspect*, 2009, **117** (12), P. 1823–1831.

[24] Lee J., Mahendra S., Alvarez P.J.J. Nanomaterials in the Construction Industry: A Review of Their Applications and Environmental Health and Safety Considerations. *ACS Nano*, 2010, **4** (7), P. 3580–3590.

[25] Coutinho P.V., Cunha F., Barrozo P. Structural, vibrational and magnetic properties of the orthoferrites $LaFeO_3$ and $YFeO_3$: A comparative study. *Solid State Communications*, 2017, **252**, P. 59–63.

[26] L'vov P.E., Svetukhin V.V. Thermodynamics of the phase equilibrium of multicomponent solid solutions containing nano-sized precipitates of the second phase. *Physics of the Solid State*, 2013, **55** (11), P. 2374–2380.

[27] Xu D., Johnson W.L. Geometric model for the critical-value problem of nucleation phenomena containing the size effect of nucleating agent. *Phys. Rev. B*, 2005, **72**, 052101.

[28] Khambaty S., Larson M.A. Crystal regeneration and growth of small crystals in contact nucleation. *I&EC Fundamentals*, 1978, **17** (3), P. 160–165.

[29] Tauson V.L., Akimov V.V. Effect of crystallite size on solid state miscibility: applications to the pyrite–cattierite system. *Gochimica et Cosmocimica Acta*, 1991, **55** (10), P. 2851–2859.

[30] Murdoch H.A., Schuh C.A. Stability of binary nanocrystalline alloys against grain growth and phase separation. *Acta Mater*, 2013, **61** (6), P. 2121–2132.

[31] Shmyt'ko I.M., Ganeeva G.R., Aronin A.S. Influence of grain boundaries on the formation of new structural states in simple rare-earth oxides. *Physics of the Solid State*, 2015, **57** (1), P. 136–141.

[32] Tsoga A., Nicolopoulos P. Surface and grain-boundary energies in yttria stabilized zirconia (YSZ –8 mol %). *J. Mater. Sci.*, 1996, **31** (20), P. 5409–5413.

[33] Vasiliev A.L., Poyato R., Padture N.P. Singlewall carbon nanotubes at ceramic grain boundaries. *Scripta Mater.*, 2007, **56** , P. 461–463.

[34] Ebeling W., Engel A., Feistel R. *Physik der Evolutionsprozesse*. Akademie-Verlag, Berlin, 1990, 371 p.

[35] Saber M., Kotan H., Koch C.C., Scattergood R.O. Thermodynamic stabilization of nanocrystalline binary alloys. *J. Appl. Phys.*, 2013, **113**, 063515.

[36] Rodionov I.A, Zvereva I.A. Photocatalytic activity of layered perovskite-like oxides in practically valuable chemical reactions. *Russ. Chem. Rev.*, 2016, **85** (3) P. 248–279.

[37] Bugrov A.N., Rodionov I.A., et al. Photocatalytic activity and luminescent properties of Y, Eu, Tb, Sm and Er-doped ZrO_2 nanoparticles obtained by hydrothermal method. *Int. J. Nanotechnology*, 2016, **13** (1/2/3), P. 147–157.

[38] De Prado N.T., Oliveir L.C.A. Nanostructured niobium oxide synthetized by a new route using hydrothermal treatment: High efficiency inoxidation reactions. *Applied Catalysis B: Environmental*, 2017, **205**, P. 481–488.
[39] Yang Q., Hu H., Wang S.S. Preparation and desulfurization activity of nano-CeO_2/γ-Al_2O_3 catalysts. *Rare Met.*, 2018, **37**, P. 554–560.
[40] Al'myasheva O.V, Vlasov E.A., Khabenskii V.B., Gusarov V.V. Thermal stability and catalytic properties of the composite amorphous Al_2O_3-nanocrystals ZrO_2. *Russ. J. Appl. Chem.*, 2009, **82** (2) P. 217–221.
[41] Livage J. Sol–gel synthesis of heterogeneous catalysts from aqueous solutions. *Catalysis Today*, 1998, **41** (1–3), P. 3–19.
[42] Li X., Tang C.J., et al. Controllable synthesis of pure-phase rare-earth orthoferrites hollow spheres with a porous shell and their catalytic performance for the CO+NO reaction. *Chem. Mater.*, 2010, **22**, P. 4879–4889.
[43] Grabowska E. Selected perovskite oxides: Characterization, preparation and photocatalytic properties – A review. *Applied Catalysis B: Environmental*, 2016, **186**, P. 97–126.
[44] Iglesia E., Barton D.G., et al. Bifunctional pathways in catalysis by solid acids and bases. *Catalysis Today*, 1997, **38** (3), P. 339–360.
[45] Chen X., Liang S.-J., et al. Self-propagating combustion synthesis of nanocrystalline yttrium iron oxide solid solution photocatalysts. *Chinese J. Inorg. Chem.*, 2009, **25** (11), P. 1922–1927.
[46] Niu X.S., Li H.H., Liu G.G. Preparation, characterization and photocatalytic properties of $REFeO_3$ (RE = Sm, Eu, Gd). *J. Mol. Catal. A: Chem.*, 2005, **232** (1–2), P. 89–93.
[47] Wu R., Xie P., et al. Hydrothermally prepared Cr_2O_3–ZrO_2 as a novel efficient catalyst for dehydrogenation of propane with CO_2. *Catalysis Communications*, 2013, **39**, P. 20–23.
[48] Lee J., Jeon H., et al. Morphology-dependent phase transformation of γ-Al_2O_3. *Applied Catalysis A: General*, 2015, **500**, P. 58–60.
[49] Falconer K.J. *Fractal geometry. Mathematical foundations and applications*. John Wiley & Sons, New York, 1990, 337 p.
[50] Lau K.-S., Ngai S.-M. Multifractal measures and a weak separation condition. *Advances in mathematics*, 1999, **141**, P. 45–96.
[51] Ni H., Zhang L., et al. Supercritical fluids at subduction zones: Evidence, formation condition, and physicochemical properties. *Earth-Science Reviews*, 2017, **167**, P. 62–71.
[52] Kefeni K.K., Msagati T.A.M., Mamba B.B. Ferrite nanoparticles: Synthesis, characterisation and applications in electronic device. *Materials Science and Engineering: B*, 2017, **215**, P. 37–55.
[53] Ahmad T., Lone I.H., et al. Multifunctional properties and applications of yttrium ferrite nanoparticles prepared by citrate precursor route. *Materials & Design*, 2017, **126**, P. 331–338.
[54] Karouia F., Boualleg M., Digne M., Alphonse P. The impact of nanocrystallite size and shape on phase transformation: Application to the boehmite/alumina transformation. *Advanced Powder Technology*, 2016, **27** (4), P. 1814–1820.
[55] Zhuravlev V.D., Lobachevskaya N.I., et al. New Vanadium Germanium Garnets. *Doklady Chemistry*, 2018, **479** (2), P. 45–48.
[56] Nakayama S. $LaFeO_3$ perovskite-type oxide prepared by oxide mixing, co-precipitation and complex synthesis methods. *Journal of Material science*, 2011, **36**, P. 5643–5648.
[57] Hakuta Y., Hayashi H., Arai K. Fine particle formation using supercritical fluids. *Current Opinion in Solid State and Materials Science*, 2003, **7** (4–5), P. 341–351.
[58] Racu A.V., Ursu D.H., et al. Direct low temperature hydrothermal synthesis of $YFeO_3$ microcrystals. *Mater. Lett.*, 2015, **140**, P. 107–110.
[59] Tugova E.A., Zvereva I.A. Formation Mechanism of $GdFeO_3$ nanoparticles under the hydrothermal conditions. *Nanosystems: Phys. Chem. Math.*, 2013, **4** (6), P. 851–856.
[60] Chislova, I.V., Matveeva A.A., Volkova A.V., Zvereva I.A. Sol-gel synthesis of nanostructured perovskite-like gadolinium ferrites. *Glass Phys. Chem.*, 2011, **37** (6), P. 653–660.
[61] Mukasyan A.S., Rogachev A.S. Combustion synthesis: mechanically induced nanostructured materials. *J. Mater. Sci.*, 2017, **52**, P. 11826–11833.
[62] Komlev A.A., Vilezhaninov E.F. Glycine-nitrate combustion synthesis of nanopowders based on nonstoichiometric magnesium-aluminum spinel. *Russ. J. Appl. Chem.*, 2013, **86** (9) P. 1344–1350.
[63] Bubnova R.S., Firsova V.A., Volkov S.N., Filatov S.K. Rietveldtotensor: Program for processing powder X-Ray diffraction data under variable conditions. *Glass Phys. Chem.*, 2018, **44** (1), P. 33–40.
[64] Berezhnaya M.V., Al'myasheva O.V., et al. Sol-gel synthesis and properties of $Y_{1-x}Ba_xFeO_3$ nanocrystals. *Russ. J. Gen. Chem.*, 2018, **88** (4), P. 626–631.
[65] Livage J., Sanchez C. Towards a soft and biomimetic nanochemistry. *Actualite Chimique*, 2005, **290–291**, P. 72–76.
[66] Van-der-Vaal's I.D., Konstamm F. Lehrbuch der Thermodynamik. Maas and van Suchtelen. *Leipzig*, 1908, **1**, 207.
[67] Samsonov V.M., Murav'ev S.D., Bazulev A.N. Surface characteristics, structure and stability of nanosized particles. *Russ. J. Phys. Chem. A*, 2000, **74** (11), P. 1791–1795.
[68] Magomedov M.N. Dependence of the surface energy on the size and shape of a nanocrystal. *Physics of the Solid State*, 2004, **46** (5), P. 954–968.
[69] Tolman R.C. The effect of droplet size on surface tension. *J. Chem. Phys. A*, 1949, **17** (203), P. 333–337.
[70] Bykov T.V., Shchekin A.K. Surface tension, tolman length, and effective rigidity constant in the surface layer of a drop with a large radius of curvature. *Inorg. Mater.*, 1999, **35** (6), P. 641–644.
[71] Krasnenko T.I., Rotermel M.V., Samigullina R.F. Stabilizing the associated non-autonomous phase upon thermal expansion of $Zn_2V_2O_7$. *Russ. J. Inorg. Chem.*, 2017, **62** (4), P. 413–417.
[72] Tovbin Yu.K. Lower size boundary for the applicability of thermodynamics. *Russ. J. Phys. Chem. A*, 2012, **86** (9), P. 1356–1369.
[73] Almjasheva O.V., Gusarov V.V. Metastable clusters and aggregative nucleation mechanism. *Nanosystems: Phys. Chem. Math.*, 2014, **5** (3), P. 405–417.
[74] Neiman A.Ya., Uvarov N.F., Pestereva N.N. Solid state surface and interface spreading: An experimental study. *Solid State Ionics*, 2007, **177** (39–40), P. 3361–3369.
[75] Gusarov V.V. The thermal effect of melting in polycrystalline systems. *Thermochim. Acta*, 1995. **256** (2), P. 467–472.
[76] Andrievski R.A. Review of thermal stability of nanomaterials. *J. Mater. Sci.*, 2014, **49** (4), P. 1449–1460.
[77] Zhao M., Jiang Q. Melting and surface melting of low–dimensional in crystals. *Solid State Communication*, 2004, **130**, P. 37–39.
[78] Gusarov V.V. Statics and dynamics of systems based on polycrystalline refractory oxides. Sc. D. Thesis, St. Petersburg State Technological Institute (Technical University), St. Petersburg, 1996, 44 p. (in Russian).

[79] Gusarov V.V., Suvorov S.A. Transformations of nonautonomous phases and densification of polycrystalline systems. *Journal of Applied Chemistry of the USSR*, 1992, **65** (7), P. 1227–1235.
[80] Gusarov V.V. Kinetic features of heat effect of melting in polycrystalline systems. *Russ. J. Appl. Chemistry*, 1994, **67** (3), P. 364–366.
[81] Gusarov V.V., Suvorov S.A. Rapid thermal packing of materials. *Russ. J. Appl. Chem.*, 1993, **66** (3), P. 431–437
[82] Gusarov V.V., Suvorov S.A. Thickness of 2-dimentional nonautonomous phases in local equilibrium polycrystalline systems based on a single bulk phase. *Russ. J. Appl. Chem.*, 1993, **66** (7), P. 1212–1216.
[83] Kikuchi R., Cahn J.W. Grain boundary melting transition in a two dimensional lattice gas model. *Phys. Rev. B*, 1980, **21** (5), P. 1893–1897.
[84] Gusarov V.V., Popov I.Yu. Flows in two-dimensional nonautonomous phases in polycrystalline systems. *Nuovo Cim. D*, 1996, **18** (7), P. 799–805.
[85] Levitas V.I. Effect of the ratio of two nanosize parameters on the phase transformations. *Scripta Materialia*, 2018, **192**, P. 155–162.
[86] Frenken J.W.M, van der Veen J.F. Observation of surface melting. *Phys. Rev. Lett.*, 1985, **54**, P. 134–141.
[87] Dash J.G. Surface melting. *Contemp. Phys.*, 1989, **30** (2), P. 89–100.
[88] Zhou F., Lee J., Dallek S., Lavernia E.J. High grain size stability of nanocrystalline Al prepared by mechanical attrition. *J. Mater. Res.*, 2001, **16**, P. 3451–3458.
[89] Zhou F., Lee J., Lavernia E.J. Grain growth kinetics of a mechanically milled nanocrystalline Al. *Scripta Materialia*, 2001, **44** (8–9), P. 2013–2017.
[90] Rao C.N.R. Kinetics and thermodynamics of the crystal structure transformation of spectroscopically pure anatase to rutile. *Can. J. Chem.*, 1961, **39**, P. 498–500.
[91] Etters R.D., Kaelberer J. Character of melting transition in small atomic aggregates. *J. of Chemical Physics*, 1977, **66** (11), P. 5112–5116.
[92] Zhou Z., Guo L., et al. Hydrothermal synthesis and magnetic properties of multiferroic rare-earth orthoferrites. *Journal of Alloys and Compounds*, 2014, **583**, P. 21–31.
[93] Mendona E.C., Tenório M.A., et al. Intrinsic dependence of the magnetic properties of $CoFe_2O_4$ nanoparticles prepared via chemical methods with addition of chelating agents. *J. Magn. Magn. Mater.*, 2015, **395**, P. 345–349.
[94] Davar F., Hassankhani A., Loghman-Estarki M.R. Controllable synthesis of metastable tetragonal zirconia nanocrystals using citric acid assisted sol–gel method. *Ceramics International*, 2013, **39** (3), P. 2933–2941.
[95] Bachina A., Ivanov V.A., Popkov V.I. Peculiarities of $LaFeO_3$ nanocrystals formation via glycine-nitrate combustion. *Nanosystems: Phys. Chem. Math.*, 2017, **8** (5), P. 647–653.
[96] Phokha S., Pinitsoontorn S., Maensiri S., Rujirawat S. Structure, optical and magnetic properties of $LaFeO_3$ nanoparticles prepared by polymerized complex method. *J. Sol-Gel science and technology*, 2014, **71** (2), P. 333–341.
[97] Proskurina O.V., Tomkovich M.V., et al. Formation of nanocrystalline $BiFeO_3$ under hydrothermal conditions. *Russ. J. Gen. Chem.*, 2017, **87** (11), P. 2507–2515.
[98] Dyachenko S.V., Martinson K.D., Cherepkova I.A. Particle size, morphology, and properties of transition metal ferrospinels of the MFe_2O_4 (M = Co, Ni, Zn) type, produced by glycine-nitrate combustion. *Russ. J. Appl. Chem.*, 2016, **89** (4), P. 417–421.
[99] Martinson K.D., Kondrashkova I.S., Popkov V.I. Synthesis of $EuFeO_3$ nanocrystals by glycine-nitrate combustion method. *Russ. J. Appl. Chem.*, 2017, **90** (8), P. 980–985.
[100] Kurdyukov D.A, Eurov D.A., et al. High-surface area spherical micro-mesoporous silica particles. *Microporous Mesoporous Mater.*, 2016, **223**, P. 225–229.
[101] Dideikin A.T., Aleksenskii A.E., et al. Rehybridization of carbon on facets of detonation diamond nanocrystals and forming hydrosols of individual particles. *Carbon*, 2017, **122**, P. 737–745.
[102] Van-der-Vaal's I.D., Konstamm F. *Course of Thermostatics*. Moscow, ONTI, 1936, 452 p. (in Russian).
[103] Defay R., Prigogine I. *Tension superficielle et adsorption*. Desoer, Liege, 1951, 295 p.
[104] Defay R., Prigogine I., Sanfeld A. Surface thermodynamics. *J. Colloid Interface Sci.*, 1977, **58** (3), P. 498–510.
[105] Al'myasheva O.V., Gusarov V.V. Features of the phase formation in the nanocomposites. *Russ. J. Gen. Chem.*, 2010, **80** (3), P. 385–390.
[106] Al'myasheva O.V., Gusarov V.V. Nucleation in media in which nanoparticles of another phase are distributed. *Dokl. Phys. Chem.*, 2009, **424** (2), P. 43–45.
[107] Popkov V.I., Almjasheva O.V., Gusarov V.V. The investigation of the structure control possibility of nanocrystalline yttrium orthoferrite in its synthesis from amorphous powders. *Russ. J. Appl. Chem.*, 2014, **87** (10), P. 1417–1421.
[108] Bejan A. Review: J.D. Lewins, Thermodynamics: Frontiers and Foundations. 2009. URL: www.oecd-nea.org/dbprog/documents/Lewins_book_review.pdf.
[109] Hansen R.S. *Surface and colloid science*. Wiley, New York, 1969, 1, 260 p.
[110] Rusanov A.I. *Phase equilibria and surface phenomena*. Khimiya, Leningrad (1967). 388 p. (in Russian).
[111] Rusanov A.I. *Thermodynamic fundamentals of mechanochemistry*. Nauka, St. Petersburg, 2006, 221 p. (in Russian).
[112] Grinfeld M.A. *Methods of continuum mechanics in theory of phase transformations*. Nauka, Moscow, 1990, 312 p. (in Russian).
[113] Fletcher N.H. Surface structure of water and ice. *Phil. Mag.*, 1962, **7**, P. 255–259.
[114] Gilpin R.R. Wire regelation at low temperatures. *Journal of Colloid and Interface Science*, 1980, **77** (2), P. 435–448.
[115] Clarke D.R. On the equilibrium thickness of intergranular glass phases in ceramic materials. *J. Am. Ceram. Soc.*, 1987, **70**, P. 15–22.
[116] Dash J.G. Thermomolecular pressure in surface melting: Motivation for frost heave. *Science*, 1989, **246**, P. 1591–1593.
[117] Gusarov V.V., Suvorov S.A. Melting points of locally equilibrium surface phases in polycrystalline systems based on a single volume phase. *J. Appl. Chem. of the USSR*, 1990, **63** (8), P. 1560–1565.
[118] Gusarov V.V. Fast solid-phase chemical reactions. *Zhurnal Obshchei Khimii*, 1997, **67** (12), P. 1959–1964.
[119] Almjasheva O.V. Heat-stimulated transformation of zirconium dioxide nanocrystals produced under hydrothermal conditions. *Nanosystems: Phys. Chem. Math.*, 2015, **6** (5), P. 697–703.
[120] Vasilevskay A.K., Almjasheva O.V., Gusarov V.V. Peculiarities of structural transformations in zirconia nanocrystals. *Journal of Nanoparticle Research*, 2016, **18**, P. 188–198.
[121] Almjasheva O.V. Formation and structural transformations of nanoparticles in the TiO_2–H_2O system. *Nanosystems: Phys. Chem. Math.*, 2016, **7** (6), P. 1031–1049.

[122] Murin I.V., Smirnov V.M., et al. Structural chemical transformations of α-Fe_2O_3 upon transport reduction. *Solid State Ionics*, 2000, **133**, P. 203–210.
[123] Zhang H., Banfield J. New kinetic model for the nanocrystalline anatase-to-rutile transformation revealing rate dependence on number of particles. *American Mineralogist*, 1999, **84** (4), P. 528–535.
[124] Bascom W.D., Cottington R.L., Singleterry C.R. *Dynamic surface phenomena in the spontaneous spreading of oils on solids*. American Chemical Society, Washington, DC, 1964, P. 355–379.
[125] Yannis K., Tassos B. Stability and dynamics of nonautonomous systems with pulsed nonlinearity. *Phys. Rev. E*, 2013, **88** (4), 042924.
[126] Gilpin R.R. A model for the prediction of ice lensing and frost heave in soils. *Water Resour. Res.*, 1980, **16** (5), P. 918–930.
[127] Nair R.R., Wu H.A., et al. Unimpeded permeation of water through helium-leak–tight graphene-based membranes. *Science*, 2012, **335**, P. 442–444.
[128] Murase Y., Kato E. Role of water vapour in crystallite growth and tetragonal – monoclinic phasetransformation of ZrO_2. *J. Am. Cream. Soc.*, 1983, **66** (3), P. 196–200.
[129] Wood G.R., Walton A.G. Homogeneous nucleation kinetics of ice from water. *J. Appl. Phys.*, 1970, **41** (7), P. 3027–3036.
[130] Findenegg G.H., Jhnert S., Akcakayiran D., Schreiber A. Freezing and melting of water confined in silica nanopores. *Chemphyschem.*, 2008., **9** (18), P. 2651–2659.
[131] Lee Penn R., Banfield J. Oriented attachment and growth, twinning, polytypism and formation of metastable phases; insights from nanocrystalline TiO_2. *American Mineralogist*, 1998, **83** (9–10), P. 1077–1082.
[132] Grulke E.A., Yamamoto K., et al. Size and shape distributions of primary crystallites in titania aggregates. *Advanced Powder Technology*, 2017, **28** (7), P. 1647–1659.
[133] Tugova E.A., Karpov O.N. Nanocrystalline perovskite-like oxides formation in Ln_2O_3 – Fe_2O_3 – H_2O (Ln = La, Gd) systems. *Nanosystems: Phys. Chem. Math.*, 2014, **5** (6), P. 854–860.
[134] Reiss H., Katz J.L., Cohen E.R. Translation-rotation paradox in the theory of nucleation. *J. Chem. Phys.*, 1968, **48** (12), P. 5553–5560.
[135] Blinova I.V., Gusarov V.V., Popov I.Yu. A model of irregular impurity at the surface of nanoparticle and catalytic activity. *Commun. Theor. Phis.*, 2012, **58** (1), P. 55–58.
[136] Tammann G. Über die abhngigkeit der zahl der kerne, welche sich in verschiedenen unterkhltenflssigkeiten bilden, von der temperature. *Zeit. f. Physik. Chemie*, 1898, **25**, P. 441.
[137] Tammann G. *Aggregatzustände*. Verlag von Leopold Voss, Leipzig, 1922, 237 p.
[138] Gusarov V.V., Suvorov S.A. Autocatalytic solid-phase reaction of chrysoberyl formation. *Zhurnal obshchei Khimii*, 1988, **58** (4), P. 932–934.
[139] Gusarov V.V., Suvorov S.A. Transformation and transport processes in polycrystalline systems and creep of materials. *Journal of Applied Chemistry of the USSR*, 1992, **65** (10), P. 1961–1964 (in Russian).
[140] Gusarov V.V., Malkov A.A., Malygin A.A., Suvorov S.A. Thermally activated transformations of 2D nonautonomous phases and contradiction of polycrystalline oxide materials. *Inorganic Materials*, 1995, **31** (3), P. 320–323.
[141] Zvereva I.A., Otrepina I.V., et al. Mechanism of formation of the complex oxide $Gd_2SrFe_2O_7$. *Russ. J. Gen. Chem.*, 2007, **77** (6), P. 973–978.
[142] Tugova E.A., Gusarov V.V. Peculiarities of layered perovskite-related $GdSrFeO_4$ compound solid state synthesis. *Journal of Alloys and Compounds*, 2011, **509** (5), P. 1523–1528.
[143] Chupakhina T.I., Melkozerova M.A., Bazuev G.V. Phase formation features and magnetic properties of complex oxides in the systems Sr–Co–M–O (M = Zn, Cu). *Russ. J. Inorg. Chem.*, 2013, **58** (3), P. 253–258.
[144] Tugova E.A. New $DySrAlO_4$ compound synthesis and formation process correlations for $LnSrAlO_4$ (Ln = Nd, Gd, Dy) series. *Acta Metallurgica Sinica (English Letters)*,2016, **29**(5), P. 450–456.
[145] Morozov M.I., Lomanova N.A., Gusarov V.V. Specific features of $BiFeO_3$ formation in a mixture of bismuth (III) and iron (III) oxides. *Russ. J. Gen. Chem.*, 2003, **73** (11), P. 1676–1680.
[146] Tugova E.A., Gusarov V.V. Processing stages of $Gd_2Sr(Al_{1-x}Fe_x)_2O_7$ series. *Rare Metals*, 2014, **33** (1), P. 47–53.
[147] Boldyrev V.V. Reactivity of solids. *J. of Thermal Analysis*, 199, **40**, P. 1041– 1062.
[148] Baranchikov A.Ye., Ivanov V.K., Tretyakov Yu.D. Kinetics and mechanism of nickel ferrite formation under high temperature ultrasonic treatment. *Ultrasonics Sonochemistry*, 2007, **14** (2), P. 131–134.
[149] Tretyakov Yu.D. Self-organisation processes in the chemistry of materials. *Russ. Chem. Rev.*, 2003, **72** (8), P. 651–679.
[150] Kalinin S.V., Vertegel A.A., Oleynikov N.N., Tretyakov Y.D. Kinetics of solid state reactions with fractal reagent. *J. Mater. Synth. Process*, 1998, **6** (5), P. 305–309.
[151] Khvostova L.V., Volkova N.E., Gavrilova L.Ya, Cherepanov V.A. Crystal structure, oxygen nonstoichiometry and properties of novel Ruddlesden-Popper phase $Sm_{1.8}Sr_{1.2}Fe_2O_7$-δ. *Materials Letters*, 2018, **213**, P. 158–161.
[152] Yi L., Liu X.Q., Chen X.M. Crystal structure and infrared reflection spectra of $SrLn_2Al_2O_7$ (Ln = La, Nd, Sm) microwave dielectric ceramics. *Int. J. Appl. Ceram. Technol.*, 2015, **12** (3), P. E33—E40.
[153] Chupakhina T.I., Mel'nikova N.V., Yakovleva E.A., Nikitina Yu.A. $La_{1.8}Sr_{0.2}Ni_{0.8}M_{0.2}O_4$ (M = Fe, Co, or Cu) complex oxides: synthesis, structural characterization, and dielectric properties. *Russ. J. Inorg. Chem.*, 2018, **63** (2), P. 141–148.
[154] Fan X. Ch., Chen X. M., Liu X. Qi. Structural dependence of microwave dielectric properties of $SrRAlO_4$ (R = Sm, Nd, La) ceramics: crystal structure refinement and infrared reflectivity study. *Chem. Mater.*, 2008, **20**, P. 4092–4098.
[155] Tugova E.A. P/RS intergrowth type phases in the Ln_2O_3–MO–Al_2O_3 systems. *Russ. J. Gen. Chem.*, 2016, **86** (11), P. 2410–2417.
[156] Karita R., Kusaba H., Sasaki K., Teraoka Y. Superiority of nitrate decomposition method for synthesis of K_2NiF_4-type $La_xSr_{2-x}MnO_4$ catalysts. *Catalysis Today*, 2007, **126**, P. 471–475.
[157] Zhou J., Chen Y., Chen G., Wu K., Cheng Y. Evaluation of $La_xSr_{2-x}FeO_4$ layered perovskite as potential electrode materials for symmetrical solid oxide fuel cells. *Journal of Alloys and Compounds*, 2015, **647**, P. 778–783.
[158] Liu Y.Y., Chen X.M., Liu X.Q. Magnetic properties and magnetoresistance of polycrystalline $SrLaCoO_4$. *Solid State Communications*, 2005, **136**, P. 576–579.
[159] Liu X.Q., Lü X.J., Chen X.M., Lü G.L. Structures and electrical conductivity of $CaNdFeO_4$ ceramics. *J. Electroceram.*, 2008, **21**, P. 487–490.

[160] Patel R., Simon Ch., Weller M.T. $LnSrScO_4$ (Ln, La, Ce, Pr, Nd and Sm) systems and structure correlations for A_2BO_4 (K_2NiF_4) structure types. *J. Solid State Chem.*, 2007, **180**, P. 349–359.
[161] Ganguli D. Cationic radius ratio and formation of K_2NiF_4-type compounds. *J. Solid State Chem.*, 1979, **30**, P. 353–356.
[162] Tugova E.A., Klyndyuk A.I., Gusarov V.V. Synthesis of solid solutions of double layered Ruddlesden–Popper phases in the Gd_2O_3-SrO-Fe_2O_3-Al_2O_3 system. *Russian Journal of Inorganic Chemistry*, 2013, **58** (7), P. 848–854.
[163] Tugova E.A., Bobrysheva N.P., Selyutin A.A., Gusarov V.V. Magnetic Properties of Complex Oxides $Gd_2SrM_2O_7$ (M = Fe, Al). *Russ. J. Gen. Chem.*, 2008, **78** (11), P. 2000–2001.
[164] Zvereva I., Smirnov Yu., et al. Complex aluminates $RE_2SrAl_2O_7$ (RE = La, Nd, Sm–Ho): Cation ordering and stability of double perovskite slab-rocksalt layer P_2/RS intergrowth. *J. Solid State Sci.*, 2003, **5**, P. 343–349.
[165] Chupakhina T.I., Melnikova N.V., Gyrdasova O.I. Synthesis, structural characteristics and dielectric properties of a new K_2NiF_4-type phase $Sr_2Mn_{0.5}Ti_{0.5}O_4$. *Journal of Alloys and Compounds*, 2016, **670**, P. 105–112.
[166] Chupakhina T.I, Bazuev G.V. Synthesis and magnetic properties of $LaSr_2CoMnO_7$. *Russ. J. Inorg. Chem.*, 2008, **53** (5), P. 681–685.
[167] Aksenova T.V., Vakhromeeva A.E., et al. Phase equilibria, crystal structure, oxygen nonstoichiometry and thermal expansion of complex oxides in the Nd_2O_3 – SrO – Fe_2O_3 system. *J. Solid State Chem.*, 2017, **251**, P. 70–78.
[168] Feng J., Wan Ch., et al. Calculation of the thermal conductivity of $L_2SrAl_2O_7$ (L = La, Nd, Sm, Eu, Gd, Dy). *Phys. Rev. B*, 2011, **84**, 024302.
[169] Tugova E.A. A comparative analysis of the processes of formation of Ruddlesden-Popper phases in the La_2O_3–SrO–M_2O_3 (M= Al, Fe) Systems. *Glass Physics and Chemistry*, 2009, **35** (4), P. 422–428.
[170] Zvereva I.A., Tugova E.A., et al. The impact of Nd^{3+}/La^{3+} substitution on the cation distribution and phase diagram in the $La_2SrAl_2O_7$–$Nd_2SrAl_2O_7$ system. *Chimica Techno Acta*, 2018, **5** (1), P. 80–85.
[171] Petrosyan A.G., Popova V.F., et al. The Lu_2O_3–Al_2O_3 system: relations for equilibrium-phase and supercooled states. *J. Cryst. Growth*, 2006, **293**, P. 74–77.
[172] Zvereva I.A., Pylkina N.S., et al. Phase equilibria in the Gd_2O_3–$SrAl_2O_4$ system. *Glass Physics and Chemistry*, 2005, **31** (6), P. 808–811.
[173] Popova V.F., Tugova E.A., Gusarov V.V., Zvereva I.A. Phase equilibria in the $LaAlO_3$–$LaSrAlO_4$ system. *Glass Physics and Chemistry*, 2004, **30** (6), P. 564–567.
[174] Kovalenko A.N. High-temperature superconductivity: From macro- to nanoscale structures. *Nanosystems: Phys. Chem. Math.*, 2016, **7** (6), P. 941–970.
[175] Novoselov A.V., Drobot D.V. Synthesis of substrate materials based on rare-earth-containing mixed-oxide solid solutions for epitaxy of high-Tc superconductors. *Inorganic Materials*, 2009, **45** (6), P. 589–595.
[176] Zvereva I.A., Reznitskii L.A., Filippova S.E. Thermochemical and structural aspects of the stability of lamellar structures. *Russ. J. Gen. Chem.*, 2004, **74** (5), P. 659–662.
[177] Pajaczkowska A., Novosselov A.V., Zimina G.V. On the dissociation and growth of $SrLaGaO_4$ and $SrLaAlO_4$ single crystals. *Journal of Crystal Growth*, 2001, **223**, P. 169–174.
[178] Smirnov Yu.E., Zvereva I.A. Cation distribution and interatomic interactions in oxides with heterovalent isomorphism: III.1 Complex aluminates $LnCaAlO_4$ (Ln = Y, La, Nd, Gd, Ho, Er, Yb). *Russ. J. Gen. Chem.*, 2001, **71** (6), P. 845–852.
[179] Chen X.M., Xiao Y., Liu X.Q., Hu X. $SrLnAlO_4$ (Ln Nd and Sm) microwave dielectric ceramics. *Journal of Electroceramics*, 2003, **10**, P. 111–115.
[180] Rao C.N.R., Raveau B. *Transition Metal Oxides: Structure, Properties and Synthesis of Ceramic Oxides*. Wiley-VCH, New York, 1998, 227 p.
[181] Meskin P.E., Ivanov V.K., et al. Ultrasonically assisted hydrothermal synthesis of nanocrystalline ZrO_2, TiO_2, $NiFe_2O_4$ and $Ni_{0.5}Zn_{0.5}Fe_2O_4$ powders. *Ultrasonics Sonochemistry*, 2006, **13** (1), P. 47–53.
[182] Bugrov A.N., Almjasheva O.V. Effect of hydrothermal synthesis conditions on the morphology of ZrO_2 nanoparticles. *Nanosystems: Phys. Chem. Math.*, 2013, **4**, P. 810–815.
[183] Li Y., Xu S. Hydrothermal synthesis of lanthanide hydroxide micro/nanorods in presence of tetrabutylammonium hydroxide. *Journal of Rare Earths*, 2016, **34** (6), P. 618–625.
[184] Gusev A.I., Kurlov A.S. Production of nanocrystalline powders by high-energy ball milling: model and experiment. *Nanotechnology*, 2008, **19** (26), P. 265302–265310.
[185] Komarneni S., Tsuji M., Wada Y., Tamaura Y. Nanophase ferrites for CO_2 greenhouse gas decomposition. *J. Mater. Chem.*, 1997, **7** (12), P. 2339–2340.
[186] Tretyakov Y.D., Oleinikov N.N., et al. Self-organization in physicochemical systems – on the path to creating novel materials. *Inorg. Mater.*, 1990, **30** (3), P. 277–290.
[187] Pomogailo A.D., Rozenberg A.S., Dzhardimalieva G.I. Thermolysis of metallopolymers and their precursors as a method for the preparation of nanocomposites. *Russ. Chem. Rev.*, 2011, **80** (3), P. 257–292.
[188] Vanetsev A.S., Tretyakov Yu.D. Microwave–assisted synthesis of individual and multicomponent oxides. *Russ. Chem. Rev.*, 2007, **76** (5), P. 397–413.
[189] Baranchikov A.Ye., Ivanov V.K., Tretyakov Yu.D. Sonochemical synthesis of inorganic materials. *Russ. Chem. Rev.*, 2007, **76** (2), P. 133–151.
[190] Lomanova N.A., Tomkovich M.V., Sokolov V.V., Gusarov V.V. Special features of formation of nanocrystalline $BiFeO_3$ via the glycine-nitrate combustion method. *Russ. J. Gen. Chem.*, 2016, **86** (10), P. 2256–2262.
[191] Türk M. *Particle formation with supercritical fluids: challenges and limitations (Chapter 7)*. Elsevier, 2014, 152 p.
[192] Tretyakov Yu.D., Lukashin A.V. Eliseev A.A. Synthesis of functional nanocomposites based on solid-phase nanoreactors. *Russ. Chem. Rev.*, 2004, **73** (9), P. 899–921.
[193] Krasilin A.A., Gusarov V.V. Redistribution of Mg and Ni cations in crystal lattice of conical nanotube with chrysotile structure. *Nanosystems: Phys. Chem. Math.*, 2017, **8**, P. 620–627.
[194] Korytkova E.N., Semyashkina M.P, et al. Synthesis and growth of nanotubes $Mg_3Si_2O_5(OH,F)_4$ composition under hydrothermal conditions. *Glass Phys. Chem.*, 2013, **39** (3), P. 294–300.

[195] Gulina L.B., Tolstoy V.P., Kasatkin I.A., Murin I.V. Facile synthesis of scandium fluoride oriented single-crystalline rods and urchin-like structures by a gas-solution interface technique. *Crystengcomm.*, 2017, **19** (36), P. 5412–5416.
[196] Komarneni S. Nanophase materials by hydrothermal, microwave-hydrothermal and microwave solvothermal methods. *Current Science*, 2003, **85** (12), P. 1730–1734.
[197] Brinker C.J., Scherer G.W. *Sol-Gel Science: The Physics and Chemistry of Sol-Gel Processing*. Academic Press, San Diego, 1990, 908 p.
[198] Tugova E., Yastrebov S., Karpov O., Smith R. $NdFeO_3$ nanocrystals under glycine nitrate combustion formation. *Journal of Crystal Growth*, 2017, **467**, P. 88–92.
[199] Komlev A.A., Vilegzhaninov E.F., et al. Formation of spinel particles in the Mg–Al–O–N system in the combustion wave front. *Bulletin of the Saint Petersburg State Institute of Technology (Technical University)*, 2013, **1**, P. 3–6.
[200] Ivleva T.P., Merganov A.G. Three–dimensional spinning waves of gasless combustion. *Doklady Akademii Nauk*, 2000, **371** (6), P. 753–758.
[201] Bhavani P., Rajababu C.H., et al. Synthesis of high saturation magnetic iron oxide nanomaterials via low temperature hydrothermal method. *Journal of Magnetism and Magnetic Materials*, 2017, **426**, P. 459–466.
[202] Adachi M., Okuyama K., Seinfeld J.H. Experimental studies of ion-induced nucleation. *J. Aerosol. Sci.*, 1992, **23** (4), P. 327–337.
[203] Fedoseev V.B., Fedoseeva E.N. Size effects during phase transformations in stratifying systems. *Russ. J. Phys. Chem. A*, 2014, **88** (3), P. 436–441.
[204] Oxtoby D.W. Nucleation of first-order phase transitions. *Acc. Chem. Res.*, 1998, **31** (2), P. 91–97.
[205] Ilhan S., Izotova S.G., Komlev A.A. Synthesis and characterization of $MgFe_2O_4$ nanoparticles prepared by hydrothermal decomposition of co-preciptated magnesium and iron hydroxides. *Ceramics International*, 2015, **41** (1), P. 577–585.
[206] Gandhi A.S., Jayaram V. Plastically deforming amorphous ZrO_2–Al_2O_3. *Acta materialia*, 2003, **51**, P. 1641–1649.
[207] Ding X.-Z., Liu X.-H. Correlation between anatase-to-rutile transformation and grain growth in nanocrystalline titania powders. *J. Mater. Res.*, 1998, **13** (9), P. 2556–2559.
[208] Lawrencaen P.J., Parker S.C. Computer simulation studies of perfect and defective surfaces in Cr_2O_3. *J. Am. Ceram. Soc.*, 1988, **71** (8), P. 389–391.
[209] Rebinder P.A., Shchukin E.D. Surface phenomena in solids during the course of their deformation and failure. *Sov. Phys. Usp.*, 1973, **15** (5), P. 533–554.
[210] Oxtoby D.W. Phase transitions: Catching crystals at birth. *Nature*, 2000, **406**, P. 464–465.
[211] Rotermel M.V., Krasnenko T.I., Mechanism of thermal expansion of structural modifications of zinc pyrovanadate. *Crystallography Reports*, 2017, **62** (5), P. 703–709.
[212] Tauson V.L., Loginov B.A., Akimov V.V., Lipko S.V. Nonautonomous phases as potential sources of incompatible elements. *Doklady Earth Sciences*, 2006, **407** (2), P. 280–283.
[213] Sdobnyakov N.Yu., Samsonov V.M. On the size dependence of surface tension in the temperature range from melting point to critical point. *CEJP*, 2005, **3** (2), P. 247–250.
[214] Samsonov V.M., Dronnikov V.V., Mal'kov O.A. The size dependence of the melting temperature of nanocrystals. *Russ. J. Phys. Chem.*, 2004, **78** (7), P. 1044–1047
[215] Tauson V.L., Akimov V.V. Introduction to the theory of forced equilibria: general principles, basic concepts, and definitions. *Geochimica et Cosmochimica Acta*, 1997, **61** (23), P. 4935–4943.
[216] Summ B.D., Samsonov V.M. Concepts of Rehbinder's school and modern theories of spreading. *Colloids and surfaces a-physicochemical and engineering aspects*, 1999, **160** (2), P. 63–77.
[217] Kondepudi D., Prigogine I. *Modern Thermodynamics. From heat engines to dissipative structures*. Wiley, UK, 1998, 506 p.
[218] Kovalenko A. Inner nonstationarness of energy conversion in non-equilibrium thermodynamic system. *Proceedings of the Fifth Baltic Heat Transfer Conference*, 21–23 September 2009, St-Petersburg, SPbGPU, 2009, P. 446–453.
[219] Green S., Sengers J.V. Critical Phenomena. *Proc. Conference on phenomena in the neighborhood of critical points*, NBS Misc. Publ. 273, Washington, 1966, P. 1–242.
[220] Kadanoff L.P. Phase Transition and Critical Phenomena. *Green. Acad. Press, New York*, 1976, **5**, P. 2–34.
[221] Widom B. Equation of state in neighborhood of the critical point. *J. Chem. Phys.*, 1965, **43** (11), P. 255–262.
[222] Sedoi V.S., Valevich V.V. Production of highly dispersed metal powders by electrical explosion in reduced-pressure nitrogen. *Technical Physics Letters*, 1999, **25** (7), P. 584–585.
[223] Kovalenko A.N., Kalinin N.V. Thermodynamic instability of compound and formation of nanosized particles nearby the critical point of phase generating media. *Nanosystems: Phys. Chem. Math.*, 2014, **5** (2), P. 258–293.
[224] Dulnev G.N., Novikov V.V. *Processes of transfer in non-uniform environments*. Energoatomizdat, Leningrad, 1991, 248 p. (in Russian).
[225] Menshikov M.V., Molchanov S.A., Sidorenko A.F. Theory of a perkolyation and some applications. *VINITI, Moscow*, 1986, **24**, P. 53–110 (in Russian).
[226] Burtsev V.A., Kalinin N.V. About conductivity at a stage actually explosion of conductors. Physics of extreme states. *Works of the international conference "Interaction of intensive streams of energy with substance"*. Chernogoloka: RAS, KBGU, 2005, P. 156–158 (in Russian).
[227] Pervov V.S. Supramolecular ensembles in eutectic alloys. *Russian Chemical Reviews*, 2003, **72** (9), P. 759–768.
[228] Pervov V.S., Mikheikin I.D., Shatilo Ya.V., Makhonina E.V. Supramolecular model of eutectics: Metastable states and structure of inorganic alloys. *Russ. J. Inorg. Chem.*, 2007, **52** (4), P. 524–531.
[229] Len G.-M. *Supramolecular chemistry. Concept and prospects*. Science, Novosibirsk, 1998, 334 p.
[230] Pervov V.S., Manokhina E.V., Dobrokhotova Zh.V., Zotova A.E. Metastable states in inorganic systems. *Inorg. Mater.*, 2011, **47** (13), P. 1407–1427.
[231] Pervov V.S., Makhonina E.V., et al. Supramolecular model of eutectics: Functional materials based on nonautonomous phases. *Inorg. Mater.*, 2009, **45** (12), P. 1382–1387.
[232] Frenkel Ya.I., Kontorova T.A. To the theory of plastic deformation and a dvoynikovaniye. *ZhETF*, 1938, **8** (12), P. 1340–1348.
[233] Zavragnov A.Y., Makhonina E.V., Mikheykin I.D., Pervov V.S. Supramolecular model of eutectics. Metastable structures in inorganic systems and a possibility of their functionalization. *Bulletin of the RFBR*, 2011, **4** (72), P. 48–54 (in Russian).

[234] Lyapunova E.A., Uvarov S.V., et al. Modification of the mechanical properties of zirconium dioxide ceramics by means of multiwalled carbon nanotubes. *Nanosystems: Phys. Chem. Math.*, 2016, **7** (1), P. 198–203.
[235] Saha S., Dutta A., Mukhopadhya P.K., Sinha T.P. Dielectric relaxation and charge transport process in $PrCrO_3$ nano-ceramic. *Nanosystems: Phys. Chem. Math.*, 2016, **7** (4), P. 613–617.
[236] Mezentseva L.P., Osipov A.V., et al. Chemical and thermal stability of phosphate ceramic matrices. *Glass Phys. Chem.*, 2017, **43** (1), P. 83–90.
[237] Bechta S.V., Krushinov E.V., et al. Phase diagram of the ZrO_2–FeO system. *Journal of Nuclear Materials*, 2006, **348** (1–2), P. 114–121.
[238] Kazin P.E., Tretyakov Yu.D. Microcomposites based on superconducting cuprates. *Russ. Chem. Rev.*, 2003, **72** (10), P. 849–865.
[239] Kenges K.M., Proskurina O.V., et al. Synthesis and properties of nanocrystalline materials based on $LaPO_4$. *Russ. J. Appl. Chem.*, 2017, **90** (7), P. 1047–1054.
[240] Almjasheva O.V., Gusarov V.V., Kovalenko A.N., Ugolkov V.L. Nanocrystals of ZrO_2 as sorption heat accumulators. *Glass Phys. Chem.*, 2007, **33** (6), P. 587–589.
[241] Matsukevich I.V., Klyndyuk A.I., et al. Thermoelectric properties of $Ca_{3-x}Bi_xCo_4O_9{+}\delta$ ($0.0 \leq x \leq 1.5$) ceramics. *Inorg. Mater.*, 2016, **52** (6), P. 593–599.
[242] Tretyakov Yu.D. Development of inorganic chemistry as a fundamental base for the design of new generations of functional materials. *Russ. Chem. Rev.*, 2004, **73** (9), P. 831–846
[243] Abdellahi M., Abhari A.S., Bahmanpourc M. Preparation and characterization of orthoferrite $PrFeO_3$ nanoceramic. *Ceramics International*, 2016, **42** (4), P. 4637–4641.
[244] Tretyakov Yu.D., Goodilin E.A. Chemical principles of preparation of metall-oxide superconductors. *Russ. Chem. Rev.*, 2000, **69** (1), P. 1–34.
[245] Pervov V.S., Ovchinnikova S.I., et al. Nanoionics: Principles of ceramic materials fabrication for electrochemical power generation. *Inorg. Mater.*, 2016, **52** (1), P. 83–88.
[246] Andrievski R.A. The role of nanoscale effects in the interaction between nanostructured materials and environments. *Protection of Metals and Physical Chemistry of Surfaces*, 2013, **49** (5), P. 528–540.
[247] Rusanov A.I. Surface thermodynamics revisited. *Surface Science Reports*, 2005, **58**, P. 111–239.
[248] Adamson A.W., Gast A.P. *Physical chemistry of surfaces*. 6th ed. A Wiley-Interscience Publication, N.Y., 1997, 784 p.
[249] Prigogine I., Defay R. *Chemical Thermodynamics*. Longmans, Green and Co., New York, 1954, 409 p.
[250] Feder J. *Fractals. Physics of Solids and Liquids*. Plenum Press, New York, 1988, 305 p.
[251] Tauson V.L., Kravtsova R.G., Grebenshchikova V.I., Lustenberg E.E. Surface typochemistry of hydrothermal pyrite: Electron spectroscopic and scanning probe microscopic data. II. Natural pyrite. *Geochemistry International*, 2009, **47** (3), P. 231–243.
[252] Tauson V.L, Lipko S.V., Shchegolkov Yu.V. Surface nanoscale relief of mineral crystals and its relation to nonautonomous phase formation. *Crystallography Reports*, 2009, **54** (7), P. 1219–1227.
[253] Roldughin V.I. Self-assembly of nanoparticles at interfaces. *Russ. Chem. Rev.*, 2004, **73** (2), P. 115–145.
[254] Kuzmenko A.P., Chakov V.V., Aung Ch.N. Operated self-assembly micro and nanostructures. *Nanotechnics*, 2013, **4** (36), P. 30–31 (in Russian).
[255] Paradisi P., Cesari R., Mainardi F., Tampieri F. The fractional Fick's law for non-local transport processes. *Physica A*, 2001, **293**, P. 130–142.
[256] Vlad M.O. Fractional diffusion on fractals: Self-similar stationare solutions in a force field derived from a logarithmic potential. *Chaos, Solutions & Fractals*, 1994, **4** (2), P. 191–199.
[257] Taukenova F.I., Shkhanukov–Lafishev M.Kh. Difference methods for solving boundary value problems for fractional differential equations. *Computational Mathematics and Mathematical Physics*, 2006, **46** (10), P. 1785–1795.
[258] Pleskachevsky Yu.M., Chigareva Yu.A. Distribution of temperature in a layer with fractal structure, 2015, `URL: https://journals.bntu.by/handle/data/14552`.
[259] Uchaykin V.V. Automodel abnormal diffusion and steady laws. *Phys. Usp.*, 2003, **46** (8) P. 821–849.
[260] Meylanov R.P., Shabanova M.R. The thermoconductivity equation for areas with fractal structure. *Modern high technologies*, 2007, **8**, 6 (in Russian).
[261] Rényi A. On a new axiomatic theory of probability. *Acta Mathematica Hungaria*, 1955, **6**, P. 285–335.
[262] Klimontovich Yu.L. Entropy and information of open systems. *Progress of physical sciences*, 1999, **169** (4), P. 443–452 (in Russian).
[263] Dozhdikova O.L., Zarichnyak Yu.P., et al. Anomalies of concentration dependence of heat conductivity of the baked compositions with an ultradisperse component in the TiN–AlN system. *Powder metallurgy*, 1992, **5** (in Russian).
[264] Dulnev G.N. *Processes of transfer in non-uniform environments*. ITMO University, Leningrad, 1985, 27 p. (in Russian).
[265] Dulnev G.N., Zarichnyak Yu.P. *Heat conductivity of mixes and composite materials*. Reference book. Energy, Leningrad, 1974, 264 p. (in Russian).
[266] Dykhne A.M., Snarskii A.A., Zhenirovskii M.I. Stability and chaos in randomly inhomogeneous two-dimensional media and LC circuits. *Phys. Uspekhi*, 2004, **47** (8), P. 821–828 (in Russian).
[267] Galkin A.A., Lunin V.V. Water in sub- and supercritical states as a universal medium for chemical reactions. *Russ. Chem. Rev.*, 2005, **74** (1), P. 21–35.
[268] Valyashko V.M. Equilibria with the participation of supercritical fluids. *Supercritical Fluids. Theory and practices*, 2006, **1**, P. 10–26.
[269] Aymonier C., Loppinet-Serani A., et al. Review of supercritical fluids in inorganic materials science. *Journal of Supercritical Fluids*, 2006, **38**, P. 242–251.
[270] Aimable A., Muhr H., et al. Continuous hydrothermal synthesis ofinorganic nanopowders in supercritical water: Towards a better control of the process. *Powder Technology*, 2009, **190**, P. 99–106.
[271] Rekhviashvili S.Sh., Kishtikova E.V. On the size dependence of the surface tension. *Technical Physics*, 2011, **56** (1), P. 143–146.
[272] Abraham F.F. Re-examination of homogeneous nucleation theory: statistical thermodynamics aspects. *J. Chem. Phys.*, 1968, **48** (2), P. 732–740.
[273] Lin J. Equilibrium distribution of droplets in the theory of nucleation. *J. Chem. Phys.*, 1968, **48** (9), P. 4128–4130.

[274] Stillinger F.H. Comment on the translation-rotation paradox in the theory of irreversible condensation. *J. Chem. Phys.*, 1968, **48** (3), P. 1430–1431.
[275] Kuni F.M., Rusanov A.I. The homogeneous nucleation theory and the fluctuation of the center of mass of a drop. *Phys. Letters A*, 1969, **29** (6), P. 337–338.
[276] Reiss H. Treatment of drop like clusters by means of the classical phase integral in nucleation theory. *J. Stat. Phys.*, 1970, **2** (1), P. 83–104.
[277] Blander M., Katz J.L. The thermodynamics of cluster formation in nucleation theory. *J. Stat. Phys.*, 1972, **4** (1), P. 55–59.
[278] Girshick S.L. Comment on: Self-consistency correction to homogeneous nucleation theory. *J. Chem. Phys.*, 1991, **94** (1), P. 826–828.
[279] Katz J.L. Nucleation theory without Maxwell Demons. *J. Coll. Interface Sci.*, 1977, **61** (2), P. 351–355.
[280] Garnier J.P., Mirabel P., Rabeony H. Experimental results of homogeneous nucleation of super saturated vapors. *J. Chem. Phys.*, 1983, **79** (4), P. 2097–2098.
[281] Ruth V., Hirth J.P., Pound G.M. On the theory of homogeneous nucleation and spinodal decomposition in condensation from the vapor phase. *J. Chem. Phys.*, 1988, **88** (11). P. 7079–7087.
[282] Auer S., Frencel D. Numerical predication of absolute crystallization rates in hard-sphere colloids. *J. Chem. Phys.*, 2004, **120** (6), P. 3015–3029.
[283] Girshick S.L., Chiu C.P. Kinetic nucleation theory: A new expression for the rate of homogeneousnucleation from an ideal supersaturated vapor. *J. Chem. Phys.*, 1990, **93** (2), P. 1273–1278.
[284] Zeng X.C., Oxtoby D.W. Gas-liquid nucleation in Lennard-Jones fluids. *J. Chem. Phys.*, 1991, **94** (6), P. 4472–4478.
[285] Cahn J.W., Hilliard J.E. Free energy of a nonuniform system. III. Nucleation in a two–component incompressible fluid. *J. Chem. Phys.*, 1959, **31** (3), P. 688–700.
[286] Lothe J., Pound G.M. Reconsideration of nucleation theory. *J. Chem. Phys.*, 1962, **36** (8), P. 2080–2085.
[287] Lothe J. Concentration of clusters in nucleation and the classical phase integral. *J. Chem. Phys.*, 1968, **48** (4), P. 1849–1852.
[288] Frenkel J.A. General theory of heterophase fluctuations and pretransition phenomena. *J. Chem. Phys.*, 1939, **7** (7), P. 538–546.
[289] Volmer M. Kinetik der Phasenbildung. *Angewandte Chemie*, 1939, **30**, P. 503–504.
[290] Tribus M. *Thermostatics and thermodynamics*. Energia, Moscow, 1970, 504 p. (in Russian).

NANOSYSTEMS: PHYSICS, CHEMISTRY, MATHEMATICS, 2018, 9 (5), P. 663–668

Synthesis and quantum yield investigations of the $Sr_{1-x-y}Pr_xYb_yF_{2+x+y}$ luminophores for photonics

S. V. Kuznetsov[1], V. Yu. Proydakova[1], O. A. Morozov[2], V. G. Gorieva[2], M. A. Marisov[2], V. V. Voronov[1], A. D. Yapryntsev[3], V. K. Ivanov[3], A. S. Nizamutdinov[2], V. V. Semashko[2], P. P. Fedorov[1]

[1]Prokhorov General Physics Institute, of the Russian Academy of Sciences, 38 Vavilova str., Moscow, 119991 Russia

[2]Kazan Federal University, 18 Kremljovskaya, Kazan, 420008 Russia

[3]Kurnakov Institute of General and Inorganic Chemistry, RAS, 31 Leninsky pr., Moscow,119991 Russia

kouznetzovsv@gmail.com

DOI 10.17586/2220-8054-2018-9-5-663-668

Single-phase praseodymium- and ytterbium-doped strontium fluoride solid solutions were prepared by co-precipitation from aqueous nitrate solutions followed by annealing at 600 °C. Based on EDX analysis, the content of rare-earth elements in solid phase is slightly higher rather than in initial aqueous solution. All the characteristic praseodymium and ytterbium luminescent bands were present. The most intense luminescence in 800 – 1100 nm range was registered in SrF_2:Pr (0.1 mol.%):Yb (10.0 mol.%) solid solution. Using the integrating sphere, the values of the quantum yield were estimated. The maximum quantum yield was 1.1 % for $Sr_{0.9495}Pr_{0.0005}Yb_{0.05}F_{2.0505}$ solid solution.

Keywords: inorganic fluorides, down-conversion luminophores, rare earths, chemical synthesis, photonics, solar cells.

Received: 21 March 2018

Revised: 14 March 2018

1. Introduction

Increasing electric power demand is one of the modern world's challenges [1–3]. The development of alternative sources of electricity, in addition to the use of natural resources, is an urgent task. One of the most advanced approaches is the use of crystalline silicon solar panels. Advantages of these panels are the availability of raw materials the case of manufacturing, and non-toxicity. One of the major drawbacks is a low efficiency [4, 5] due to a limited spectral range of photoresponse, which is located mostly in the near-infrared spectral range with a maximum in the 1 μm region [2]. In the green and red regions of the visible spectrum, crystalline silicon is also photosensitive, but to a lesser extent. There are various approaches to increase the efficiency of converting sunlight to electric power, among which it is worth noting the use of additional fluorescent coatings that convert sunlight into the region of spectral susceptibility of solar cells. It is proposed to use up-conversion phosphors that allow low-energy IR radiation to be transformed to the visible light range, as well as down-conversion phosphors that transform high-energy UV pumping to the luminescence of the visible and near-infrared light range. Among the up-conversion phosphors, one of the most popular compositions is a hexagonal modification of $NaYF_4$ doped with ytterbium and erbium or ytterbium and thulium [6–9]. Earlier we have proposed another efficient matrix based on strontium fluoride doped with ytterbium and erbium [10–12]. It should also be noted that the quantum yield of up-conversion luminescence is not high and usually stays at the level of few percents. Solid solutions powders based on SrF_2 doped by rare earth elements can be synthesized by different techniques: co-precipitation from aqueous solutions by various fluorinating agents such as HF, NH_4F, KF, NaF [13–15], sol-gel processing in organic solution [16], combustion [17] and hydrothermal synthesis [18–20]. Sol-gel processing in organic solution used gaseous HF, which is very dangerous. Hydrothermal synthesis is also dangerous because of working at high pressures. Combustion product contain typically carbon impurities which result in quenching of luminescence. Luminescence quantum yield for co-precipitation from aqueous solution technique was lower because samples had hydroxyl anion in the crystal structure. The highest luminescence characteristics were attained using ammonium fluoride as fluorinating agent. The exiting literature contain only scarce experimental data on the study of solid solutions of SrF_2:Yb:Pr synthesized by co-precipitation from aqueous solutions with ammonium fluoride as fluorination agent. Thus, in this paper, we carried out a complex study of the synthesis and down-conversion luminescent characteristics of $Sr_{1-x-y}Pr_xYb_yF_{2+x+y}$ solid solutions.

2. Experimental

We used 99.99 wt% pure ytterbium and praseodymium nitrate hexahydrates, strontium nitrate (LANHIT, Russia), 99.9 % ammonium fluoride (Chimmed, Russia) and doubly-distilled water as the starting materials without further purification. SrF_2:Yb:Pr solid solution precipitates were synthesized according to our previously published protocol [12]. Aq. rare earth and strontium nitrate solution of 0.08 M concentration was added dropwise to 7 % excess of 0.16 M aqueous ammonium fluoride under intense stirring. After precipitation of SrF_2:Yb:Pr solid solution, the matrix solution was decanted. Precipitates were washed with double distilled water until negative nitrate anion test with diphenylamine. Obtained powders were dried in air at 45 °C (5 hours) and annealed in platinum crucibles in air at 600 °C (1 hour).

All the samples were analyzed by X-ray powder diffraction on a Bruker D8 Advance (Cu Kα radiation) diffractometer. Particle size, morphology and composition of the samples were detected using a Carl Zeiss NVision 40 scanning electron microscope equipped with an EDX analyzer. The diffuse reflectance spectra of the samples were recorded using a Lambda 950 Perkin Elmer spectrophotometer. Fluorescence of the samples was excited by a 443 nm cw laser diode (152.8 W/cm^2). The luminescence spectra were recorded with Stellarnet EPP 2000 spectrometer using a 5 mm filter (ZhS-16) and corrected for the spectral sensitivity of spectrometer. Quantum yield (QY) in 800 – 1100 nm range was evaluated by integrating sphere upon pumping by a 443 nm cw laser diode (3.567 W/cm^2). Experimental data obtained using the integrating sphere was analyzed based approach which described in [21]. Reference calibration lasers (443 nm, 532 nm, 980 nm) were used. In all experiments, the spectral sensitivity of optical systems was calibrated using a SIRSH-2850 lamp.

3. Results

Our earlier studies of SrF_2:Yb:Er, SrF_2:Yb:Tm precipitates confirmed the formation of hydrated solid solutions by co-precipitation from aqueous solution technique [10, 22]. Water and hydroxy-groups can be removed by annealing at 600 °C. Based on this protocol, we synthesized the set of powder samples.

Typical X-ray diffraction pattern of SrF_2:Yb:Pr solid solution is presented in Fig. 1. All observed reflections are in a good agreement with JCPDS Card #06-0262 data ($a = 5.800$ Å). XRD results have confirmed that synthesized samples contained the only fluorite-type phase. The lines in X-ray pattern of the sample, dried at 45 °C (Fig. 1a), were much broader than the lines for the sample annealed at 600 °C (Fig. 1b). Thus, annealing at 600 °C leads to increased crystallite size.

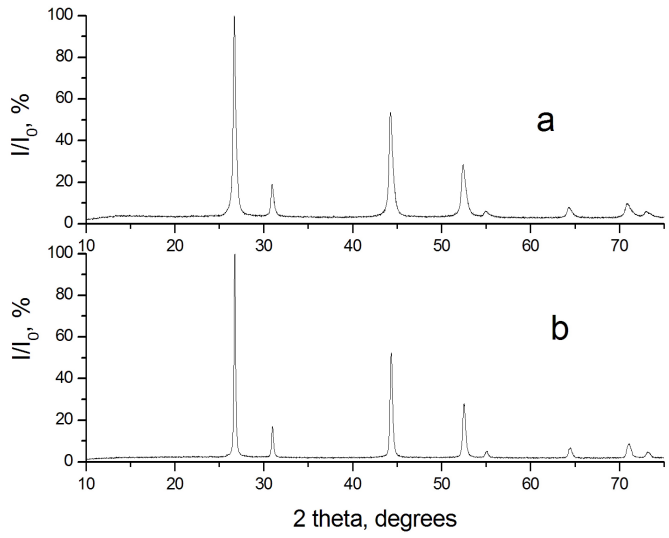

FIG. 1. XRD patterns for sample 3: a – after drying at 45 °C, b – after annealing at 600 °C

We have calculated the unit cell parameters based on XRD data. XRD results are listed in Table 1. Table 1 data analysis also indicate that the increase in the dopant content resulted in the expected simultaneous decrease of $Sr_{1-x-y}Yb_xPr_yF_{2+x+y}$ solid solution unit cell parameter due to the action of additional interstitial fluorine ions and smaller ionic radii of the rare earth dopants compared with strontium ion [23]. Annealing at 600 °C also

resulted in expected small decrease in the unit cell parameter in comparison with the data for the same composition samples dried at 45 °C. One of the reason is a smaller ionic radii of fluorine compared to hydroxyl.

TABLE 1. X-Ray diffraction data for SrF_2:Yb:Pr powders

Sample*	Nominal composition, mol.%	T, °C	Unit cell parameter, Å	Weight loss upon annealing (wt. %)
1	SrF_2: Yb(5.00):Pr(0.05)	45	a = 5.789 (2)	2.84
		600	a = 5.7821 (4)	
2	SrF_2: Yb(5.00):Pr(0.1)	45	a = 5.7999 (7)	5.62
		600	a = 5.7803 (4)	
3	SrF_2: Yb(5.00):Pr(0.5)	45	a = 5.789 (1)	2.60
		600	a = 5.7790 (6)	
4	SrF_2: Yb(10.00):Pr(0.05)	45	a =5.771(3)	3.8
		600	a = 5.7637 (2)	
5	SrF_2: Yb(10.00):Pr(0.1)	45	a = 5.850 (8)	3.5
		600	a = 5.746 (2)	
6	SrF_2: Yb(10.00):Pr(0.5)	45	a = 5.760 (3)	3.4
		600	a = 5.7552 (8)	

*The sample labeling, presented in Table 1, is maintained across the whole paper for the readers convenience

Scanning electron microscopy image of SrF_2:Yb (5.0%):Pr (0.5) sample dried at 45 °C is shown in Fig. 2a. It appeared to be typical for all the samples. There are two types of particles observed: flat particles with an average size about 14 nm and cubic particles with size about 84 nm. Apparently flat small particles were produced from cubic particles upon milling powder in a mortar which was the preliminary stage for preparing powders for analysis. It is well-known that the alkaline-earth fluorides have perfect cleavage. It results in cracking at mechanical stress. Obviously, in this image we can see with the same situation at nanosized level. One of the arguments is that the ratio of particle sizes complies the 84 nm/14 nm = 6. Annealing at 600 °C resulted in an increase of the average particle sizes up to 119 nm (Fig. 2b). As an explanation of the driving forces of such an evolution, it can be assumed that the system is driven to a minimum of its own energy, and also to the destruction of the original self-fluorinating precursor $Sr_{1-x-y-z}Yb_xPr_y(NH_4)_zF_{2+x+y-z}$. In Fig. 2b, SEM image in BSE regime is shown. The uniform color of the image on Fig. 2b revealed a uniform chemical composition of the samples. Evaluation of chemical composition based on EDX measurements is summarized in Table 2. The content of ytterbium fluoride in solid solution is high rather than in water solution. The EDX composition determination error is 0.5 mol.%. This means that the concentration of praseodymium in the samples cannot be determined. Mean value of ytterbium distribution coefficient about 1.15. This means that crystallization process occurs in an incongruent manner.

Diffusion reflectance spectra (Fig. 3) for samples 1, 2, 4 after annealing at 600 °C contained absorption bands typical for praseodymium (III) and ytterbium (III) ions [24]. The intense absorption band of praseodymium is located at 443 nm. Based on this, we have chose 443 nm excitation wavelength.

We have registered the luminescence spectra for annealed samples (Fig. 4). In the visible spectral range, we have recognized characteristic Pr^{3+} ion luminescence in 450 – 750 nm range [25–27] and intense luminescence within 900 – 1100 nm range corresponding to $^2F_{5/2}-^2F_{7/2}$ transitions of Yb^{3+} ions. The maximum luminescence intensity was recorded for the composition SrF_2:Pr (0.1 mol.%):Yb (10.0 mol.%).

For a more detailed estimation of the down-conversion efficiency we have evaluated the quantum yields of luminescence. There are two main approaches described in many papers. The first is investigation of the lifetime of excited states. This approach appears to be very complicated. The second is the use of the integrating sphere. This approach is more correct, because it consists in registration of a photon flux energy and calculation of quantum yields from the data on energy yields. We have evaluated the quantum yields by means of integrating sphere with

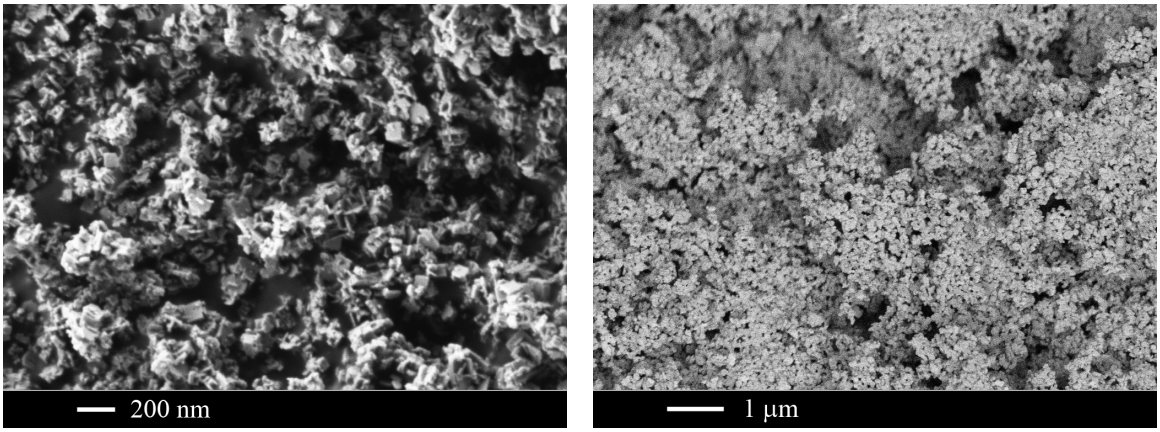

a b

FIG. 2. a – SEM image in SE2 regime of sample 3 after drying at 45 °C, b – SEM image in BSE regime of sample 3 after annealing at 600 °C

TABLE 2. EDX data for SrF_2:Yb:Pr powders

No.	Nominal content Pr/Yb, mol.%	EDX content Pr/Yb, mol.%	The effective distribution coefficient of Yb
1	0.05/5.0	–/5.0	1.0
2	0.10/5.0	–/5.86	1.17
3	0.5/5.0	–/6.0	1.20
4	0.05/10.0	–/12.4	1.24
5	0.10/10.0	–/11.5	1.15

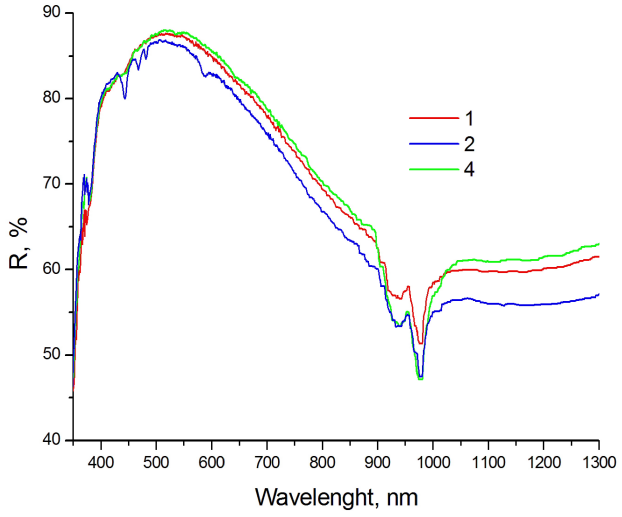

FIG. 3. Diffusion reflection spectra (Fig. 3) for samples 1, 2, 4 after annealing at 600 °C

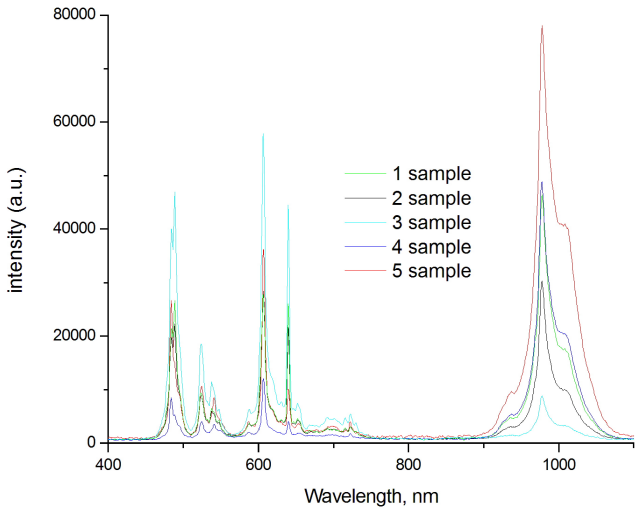

FIG. 4. Luminescence spectra of $Sr_{1-x-y}Yb_xPr_yF_{2+x+y}$ solid solutions after annealing at 600 °C

pumping by a 443 nm cw laser diode with power density 3.567 W/cm^2 (Table 3). An analysis of the results have showed that at a constant ytterbium content of 5 mol.%, the highest quantum yield is demonstrated by a sample with a praseodymium content of 0.05 mol.%. The increase of praseodymium content by 10 times leads to the quantum yield decrease by 10 times. At the same time, in the samples with 10 mol.% of ytterbium, an increase in the praseodymium content leads to an increase in the quantum yield. As a result, a quantum yield of 1.1 % has been achieved, but further increase of this value with an ytterbium content of 5 mol.% appears to be impossible.

TABLE 3. Quantum yields for SrF_2:Yb:Pr powder samples

No.	Sample composition	Quantum yield, %
1	SrF_2 : Yb (5 %) : Pr (0.05)	1.1
2	SrF_2 : Yb (5 %) : Pr (0.1)	0.7
3	SrF_2 : Yb (5 %) : Pr (0.5)	0.1
4	SrF_2 : Yb (10 %) : Pr (0.05)	0.5
5	SrF_2 : Yb (10 %) : Pr (0.1)	0.8

4. Conclusions

As a result of the study, single-phase samples of $Sr_{1-x-y}Yb_xPr_yF_{2+x+y}$ solid solutions were obtained, which was confirmed by XRD, SEM, and EDX measurements. The shape of the particles dried at 45 °C is cubic of about 84 nm in size and a plate-like with a thickness of 14 nm, which is probably the result of splitting the cubes along the cleavage planes. Annealing at 600 °C leads to a change in the size and the morphology of the particles. In this case, spheres with the size of 119 nm appear. It should be noted that particles do not tend to agglomeration. EDX analysis have shown that the ytterbium concentration in solid solutions is greater than in the initial aqueous solutions. The effective average distribution coefficient was 1.15, which indicates the incongruent type of the precipitation process from aqueous solutions. The diffuse reflectance spectra contain characteristic absorption bands of praseodymium and ytterbium, which confirms their entry into the crystal lattice. Considering the fact that the maximum photoconversion of solar power in crystalline silicon is attained in the region of 1 μm, the best composition determined on the basis on the quantum yield measurements is SrF_2: Yb(5.00): Pr(0.05) solid solution with QY = 1.1 %.

Acknowledgement

The study was funded by a grant from the Russian Science Foundation (project # 17-73-20352).

References

[1] Green M.A., Bremner S.P. Energy conversion approaches and materials for high-efficiency photovoltaics. *Nature Mater*, 2017, **16**, P. 23–34.
[2] Huang X., Han S., Huang W., Liu X. Enhancing solar cell efficiency: the search for luminescent materials as spectral converters. *Chem. Soc. Rev.*, 2013, **42**, P. 173–201.
[3] Han G., Zhang S., Boix P.P., Wong L.H., Sun L., Lien S.Y. Towards high efficiency thin film solar cells. *Progress in Materials Science*, 2017, **87**, P. 246–291.
[4] Engelhart P., Wendt J., Schulze A., Klenke C., Mohr A., Petter K., Stenzel F., Hörnlein S., Kauert M., Junghänel M., Barkenfelt B., Schmidt S., Rychtarik D., Fischer M., Müller J.W., Wawer P. R&D pilot line production of multi-crystalline Si solar cells exceeding cell efficiencies of 18 %. *Energy Procedia*, 2011, **8**, P. 313–317.
[5] Yang J., Myong S.Y., Lim K.S. Novel ultrathin LiF interlayers for efficient light harvesting in thin-film Si tandem solar cells. *Solar Energy*, 2015, **114**, P. 259–267.
[6] Ren W., Tian G., Jian S., Gu Z., Zhou L., Yan L., Jin S., Yin W., Zhao Y. Tween coated $NaYF_4$:Yb,Er/$NaYF_4$ core/shell upconversion nanoparticles for bioimaging and drug delivery. *RSC Advances*, 2012, **2**, P. 7037–7041.
[7] Zhao J., Jin D., Schartner E.P., Lu Y., Liu Y., Zvyagin A.V., Zhang L., Dawes J.M., Xi P., Piper J.A., Goldys E.M., Monro T.M. Single-nanocrystal sensitivity achieved by enhanced upconversion luminescence. *Nature Nanotechnology*, 2013, **8**, P. 729–734.
[8] Conference book of 1st Conference and spring school on properties, design and applications of upconverting nanomaterials, Wroclaw, Poland, 23-27 May 2016.
[9] Kuznetsov S.V., Yasyrkina D.S., Ryabova A.V., Pominova D.V., Voronov V.V., Baranchikov A.E., Ivanov V.K., Fedorov P.P. α-$NaYF_4$:Yb:Er@AlPc$(C_2O_3)_4$ -based efficient up-conversion luminophores capable to generate singlet oxygen under IR excitation. *J. Fluor. Chem.*, 2016, **182**, P. 104–108.
[10] Pak A.M., Ermakova J.A., Kuznetsov S.V., Ryabova A.V., Pominova D.V., Voronov V.V. Efficient visible range SrF_2:Yb:Er- and SrF_2:Yb:Tm-based up-conversion luminophores. *J. Fluor. Chem.*, 2017, **194**, P. 16–22.
[11] Rozhnova Yu.A., Luginina A.A., Voronov V.V., Ermakov R.P., Kuznetsov S.V., Ryabova A.V., Pominova D.V., Arbenina V.V., Osiko V.V., Fedorov P.P. White light luminophores based on Yb^{3+}/Er^{3+}/Tm^{3+}-coactivated strontium fluoride powders. *Mater. Chem. Phys.*, 2014, **148**, P. 201–207.
[12] Rozhnova Yu.A., Kuznetsov S.V., Luginina A.A., Voronov V.V., Ryabova A.V., Pominova D.V., Ermakov R.P., Usachev V.A., Kononenko N.E., Baranchikov A.E., Ivanov V.K., Fedorov P.P. New $Sr_{1-x-y}R_x(NH_4)_yF_{2+x-y}$ (R = Yb, Er) solid solution as precursor for high efficiency up-conversion luminophor and optical ceramics on the base of strontium fluoride. *Mater. Chem. Phys.*, 2016, **172**, P. 150–157.
[13] Fedorov P.P., Kuznetsov S.V., Mayakova M.N., Voronov V.V., Ermakov R.P., Baranchikov A.E., Osiko V.V. Coprecipitation from aqueous solutions to prepare binary fluorides. *Rus. J. Inorg. Chem.*, 2011, **56**, P. 1525–1531.
[14] Mayakova M.N., Luginina A.A., Kuznetsov S.V., Voronov V.V., Ermakov R.P., Baranchikov A.E., Ivanov V.K., Karban O.V., Fedorov P.P. Synthesis of SrF_2-YF_3 nanopowders by co-precipitation from aqueous solutions. *Mendeleev Communications*, 2014, **24**, P. 360–362.
[15] Fedorov P.P., Mayakova M.N., Maslov V.A., Baranchikov A.E., Ivanov V.K., Pynenkov A.A., Uslamina M.A., Nishchev K.N. The solubility of sodium and potassium fluorides in the strontium fluoride. *Nanosystems: PHYSICS, CHEMISTRY, MATHEMATICS*, 2017, **8**, P. 830–834.
[16] Ritter B., Haida P., Krahl T., Scholz G., Kemnitz E. Core–shell metal fluoride nanoparticles via fluorolytic sol–gel synthesis – a fast and efficient construction kit. *J. Mater. Chem.*, 2017, **C5**, P. 5444–5450.
[17] Rakov N., Guimarães R.B., Franceschini D.F., Maciel G.S. Er:SrF_2 luminescent powders prepared by combustion synthesis. *Mater. Chem. Phys.*, 2012, **135**, P. 317–321.
[18] Peng J., Hou S., Liu X., Feng J., Yu X., Xing Y., Su Z. Hydrothermal synthesis and luminescence properties of hierarchical SrF_2 and SrF_2:Ln^{3+} (Ln = Er, Nd, Yb, Eu, Tb) micro/nanocomposite architectures. *Mater. Res. Bull.*, 2012, **47**, P. 328–332.
[19] Yagoub M.Y.A., Swart H.C., Noto L.L., O'Connel J.H., Lee M.E., Coetsee E. The effects of Eu-concentrations on the luminescent properties of SrF_2:Eu nanophosphor. *J. Lumin.*, 2014, **156**, P. 150–156.
[20] Yagoub M.Y.A., Swart H.C., Noto L.L., Bergman P., Coetsee E. Surface Characterization and Photoluminescence Properties of Ce^{3+}, Eu Co-Doped SrF_2 Nanophosphor. *Materials*, 2015, **8**, P. 2361–2375.
[21] Ryabova A.V., Pominova D.V., Krut'ko V.A., Komova M.G., Loschenov V.B. Spectroscopic research of upconversion nanomaterials based on complex oxide compounds doped with rare-earth ion pairs: benefit for cancer diagnostics by upconversion fluorescence and radiosensitive methods. *Photonics&Lasers in Medicine*, 2013, **2**, P. 117–128.
[22] Kuznetsov S., Ermakova Yu., Voronov V., Fedorov P., Busko D., Howard I.A., Richards B., Turshatov A. Up-conversion Quantum Yield of SrF_2:Yb^{3+},Er^{3+} Sub-micron Particles Prepared by Precipitation from Aqueous Solution. *J. Mater. Chem.*, 2018, **C6**, P. 598–604.
[23] Fedorov P.P., Sobolev B.P. Concentration dependence of unit-cell parameters of phases $M_{1-x}R_xF_{2+x}$ with the fluorite structure. *Sov. Phys. Crystallogr.*, 1992, **37**, P. 651–656.
[24] Dieke G.H., Crosswhite H.M. The spectra of the doubly and triply ionized rare earths. *Appl. Opt.*, 1963, **2**, P. 675–686.
[25] Kuzmanoski A., Pankratov V., Feldmann C. Energy transfer of the quantum-cutter couple Pr^{3+}–Mn^{2+} in CaF_2:Pr^{3+}, Mn^{2+} nanoparticles. *J. Lumin.*, 2016, **179**, P. 555–561.
[26] Meijerink A., Wegh R., Vergeer P., Vlugt T. Photon management with lanthanides. *Opt. Mater.*, 2006, **28**, P. 575–581.
[27] Yagoub M.Y.A., Swart H.C., Coetsee E. Concentration quenching, surface and spectral analyses of SrF_2:Pr^{3+} prepared by different synthesis techniques. *Opt. Mater.*, 2015, **42**, P. 204–209.

NANOSYSTEMS: PHYSICS, CHEMISTRY, MATHEMATICS, 2018, 9 (5), P. 669–675

Electrocatalytic properties of γ-NiOOH nanolayers, synthesized by successive ionic layer deposition, during the oxygen evolution reaction upon water splitting in the alkaline medium

A. A. Lobinsky, V. P. Tolstoy, I. A. Kodinzev

Institute of Chemistry, Saint Petersburg State University,
26 University Pr., St. Peterhof, Saint Petersburg, 198504, Russia

lobinsky.a@gmail.com, v.tolstoy@spbu.ru, i.a.kod@mail.ru

PACS 82.65+r **DOI 10.17586/2220-8054-2018-9-5-669-675**

Nickel oxyhydroxide nanolayers were synthesized on the surface of nickel foam and single crystalline silicon through Successive Ionic Layer Deposition (SILD) method by using aqueous solutions $NiSO_4$ and $K_2S_2O_8$. The obtained nanolayers were characterized by SEM, XRD, FTIR and XPS spectroscopy. The electrochemical properties of the electrodes were defined from polarization curves. SEM images revealed that nanolayers are formed by nanosheets with a thickness of 6 – 10 nm. The nanolayers were shown to exhibit electrocatalytic properties during the oxygen evolution reaction upon water splitting in the alkaline medium. By setting the number of SILD cycles, these properties can be changed precisely. For a number of samples, synthesized after 30 – 120 SILD cycles, it was found that in the oxygen evolution reaction the lowest overpotential value of 260 mV and the lowest Tafel slope of 54 mV/dec are achieved for the sample, synthesized after 90 SILD cycles.

Keywords: NiOOH, nanolayers, SILD, oxygen evolution reaction.

Received: 21 August 2018

1. Introduction

One of the practical approaches to hydrogen production is the splitting of water. Recently it has grown in importance due to the development of new methods for energy conservation, including renewable ones. The method of energy conservation during electrolytic water splitting allows working the problems of cyclicity and instability of energy receiving in solar and wind power areas as well as those of free capacity use during periods of no peak hours, for instance, in the nuclear power field. One of the significant features of the energy conversion is its environmental friendliness, since this process only requires water and electricity. Today it is important to reduce energy consumption for water electrolysis in such devices through overpotential reduction on the electrodes which is caused by using specific electrocatalysts. Even having been developing for more than 40 years, the history of these electrocatalysts has recently gained interest due to production of new electrocatalysts, composed of generally available transition metals such as Ni, Co and Fe [1–3]. It was mentioned [4] that catalysts based on nickel oxides or hydroxides, exhibiting high stability to oxidation in alkaline medium, are among the best.

Taking into account the practical importance of challenges to synthesize electrocatalysts, to date, a variety of methods of preparative inorganic chemistry has been used. The methods had been previously tested by producing a wide range of other metal-oxygen compounds. Such methods include, for example, sol-gel [5], hydrothermal [6], coprecipitation [7], electrochemical [8] etc.

Meanwhile, analysis of the literature reveals that there are few works describing Layer-by-Layer (LbL) synthesis as method to obtain such electrocatalysts. These include, for example, the works, devoted to the synthesis of electrocatalytic layers IrO_2 [9] and Co_3O_4 [10]. This method of synthesis based on a successive and multiple treatments of substrate in salt or colloidal solutions and polyelectrolytes, forming an insoluble nanolayers of new compound upon interaction at the surface. The SILD method is one of LbL synthesis methods without the using of polyelectrolite solutions. We believe there are particular advantages in using SILD synthesis to create highly efficient electrocatalysts: the possibility to deposit nanolayers with a precisely defined thickness onto the surface of the electrodes of complex shape, producing such nanolayers under ”soft chemistry” conditions almost at room temperature, the use of diluted and available metal salts solutions in synthesis, etc. These features of the SILD synthesis had defined its efficiency, for example, when creating new supercapacitor electrodes [11], superparamagnetic materials [12], sensors active elements [13], etc.

The purpose of this work is to study the electrocatalytic properties of γ-NiOOH nanolayers, synthesized by SILD method using the previously proposed synthesis scheme with salts $NiSO_4$ and $K_2S_2O_8$ [14], for the oxygen evolution reaction upon water splitting in the alkaline KOH solution.

2. Experimental methods

Nickel foam plates by AO (JSC) "ECAT" with a porosity of 80 PPI and a size of approximately 5×25 mm, pressed to 0.25 mm, as well as plates of single crystalline silicon with orientation of $\langle 100 \rangle$ and a size of approximately 0.35×10×25 mm were used as substrates for synthesis of nanolayers. Before the synthesis, nickel foam substrates had been treated according to the method [15], namely in acetone using ultrasonication for 30 minutes and then in 6 M HCl solution for 15 minutes to remove the oxide layer. Further, the substrates were washed with deionized water three times and air-dried at 70°C for 30 minutes. Single crystalline silicon wafers were washed in acetone to remove the organic impurities and etched in concentrated HF for 15 minutes, then washed in distilled water multiple times to remove the acid excess. After that they were treated for 20 minutes in the diluted KOH solution with pH∼9,0.

The synthesis of nanolayers was conducted using SILD method, utilizing $NiSO_4$ solution as the precursor with a concentration of 0.01 M and the equilibrium pH value as well as $K_2S_2O_8$ solution with a concentration of 0.01 M and pH=10.5, achieved by adding 0.5 M aq. KOH to the $K_2S_2O_8$ solution dropwise. During the synthesis, the substrates were fixed in a holder of a special automated setup and successively immersed for 30 seconds in chemical vessels with $NiSO_4$ solution, distilled water, $K_2S_2O_8$ solution and distilled water again. Such treatment constituted one SILD cycle, which has been repeated several times.

XRD patterns were obtained using a Rigaku Miniflex II X-ray diffractometer with Cu $K\alpha$ radiation (λ= 0.154056 nm). The morphology and composition of synthesized films was investigated by SEM at accelerating voltage 4 kV on Zeiss Merlin microscope and EDX used detector Oxford INCAx-act. FTIR transmission spectra of synthesized films on silicon surface were registered by FCM-2201 spectrophotometer using differential technique with respect to spectra of bare silicon plate. X-ray photoelectron spectroscopy (XPS) was obtained used ESCALAB 250Xi electron spectrometer, with Al $K\alpha$ radiation (14.866 eV)

Electrocatalytic characteristics of electrodes for oxygen evolution reaction were recorded using potentiostat Elins P-45X and a three-electrode cell, where an electrode based on the pressed nickel foam with an electroactive substance, deposited via SILD method, and electroactive area of 0.5 cm^2 was used as a working one. The Ag/AgCl electrode and a platinum foil were used as reference electrode and counter electrode, respectively. Overpotentials, recorded in this study, were calibrated for a reversible hydrogen electrode (E_{RHE}) according to the Nernst equation $E_{RHE} = E^o_{Ag/AgCl}$+0.059·pH+$E_{Ag/AgCl}$, where $E^o_{Ag/AgCl}$ is a standard potential for the Ag/AgCl electrode (0.197 mV), and $E_{Ag/AgCl}$is the potential for the Ag/AgCl electrode, obtained in the measurement. All the measurements have been carried out at room temperature and atmospheric pressure in 1 M aq. KOH (pH=14) solution as electrolyte. Polarization curves were usually shot at scan rate of 5 mV/sec. Overpotential (η) was determined from the polarization curve, obtained through linear potential sweep with IR compensation, as the difference between the recorded potential (at a current density of 10 mA/cm^2) and water splitting potential for the reversible hydrogen electrode of 1.23 V.

3. Results

As shown in the electron micrograph (Fig. 1), in the composition of the nanolayers, synthesized after 50 SILD cycles, it is possible to separate individual flat nanocrystals approximately 6 – 10 nm thick, oriented mainly perpendicular to the surface of the substrate. We assume that the appearance of such mainly oriented nanocrystals on the surface is a proof of the previously established model of their growth [16], which is based on the idea of the formation of the 2D NiOOH nanocrystals arranged in the same plane on the surface after the first SILD cycles. These nanocrystals possess the morphology of nanosheets that, as the number of SILD cycles increases, change their planar geometry due to the repulsive interaction of areas of equal charge. These equally charged nanosheets appear on the surface in each SILD cycle at the stages of treatment in salt solutions, when the adsorption of, for instance, cations Ni^{2+} appears on the surface.

Figure 2 shows an X-ray diffraction pattern, where the peaks at 22.4, 44.6, 50.3° are to be noted, and which, according to JCPDS 06-0075, can be attributed to the crystal planes (003), (102) and (105) of γ-NiOOH with hexagonal crystal structure; as well as peaks at 22.4, 40.1, 43.3, 72.4 and 78.5° that, according to JCPDS 06-0144, are related to $Ni_3O_2(OH)_4$ planes (003), (100), (006), (110) and (114) and have the hexagonal structure too. It can be noticed that in the latter compound some of the Ni cations have the oxidation state of 2+. Unfortunately, it is impossible to determine the percentage of each compound from the X-ray diffraction pattern because of the width of the observed peaks, which is related to the nanosize of such crystals. However, we can state that the synthesis results in the formation of γ-NiOOH nanocrystals on the substrate surface. After being in air for several days these nanocrystals partly transform in $Ni_3O_2(OH)_4$ nanocrystals. This effect can be noted visually by observing that the color of the as-prepared synthesized samples changes and becomes lighter after drying and storage on air. At the

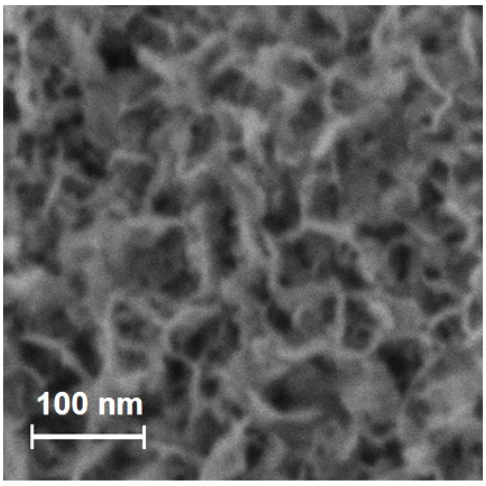

FIG. 1. The SEM micrograph of the nanolayer synthesized after 50 SILD cycles

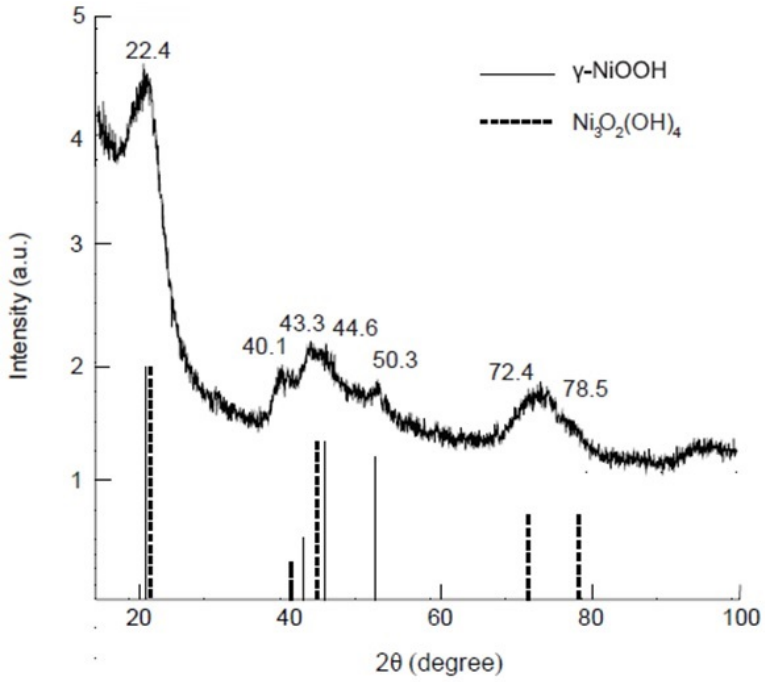

FIG. 2. X-ray diffraction pattern of the nanolayer synthesized after 50 SILD cycles

same time, we cannot exclude the incomplete oxidation of Ni^{2+} cations during the sample treatment in $K_2S_2O_8$ solution because the reaction proceeds in alkaline medium, where, in the first place, the hydrolysis of cations is to be seen and only after that - their oxidation. We assume that the bi-phase composition of the investigated nanolayers has no effect on the electrocatalytic properties of such nanolayers because in the OER the nanolayers of the electrocatalyst is on the anode's surface, and under electrolysis conditions the positive voltage is applied on that nanolayers. The voltage is higher than the oxidation potential $Ni^{2+} \rightarrow Ni^{3+}$, due to which all Ni^{2+} ions become Ni^{3+} ions and it is γ-NiOOH that is involved in the electrocatalysis.

The study of the nanolayers by FTIR spectroscopy revealed a spectrum, shown in Fig. 3. The spectrum happens to be similar to the spectrum, recorded in [14]. As can be seen from the Fig. 3, the composition of the nanolayers includes water molecules, corresponding to absorption bands with peaks at 3440 cm^{-1} and 1640 cm^{-1}. According to [17], bands with peaks at 1470 and 1383 cm^{-1} can be attributed to carbon-oxygen stretching vibrations in CO_3^{2-} anions, which apparently appeared on the surface due to the adsorption of CO_2 molecules upon sample contact with the atmosphere. We can also mention an adsorption band with peak at 1083 cm^{-1},

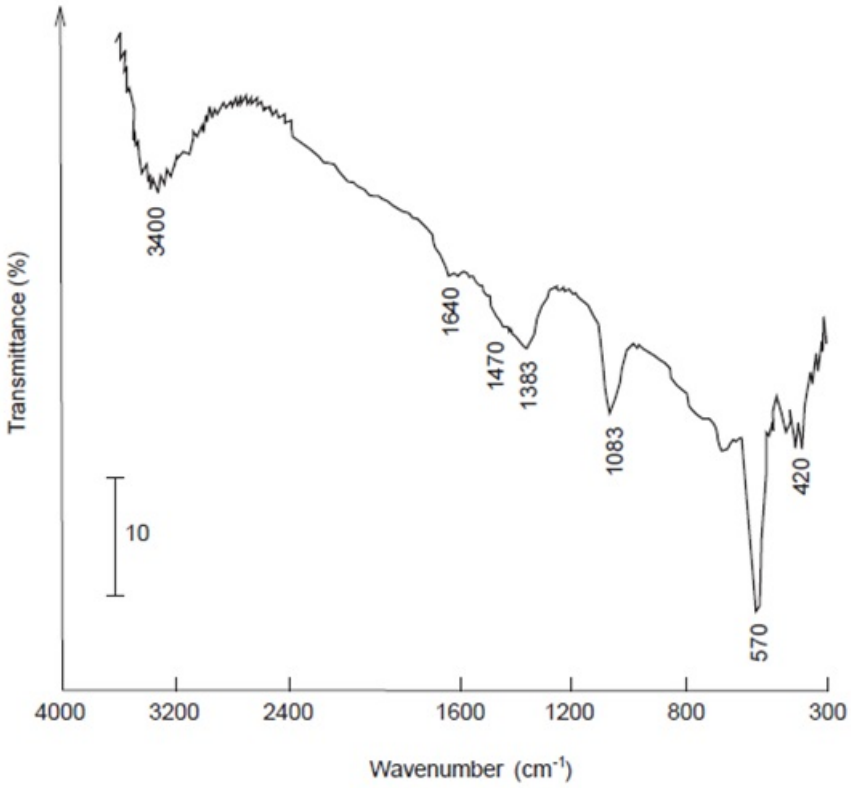

FIG. 3. FTIR transmittance spectrum of nanolayer synthesized on the silicon surface after 50 SILD cycles

corresponding to S-O stretching vibrations in sulfate anions [17], remained apparently in the nanolayers after the synthesis that involved the above mentioned reagent solutions. A band with peak at 570 cm^{-1} can be attributed to Ni^{3+}-O stretching vibrations in γ-NiOOH, and a band with peak at 420 cm^{-1} – to Ni^{2+}-O stretching vibrations in $Ni_3O_2(OH)_4$ [18–20].

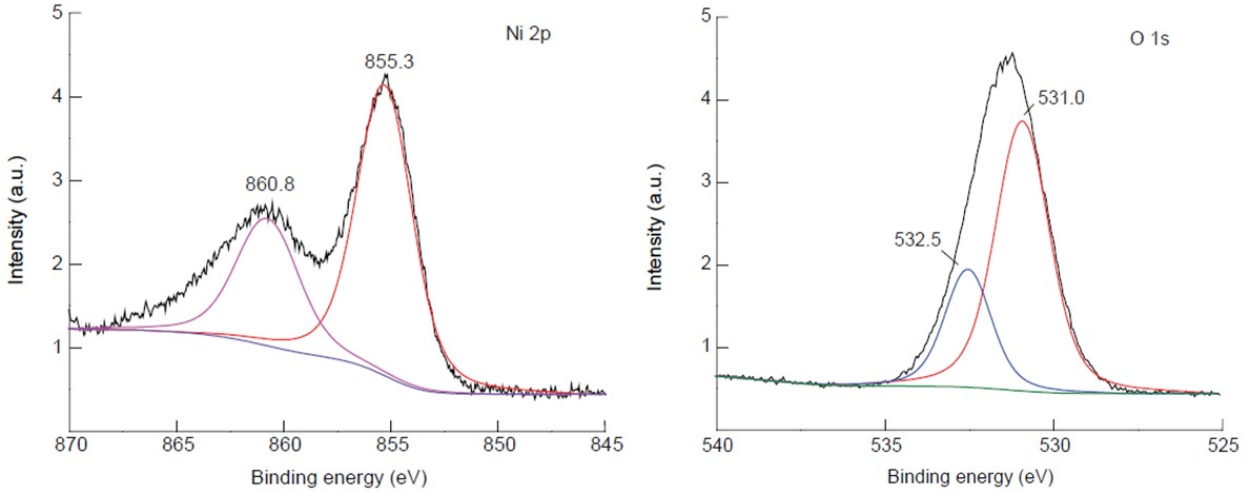

FIG. 4. X-ray photoelectron spectra of Ni 2*p* and O 1*s* electrons of the nanolayer, synthesized on the silicon surface after 50 SILD cycles

Figure 4 shows X-ray photoelectron spectra in the energy range typical for Ni 2*p* and O 1*s* electrons. Broad peaks at 855.3 eV and 860.8 eV can be attributed, similar to work [21], to the signals from Ni $2p_{3/2}$ and $2p_{1/2}$ electrons in the oxidation states of 3+ and 2+. The peaks at 531.0 eV and 532.5 eV can be attributed to the signals

from $1s$ electrons of O atoms in Ni-OH and to those from adsorbed H_2O, respectively [22]. When analysing XPS results, indicating the presence of Ni of two oxidation states in the nanolayers, it should be taken into account that Ni^{3+} hydroperoxides are partly unstable after being kept in air for several days, as noted in [23].

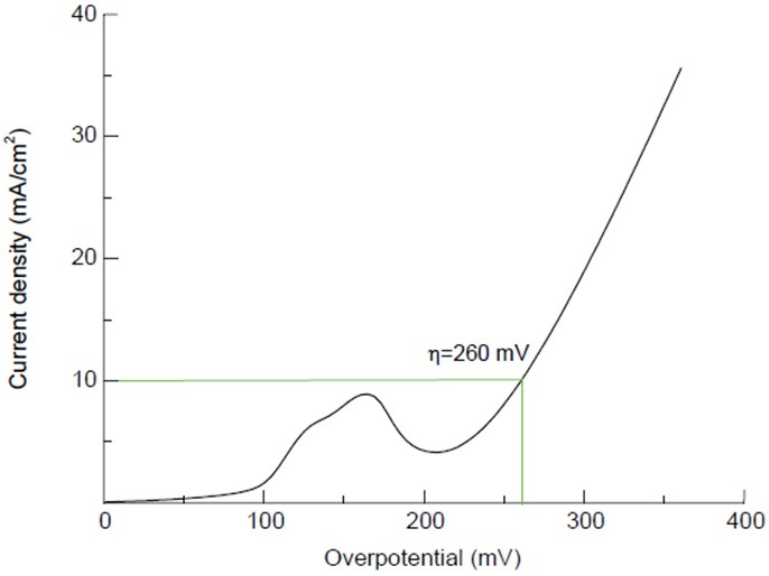

FIG. 5. LSV curve of the nickel foam electrode with nanolayer synthesized after 90 SILD cycles

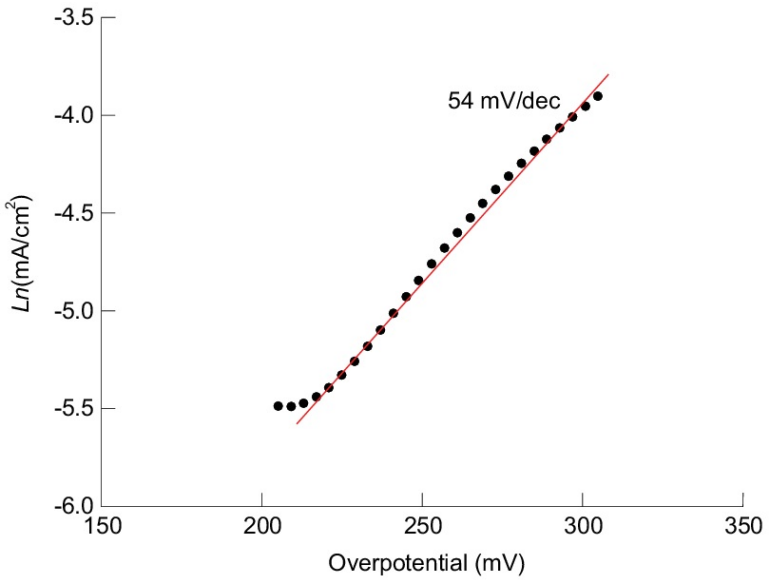

FIG. 6. Tafel plot of the nickel foam electrode with nanolayer synthesized after 90 SILD cycles

As an example of the results obtained experimentally from the studying of electrocatalytic properties of obtain nanolayers. Fig. 5. shows the change of current density vs. overpotential for the electrode based on nickel foam and nanolayer, synthesized after 90 SILD cycles. From the figure can be observed that overpotential value at a current density of 10 mA/cm^2 is 260 mV. An important parameter characterising the microkinetics of catalytic processes in OER is the Tafel slope, which can be measured as the current density logarithm versus overpotential. The calculation of Tafel slope for this sample from the data obtained allowed finding its value, which was 54 mV/dec (Fig. 6).

The analysis of overpotential and Tafel slope values has been carried out for a series of electrocatalysts samples synthesized after various number of SILD cycles. The results of the analysis are presented in Table 1. The table

shows that as the number of SILD cycles increases, overpotential and Tafel slope values decrease, however after 120 SILD cycles they increase insignificantly. That allowed us to choose an electrocatalyst nanolayer, synthesized after 90 SILD cycles, as the one with the optimal properties. This effect of the properties' change in a series of similar samples, synthesized after various number of SILD cycles, is apparently due to the fact that as the number of SILD cycles increases, the number of nanocrystals of the catalytically active species on the surface of nickel foam increases as well. However, after 90 treatment cycles the nanolayers have relatively high electrical resistivity, which leads to the increase of overpotential and Tafel slope values.

In general, it should be mentioned that the obtained results are close, and in some cases even superior, to the electrocatalytic characteristics of similar materials, synthesized by other methods [24–26]. We can assume that this is due to the unique morphological features of the obtained γ-NiOOH nanocrystals and to the presence of pores between them that contribute to the more effective removal of oxygen bubbles in that electrochemical process. The similar assumption has been made in the work [27] that studied electrocatalytic properties of Ni/Sn layers. An important feature of the proposed synthesis method of the electrocatalytic material is the possibility to set the conditions of the synthesis precisely. For instance, by setting the number of SILD cycles and therefore by obtaining a series of similar samples of electrocatalysts, among which we can choose the samples with optimal electrochemical characteristics. Undoubtedly, the properties of such materials can be further improved, particularly, by doping the nanolayers with various electrocatalytically active metals. However, this subject is beyond the scope of this article.

TABLE 1. A comparison of overpotential and Tafel slope values for nickel foam-based electrodes and nickel oxyhydroxides nanolayers synthesized after different number of SILD cycles

Number of SILD	Overpotential, mV at current density 10 mA/cm^2	Tafel slope, mV/dec
30	305	63
60	293	60
90	260	54
120	278	56

4. Conclusion

The treatment of nickel foam according to SILD method by $NiSO_4$ and $K_2S_2O_8$ solutions with the equilibrium pH value and pH = 10.5, respectively, allows synthesis a nanolayers of nickel oxyhydroxides on the surface of nickel foam. The nanolayers contains γ-NiOOH and $Ni_3O_2(OH)_4$ nanocrystals with nanosheet morphology, the sheets are 6 – 10 nm thick and are oriented mainly perpendicular to the substrate surface. The nanolayers shows electrocatalytic properties during the oxygen evolution reaction upon water splitting in the alkaline medium, which can be changed precisely by setting synthesis conditions, namely, the number of SILD cycles. For a number of samples, synthesized after 30 – 120 SILD cycles, it was found experimentally that in the oxygen evolution reaction the minimum overpotential value of 260 mV and the minimum value of Tafel slope of 54 mV/dec are achieved for the sample, synthesized after 90 SILD cycles.

Acknowledgement

This work was supported by the Russian Science Foundation (project No. 18-19-00370). We grateful to the Centres for X-ray Diffraction Studies, Nanotechnology and Physical Methods of Surface Investigation of Saint-Petersburg State University for their technical assistance with the investigation of the synthesized product.

References

[1] Bandal H., Koteshwara Reddy K., Chaugule A., Kim H. Iron-based heterogeneous catalysts for oxygen evolution reaction; change in perspective from activity promoter to active catalyst. *J. Power Sources*, 2018, **395**, P. 106–127.

[2] Hunter B.M., Winkler J.R., Gray H.B. Iron is the active site in nickel/iron water oxidation electrocatalysts. *Molecules*, 2018, **4**, P. 903–910.

[3] Ya Yan, Bao Yu Xia, Bin Zhao, Xin Wang. A review on noble-metal-free bifunctional heterogeneous catalysts for overall electrochemical water splitting. *J. Mater. Chem. A*, 2016, **4**, P. 17587–17603.

[4] Yuanyuan Ma, Xiaoli Dong, Renhe Wang, Duan Bin, Yonggang Wang, Yongyao Xia. Combining water reduction and liquid fuel oxidization by nickel hydroxide for flexible hydrogen production. *Energy Storage Materials*, 2018, **11**, P. 260–266.

[5] Sarycheva A.S., Semenova A.A., Goodilin E.A. Vapor phase SERS sensor based on mesoporous silica decorated with silver nanoparticles. *Nanosystems: Physics, Chemistry, Mathematics*, 2017, **8**(5), P. 579–585.

[6] Krasilin A.A., Gusarov V.V. Redistribution of Mg and Ni cations in crystal lattice of conical nanotube with chrysotile structure. *Nanosystems: Physics, Chemistry, Mathematics*, 2017, **8**(5), P. 620–627.
[7] Nguyen A.T., Phan Ph.H.Nh., Mittova I.Ya., Knurova M.V., Mittova V.O. The characterization of nanosized $ZnFe_2O_4$ material prepared by coprecipitation. *Nanosystems: Physics, Chemistry, Mathematics*, 2016, **7**(3), P. 459–463.
[8] Mingshu Xiao, Yanping Tian, Yuhua Yan, Kai Feng, Yuqing Miao. Electrodeposition of $Ni(OH)_2$/NiOOH in the presence of urea for the improved oxygen evolution. *Electrochimica Acta*, 2015, **164**, P. 196–202.
[9] Hidalgo-Acosta J.C., Scanlon M.D., Méndez M.A., Amstutz V., Vrube H., Opallo M., Giraulta H.H.. Boosting water oxidation layer-by-layer. *Phys. Chem. Chem. Phys.*, 2016, **13**, P. 9295–9304.
[10] Bryan H.R. Suryanto, Xunyu Lua, Chuan Zhao. Layer-by-layer assembly of transparent amorphous Co_3O_4 nanoparticles/graphene composite electrodes for sustained oxygen evolution reaction. *J. Mater. Chem. A*, 2013, **1**, P. 12726–12731.
[11] Lobinsky A.A., Tolstoy V.P. Red-ox reactions in aqueous solutions of $Co(OAc)_2$ and $K_2S_2O_8$ and synthesis of CoOOH nanolayers by the SILD method. *Nanosystems: Physics, Chemistry, Mathematics*, 2015, **6**(6), P. 1–7.
[12] Kuklo L.I., Tolstoy V.P. Successive ionic layer deposition of Fe_3O_4@$HxMoO_4 \cdot nH_2O$ composite nanolayers and their superparamagnetic properties. *Nanosystems: Physics, Chemistry, Mathematics*, 2016, **7**(6), P. 1050–1054.
[13] Tolstoy V.P., Kodintsev I.A., Reshanova K.S., Lobinsky A.A. A brief review of metal oxide (hydroxide)-graphene nanocomposites synthesis by layer-by-layer deposition from solutions and synthesis of CuO nanorods-graphene nanocomposite. *Rev. Adv. Mater. Sci.*, 2017, **49**, P. 28–37.
[14] Lobinsky A.A., Tolstoy V.P., Gulina L.B. A novel oxidation-reduction route for successive ionic layer deposition of $NiO_{1+x} \cdot nH_2O$ nanolayers and their capacitive performance. *Materials Research Bulletin*, 2016, **76**, P. 229–234.
[15] Mingjun Pang, Guohui Long, Shang Jianc, Yuan Ji, Wei Han, Biao Wang, Xilong Liu, Yunlong Xi. One pot low-temperature growth of hierarchical d-MnO_2 nanosheets on nickel foam for supercapacitor applications. *Electrochim. Act.*, 2015, **161**, P. 297–304.
[16] Lobinsky A.A., Tolstoy V.P., Gulina L.B. Direct synthesis of $Co_2Al(OH)_{7-2x}(CO_3)_x \cdot nH_2O$ layered doublehydroxide nanolayers by successive ionic layer deposition and their capacitive performance. *Applied Surface Science*, 2014, **320**, P. 609–613.
[17] Tolstoy V.P., Chernyshova I.V., Skryshevsky V.A. *Handbook of infrared spectroscopy of ultrathin films*. John Wiley & Sons, Inc., Hoboken, New Jersey, 2003, 710 p.
[18] Kashani M.M., Youzbashi A.A., Hashemzadeh F., Sabaghzadeh L. Structural properties of nickel hydroxide/oxyhydroxide and oxide nanoparticles obtained by microwave-assisted oxidation technique. *Powder Technol.*, 2013, **237**, P. 562–568.
[19] Cerc Korošeca R., Bukoveca P., Pihlar B., Šurca Vukb A., Orelb B., Dražič G. Preparation and structural investigations of electrochromic nanosized NiO_x films made via the sol-gel route. *Solid State Ionics*, 2003, **165**, P. 191–200.
[20] Ren Y., Chim W.K., Guo L., Tanoto H., Pan J., Chiam S.Y. The coloration and degradation mechanisms of electrochromic nickel oxide. Solar Energy Mater. *Solar Cells*, 2013, **116**, P. 83–88.
[21] Gui Chen, Lingjing Chen, Siu-Mui Ng, Tai-Chu Lau. Efficient chemical and visible-light-driven water oxidation using nickel complexes and salts as precatalysts. *Chem. Sus. Chem.*, 2014, **7**, P. 127–134.
[22] Biesinger M.C., Payne B.P., Grosvenor A.P., Lau L.W.M., Gerson A.R., Smart R.St.C. Resolving surface chemical states in XPS analysis of first row transition metals, oxides and hydroxides: Cr, Mn, Fe, Co and Ni. *Appl. Surf. Sci.*, 2011, **257**, P. 2717–2730.
[23] Fomanyuk S.S. Electrochromic and gasochromc properties thin films of nickel hydroxide. *Metal physics and advanced technologies*, 2011, **33**, P. 297–306.
[24] Kim B., Oh A., Kabiraz M.K., Hong Y., Joo J., Baik H., Choi S.-I., Lee K. NiOOH exfoliation-free nickel octahedra as highly active and durable electrocatalysts toward the oxygen evolution reaction in an alkaline electrolyte. *ACS Appl. Mater. Interfaces*, 2018, **10**, P. 10115–10122.
[25] Qiong Zhang, Cancan Zhang, Jianbo Liang, Penggang Yin, Yang Tian. Orthorhombic α-NiOOH nanosheet arrays: phase conversion and efficient bifunctional electrocatalysts for full water splitting. *ACS Sustainable Chem. Eng.*, 2017, **5**(5), P. 3808–3818.
[26] Diaz-Morales O., Ferrus-Suspedra D., Koper M.T.M. The importance of nickel oxyhydroxide deprotonation on its activity towards electrochemical water oxidation. *Chem Sci.*, 2016, **7**(4), P. 2639–2645.
[27] Cian-Tong Lu, Yen-Wen Chiu, Mei-Jing Li, Kan-Lin Hsueh, Ju-Shei Hung. Reduction of the electrode overpotential of the oxygen evolution reaction by electrode surface modification. *Int. J. of Electrochem.*, 2017, **2017**, 7494571.

NANOSYSTEMS: PHYSICS, CHEMISTRY, MATHEMATICS, 2018, 9 (5), P. 676–687

Formation mechanism, thermal and magnetic properties of $(Bi_{1-x}Sr_x)_{m+1}Fe_{m-3}Ti_3O_{3(m+1)-\delta}$ (m = 4 – 7) ceramics

N. A. Lomanova[1], M. V. Tomkovich[1], V. L. Ugolkov[2], M. P. Volkov[1], I. V. Pleshakov[1], V. V. Panchuk[3,4], V. G. Semenov[3,4]

[1]Ioffe Institute, 26 Polytekhnicheskaya Str., St. Petersburg 194021, Russian Federation

[2]Grebenshchikov Institute of Silicates Chemistry RAS, Adm. Makarova emb. 2, St. Petersburg, 199034, Russian Federation

[3]St. Petersburg State University, 7-9 Universitetskaya Emb., St. Petersburg, 199034, Russian Federation

[4]Institute for Analytical Instrumentation of RAS, St. Petersburg, ul. Ivana Chernykh, 31-33, lit. A., 198095, Russian Federation

natus@mail.ioffe.ru

DOI 10.17586/2220-8054-2018-9-5-676-687

Specific features of the formation of Aurivillius phases $(Bi_{1-x}Sr_x)_{m+1}Fe_{m-3}Ti_3O_{3(m+1)-\delta}$ ($m = 4-7$; $x = 0.0-0.7$) with a perovskite-like block having a nanometric thickness (h) of 2 – 3 nm are described. It has been established that the degree of isomorphous substitution in the bismuth sublattice and thermal stability of phases tend to reduce with the increasing h. It has been demonstrated that the magnetic ions inside the perovskite-like block can have antiferromagnetic interaction exchange that influences magnetic properties of the Aurivillius phases.

Keywords: aurivillius phases, nanolayers, perovskite-like nanoblocks, formation mechanism, thermal properties, magnetic properties.

Received: 21 August 2018

Revised: 26 September 2018

1. Introduction

The search for and design of new perovskite-like multiferroics is a promising trend in material science, as media possessing both ferroelectric and magnetic order are among the most highly demanded materials in modern technology [1–4]. The interest in layered Aurivillius phase multiferroics is determined by the possibility of the nanolayers' structural stabilization during the formation of those nanostructured materials [5, 6].

In general, the structures of the layered perovskite-like oxides such as the Aurivillius phases $Bi_{m+1}Fe_{m-3}Ti_3O_{3m+3}$ consist of alternating fluorite-like $\{(Bi_2O_2)^{2+}\}_\infty$ nanolayers and bismuth orthoferrite-based perovskite-like blocks of $\{(Bi_{m+1}Fe_{m-3}Ti_3O_{3m+1})^{2-}\}_\infty$ [7]. The thickness h of the perovskite-like blocks differs depending on the number of nanolayers m.

Bismuth orthoferrite-based ($BiFeO_3$) materials are known to have high values of the Neel temperature ($T_N \approx 370$ °C) and the Curie point ($T_C \approx 830$ °C), and currently have very attractive properties from a magnetoelectronics point of view. The main interest in the design of the Aurivillius phase-structured materials is also associated with the possibility of controlling their functional properties by varying the composition and thickness of the perovskite-like blocks up to nanometric values [1–6, 8–23]. In the Aurivillius phases with m=7-9, the perovskite-like block has a thickness of 3 – 4 nm [5].

In a unit cell of $Bi_{m+1}Fe_{m-3}Ti_3O_{3m+3}$, titanium and iron ions have octahedral structurally nonequivalent positions in the inner and outer layers of a perovskite-like block. It is shown in [6, 9–17] that the distribution of cations within a perovskite-like block depends on m and may affect stability and properties of the Aurivillius phases. In particular, it can influence the conductivity of these compounds and their magnetic behavior [13, 14, 17].

The Aurivillius phases' thermal behavior, phase equilibria and transformations in binary and quasi-binary sections of the Bi_2O_3–SrO–TiO_2–Fe_2O_3 system were studied in [10, 17–21]. It was demonstrated for the non-doped Aurivillius phases $Bi_{m+1}Fe_{m-3}Ti_3O_{3m+3}$ that an increase in the perovskite-like block thickness up to the nanosize values leads to a decrease in their thermal stability. The Aurivillius phases $Bi_{m+1}Fe_{m-3}Ti_3O_{3m+3}$ have the values of the temperature of transition to the magnetically ordered state (Neel point, T_N) within the 77–360 K range, and the ferroelectric transition temperature (Curie point, T_C) within the range of 923 – 1023 K [11, 14, 15, 17, 21–26]. Along with that, magnetic ordering may be expected around room temperature in substances with $h \geq 3$ ($m \geq 7$) [14]. Above T_C (923–1023 K), the structures of the Aurivillius phases $Bi_{m+1}Fe_{m-3}Ti_3O_{3m+3}$ are tetragonal, while in the ferroelectric phase the crystal lattice is either orthorhombic or monoclinic [15, 24].

The influence of isomorphous substitution in the Aurivillius phase structures on their phase transition temperatures requires systematic study.

The methods of synthesizing simple bismuth-containing perovskites and layered perovskite-like oxides, which make it possible to perform the synthesis of materials while varying their morphology and particle sizes within a broad range by changing technological parameters, are described, for example, in [27–40]. It is shown that irrespective of the technology, material formation begins at the melting temperature of the surface (non-autonomous) bismuth oxide-based phase, at which mass transfer in the reaction system is activated [41–43]. A study of the formation of phases with variable composition during the isomorphous substitution of ions in the Aurivillius phases structure requires refining of the mechanism of phase formation.

The present work offers a study of the formation processes, as well as of thermal and magnetic properties of ceramic materials based on the Aurivillius phases $(Bi_{1-x}Sr_x)_{m+1}Fe_{m-3}Ti_3O_{3(m+1)-\delta}$ with different degrees of isomorphous substitution for strontium in the bismuth sublattice.

2. Experimental

The method of solid-phase chemical reactions was used for producing samples with a nominal composition corresponding to $(Bi_{1-x}Sr_x)_{m+1}Fe_{m-3}Ti_3O_{3(m+1)-\delta}$ (m = 4, 5, 6, 7 and x = 0.0 – 0.7).

The reagents used were the bismuth oxide, iron(III) oxide, titanium oxide and strontium carbonate (all of the 99.9% purity).

The samples were heat treated in the "heating – isothermal exposure – cooling" mode. The isothermal exposure was performed from 500 – 1000 °C for 5 – 80 hours at each temperature, depending on the degree of synthesis completion. The phase composition of the samples at each stage of synthesis was determined by X-ray diffraction (XRD-7000 Shimadzu diffractometer, CuK_α-radiation). The unit cell parameters were calculated using the PDWin 4.0 software package.

The microstructure and elemental composition of the samples were determined by scanning electron microscopy and elemental energy-dispersive microanalysis (FEI Quanta 200 SEM with EDAX attachment). The chemical formula of the synthesized substance was calculated according to stoichiometry and based on the assumption that the oxidation states of Bi, Sr, Ti and Fe are III, II, IV and III, respectively. In order to determine the main phase, the sample area and individual smaller sites were subjected to the elemental analysis.

The samples' thermal behavior was studied by differential scanning calorimetry (DSC) using the NETZSCH STA 429 calorimeter, in air, with the heating rate of 10 °C/min. The changes in the samples' linear dimensions were determined by dilatometry using the NETZSCH DIL 402 E dilatometer, in air, with the heating rate of 10 °C/min. A pellet-shaped sample, 5 mm in diameter and 3 mm thick, was used. The linear thermal dilation coefficient (α_t) was determined within the 200 – 400 °C range, in which phase transformations are absent.

The Mössbauer spectroscopy of the samples was accomplished using the WISSEL spectrometer in the absorption geometry at room temperature, using a ^{57}Co(Rh) source. The isomer shift values were determined with reference to the α-Fe isomer shift.

The samples' magnetic behavior was determined using a Physical Properties Measuring System, Quantum Design vibration magnetometer. Specific magnetization M as a function of temperature was studied in the presence of a constant field H = 500 Oe and in the zero field cooling (ZFC) mode. The $M(H)$ dependence was measured at 5 and 300 K within the 0 – 50 kOe range.

3. Results and discussion

The Aurivillius phase-structured solid solutions $(Bi_{1-x}Sr_x)_{m+1}Fe_{m-3}Ti_3O_{3(m+1)-\delta}$ have been synthesized in the Bi_2O_3–SrO–TiO_2–Fe_2O_3 system. The value of δ can vary depending on the charge compensation character during formation of the $(Bi_{1-x}Sr_x)_{m+1}Fe_{m-3}Ti_3O_{3(m+1)-\delta}$ solid solution. If the charge is compensated at the expense of the change in the iron ions charge from Fe^{3+} to Fe^{4+}, then $\delta = 0$, while in the case of oxygen vacancies creation $\delta = 0.5x(m+1)$. The possible character of the charge compensation may be determined from the Mössbauer data given below.

As is shown in [19], the structure of the homologous series $(Bi_{1-x}Sr_x)_{m+1}Fe_{m-3}Ti_3O_{3(m+1)-\delta}$ contains a perovskite-like block with the number of nanolayers m = 4 – 7 and thickness h of about 2 – 3 nm. Along with that, the limit of isomorphous substitution of bismuth for strontium (x) depends on the perovskite-like block thickness h. The $x(m)$ and, correspondingly, $x(h)$ dependences are illustrated in Fig. 1. It can be noted that the substitution of bismuth for strontium in the Aurivillius phases with the given composition occurs at an m up to ~7 (h ~3 nm). In this case, the isomorphous capacity of the system decreases with increasing thickness of the perovskite-like block to a nanosize value, and this influences the formation mechanisms of these substances, as well as thermal

and magnetic properties of ceramic materials based on them. The experimental results presented below have been analyzed in comparison with the corresponding data on the features of the solid-phase synthesis, structure and properties of the non-doped Aurivillius phases $Bi_{m+1}Fe_{m-3}Ti_3O_{3(m+1)}$, described in [6, 10, 14, 17, 21]. Synthesis conditions, elemental and phase compositions of the obtained samples are presented in Table 1.

TABLE 1. Synthetic conditions and sample composition

No.	Nominal composition	m	Synthesis conditions	Composition of the Aurivillius phases $(Bi_{1-x}Sr_x)_{m+1}Fe_{m-3}Ti_3O_{3(m+1)-\delta}$ after EDS-analysis	$m^{*)}$	Phase composition by XRD analysis
1	$Bi_5FeTi_3O_{15}$	4	900 °C, 5 h	$Bi_{5.1\pm0.1}Fe_{1.2\pm0.1}Ti_3O_{15.5\pm0.3}$	4.1	A
1-1	$Bi_{4.9}Sr_{0.1}FeTi_3O_{14.75}$	4	900 °C, 10 h	$Bi_{5.3\pm0.3}Sr_{0.2\pm0.1}Fe_{1.2\pm0.1}Ti_3O_{16.0\pm0.3}$	4.3	A
1-2	$Bi_{4.7}Sr_{0.3}FeTi_3O_{14.25}$	4	1000 °C, 10 h	$Bi_{4.9\pm0.2}Sr_{0.3\pm0.2}Fe_{1.1\pm0.3}Ti_3O_{15.3\pm0.2}$	4.1	A
1-3	$Bi_{4.5}Sr_{0.5}FeTi_3O_{13.75}$	4	1000 °C, 10 h	$Bi_{4.7\pm0.2}Sr_{0.4\pm0.2}Fe_{1.3\pm0.2}Ti_3O_{15.4\pm0.2}$	4.2	A
1-4	$Bi_{4.3}Sr_{0.7}FeTi_3O_{13.25}$	4	1000 °C, 10 h	$Bi_{4.6\pm0.1}Sr_{0.6\pm0.1}Fe_{1.1\pm0.2}Ti_3O_{15.2\pm0.1}$	4.1	A
1-5	$Bi_{4.1}Sr_{0.9}FeTi_3O_{12.75}$	4	1000 °C, 10 h	$Bi_{3.9\pm0.2}Sr_{1.2\pm0.4}Fe_{1.2\pm0.2}Ti_3O_{14.9\pm0.1}$	4.1	A, P, M
2	$Bi_6Fe_2Ti_3O_{18}$	5	890 °C, 5 h	$Bi_{5.8\pm0.2}Fe_{1.8\pm0.2}Ti_3O_{17.4\pm0.2}$	4.8	A
2-1	$Bi_{5.7}Sr_{0.3}Fe_2Ti_3O_{17.1}$	5	900 °C, 10 h	$Bi_{5.9\pm0.2}Sr_{0.3\pm0.1}Fe_{2.3\pm0.1}Ti_3O_{18.6\pm0.2}$	5.2	A, M
3	$Bi_7Fe_3Ti_3O_{21}$	6	870 °C, 5 h	$Bi_{7.4\pm0.3}Fe_{3.0\pm0.2}Ti_3O_{21.6\pm0.2}$	6.3	A
3-1	$Bi_{6.7}Sr_{0.3}Fe_3Ti_3O_{19.95}$	6	900 °C, 20 h	$Bi_{6.8\pm0.2}Sr_{0.4\pm0.1}Fe_{3.2\pm0.2}Ti_3O_{21.4\pm0.3}$	6.2	A, M, S
4	$Bi_8Fe_4Ti_3O_{24}$	7	870 °C, 5 h	$Bi_{8.0\pm0.1}Fe_{4.2\pm0.2}Ti_3O_{24.3\pm0.3}$	7.1	A, M
4-1	$Bi_{7.7}Sr_{0.3}Fe_4Ti_3O_{22.8}$	7	900 °C, 20 h	$Bi_{7.5\pm0.1}Sr_{0.4\pm0.1}Fe_{4.0\pm0.2}Ti_3O_{23.7\pm0.1}$	7.0	A, M
			870 °C, 10 h	$Bi_{6.5\pm0.1}Sr_{0.4\pm0.2}Fe_{2.2\pm0.2}Ti_3O_{19.5\pm0.3}$	5.5	A, P
				$Bi_{7.5\pm0.1}Sr_{0.4\pm0.1}Fe_{3.2\pm0.1}Ti_3O_{22.5\pm0.5}$	6.5	
				$Bi_{1.1\pm0.1}Sr_{0.1\pm0.1}Fe_{0.7\pm0.1}Ti_{0.3}O_{3.4\pm0.2}$	—	

*) average value from EDS- analysis. Notation: A – Aurivillius phases, P – $BiFeO_3$, M – $Bi_2Fe_4O_9$, S – $Bi_{25}FeO_{39}$

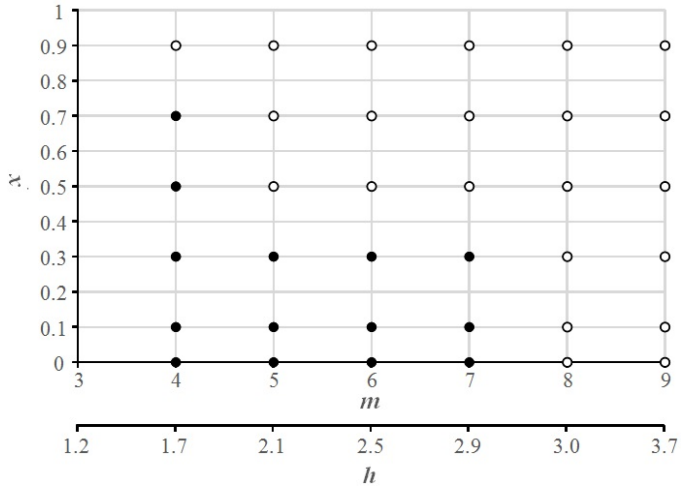

FIG. 1. Scheme for isomorphous substitution of bismuth by strontium in Aurivillius phases $(Bi_{1-x}Sr_x)_{m+1}Fe_{m-3}Ti_3O_{3(m+1)-\delta}$ structure

X-ray diffractograms of the Sr-doped Aurivillius phases $(Bi_{1-x}Sr_x)_{m+1}Fe_{m-3}Ti_3O_{3(m+1)-\delta}$, presented in Fig. 2 illustrate the phase composition of the samples at a synthesis stage from 500 – 1000 °C. At 500 – 600 °C, that is, after melting of the bismuth oxide-based surface phase [28, 33] and hence, after activation of mass transfer in the reaction system [41–43], α-Bi_2O_3 interacts with titanium and iron oxides yielding the main phase $Bi_{25}FeO_{39}$.

At 700 °C, small amounts of $BiFeO_3$ and Aurivillius phases start to appear in the reaction system (Fig. 2). The sillenite-structured $Bi_{25}FeO_{39}$ and perovskite-structured $BiFeO_3$ are the intermediate products in the synthesis of the Aurivillius phases. Their formation in the reaction system facilitates the formation of a layered perovskite-like structure with a predetermined composition due to a gradual rearrangement in the first coordination sphere of bismuth [28]. According to the quantitative X-ray phase analysis, the share of $BiFeO_3$ increases along with the increasing Sr content in the reaction system, and with the increasing h. At temperatures above the initiation of $Bi_{25}FeO_{39}$ decomposition (above 700 °C), diffractograms of the samples with $m = 4$ show reflexes of only Aurivillius phases and $BiFeO_3$, their ratio being the evidence of the gradual formation of a layered perovskite-like structure. Formation of the target product occurs at temperatures above that of metastable $BiFeO_3$ decomposition (855±5 °C [39]).

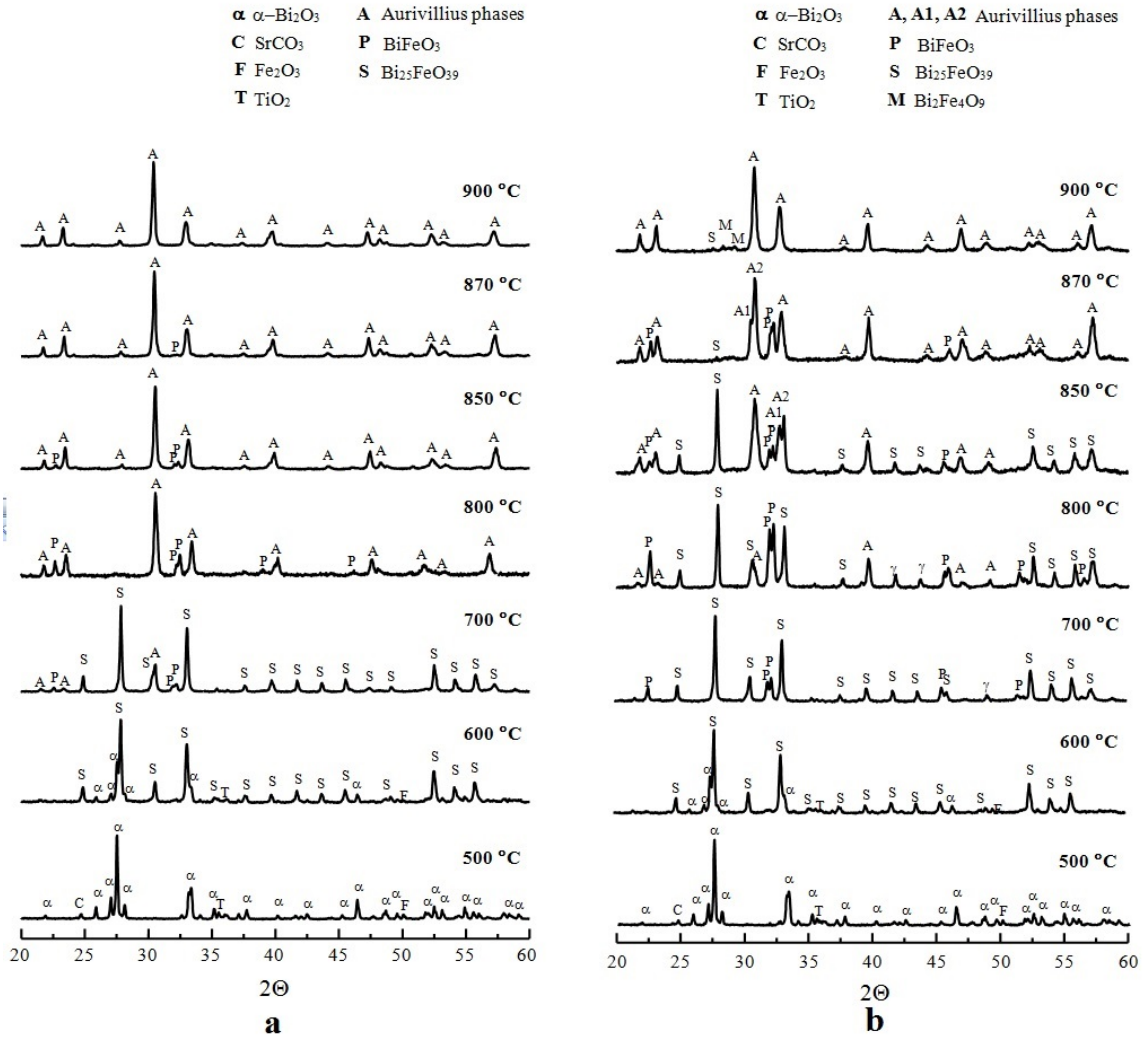

FIG. 2. X-ray diffractograms (λ= 1.54056 Å) of $(Bi_{1-x}Sr_x)_{m+1}Fe_{m-3}Ti_3O_{3(m+1)-\delta}$ after thermal treatment at 500, 600, 700, 800, 850, 870 and 900 °C: a – $Bi_{4.7}Sr_{0.3}FeTi_3O_{15-\delta}$ ($m = 4$); b – $Bi_{6.7}Sr_{0.3}Fe_3Ti_3O_{21-\delta}$ ($m = 7$)

Diffractograms of the multilayered Aurivillius phases with $m > 5$ ($h > 2.5$ nm) show that the process of $Bi_{25}FeO_{39}$ decomposition proceeds gradually up to 850°C, and the substance of this phase is spent to increase the share of $BiFeO_3$ in the reaction system. At 870 °C, the diffractogram of a $Bi_{7.7}Sr_{0.3}Fe_4Ti_3O_{24-\delta}$ sample with $m = 7$ shows that the two main products are $(Bi_{1-x}Sr_x)_{m+1}Fe_{m-3}Ti_3O_{3(m+1)-\delta}$ and the perovskite-like $BiFeO_3$. It should be noted that the reflexes observed at the intermediate stages of synthesis correspond to the Aurivillius phases with a smaller m, which is confirmed by the elemental analysis for the sample with $m = 7$, heat treated at 870 °C (Table 1).

When the temperature is further increased, the perovskite-like $BiFeO_3$ builds into the layered structure, and it leads to the formation of the target product ($Bi_{7.3}Sr_{0.3}Fe_4Ti_3O_{24-\delta}$) with an output around 95%. Some quantity of the impurity phases on the basis of $Bi_{25}FeO_{39}$, and $Bi_2Fe_4O_9$ resulting from its decomposition, are observed at the final stages of $(Bi_{1-x}Sr_x)_{m+1}Fe_{m-3}Ti_3O_{3(m+1)-\delta}$ synthesis. Their quantity is increasing along with the number of layers m and, hence thickness of the nano-sized perovskite-like block. In contrast to the Sr-doped Aurivillius phases, the $Bi_{m+1}Fe_{m-3}Ti_3O_{3(m+1)}$ homologous series can have a higher degree of homogeneity, having been synthesized at a lower temperature and a shorter isothermal exposure (see Table 1).

X-ray diffractograms of the obtained materials with the phase and elemental composition corresponding to the target product output of over 90 % (see Table 1) are presented in Fig. 3(a,b). It may be noted that the Sr-doped Aurivillius phases with $m > 5$ perovskite-like layers contain a small number of impurity phases (Fig. 3b). The data on the orthorhombic unit cell volume (Table 2) suggest that it poorly depends on the isomorphous substitution in the structure and increases with the increasing m.

TABLE 2. Sample characteristics

No	Samples	m	V^*, A^3	T_K, °C	T_{dec}, °C	T_S, °C	α_t, 1/K	M,emu/g, at 20kOe
1	$Bi_5FeTi_3O_{15}$	4	1226	740 [7, 23]	1100	840 [7, 20, 21]	10 [21]	0.10
1-1	$Bi_{4.9}Sr_{0.1}FeTi_3O_{15-\delta}$	4	1224	740	1050	770	9	—
1-2	$Bi_{4.7}Sr_{0.3}FeTi_3O_{15-\delta}$	4	1222	710 [7]	1080	765	10	0.10
1-3	$Bi_{4.5}Sr_{0.5}FeTi_3O_{15-\delta}$	4	1218	700	1130	700	8	0.10
1-4	$Bi_{4.3}Sr_{0.7}FeTi_3O_{15-\delta}$	4	1213	—	1150	650	9	0.11
2	$Bi_6Fe_2Ti_3O_{18}$	5	1520	690 [7, 23]	980 [7, 20, 21]	720 [7, 20, 21]	13 [21]	—
2-1	$Bi_{5.3}Sr_{0.3}Fe_2Ti_3O_{18-\delta}$	5	1516	625 [19]	900 [19]	680	10	0.13
3	$Bi_7Fe_3Ti_3O_{21}$	6	1710	682 [7]	980 [7, 20, 21]	635 [7, 20, 21]	11 [21]	0.13 [14]
3-1	$Bi_{6.7}Sr_{0.3}Fe_3Ti_3O_{21-\delta}$	6	1708	620 [19]	940 [19]	660	8	—
4	$Bi_8Fe_4Ti_3O_{24}$	7	1978	665 [7]	970[7, 21]	765 [7, 20, 21]	12 [21]	0.15 [14]
4-1	$Bi_{7.3}Sr_{0.3}Fe_4Ti_3O_{24-\delta}$	7	1965	590 [19]	935[19]	590	10	0.14

Typical SEM images of the samples after the final stage of heat treatment (Fig. 4) show the lamellar morphology of the resulting ceramic materials. The elemental chemical analysis data show that the main phase in the samples at the final stage of synthesis corresponds to the target product sufficiently well (Table 1). In order to refine the mechanism of formation of the layered perovskite-like structure, the composition of the $Bi_{7.3}Sr_{0.3}Fe_4Ti_3O_{24-\delta}$ sample ($m = 7$) was analyzed in more detail at the intermediate stage of synthesis. According to the obtained result, at 870°C the sample contains the Aurivillius phases $(Bi_{0.6}Sr_{0.4})_{m+1}Fe_{m-3}Ti_3O_{3(m+1)-\delta}$ with $m < 7$, that is, with a smaller m value than that specified by stoichiometry (Table 1). Along with these phases, the bismuth orthoferrite-based solid solution $Bi_{1.1}Sr_{0.1}Fe_{0.7}Ti_{0.3}O_{2.7}$ is recorded. Under further thermal treatment, a part of its substance is used in the Aurivillius phase formation, while another part is engaged in formation of a mullite-like impurity phase $Bi_{2-x}Sr_xFe_4O_{9-x}$. The small quantity of this phase prevents precise determination of its composition. However, it was shown in [19] that increasing the quantity of the impurity in the system, along with the increase in m and the limited solubility of $(Bi_{1-x}Sr_x)_{m+1}Fe_{m-3}Ti_3O_{3(m+1)-\delta}$, allowed a suggestion that one of the factors that complicates synthesis of the multilayered Sr-doped Aurivillius phases is the structural stabilization of impurity phases under isomorphous substitution in the bismuth sublattice.

Figure 5 and Table 2 present the results of the Sr-doped Aurivillius phase's thermal analysis. The influence of the isomorphous substitution in the bismuth sublattice on the thermal behavior of $(Bi_{1-x}Sr_x)_{m+1}Fe_{m-3}Ti_3O_{3(m+1)-\delta}$ has been considered for the first time in [19] for the fixed x value of 0.3. It was shown that such a degree of substitution makes the Curie point lower if compared with that for the non-doped Aurivillius phases, and the temperature of their decomposition insignificantly higher (see Table 2). The influence of isomorphous substitution on phase transformations and on the decomposition temperature has been studied for the four-layered Sr-doped Aurivillius phase $Bi_{5-x}Sr_xFeTi_3O_{15-\delta}$ (x = 0.0, 0.3, 0.5, 0.7), because this material shows the maximum degree of isomorphous substitution in the bismuth sublattice (see Fig. 5a).

The DSC curves for the $Bi_{5-x}Sr_xFeTi_3O_{15-\delta}$ samples show small endothermal effects in the medium temperatures domain (T_C =650 – 750 °C, which correspond to a phase transition of the second kind from orthorhombic symmetry to tetragonal symmetry (Curie point) [22, 24]. Thermal effects in the high temperature domain

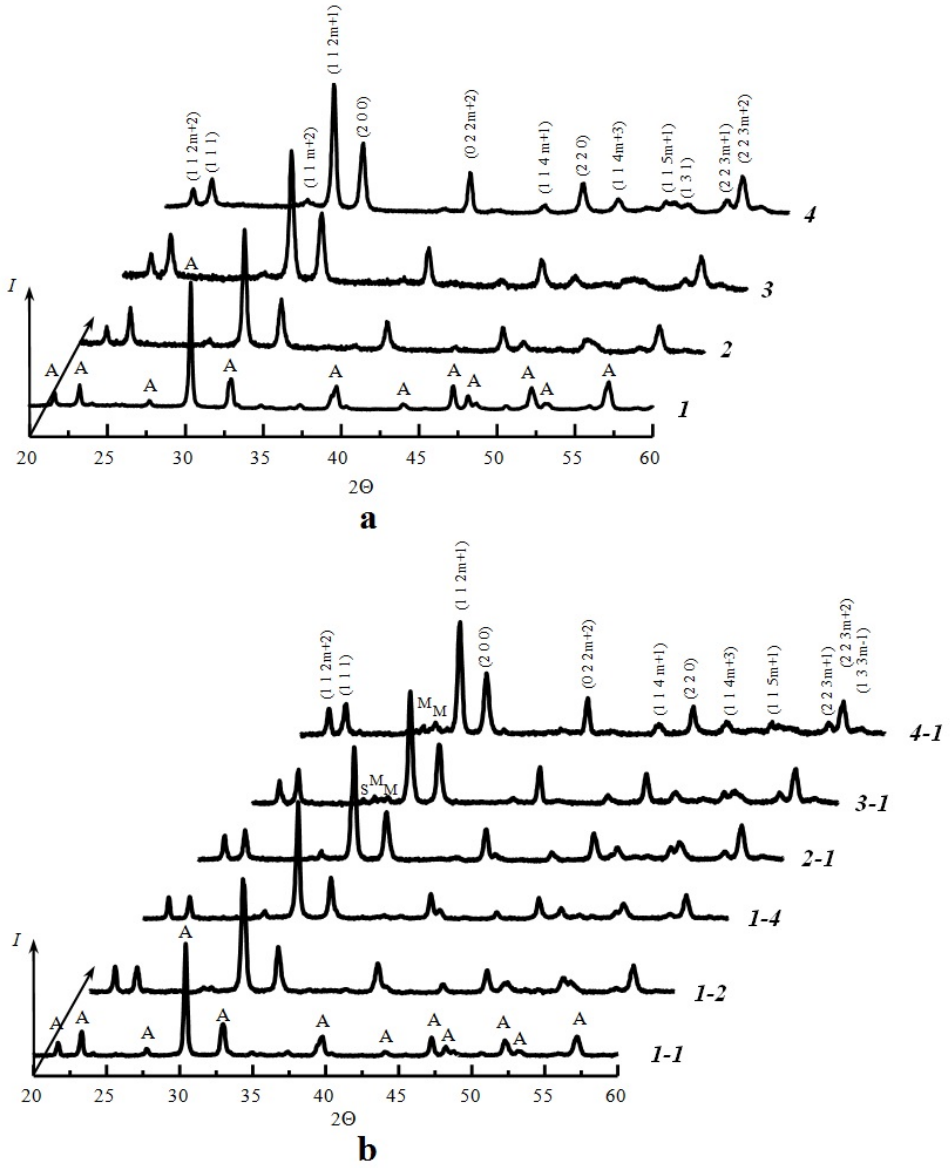

FIG. 3. X-ray diffractograms (λ= 1.54056 Å) of $(Bi_{1-x}Sr_x)_{m+1}Fe_{m-3}Ti_3O_{3(m+1)-\delta}$ after thermal treatment at 900°C: a – un-doped samples; b – Sr-doped samples. The curve number corresponds to the sample number (Table 1). Notation: A – Aurivillius phases, P – $BiFeO_3$, M – $Bi_2Fe_4O_9$, S – $Bi_{25}FeO_{39}$

($T_{dec} > 900$ °C) are related to the Aurivillius phase decomposition [10, 18, 20, 21]. As can be seen, a peak at 740±5°C is well-expressed for the non-doped sample $Bi_{5-x}Sr_xFeTi_3O_{15-\delta}$ (x = 0.0). For the Sr-doped Aurivillius phase, thermal effects at the Curie point are more diffuse. Along with that, no significant difference is observed for the T_C value in the case of bismuth ion substitution with a larger-radius ion ($r_{Bi3+(VIII)}$=1.25 Å, $r_{Sr2+(VIII)}$=1.39 Å [44]). It follows from the analysis of high-temperature effects in DSC curves at different x values, that T_{dec} gradually grows together with the increasing degree of bismuth substitution with Sr, and in fact does not depend on thickness of the perovskite-like block at $m > 5$.

The curves of the Sr-doped Aurivillius phases' thermal expansion $dL/L_0(T)$ are presented in Fig. 5b. The sintering initiation temperature (T_S), was determined from the maximum of the $dL/L_0(T)$ curves. It lies within the 590 – 765 °C interval and tends to decrease with fewer fusible components in the system, that is, of bismuth and strontium oxides which localize on the grains' surface, as a rule. As is seen from Table 2, there is a correlation between T_S and T_C, which apparently suggests the activation of diffusion in the reaction system during a structural transition. The coefficient of linear thermal expansion of the obtained materials is $\alpha_t = 9 \pm 1 \cdot 10^{-6}$ K^{-1} (see

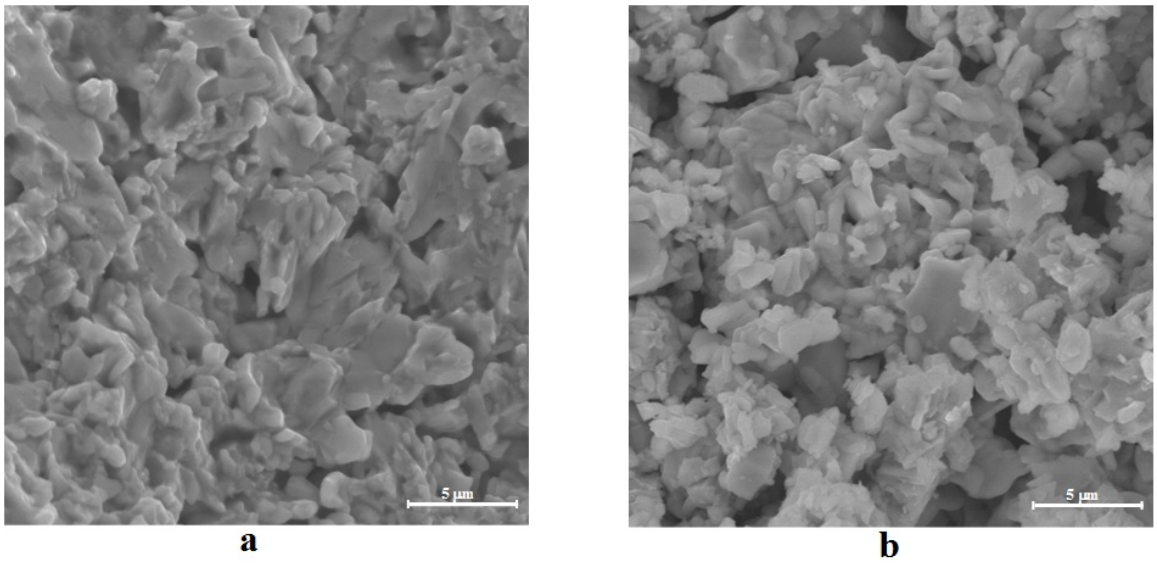

FIG. 4. SEM-images of $(Bi_{1-x}Sr_x)_{m+1}Fe_{m-3}Ti_3O_{3(m+1)-\delta}$ (m = 7) after its heat treatment at 900 °C: a – un-doped samples; b – Sr-doped samples

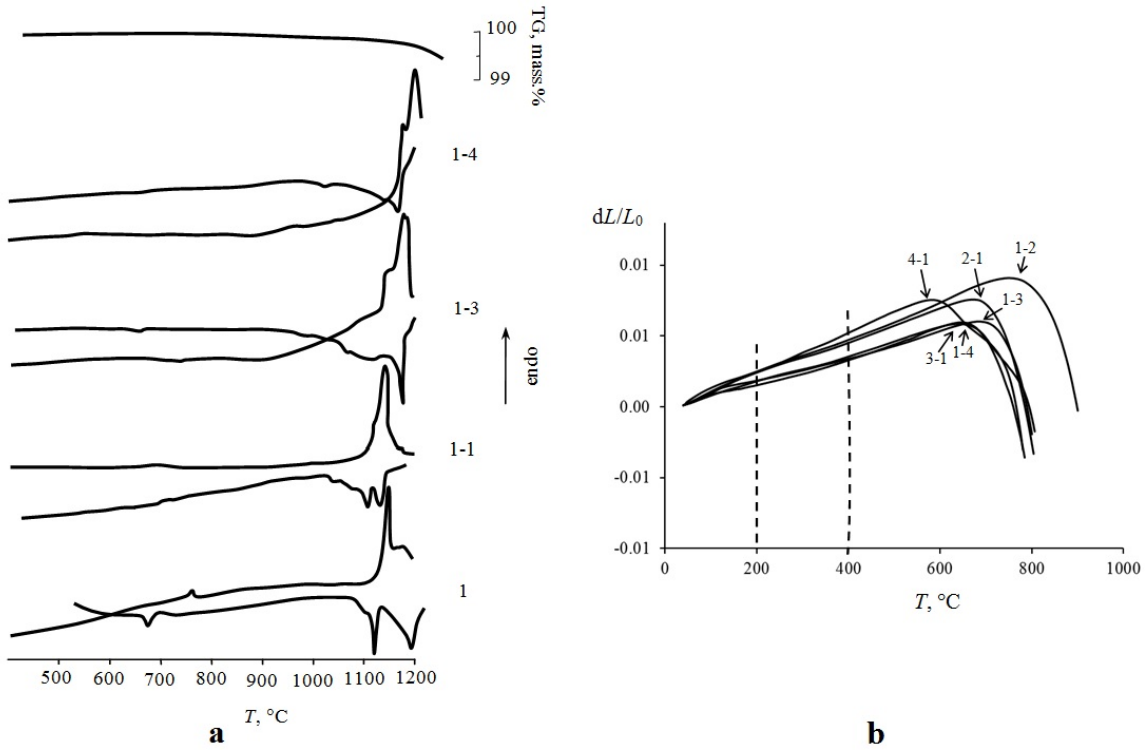

FIG. 5. Thermal analysis: a – DSC and TG curves of $(Bi_{1-x}Sr_x)_{m+1}Fe_{m-3}Ti_3O_{3(m+1)-\delta}$ with $m = 4$; b – dilatometric curves of the samples with different m. The curve number corresponds to the sample number (Table 1)

Table 2). A comparison of the obtained α_t with its values for the non-doped Aurivillius phases given in [21] shows that it poorly depends on the degree of isomorphous substitution and the number of layers in the perovskite-like block.

A Mössbauer study has been performed to analyze the effect of isomorphous substitution in the bismuth sublattice on the state of iron ions and on the character of cationic distribution over the structurally nonequivalent octahedral positions in the inner (I) and outer (II) layers of the perovskite-like block. The Mössbauer data for the studied Sr-doped Aurivillius phases with m = 4 – 7 are presented in Fig. 6. The spectral parameters for the samples given in Table 3 show that the obtained materials do not contain magnetically ordered phases at room temperature. The isomer shift (IS) and quadrupole splitting (QS) values determined for $(Bi_{1-x}Sr_x)_{m+1}Fe_{m-3}Ti_3O_{3(m+1)-\delta}$ (x = 0 – 0.3; m = 4 – 7), are characteristic for the Fe^{3+} ions in an octahedral environment (see Table 3), that is, the charge compensation at the substitution of Bi^{3+} for Sr^{2+} occurs mainly at the expense of vacancies appearing in the oxygen sublattice. The materials based on the four-layer Aurivillius phase $Bi_{5-x}Sr_xFeTi_3O_{15-\delta}$ (x = 0.5, 0.7) contain a small amount of iron as Fe^{4+}, it being an evidence of the possible charge compensation in presence of high strontium content in the solid solution, and at the expense of the conversion of some Fe^{3+} ions into Fe^{4+}.

TABLE 3. Mössbauer spectral parameters for room temperature samples

	Samples	m	Doublet	Isomer shift, mm/s	Quadrupole splitting, mm/s	Integral intensities ratio, %
1	$Bi_5FeTi_3O_{15}$	4	1	0.37	0.60	76
			2	0.17	0.58	24
1-2	$Bi_{4.7}Sr_{0.3}FeTi_3O_{15-\delta}$	4	1	0.38	0.60	93
			2	0.20	0.73	12
1-3	$Bi_{4.5}Sr_{0.5}FeTi_3O_{15-\delta}$	4	1	0.36	0.60	91
			2	−0.02	1.68	9
1-4	$Bi_{4.3}Sr_{0.7}FeTi_3O_{15-\delta}$	4	1	0.35	0.59	91
			2	0.01	1.72	9
4	$Bi_8Fe_4Ti_3O_{24}$	7	1	0.38	0.57	73
			2	0.31	0.61	27
4-1	$Bi_{7.3}Sr_{0.3}Fe_4Ti_3O_{24-\delta}$	7	1	0.38	0.60	93
			2	0.20	0.73	7

The general shape of the IS(m) and QS(m) curves for the non-doped compounds $Bi_{m+1}Fe_{m-3}Ti_3O_{3(m+1)}$, plotted with an account for the parameters of spectra of iron ions in positions I and II, is described in [6,9,11]. The Sr-doped Aurivillius phases show similar dependences, however with a number of peculiarities. For instance, for the inner layer of the perovskite-like block (I) with the highest concentration of the magnetic ions, the IS value is independent of both m and the degree of isomorphous substitution x. The outer layers of the perovskite-like block (II) in the Aurivillius phases are presumably subjected to structural distortion, and with m >5 significantly differ in the IS and QS values (Fig. 6a,b). This is especially expressed in the Aurivillius phase with m = 4, the structure of which contains only 25 % Fe^{3+} ions, which are apparently localized predominantly at the internal positions of the perovskite-like block (Fig. 6). The isomorphous substitution in the bismuth sublattice insignificantly deflects this distribution from the ideal, while for the Aurivillius phases with $m > 5$ this deflection is more apparent. Therefore, the difference between the average charge state and symmetry of the environment of iron ions in positions I and II is more noticeable in solid solutions with $m = 4$ if compared with the phases with $m \geq 5$. The multilayered Aurivillius phases have iron ion content $>$ 40 %, which are apparently distributed less orderly within the perovskite-like block.

The IS values determined for the iron ions in positions I and II converge for the non-doped Aurivillius phases with $m > 5$. The IS value for positions I and II poorly depends on m for the phases $(Bi_{1-x}Sr_x)_{m+1}Fe_{m-3}Ti_3O_{3(m+1)-\delta}$ with $x = 0.3$. Apparently, such a degree of bismuth substitution for strontium has no influence on the effective charge of iron ions in the perovskite-like block inner layer and weakly increases the charge in the external layers. As was previously mentioned, the $Bi_{5-x}Sr_xFeTi_3O_{15-\delta}$ solid solutions ($m = 4$) have a large isomorphous capacity, and the dependence of IS and QS on x is more pronounced in them (see inserts in Fig. 6a,b). It can be seen that the IS and QS values determined for the iron ions in the inner position I, are also independent of x. The greatest difference in the value of the iron ions effective charge is observed for the external position (II) at x=0.5, 0.7

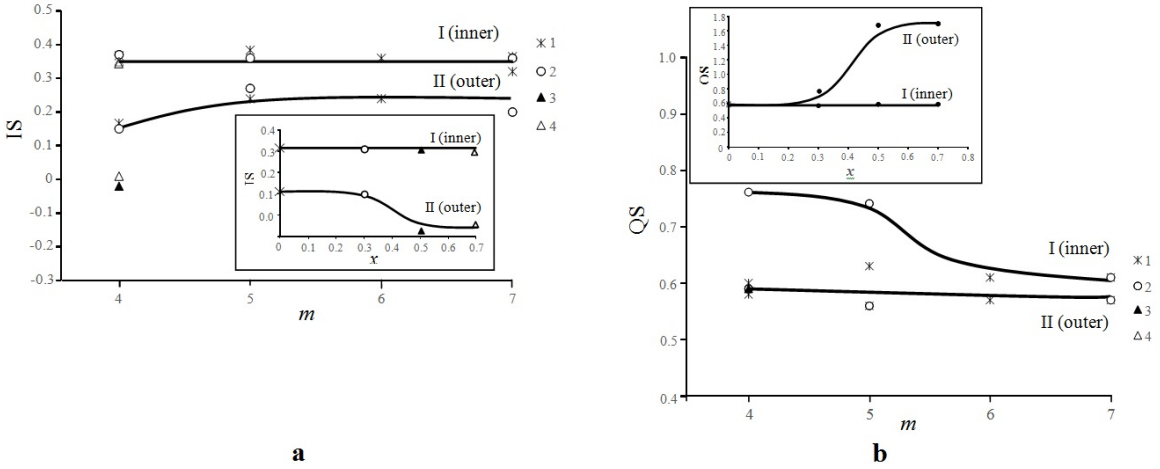

FIG. 6. Mössbauer spectral parameters of $(Bi_{1-x}Sr_x)_{m+1}Fe_{m-3}Ti_3O_{3(m+1)-\delta}$: a – the dependence of isomer shift (IS) value on m (insert: the dependence of IS of the Aurivillius phase with $m = 4$ on x); b – the dependence of quadrupole splitting (QS) value on m (insert: the dependence of QS of the Aurivillius phase with $m = 4$ on x). 1 – un-doped Aurivillius phases; 2 – Sr-doped Aurivillius phases with m = 4 – 7, x = 0.3; 3 – Sr-doped Aurivillius phases with $m = 4$, $x = 0.5$; 4 – Sr-doped Aurivillius phases with $m = 4$, $x = 0.7$

(see insert in Fig. 6a), which is accompanied by an increase in the symmetry of their environment (see insert in Fig. 6b). Apparently, this may indicate the dominating localization of strontium atoms in the outer layers of the perovskite-like block.

The results of magnetic measurements of the obtained materials are shown in Figs. 7,8 (for the samples' composition, see Table 1). It can be seen that at 5 K, the samples have a pronounced dependence of the $M(H)$ magnetization curves shape on m. For the samples with $m > 5$, regardless of the degree of isomorphous substitution, there is a deviation from linearity that decreases with the increasing h. It should be noted that even at low temperatures and very large fields, magnetic saturation is not achieved. For the Aurivillius phases with $m > 5$, the $M(H)$ dependences are close to linear. At $T = 5$ K, the hysteresis loops are absent in all samples, which can indicate their paramagnetic state at any temperature, however a noticeable deviation from linearity for the compounds with $m \leq 5$ suggests that this is not true, at least for these samples. When the temperature increases up to 300 K, all the $M(H)$ dependences become linear. At 300 K, the magnitude of the Aurivillius phase's magnetic moment obtained in the present work, as well as of those described in [14], is 0.1 – 0.2 emu/g at 20 kOe (see Table 2). As can be seen, the essential differences in their composition and, correspondingly, the differences in the Fe^{3+} magnetic ion content in the structure, practically do not affect the value of M near room temperature.

Figure 8a shows the temperature dependences of the specific magnetization $M(T)$, the shape of which is typical for paramagnets. The values of the magnetic responses differ significantly in this case. For instance, the Aurivillius phases with $m = 7$ have approximately four-fold less magnetization at $T = 5$ K than the phases with $m = 4$. However, the analysis performed on the reverse temperature dependences of the magnetization $1/M(T)$ (Fig. 8b) shows that it is impossible to isolate a linear section, that is, it is impossible to accurately describe the obtained curves by the Curie–Weiss law.

Nevertheless, it is possible to note their similarity, from which only the $m = 7$ Aurivillius phases sharply deviate. The violation of the strictly paramagnetic behavior can be due to the presence of a magnetically ordered state or, more likely, magnetic fluctuations. Although a number of studies have reported that $Bi_5Ti_3FeO_{15}$ ($m = 4$) demonstrates paramagnetic behavior without the long-range magnetic order up to very low temperatures [16, 26], there are indications of the appearance of an antiferromagnetic transition in the 50 – 80 K range. A theoretical analysis of [12] shows that the magnetic behavior of the given compound can be described as a short-range (localized) antiferromagnetic interaction, which confirms the assumption made.

According to Mössbauer data, the magnetic ions of the non-doped and Sr-doped Aurivillius phases with $m < 5$ are distributed over the perovskite-like block more orderly. Magnetometric results show the greatest deviation from paramagnetic behavior particularly for these samples. Taking into account the fact that the exchange interaction is most strongly manifested in the nearest magnetic ion neighbors, it can be concluded that in the case when antiferromagnetic fluctuations exist in the system, they should be localized predominantly inside these blocks.

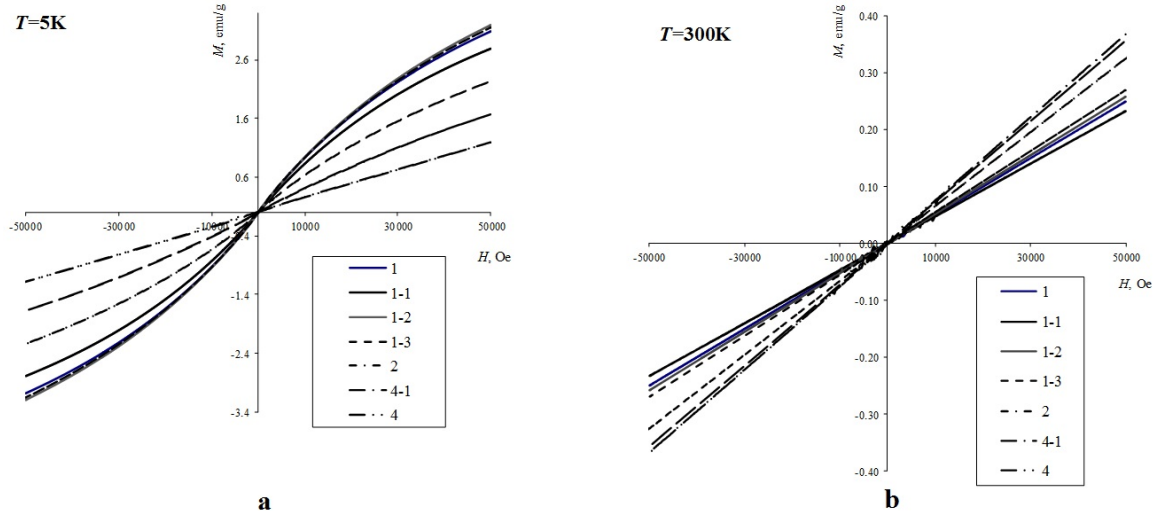

FIG. 7. Magnetization curves of $(Bi_{1-x}Sr_x)_{m+1}Fe_{m-3}Ti_3O_{3(m+1)-\delta}$ measured at 2K (a) and 300K (b). The curve number corresponds to the sample number (Table 1)

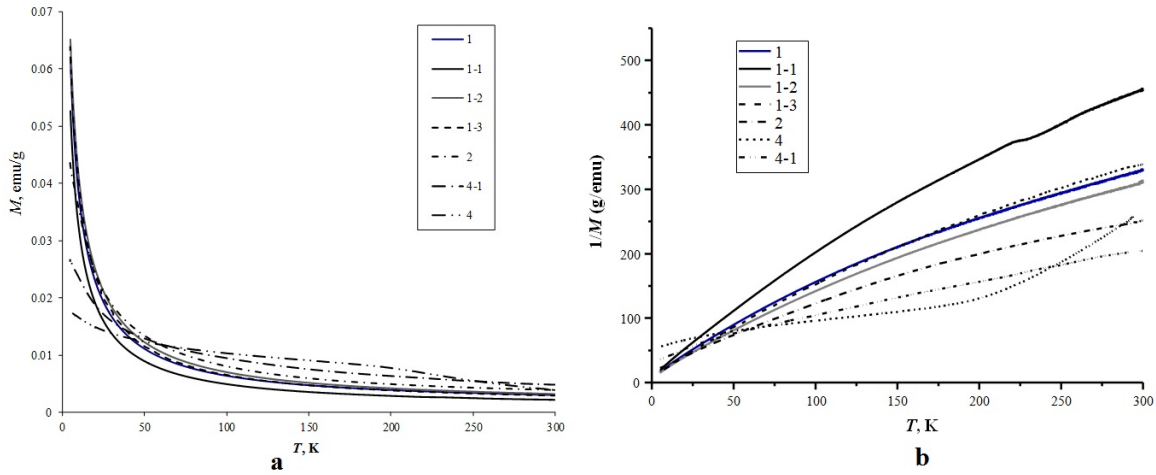

FIG. 8. Temperature dependences of inverse magnetization (a) and inverse magnetization (b) of $(Bi_{1-x}Sr_x)_{m+1}Fe_{m-3}Ti_3O_{3(m+1)-\delta}$. The curve number corresponds to the sample number (Table 1)

Thus, the magnetic characteristics of the structures based on the Sr-doped Aurivillius phases have been obtained and found to be associated with the presence of a paramagnetic system formed by the magnetic moments of iron ions, between which, there exists an exchange interaction of the antiferromagnetic type. The features of the magnetic behavior of these phases can be presumably explained by magnetic fluctuations.

4. Conclusions

The features of the solid-phase formation of the layered perovskite-like oxides of the Aurivillius phase type $(Bi_{1-x}Sr_x)_{m+1}Fe_{m-3}Ti_3O_{3(m+1)-\delta}$ (x = 0.0 – 0.7; m = 4 – 7) with a perovskite-like block ≈2 – 3 nm thick have been described. The optimal conditions for the production of ceramic-based materials have been determined. The degree of isomorphous substitution in the bismuth sublattice was found to decrease along with the increase of m and, accordingly, of h. The formation of a layered perovskite-like structure of the Aurivillius phases with a predetermined stoichiometry occurs with a gradual increase of m, while at $m > 5$ and $h > 2$ nm, isomorphous substitution leads to an increasing amount of impurities in the reaction system.

Thermal analysis data showed that the temperature for the initiation of materials decomposition gradually decreases along with the increasing m, and the Curie point and the sintering onset temperature are in one temperature domain.

The results of the Mössbauer and magnetometric studies made it possible to make an assumption that the magnetic ions in the internal positions of a perovskite-like block are engaged in an antiferromagnetic-type exchange interaction that affects the magnetic properties of the studied materials. The effect of isomorphous substitution in the bismuth sublattice on the nature of the iron ions distribution and the magnetic behavior of the Aurivillius phases is less pronounced. The features of the magnetic behavior of the obtained materials can be presumably explained by magnetic fluctuations.

Acknowledgement

This work was financially supported by the Russian Foundation for Basic Research (Grant No. 16-03-01056).

References

[1] Keeney L., Downing C., Schmidt M., Pemble M.E., Nicolosi V., Whatmore R.W. Direct atomic scale determination of magnetic ion partition in a room temperature multiferroic material. *Sci. Rep.*, 2017, **7**(1), P. 1737–1748.
[2] Faraz A., Maity T., Schmidt M., Deepak N., Roy S., Pemble M.E., Whatmore R.W., Keeney L. Direct visualization of magnetic-field-induced magnetoelectric switching in multiferroic Aurivillius phase thin films. *J. Am. Cer. Soc.*, 2017, **100**(3), P. 975–987.
[3] Keeney L., Maity T., Schmidt M., Amann A., Deepak N., Petkov N., Roy S., Pemble M. E., Whatmore R. W. Magnetic field-Induced ferroelectric switching in multiferroic Aurivillius phase thin films at room temperature. *J. Am. Ceram. Soc.*, 2013, **96**(8), P. 2339–2357.
[4] Varentsova A.S., Potkina M.N., von Malottki S., Heinze S., Bessarab P.F. Interplay between size and stability of magnetic skyrmions. *Nanosystems: Phys. Chem. Math.*, 2018, **9**(3), P. 356–363.
[5] Lomanova N.A., Gusarov V.V. On the limiting thickness of the perovskite-like block in the Aurivillius phases in the Bi_2O_3-TiO_2-Fe_2O_3 system. *Nanosystems: Phys. Chem. Math.*, 2011, **2**(3), P. 93–101.
[6] Lomanova N.A., Semenov V.G., Panchuk V.V., Gusarov V.V. Structural changes in the homologous series of the Aurivillius phases $Bi_{n+1}Fe_{n-3}Ti_3O_{3n+3}$. *J. Alloys Comp.*, 2012, **528**, P. 103–108.
[7] Aurrivillius B. Mixed bismuth oxides with layer lattices. I. *Ark. Kemi.*, 1949, **1**(1), P. 463–471.
[8] Sosnowska I., Peterlin-Neumaier T., Steichele E.J. Spiral magnetic ordering in bismuth ferrite. *Phys. C: Solid State Phys.*, 1982, **15**, P. 4835–4846.
[9] Lomanova N.A., Semenov V.G., Panchuk V.V., Gusarov V.V. Structural features and stability of the Aurivillius phases $Bi_{n+1}Fe_{n-3}Ti_3O_{3n+3}$. *Dokl. Chem.*, 2012, **447**(2), P. 293–295.
[10] Lomanova N.A., Morozov M.I., Ugolkov V.L., Gusarov V.V. Properties of Aurivillius phases in the $Bi_4Ti_3O_{12}$-$BiFeO_3$ system. *Inorganic Materials*, 2006, **42**(2), P. 189–195.
[11] Jartych E., Gaska K., Przewoznik J., Kapusta C., Lisinska-Czekaj A., Czekaj D., Surowiec Z. Hyperfine interactions and irreversible magnetic behavior in multiferroic Aurivillius compounds. *Nukleonika*, 2013, **58**, P. 47–51.
[12] Birenbaum A.Y., Ederer C. Potentially multiferroic Aurivillius phase $Bi_5FeTi_3O_{15}$: cation site preference, electric polarization, and magnetic coupling from first principles. *Phys. Rev. B*, 2014, **90**, P. 214109–214121.
[13] Lomanova N.A., Gusarov V.V. Impedance spectroscopy of polycrystalline materials based on the Aurivillius phase system $Bi_4Ti_3O_{12}$-$BiFeO_3$. *Nanosystems: Phys. Chem. Math.*, 2012, **3**(6), P. 112–122.
[14] Lomanova N.A., Pleshakov I.V., Volkov M.P., Gusarov V.V. Magnetic properties of Aurivillius phases $Bi_{m+1}Fe_{m-3}Ti_3O_{3m+3}$ with m=5.5, 7, 8. *Mat. Sci. Eng. B*, 2016, **214**, P. 51–56.
[15] Huang Y., Wang G., Sun Sh., Wang J., Peng R., Lin Y., Zhai X., Fu Zh., Lu Y.. Observation of exchange anisotropy in single-phase layer structured oxides with long periods. *Sci. Rep.*, 2015, **5**, P. 15261–15266.
[16] Pikula T., Dzik J., Guzdek P., Mitsiuk V.I., Surowiec Z., Panek R., Jartych E. Magnetic properties and magnetoelectric coupling enhancement in $Bi_5Ti_3FeO_{15}$ ceramics. *Ceram. Int.*, 2017, **43**(14), P. 11442–11449.
[17] Lomanova N.A., Pleshakov I.V., Volkov M.P., Gusarov V.V. The thermal behavior of mixed-layer Aurivillius phase $Bi_{13}Fe_5Ti_6O_{39}$. *J. Therm. Anal. Calorim.*, 2018, **131**, P. 473–478.
[18] Lomanova N.A., Tomkovich M.V., Ugolkov V.L., Gusarov V.V. Formation and thermal properties of nanocrystalline $Bi_4Ti_3O_{12}$. *Russ. J. Appl. Chem.*, 2017, **90**(6), P. 831–837.
[19] Lomanova N.A., Ugolkov V.L., Panchuk V.V., Semenov V.G. Formation and thermal behaviors of the Aurivillius phases $A_{m-1}Bi_2Fe_{m-3}Ti_3O_{3m+3-\delta}$ (A-Bi, Sr). *Russ. J. Gen. Chem.*, 2017, **87**(3), P. 365–372.
[20] Lomanova N.A., Gusarov V.V. Phase states in the $Bi_4Ti_3O_{12}$-$BiFeO_3$ section in the Bi_2O_3-TiO_2-Fe_2O_3 system. *Russ. J. Inorg. Chem.*, 2011, **56**(4), P. 616–620.
[21] Lomanova N.A., Ugolkov V.L., Gusarov V.V. Thermal behavior of layered perovskite-like compounds in the $Bi_4Ti_3O_{12}$-$BiFeO_3$system. *Glass Physics and Chemistry*, 2007, **33**(6), P. 608–612.
[22] Isupov V.A. Curie Temperatures of $A_{m-1}Bi_2M_mO_{3m+3}$ layered ferroelectrics. *Inorganic Materials*, 1997, **33**(9), P. 1106–1110.
[23] Snedden A., Hervoches Ch. H., Lightfoot Ph. Ferroelectric phase transition in $SrBi_2Nb_2O_9$ and $Bi_5Ti_3FeO_{15}$: a powder neutron diffraction study. *Phys. Rev.*, 2003, **67**, P. 092102–092105.
[24] Krzhizhanovskaya M., Filatov S., Gusarov V., Paufler P., Bubnova R., Morozov M., Meyer D.C. Aurivillius phases in the $Bi_4Ti_3O_{12}$-$BiFeO_3$ system: thermal behaviour and crystal structure. *Z. Anorg. Allg. Chem.*, 2005, **631**, P. 1603–1608.
[25] Yang J., Tong W., Liu Z., Zhu X.B., Dai J.M., Song W.H., Yang Z. R., Sun Y.P. Structural, magnetic, and EPR studies of the Aurivillius phase $Bi_6Fe_2Ti_3O_{18}$ and $Bi_6FeCrTi_3O_{18}$. *Phys. Rev. B*, 2012, **86**, P. 104410–104417.
[26] Dong X.W., Wang K.F., Wan J.G., Zhu J.S., Liu J.-M. Magnetocapacitance of polycrystalline $Bi_5Ti_3FeO_{15}$ prepared by sol-gel method. *J. Appl. Phys.*, 2008, **103**, P. 0941010–0941014.
[27] Morozov M.I., Mezentseva L.P., Gusarov V.V. Mechanism of formation of $Bi_4Ti_3O_{12}$. *Russ. J. Gen. Chem.*, 2002, **72**(7), P. 1038–1040.
[28] Morozov M.I., Gusarov V.V. Synthesis of $A_{m-1}Bi_2M_mO_{3m+3}$compounds in the $Bi_4Ti_3O_{12}$-$BiFeO_3$system. *Inorganic Matials*, 2002, **38**(7), P. 723–729.

[29] Lomanova N.A., Tomkovich M.V., Sokolov V.V., Gusarov V.V. Special features of formation of nanocrystalline $BiFeO_3$ via the glycine-nitrate combustion method. *Russ. J. Gen. Chem.*, 2016, **86**(10), P. 2256–2262.
[30] Proskurina O.V., Tomkovich M.V., Bachina A.K., Sokolov V.V., Danilovich D.P., Panchuk V.V., Semenov V.G., Gusarov V.V. Formation of nanocrystalline $BiFeO_3$ under hydrothermal conditions. *Russ. J. Gen. Chem.*, 2017, **87**(11), P. 2507–2515.
[31] Dubey S., Subohi O., Kurchania R. Optimization of calcination and sintering temperature of sol-gel synthesised $Ba_2Bi_4Ti_5O_{18}$, $Pb_2Bi_4Ti_5O_{18}$ and $Sr_2Bi_4Ti_5O_{18}$ ceramics. *Ceram. Int.*, 2017, **43**(15), P. 12755–12763.
[32] Lomanova N.A., Gusarov V.V. Effect of the phase composition of the starting mixture on the formation of the layered perovskite-like compound $Bi_7Fe_3Ti_3O_{21}$. *Russ. J. Inorg. Chem.*, 2010, **55**(10), P. 1541–1545.
[33] Lomanova N.A., Gusarov V.V. Effect of surface melting on the formation and growth of nanocrystals in the Bi_2O_3–Fe_2O_3 system. *Russ. J. Gen. Chem.*, 2013, **83**, P. 2251–2253.
[34] Tugova E.A., Travitskov A.V., Tomkovich M.V., Sokolov V.V., Nenasheva E.A. Solid -phase synthesis and dielectric properties of materials based on $LaAlO_3$–$CaTiO_3$ system. *Russ. J. Appl. Chem.*, 2017, **90**(11), P. 1738–1745.
[35] Tugova E.A. New $DySrAlO_4$ compound synthesis and formation process correlations for $LnSrAlO_4$ (Ln - Nd, Gd, Dy) series. *Acta Metallurgica Sinica (English Letters)*, 2016, **29**(5), P. 450–456.
[36] Popkov V.I., Tugova E.A., Bachina A.K., Almyasheva O.V. The formation of nanocrystall ine orthoferrites of rare-earth elements $XFeO_3$ (X -Y, La, Gd) via heat treatment of coprecipitated hydroxides. *Russ. J. Gen. Chem.*, 2017, **87**(11), P. 2516–2524.
[37] Ostroushko A.A., Russkikh O.V. Oxide material synthesis by combustion of organic-inorganic. *Nanosystems: Phys. Chem. Math.*, 2017, **8**(4), P. 476–502.
[38] Tugova E., Yastrebov S., Karpov O., Smith R. $NdFeO_3$ nanocrystals under glycine-nitrate combustion formation. *J. Cryst. Grow.*, 2017, **467**, P. 88–92.
[39] Morozov M.I., Lomanova N.A., Gusarov V.V. Specific Features of $BiFeO_3$ formation in a mixture of bismuth(III) and iron(III) oxides. *Russ. J. Gen. Chem.*, 2003, **73**, P. 1772–1776.
[40] Bespalova Zh.I., Khramenkova A.V. The use of transient electrolysis in the technology of oxide composite nanostructured materials: review. *Nanosystems: Phys. Chem. Math.*, 2016, **7**(3), P. 433–450.
[41] Gusarov V.V., Suvorov S.A. Melting-point of locally equilibrium surface phases in polycrystalline systems based on a single volume phase. *Russ. J. Appl. Chem.*, 1990, **63**(8), P. 1479–1484.
[42] Gusarov V.V. The thermal effect of melting in polycrystalline systems. *Thermochimica Acta*, 1995, **256**(2), P. 467–472.
[43] Gusarov V.V. Fast Solid-Phase Chemical Reactions. *Russ. J. Gen. Chem.*, 1997, **67**(12), P. 1846.
[44] Shannon R.D., Prewitt C.T. Effective ionic radii in oxides and fluorides. *Acta Cristallogr. B.*, 1969, **25**(6), P. 928–929.

NANOSYSTEMS: PHYSICS, CHEMISTRY, MATHEMATICS, 2018, 9 (5), P. 688–695

Effect of Ce cations on the crystallite size and pore structure genesis in nanostructured rutile after calcination

N. V. Shikina[1], E. V. Bessudnova[1], V. A. Ushakov[1], A. P. Nikitin[2], M. S. Mel'gunov[1], A. V. Ishchenko[1], Z. R. Ismagilov[1,2]

[1]Boreskov Institute of Catalysis SB RAS, 5 Lavrentiev Ave., 630090, Novosibirsk, Russia
[2]Institute of Coal Chemistry and Materials Science, Federal Research Center of Coal and Coal Chemistry SB RAS, 18 Sovetskiy pr., 650000, Kemerovo, Russia
shikina@catalysis.ru

DOI 10.17586/2220-8054-2018-9-5-688-695

A method for the low-temperature synthesis of titania with the 3D rutile nanostructure was developed, and the effect of introduced cerium ions on the thermal stability of the material was studied. According to XRD, TEM, Raman spectroscopy and BET data, the introduction of 3 – 10 wt.% Ce into the rutile matrix decreases the growth of nanorutile crystallites under the action of high temperatures ranging from 300 – 1000 °C and provides the formation of a more porous structure in comparison with unmodified samples. Cerium cations are stabilized in the region of interblock boundaries or in the structural defects of rutile TiO_2 and are released as the bulk CeO_2 phase only at 1000 °C, which does not exert a stabilizing effect at this temperature.

Keywords: titanium dioxide, nanostructured rutile, hierarchical architecture, porous structure, thermal treatment.

Received: 31 May 2018

Revised: 3 August 2018

1. Introduction

In recent years, the study of TiO_2 hierarchical nanostructures has been a hot topic of research in the field of effective photocatalytic materials due to their high specific surface area, beneficial light absorption, and appropriate refractive index, along with other excellent physical and chemical properties [1–3]. The potent photocatalytic properties of TiO_2 hierarchical nanostructures with rutile modification have been established in degradation of methyl orange, methylene blue and brilliant red X-3B [4–7]. Rutile TiO_2 has a high refractive index, which determines its application not only in photocatalysis but also in optical filters, protected printing and production of cosmetics and dyes [8].

Bulk rutile is the most stable phase among polymorphous modifications of titania (anatase, brookite and rutile). The formation of rutile from anatase or amorphous TiO_2 species occurs after reaching a critical size of the particles and temperatures above 465 °C. At the polymorphous transition temperatures the particles agglomerate and the specific surface area decreases below 7 m^2/g [9]. The emphasis is now focused on the development of synthetic strategies for nanostructured titania that would permit its controllable three-dimensional formation. TiO_2 synthesis under conditions leading to the formation of 3D structures with hierarchical packing of nanostructured particles makes it possible to obtain a material with the stable rutile phase and high specific surface area [10].

The properties of a composite hierarchical system are determined mostly by the properties of agglomerated particles, their packing and morphology, i.e. the texture of the material. Hierarchical rutile TiO_2 microspheres assembled by nanowire bundles were synthesized upon hydrothermal conditions and then treated by thermally annealed in [4]. T. Yan and co-authors relate structural defects and high functional properties of rutile to the "microcavity" structure which existed between the roughly parallel nanowires of TiO_2 microspheres. Upon annealing at 300 and 500 °C the microspherical shape was maintained, whereas the interface of the nanowire bundles became blurred and the related microstructural feature greatly changed. At 700 °C, nanowires were converted into larger nanorods. The authors attribute such integration between quasi-parallel nanowires to a possible growth of crystals in the perpendicular direction. It is clear that the annealing treatment seriously destroyed the microcavity structure.

Our earlier studies [11–13] demonstrated the possibility of obtaining rutile with a hierarchical 3D nanostructure composed of fan-shaped nanofibers (specific surface area > 140 m^2/g) at atmospheric pressure and a temperature below 100 °C. This revealed the control the main synthesis parameters (e.g. temperature, concentration of Ti^{4+} and Cl^- ions) had on the formation of the rutile phase. However, the produced material has a low crystallinity and a high defect content and interblock boundaries, which determine the low stability of its textural properties after thermal treatment [14]. Changes in the morphology of the material were observed at the 300 – 400 °C, lower than temperatures previously reported in [4]. The enhancement of thermal stability of the material is a topical task

because textural characteristics of nanostructured rutile are of key importance for its application as a support of catalysts or photocatalysts.

In [15–17], titania was modified with different metal cations, shifting the anatase $\rightarrow$ rutile polymorphous transformations to higher temperatures, which is accomplished by inhibiting the growth of crystallites stabilized by CeO_2 [15], SiO_2 [16] or Y_2O_3 [17] interlayers. Such modification results in the formation of nanocrystalline anatase structure comprising incoherently intergrown particles; this significantly hinders the growth of anatase crystallites to the critical values at which anatase converts to rutile. In [18, 19] it was shown that modification with La and Ce ions [18] or La and Mg ions [19] stabilizes the alumina pore structure and specific surface area. The authors revealed a relation between the effect exerted by metal cations on polymorphous transformations in alumina and its structural-mechanical properties.

In the present work, we explored the possibility of decreasing rutile crystallite growth and preventing the deterioration of its pore structure parameters during thermal treatment upon modification of the initial low-temperature rutile samples with cerium cations. Since rutile is a stable phase of titania, it is evident that polymorphous transformations will not occur; however, the formation of the stabilizing ceria interlayers in nanostructured rutile may hinder the growth of nanofiber crystallites in the perpendicular direction.

2. Experimental

The method employed for the synthesis of nanostructured rutile is described in detail in [13]. Briefly, titania (rutile) was synthesized by the sol-gel method via the hydrolysis of titanium tetrachloride in water under the following conditions: molar ratios $[Cl^{1-}]/[Ti^{4+}]$ = 4 and $[H_2O]/[Ti^{4+}]$ = 39, and the hydrolysis temperature of 90 °C. To improve thermal stability, an aqueous solution $Ce(NO_3)_3 \cdot 6H_2O$ was deposited on the dried rutile powder by incipient wetness impregnation to obtain 3, 5, 7 and 10 wt.% CeO_2 content in the final samples. After that, the samples with different CeO_2 content were calcined at 300, 500, 700 and 1000 °C. A series of rutile samples modified with ceria was examined by XRD, BET, Raman spectroscopy and TEM. A rutile sample without CeO_2 served as the reference sample.

The chemical compositions of the synthesized samples were estimated by inductively coupled plasma atomic emission spectroscopy on an Optima 4300 DV instrument and by X-ray fluorescence analysis on an ARL-Advant'x analyzer with an Rh-anode X-ray tube. XRD studies were performed using an HZG-4C (Freiberger Präzisionsmechanik) X-ray diffractometer with a CoKα monochromatic source ($\lambda = 1.79021$ Å) in a continuous mode over the 2θ angular range from 20 to 85°. Crystallite sizes were estimated by the Scherrer formula. The measurement error is in the range of: 30 – 50 $\pm$ 2; 50 – 80 $\pm$ 5; 80 – 120 $\pm$ 10; 120 – 180 $\pm$ 25; 180 – 250 $\pm$ 40; 250 – 300 $\pm$ 80 Å. Raman spectroscopy studies were carried out on a Renishaw Invia Basis spectrometer at 3600 – 100 cm^{-1}. Textural properties (specific surface area and pore volume) were analyzed by low-temperature nitrogen adsorption (ASAP-2400, Micromeritics) and mercury porosimetry (AutoPore IV 9500 V1.09, Micromeritics). The measurement error of textural parameters is 5 %. Transmission electron microscopy (TEM) and high resolution transmission electron microscopy (HR-TEM) images were obtained using a JEM-2010 (JEOL, Japan) microscope.

3. Results and discussion

Particles of the material obtained by $TiCl_4$ hydrolysis belong to the rutile phase and have an intricate packing system; their characteristics correspond to those of 3D hierarchical structures. At the first structural level, the primary particles coherently inter-grow to form nanofibers. The oriented addition of the primary particles includes a spontaneous self-organization of adjacent particles due to which they become involved in the joint crystallographic orientation with subsequent agglomeration of the particles at the plane interface [20]. Binding of the particles decreases the total energy of their aggregates due to the surface energy of uncompensated bonds of primary particles, thus leading to the coherent intergrowth of particles, which is more favorable in terms of energy. Nanofibers forming the first structural level are joined into the fan-shaped aggregates that constitute the second structural level. At the third level the aggregates merge into large 3D particles [13].

3.1. XRD

X-ray diffraction (XRD) studies of the samples showed that the crystallite size of rutile is 55 – 70 Å along the (110) direction and 140 – 200 Å along (002) [11]. A clear dependence of crystallite sizes on the synthesis temperature was not observed. However, substantial changes in the crystallite size were revealed after calcination of the samples at 300, 500, 700 and 1000 °C (Table 1). Upon calcination at 300 – 500 °C the crystallite size of rutile increased 2 – 3-fold, and calcination at 700 and 1000 °C resulted in the formation of large crystallites with the size greater than 1000 Å along all crystallographic directions. Thus, calcination at temperatures above 700 °C does not produce noticeable changes in the XRD pattern of the samples.

The rutile samples modified with cerium cations also showed an increase in the crystallite size upon calcination (Table 1). However, the crystallite size of the samples with Ce is much smaller in all crystallographic directions as compared to the rutile samples without cerium addition at a temperature up to 700 °C. On diffraction patterns of the rutile samples modified with 3 – 10 % CeO_2, the bulk ceria phase manifests itself only after calcination at 1000 °C (Fig. 1); at this temperature ceria does not exert a stabilizing effect. The crystallite size of the 1000 °C samples strongly exceeds 1000 Å both in the modified rutile series and in the samples without additives. Peaks corresponding only to the rutile phase are observed on diffraction patterns of the samples calcined at 300 – 700 °C. Peaks corresponding to the interaction phases in the Ce–Ti–O system were also not detected, and the crystal lattice parameters of rutile correspond to those of pure rutile. Supposedly, ceria is in a highly dispersed state and is located mostly on the surface of rutile crystallites, thus preventing their intergrowth upon calcination.

TABLE 1. Crystallite sizes of the calcined samples of nanostructured rutile with different ceria content

T_{calc}, °C	CeO_2, %	Crystallite sizes (E) along crystallographic directions				
		110 32.00°	**101 42.19°**	**111 48.30°**	**211 64.09°**	**002 74.45°**
After synthesis 90	0	60	130	120	70	165
300	0	125	200	190	140	230
	3	95	170	170	100	230
	5	70	170	170	95	230
	7	70	170	170	95	230
	10	70	170	170	95	230
500	0	190	250	240	200	250
	3	140	200	200	130	250
	5	110	200	200	150	250
	7	110	200	200	150	250
	10	110	200	200	150	250
700	0	≫1000	≫1000	≫1000	≫1000	≫1000
	3	220	400	300	160	190
	5	180	270	300	160	190
	7	170	210	270	150	200
	10	170	180	250	150	200
1000	0	≫1000	≫1000	≫1000	≫1000	≫1000
	3	≫1000	≫1000	≫1000	≫1000	≫1000
	5	≫1000	≫1000	≫1000	≫1000	≫1000
	7	≫1000	≫1000	≫1000	≫1000	≫1000
	10	≫1000	≫1000	≫1000	≫1000	≫1000

3.2. Raman spectroscopy

Rutile has only three active modes in the Raman spectra: $145A_{1g}$, $447E_g$, and $612B_{1g}$ [21]. Along with the indicated modes, a peak at ca. 240 cm^{-1}, which can be assigned to the composite vibration, appears in the spectrum. Ceria has a cubic crystal structure of the fluorite type and manifests only one resolved combination mode, $465F_{2g}$ [22]. The Raman data obtained for the samples of pure rutile and rutile with the addition of 5 % CeO_2 are listed in Table 2.

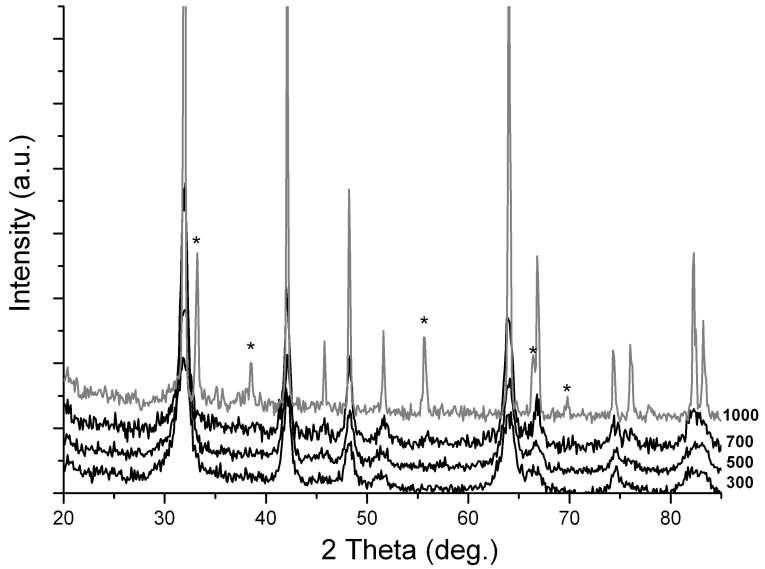

FIG. 1. The diffraction pattern of the rutile samples modified with 5 % CeO_2 after their calcination at 300, 500, 700 and 1000 °C (peaks corresponding to the CeO_2 phase are marked by asterisks)

TABLE 2. Main and additional peaks of rutile in the Raman spectra

$T_{calcination}$, $T_{synthesis}$, °C	Position of main peaks / Half-width, cm^{-1}				Additional peaks, cm^{-1}
Rutile + 5 % CeO_2					
100	141 / 5	234 / 77	444 / 45	608 / 45	822, 1601
300	142 / 4	248 / 68	424 / 71	606 / 76	169 / 12, 1597
500	141 / 4	242 / 92	433 / 55	607 / 63	167 / 7, 1599
700	141 / 5	234 / 87	442 / 43	608 / 50	821, 1603
1000	142 / 5	234 / 87	444 / 44	609 / 45	821, 1606
Rutile					
90	—	239 / 63	437 / 49	605 / 55	1601
300	145 / 12	234 / 67	440 / 56	608 / 54	821, 1601
500	142 / 8	233 / 81	442 / 43	609 / 48	821, 1602
700	142 / 6	231 / 89	444 / 39	609 / 43	819, 1603
1000	142 / 5	231 / 87	444 / 39	608 / 44	824, 1604

For all the samples, the B_{1g} peak did not change its position. In the case of rutile samples synthesized without CeO_2, the half-width of the B_{1g} peak decreased with raising the temperature from 55 to 43 cm^{-1}, which testifies to the growth of crystallites. For the modified samples, at a calcination temperature of 300 °C the half-width of this peak increased from 45 to 76 cm^{-1}, which indicates a decrease in the size of initial nanoparticles or a structural disordering with an increase in the bond length between atoms in the crystal lattice at the retained translational symmetry. This may occur due to intercalation of cerium cations between crystallites in the region of interblock boundaries where the rutile structure is strongly disordered, which makes the structural defects even more pronounced. As the temperature is raised to 1000 °C, the half-width of the B_{1g} peak decreases, similar to the case without CeO_2. The main active vibration of CeO_2 does not appear in the Raman spectra up to 1000 °C.

The most pronounced changes in the E_g peak of the modified Ce samples are observed upon calcination at 300 °C: the position of the peak shifts to the red region from 444 to 424 cm^{-1} with a simultaneous broadening of the band from 45 to 71 cm^{-1}, which supports the assumption that defects in the nanoparticles increases, thus decreasing their sizes. A further increase in the temperature shifts the E_g peak to its initial value.

The Raman spectra of the modified samples after calcination at 300 and 500 °C show the peak at ca. 165 cm^{-1}, which can be attributed to a minor decrease in the lattice symmetry. This vibration disappears at elevated temperatures, which testifies to restoration of the structure.

As seen in Table 2, at similar calcination temperatures the half-widths of all peaks of the modified samples are greater than the half-widths of peaks of the samples without CeO_2; this testifies to a smaller size of the rutile particles with CeO_2, which agrees with the XRD data.

3.3. BET

Investigation of the textural properties of rutile samples by low-temperature nitrogen adsorption revealed that in the entire range of temperatures the modified samples have a more developed pore structure with a higher specific surface area as compared to the zero sample (Table 3). All the samples with CeO_2 and pure rutile that were calcined at 300 and 500 °C have comparable pore volumes that range from 0.1 to 0.13 cm^3/g. As the calcination temperature is raised, the pore volume values remain constant, whereas the specific surface area decreases and the average pore size increases; this testifies to implementation of the surface-diffusion sintering mechanism in the temperature range of 300 – 500 °C [15]. Pore broadening upon elevation of the calcination temperature from 300 to 500 °C is observed also on differential curves of the pore size distribution (Fig. 2). It should be noted that although the distribution curves are close to each other, the amount of thin pores with the effective diameter 3.5 nm

TABLE 3. Pore structure parameters for nanostructured rutile samples with different CeO_2 content

T_{calc}, °C	% CeO_2	A_{BET}, m^2/g	V_Σ, cm^3/g	D_{pore}, nm
300	0	48.9	0.11	8.7
	3	63.2	0.12	7.9
	5	76.9	0.13	6.6
	7	71.4	0.11	6.3
	10	62.2	0.10	6.8
500	0	35.3	0.11	13
	3	39.1	0.11	11.6
	5	42.4	0.11	10.4
	7	41.8	0.10	9.5
	10	39.2	0.10	10.2
700	0	5.1	0.03	27.7
	3	14.8	0.09	23.3
	5	15.1	0.08	22.6
	7	14.2	0.08	23.2
	10	14.5	0.08	21.8
1000	0	1.2	0.005	16.2
	3	2	0.006	11.7
	5	2.2	0.005	9.7
	7	2.1	0.006	11.9
	10	2.1	0.01	21

is greater in the modified samples than in pure rutile. Calcination at 700 and 1000 °C decreases both the specific surface area and the pore volume of all the samples; therewith, a decrease in the pore structure parameters for modified samples is less pronounced than for the calcined samples of pure rutile (Table 3). At 700 °C the specific surface area and pore volume of the samples with Ce are three times higher than the corresponding characteristics of pure rutile. The optimal ceria content in the samples is 5 wt.%. A further increase in the CeO_2 concentration does not produce an additional beneficial effect. At 1000 °C sintering of meso- and macropores occurs, the pore structure parameters are extremely low for all the samples, and these samples can be characterized as nonporous. The revealed regularities are clearly seen on differential curves of the pore size distribution for the series of 700 and 1000 °C samples (Fig. 2).

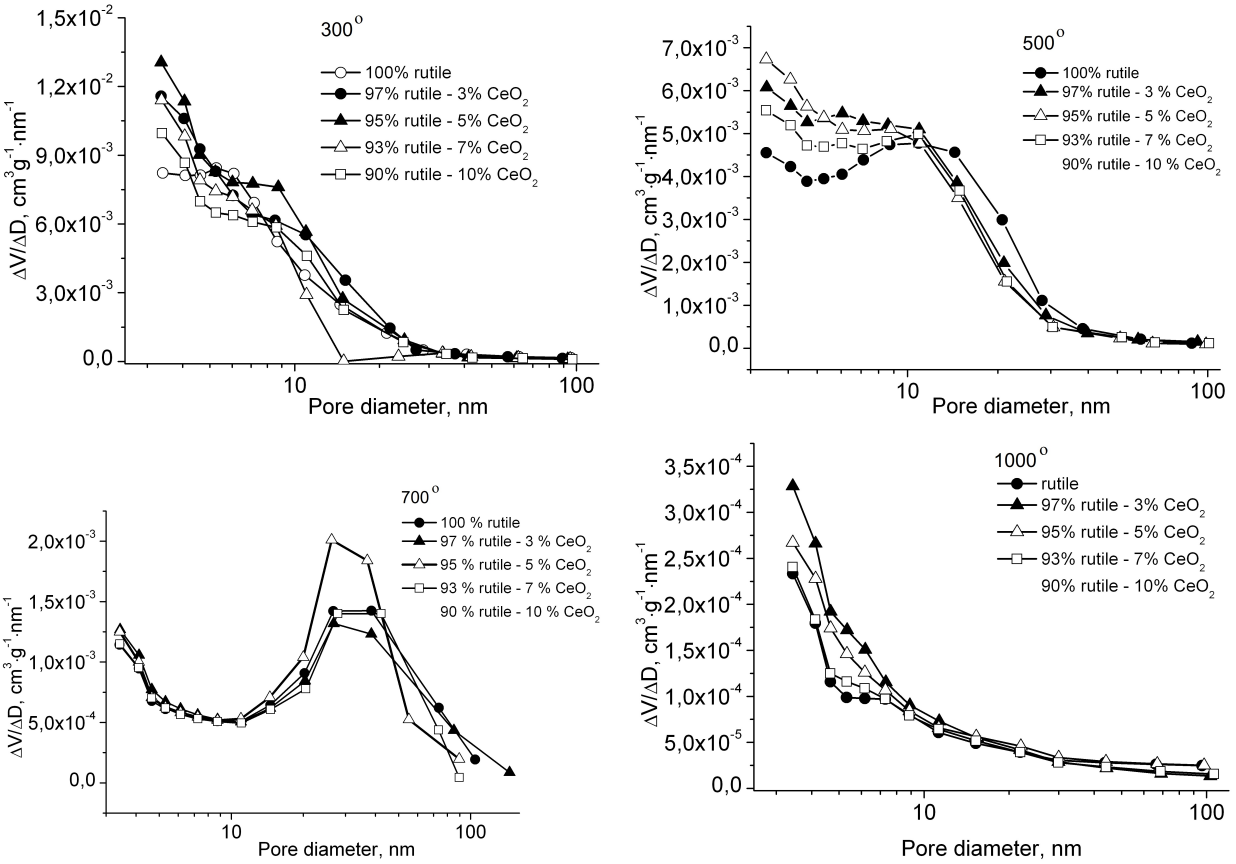

FIG. 2. Differential curves of the pore size distribution for the calcined rutile samples with different ceria content

3.4. HRTEM

High-resolution TEM images (Fig.3(a,b)) illustrate the intergrowth of pure rutile crystallites along interblock boundaries at 500 °C (Fig. 3(a)) and 700 °C (Fig. 3(b)). At 500 °C, the pore structure formed by narrow slit-like pores is retained (the pores are marked by arrows in the Figure 3). At 700 °C the pores virtually disappear. A different pattern is observed for the rutile sample modified with 5 % CeO_2 (Fig. 3(c,d)): the well developed pores between rutile crystallites are observed at both 500 °C (Fig. 3(c)) and 700 °C (Fig. 3(d)).

The TEM images also clearly demonstrate the difference in the crystallite sizes of rutile. The introduction of the Ce cation into the rutile matrix decreases the growth of its crystallites virtually by a factor of 2. Between rutile particles one can see the interlayers of weakly crystallized ceria (Fig. 3(d), within the oval), which prevent the intergrowth of rutile crystallites along the interblock boundaries. Fig. 3 displays TEM images only for the samples calcined at 500 and 700 °C, but this trend is observed also at other calcination temperatures.

It should be noted that the crystallized ceria phase was not detected in the samples calcined at 300 – 700 °C that were examined by XRD, Raman spectroscopy and TEM (using the measured interplanar distances). Most likely, titania inhibits the crystallization of ceria, which concentrates in the region of interblock boundaries of rutile

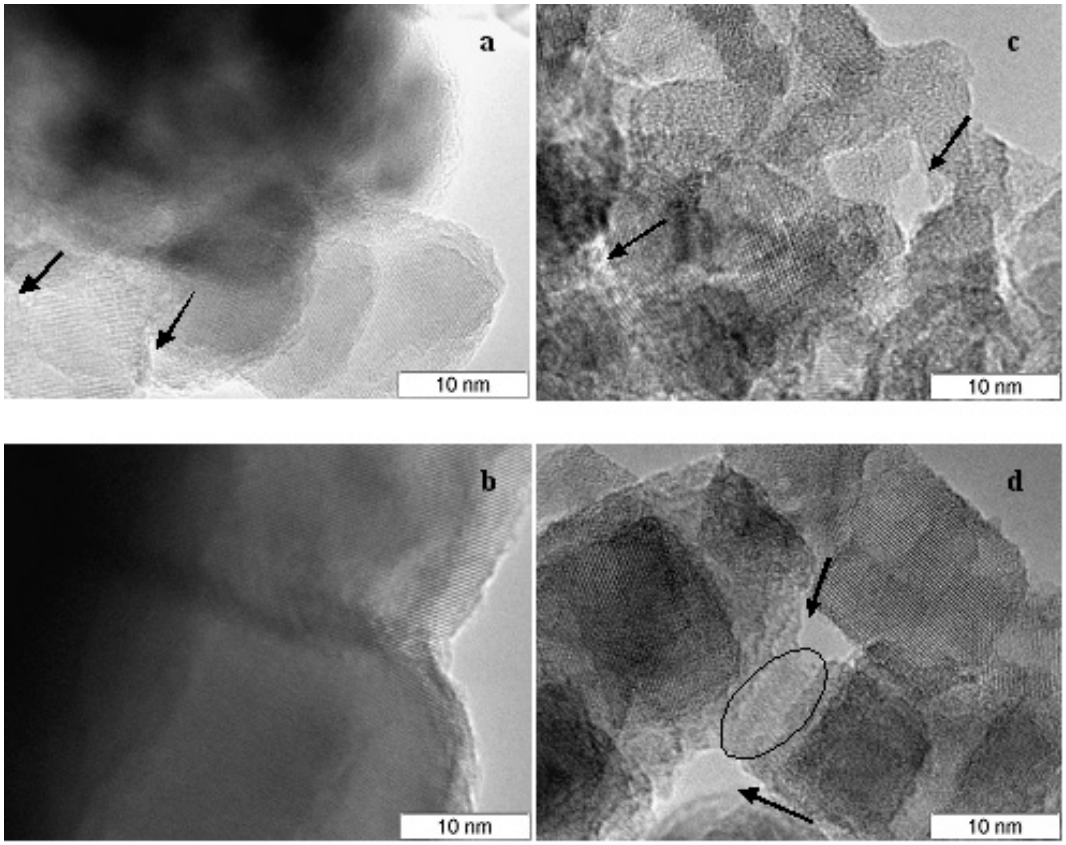

FIG. 3. High resolution TEM images of pure rutile samples calcined at 500 (a) and 700 °C (b) and rutile samples with the addition of 5 % CeO_2 calcined at 500 (c) and 700 °C (d)

in the amorphized state. And only upon calcination at 1000 °C a part of cerium is released as an oxide from the region of interblock boundaries with the formation of surface CeO_2 clusters and then the bulk CeO_2 phase having the fluorite structure.

4. Conclusion

TiO_2 (rutile) samples with the hierarchical 3D nanostructure were synthesized and modified with cerium cations; the effect of the modifying additive on the structural, textural and morphological properties of nanorutile was studied as a function of the calcination temperature. According to XRD, TEM, Raman spectroscopy and BET data, the introduction of 3 – 10 wt.% cerium into the rutile matrix decreases the growth of nanorutile crystallites at high temperatures ranging from 300 – 1000 °C and provides the formation of a more porous structure in comparison with unmodified samples. The optimal ceria content in the samples was found to be 5 wt.%. A further increase in the CeO_2 concentration does not produce an additional beneficial effect. Cerium cations are stabilized in the region of interblock boundaries or in the structural defects of TiO_2 and are released as the bulk CeO_2 phase only at 1000 °C, which does not exert a stabilizing effect at this temperature.

Acknowledgements

This work was conducted within the framework of the budget project # AAAA-A17-117041710090-3 for Boreskov Institute of Catalysis.

References

[1] Wu Z., Wu Q., et al. Progress in the synthesis and applications of hierarchical flower-like TiO_2 nanostructures. *Particuology*, 2014, **15**, P. 61–70.

[2] Liu W., Wang A., et al. Preparation and photocatalytic activity of hierarchically 3D ordered macro/mesoporous titania inverse opal films. *Microporous and Mesoporous Materials*, 2015, **204**, P. 143–148.

[3] Chen P.C., Tsai M.C., et al. The “cascade effect” of nano/micro hierarchical structure: A new concept for designing the high photoactivity materials – An example for TiO_2. *Applied Catalysis B: Environmental*. 2013, **142–143**, P. 752–760.

[4] Yan T., Yuan R., Li W., You J. Origin of superior photocatalytic activity in rutile TiO_2 hierarchical microspheres: The dominate role of "microcavity" structure. *Applied Catalysis A: General*, 2014, **478**, P. 204–210.
[5] Noh J., Yi M., et al. A facile synthesis of rutile-rich titanium oxide nanoparticles using reverse micelle method and their photocatalytic applications. *Journal of Industrial Engineering Chemistry*, 2016, **33**, P. 369–373.
[6] Zhang J., Liu P., et al. One-step synthesis of rutile nano-TiO_2 with exposed $\{1\ 1\ 1\}$ facets for high photocatalytic activity. *Journal of Alloys and Compounds*, 2015, **632**, P. 133–139.
[7] Li Y., Liu J., Jia Z. Morphological control and photodegradation behavior of rutile TiO_2 prepared by a low-temperature process. *Materials Letters*, 2006, **60**, P. 1753–1757.
[8] Pffaf G., Reynders P. Angle-Dependent Optical Effects Deriving from Submicron Structures of Films and Pigments. *Chemical Reviews*, 1999, **99**, P. 1963–1981.
[9] Gribb A.A., Banfield J.F. Particle size effects on transformation kinetics and phase stability in nanocrystalline TiO_2. *American Mineralogist*, 1997, **82**, P. 717–728.
[10] Fattakhova-Rohlfing D., Zaleska A., Bein T. Three-Dimensional Titanium Dioxide Nanomaterials. *Chemical Reviews*, 2014, **114**, P. 9487–9558.
[11] Ismagilov Z.R., Shikina N.V., Bessudnova E.V., Ushakov V.A. Effect of synthesis temperature on properties of nanoscale rutile with high surface area. *Nanotechnologies in Russia*, 2014, **9** (1–2), P. 21–25.
[12] Bessudnova E.V., Shikina N.V., Ismagilov Z.R. Nanoscale titanium dioxide synthesized by sol-gel method. *International Scientific Journal for Alternative Energy and Ecology*, 2014 , **7** (147), P. 39–47.
[13] Bessudnova E.V., Shikina N.V., Ismagilov Z.R. Synthesis and characterization of 3D hierarchical rutile nanostructures: Effects of synthesis temperature and reagent concentrations on the texture and morphology. *Nanotechnologies in Russia*, 2017, **12** (3–4), P. 156–164.
[14] Shikina N.V., Bessudnova E.V., et al. Study of nanostructured TiO_2 rutile with hierarchical 3-D architecture. Effect of the synthesis and calcinations temperature. *Journal of Nanoscience and Nanotechnology*, sent to the press.
[15] Zenkovets G.A., Shutilov A.A., et al. Formation of the structure of cerium oxide-modified titanium dioxide. *Kinetics and Catalysis*, 2007, **48** (5), P. 742–748.
[16] Zenkovets G.A., Gavrilov V.Yu., Shutilov A.A., Tsybulya S.V. Effect of silicon dioxide on the formation of the phase composition and pore structure of titanium dioxide with the anatase structure. *Kinetics and Catalysis*, 2009, **50** (5), P. 760–767.
[17] Shutilov A.A., Zenkovets G.A., Gavrilov V.Yu., Tsybulya S.V. Effect of yttrium oxide on the formation of the phase composition and porous structure of titanium dioxide. *Kinetics and Catalysis*, 2011, **52** (1), P. 111–118.
[18] Koryabkina N.A., Shkrabina R.A., et al. Study of the Catalysts of Fuel Combustion. XVII. Effect of Lanthanum and Cerium on Structural and Mechanical Properties of Alumina. *Kinetics and Catalysis*, 1997, **38** (1), P. 112–116.
[19] Koryabkina N.A., Shkrabina R.A., Ushakov V.A., Ismagilov Z.R. Synthesis of a mechanically strong and thermally stable alumina support for catalyst used in combustion processes. *Catalysis Today*, 1996, **29** (1–4), P. 427–431.
[20] Penn R.L., Banfield J.F. Imperfect oriented attachment: dislocation generation in defect-free nanocrystals. *Science*, 1998, **281**, P. 969–971.
[21] Handbook of Minerals Raman Spectra (ENS-Lyon). Free database 2000–2018. `URL: www.ens-lyon.fr/LST/Raman/spectrum.php?nom=rutile`.
[22] Cui J., Hope G.A. Raman and Fluorescence Spectroscopy of CeO_2, Er_2O_3, Nd_2O_3, Tm_2O_3, Yb_2O_3, La_2O_3, and Tb_4O_7. *Journal of Spectroscopy*, 2015, **2015**, 940172.

NANO Ф&Х&М

NANOSYSTEMS:

PHYSICS, CHEMISTRY, MATHEMATICS

INFORMATION FOR AUTHORS

The journal publishes research articles and reviews, and also short scientific papers (letters) which are unpublished and have not been accepted for publication in other magazines. Articles should be submitted in English. All articles are reviewed, then if necessary come back to the author to completion.

The journal is indexed in Web of Science Core Collection (Emerging Sources Citation Index), Chemical Abstract Service of the American Chemical Society, Zentralblatt MATH and in Russian Scientific Citation Index.

Author should submit the following materials:

1. Article file in English, containing article title, the initials and the surname of the authors, Institute (University), postal address, the electronic address, the summary, keywords, MSC or PACS index, article text, the list of references.
2. Files with illustrations, files with tables.
3. The covering letter in English containing the article information (article name, MSC or PACS index, keywords, the summary, the literature) and about all authors (the surname, names, the full name of places of work, the mailing address with the postal code, contact phone number with a city code, the electronic address).
4. The expert judgement on possibility of publication of the article in open press (for authors from Russia).

Authors can submit a paper and the corresponding files to the following addresses: nanojournal.ifmo@gmail.com, popov1955@gmail.com.

Text requirements

Articles should be prepared with using of text editors MS Word or LaTex (preferable). It is necessary to submit source file (LaTex) and a pdf copy. In the name of files the English alphabet is used. The recommended size of short communications (letters) is 4-6 pages, research articles– 6-15 pages, reviews – 30 pages.

Recommendations for text in MS Word:

Formulas should be written using Math Type. Figures and tables with captions should be inserted in the text. Additionally, authors present separate files for all figures and Word files of tables.

Recommendations for text in LaTex:

Please, use standard LaTex without macros and additional style files. The list of references should be included in the main LaTex file. Source LaTex file of the paper with the corresponding pdf file and files of figures should be submitted.

References in the article text are given in square brackets. The list of references should be prepared in accordance with the following samples:

[1] Surname N. *Book Title*. Nauka Publishing House, Saint Petersburg, 2000, 281 pp.
[2] Surname N., Surname N. Paper title. *Journal Name*, 2010, **1** (5), P. 17-23.
[3] Surname N., Surname N. Lecture title. In: Abstracts/Proceedings of the Conference, Place and Date, 2000, P. 17-23.
[4] Surname N., Surname N. Paper title, 2000, URL: http://books.ifmo.ru/ntv.
[5] Surname N., Surname N. Patent Name. Patent No. 11111, 2010, Bul. No. 33, 5 pp.
[6] Surname N., Surname N. Thesis Title. Thesis for full doctor degree in math. and physics, Saint Petersburg, 2000, 105 pp.

Requirements to illustrations

Illustrations should be submitted as separate black-and-white files. Formats of files – jpeg, eps, tiff.

NANOSYSTEMS:

PHYSICS, CHEMISTRY, MATHEMATICS

Журнал зарегистрирован
Федеральной службой по надзору в сфере связи, информационных технологий и массовых коммуникаций
(свидетельство ПИ № ФС 77 - 49048 от 22.03.2012 г.)
ISSN 2220-8054

Учредитель: федеральное государственное автономное образовательное учреждение высшего образования
«Санкт-Петербургский национальный исследовательский университет информационных технологий, механики и оптики»

Издатель: федеральное государственное автономное образовательное учреждение высшего образования
«Санкт-Петербургский национальный исследовательский университет информационных технологий, механики и оптики»

Отпечатано в Учреждении «Университетские телекоммуникации»
Адрес: 197101, Санкт-Петербург, Кронверкский пр., 49

Подписка на журнал НФХМ
На первое полугодие 2019 года подписка осуществляется через
ОАО Агентство «Роспечать»
Подписной индекс 57385 в каталоге «Издания органов научно-технической информации»